NASA TN D-1481

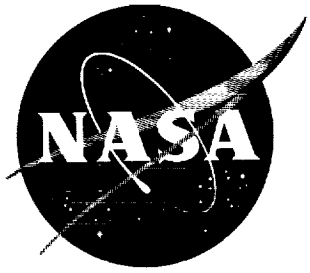

TECHNICAL NOTE

D-1481

AERODYNAMIC CHARACTERISTICS OF FOUR-DUCT TANDEM VTOL-AIRCRAFT CONFIGURATIONS

By William A. Newsom, Jr.

Langley Research Center
Langley Station, Hampton, Va.

NATIONAL AERONAUTICS AND SPACE ADMINISTRATION
WASHINGTON
January 1963

code 1
copy #1

NATIONAL AERONAUTICS AND SPACE ADMINISTRATION

TECHNICAL NOTE D-1481

AERODYNAMIC CHARACTERISTICS OF FOUR-DUCT TANDEM VTOL-AIRCRAFT CONFIGURATIONS

By William A. Newsom, Jr.

SUMMARY

This paper presents a summary of several wind-tunnel investigations conducted for the study of the aerodynamic and stability and control characteristics of four similar configurations of vertical take-off and landing (VTOL) aircraft powered by four tilting ducted propellers arranged in tandem pairs. Specifically, the two rear ducts were mounted close alongside the upper rear portion of the fuselage with small wing panels attached to the outboard side of the ducts or were mounted outboard on the tips of a small wing located high on the rear portion of the fuselage. The two front ducts were always mounted close inboard on the forward part of the fuselage and were mounted either in a high or low position on the fuselage.

The results of the investigation indicated that aircraft of this type could have acceptable aerodynamic and static longitudinal and lateral stability and control characteristics in both transition and cruise flight. However, the lateral force due to sideslip is abnormally high and might cause the aircraft to be too sensitive to side gusts.

INTRODUCTION

For vertical take-off and landing (VTOL) aircraft, configurations powered by four ducted propellers arranged in pairs fore and aft have certain attractive features for the VTOL phase of operation. Specifically, for hovering and transition flight, the tandem arrangement has certain advantages in control-system simplicity, one of which is the possibility of efficiently achieving a large amount of pitch control by simply varying the pitch of the forward and rearward propellers. The configuration, particularly with all ducts mounted next to the fuselage, also offers advantages for carrier operation in terms of compactness. In order to evaluate properly such novel configurations, it is necessary to know something of their aerodynamic and stability and control characteristics. An exploratory series of wind-tunnel investigations has, therefore, been conducted at the Langley Research Center of the National Aeronautics and Space Administration to provide some basic aerodynamic and stability and control data on four-duct tandem VTOL aircraft configurations.

SYMBOLS

All forces and moments are referred to the stability-axis system, which is an orthogonal system with the origin at the center of gravity. The Z-axis is in the plane of symmetry and perpendicular to the relative wind, the X-axis is in the plane of symmetry and perpendicular to the Z-axis, and the Y-axis is perpendicular to the plane of symmetry. The center of gravity is assumed to be at a station halfway between the forward- and rearward-duct pivot axes and halfway between the top and bottom surfaces of the fuselage.

b reference span, twice the span of one set of inboard-mounted ducts, 8.32 ft

C_D' drag coefficient, F_D'/qS

C_L lift coefficient, F_L/qS

C_l rolling-moment coefficient, M_X/qSb

C_m pitching-moment coefficient, M_Y/qSc

C_n yawing-moment coefficient, M_Z/qSb

C_Y side-force coefficient, F_Y/qS

c reference chord, twice the chord of one set of ducts, 1.50 ft

e span efficiency factor, $\left(\frac{SC_L^2}{\pi C_D'}\right)\frac{1}{b^2}$

F_D' drag force, lb

F_L lift force, lb

F_Y side force, lb

g acceleration due to gravity, ft/sec^2

i_d incidence of duct thrust axis relative to fuselage center line, positive upward (refers to all ducts unless used with subscript), deg

i_w incidence of wing panels relative to fuselage center line, positive with leading edge up, deg

M_X rolling moment, ft-lb

$M_{X_\beta} = \frac{\partial M_X}{\partial \beta}$

M_Y pitching moment, ft-lb

$M_{Y_\alpha} = \frac{\partial M_Y}{\partial \alpha}$

M_Z yawing moment, ft-lb

$M_{Z_\beta} = \frac{\partial M_Z}{\partial \beta}$

q free-stream dynamic pressure, lb/sq ft

S reference area, twice the area of one set of inboard-mounted ducts, 6.24 sq ft

T thrust of ducts (including forces on outside of ducts), lb

T_c' thrust coefficient, T/qS

V velocity, ft/sec

α angle of attack, deg

β angle of sideslip, deg

Subscripts:

F front duct

R rear duct

MODEL

The model used in this investigation was powered by four tilting ducted propellers arranged in tandem pairs. The two rear ducts were mounted close alongside the upper rear portion of the boxy cargo type of fuselage and had small wing panels attached to the outboard side of the ducts; or, they were mounted outboard on the tips of a small wing located high on the rear portion of the fuselage. The two front ducts were always mounted close inboard on the forward part of the fuselage and were mounted either in a high or low position on the fuselage. Vanes behind the ducts varied in size for the various configurations. Three-view drawings of the model including the four duct arrangements are shown in figure 1 and dimensional characteristics are shown in table I. These four configurations are identified in terms of the positions of the rear and front ducts by the following nomenclature:

IB-HI rear ducts inboard, front ducts high

IB-LO rear ducts inboard, front ducts low

OB-HI rear ducts outboard, front ducts high

OB-LO rear ducts outboard, front ducts low

The model was provided with two different types of vertical tails - a single center-line tail, or twin tails mounted on the ducts. (See fig. 1(a).) The tota area and the aspect ratio of the twin tails were the same as the area and the aspect ratio of the single tail.

Power for the model was provided by a-c induction motors which were of identical design and were mounted in the center of each duct. The motors were not mechanically interconnected, but they were wired in parallel and were operated from a common variable-frequency power supply so that all four motors ran at very nearly the same speed. The propellers of the model had fixed pitch and all of the propellers were set at the same pitch. Changes in thrust were accomplished by changing the propeller rotational speed. Each pair of ducts was pivoted about a spanwise axis passing through the 50-percent-chord station of the duct; the rear-wing surface was also pivoted on the rear-duct pivot axis to permit changes in wing incidence.

TESTS

With the model mounted on an internal strain-gage balance in a low-speed wind tunnel which had a 12-foot octagonal test section, a short series of preliminary tests were made to determine a suitable distribution of projected area forward and rearward of the center of gravity to give reasonable static longitudinal stability in the cruise condition $\left(\frac{dC_m}{dC_L} \approx -0.10\right)$ for the IB-LO and OB-HI configurations. In these tests, the size of the wing and the size of the vanes behind the ducts were varied to adjust the static longitudinal stability. The configurations selected as a result of these tests are those shown in figure 1. No vanes were used behind the front ducts and large vanes were used behind the rear ducts when the rear ducts were mounted in the inboard position. With the rear ducts mounted in the outboard position, however, all the ducts were equipped with the same size vanes. All the tests discussed in this paper were made with the four duct-wing configurations developed in these preliminary tests and shown in figure 1. These preliminary tests were followed by three series of extensive tests.

Tests were made for the cruise flight configurations (duct and wing incidence angles near 0°) for the windmilling power condition and for a power-on condition ($T_c' = 0.5$) corresponding to a level flight condition at a high lift coefficient (C_L about 2.0). The tests were made over an angle-of-attack range from -8° to 20° with angles of wing incidence from -15° to 15° for each of the four

configurations. This first group of tests was made with $i_{d,F} = i_{d,R} = 0^\circ$. In order to determine the effect on the static longitudinal stability of using the front ducts to obtain some pitching-moment trim, the tests were repeated for a range of front-duct incidence angles from -5° to 5° with $i_{d,R} = 0^\circ$.

There were two faults with the data from this first series of tests: one, that the gaps between the ducts, the body, and the wings were not sealed, and the other, that the model was heavy so that a very strong balance had to be used. The drag channel of this balance was not sufficiently sensitive to provide reliable drag data for the cruise conditions at the airspeeds at which the tests could be run with the power installed in the model. These were the only tests made, however, that showed the effect of power on longitudinal stability and trim for the cruise flight configurations.

Another series of tests was made to study the drag of the model in the cruise flight condition. For these tests, the model was lightened by removing the entire centerbody of the ducts (motors, propellers, and fairings) so that a more sensitive balance could be used, and the gaps between the body, ducts, and wings were sealed. The horizontal vanes were not removed from the ducts. These tests were, of course, made only for the power-off condition, and they were also made in the 12-foot test section. The power-off tests were essentially the same as the previous series of tests with slight differences in the angle-of-attack and wing-incidence ranges.

A third series of tests was conducted in the Langley full-scale tunnel on the IB-LO configuration to study both the longitudinal- and lateral-stability characteristics of the model in the transition range. The longitudinal tests were made for power-on conditions of drag trimmed (zero acceleration), 0.25g acceleration and 0.25g deceleration for a range of duct incidence angles from 15° to 75°. For the lateral tests, a test condition of zero acceleration at $\beta = 0^\circ$ and at angles of attack of 0°, 5°, 10°, and 15° was established and the rolling moment, yawing moment, and side force were measured over a range of sideslip angles from -15° to 15° and at angles of duct incidence from 0° to 60°. Tests were made with two vertical-tail arrangements and with no vertical tail.

RESULTS AND DISCUSSION

The data for the cruise flight tests (i_d near 0°) are presented in coefficient form, but since the coefficients approach infinity and become essentially meaningless as the velocity approaches zero, the data for the transition flight tests ($i_d = 15^\circ$, 30°, 45°, 60°, and 75°) were left in dimensional form and have been scaled up to a weight of 102 pounds. It should be noted, however, that although the data have been scaled up to a weight of 102 pounds for tests made at power settings that gave zero net drag and acceleration or deceleration of 0.25g at $\alpha = 0^\circ$, the data can be interpolated and rescaled in terms of other conditions such as climb or glide or trim at other angles of attack. If the data were rescaled, all forces and moments would simply be multiplied by the factor required to make the lift equal to the desired value for the desired condition, and the

velocity, multiplied by the square root of this factor. Equations for the rescaling operations are given in the appendix of reference 1. A summary of the configurations tested and of the figures that present the basic data (figs. 2 to 37) is given in table II.

Lift

Lift curves at the trimmed condition ($C_m = 0$) for the configurations with the rear ducts located outboard and inboard are summarized in figure 38. Only two curves are shown because the curves are almost identical for configurations with the front ducts high or low. These curves were taken from the power-off tests with the propellers and duct centerbodies removed and with the gaps between the body, ducts, and wing panels sealed. (See figs. 14 to 33.)

The lift curves are nonlinear, but measurements of the lift-curve slope (either the slope at zero lift or the average slope) shows that lift-curve slope C_{L_α} is about 20 percent higher for the configuration with the rear ducts outboard than for the configuration with the rear ducts inboard. This is a considerably greater difference than would be expected on the basis of the 2-percent greater lifting area and 4-percent greater span of the configurations with the rear ducts located outboard. The difference in lift-curve slope probably results partly from the fact that the ducts on the tip of the rear wing give it a higher effective aspect ratio (end-plate effect) and partly from the fact that the downwash from the front ducts reduces the lift-curve slope of the smaller lifting surface of the rear wing panel rather than the larger biplane-type lifting surface of the rear ducts.

Drag

The drag characteristics of the model are summarized in figure 39 for configurations IB-LO and OB-HI. Drag data are not shown for the other two configurations since their drag curves were so irregular as to be of little use in analysis. The drag curves shown in figure 39 were taken from the power-off tests with the propellers and duct centerbodies removed and with the gaps between the body, ducts, and wing panels sealed. (See figs. 14 to 33.) These drag curves are for the trimmed condition ($C_m = 0$) with the model trimmed with the most favorable combination of incidence of the front ducts and of the rear wing panel.

The data of figure 39 show that the induced drag of the OB-HI configuration is considerably lower than that of the IB-LO configuration, even though the wing span and total lifting area of the two configurations are very nearly the same. In fact, the span efficiency factor e of the configuration with the rear ducts outboard calculated from these curves is 0.76, whereas for the configurations with the rear ducts inboard it is 0.65. Or, in other terms, the ratio of effective span to actual span for the OB-HI configuration is 8 percent greater than that for the IB-LO configuration. This fact in itself does not necessarily indicate a superiority of one configuration over the other. The induced drag of the IB-LO configuration could presumably be made as low as that of the OB-HI configuration by increasing its wing span and taking other appropriate steps to adjust the

longitudinal stability. These values of span efficiency factor (0.76 and 0.65) may seem low compared with those of conventional aircraft, but the value of 0.76 is actually fairly representative of the value of e of a conventional multi-engine airplane model of the same low scale.

Static Stability in Cruise Flight

Longitudinal.- The longitudinal-stability characteristics of the model in the cruise flight range are summarized in figure 40 in which pitching moment is plotted against lift coefficient. This figure shows the stability curves for the four configurations for three angles of incidence of the front ducts and for two power conditions (windmilling propellers and $T_c' = 0.5$). In all cases in which the model was stable, the curve is shown for the angle of incidence of the rear wing panel (not including the rear ducts or vanes behind the ducts) required for trim at a lift coefficient of 1.0, which corresponds to a cruise condition near maximum lift-drag ratio. These data were taken from tests in which the gaps between the body, ducts, and wing panels were not sealed. (See figs. 2 to 13.) Other power-off tests with the gaps sealed, however, showed that sealing the gaps caused only a small increase in stability $\left(\frac{dC_m}{dC_L}\right.$ about 0.03 more negative$\left.\right)$.

Three main points can be made from the data of figure 40(a) for the configurations having the rear duct in the inboard location. First, the stability characteristics seem reasonable except for the condition of $i_{d,F} = 5^\circ$ which has a marked pitch-up tendency. This pitch-up is evidently the result of early stall of the rear wing panels at the high angles of incidence required for trim with the front duct at 5° incidence. This stall may well be aggravated by upwash caused by the tip vortices from the front ducts. The second point is that there is not consistent effect of power on stability, and that the effect of power is not extremely large. And, the third point is that there is little change in the value of i_w required for trim with power at $i_{d,F} = 0^\circ$ for the IB-LO configuration.

Three main points are also brought out by the data of figure 40(b) for the configurations having the rear duct in the outboard location. First, comparison of these data with those of figure 40(a) shows that these configurations are more prone to pitch-up than are the configurations with the rear ducts inboard. All of the configurations except the OB-HI configuration with $i_{d,F} = 0^\circ$ show a pronounced pitch-up. The second point is that power has a major effect on stability in relieving the pitch-up. This effect of power evidently results from the fact that the increased downwash from the front duct caused by power reduces the angle of attack of the rear wing panel and delays its stall. And, the third point is that power has little effect on the value of i_w required for trim for the condition in which $i_{d,F} = 0^\circ$.

Lateral.- The lateral-stability characteristics of the model in the cruise condition are summarized in figure 41 for configuration IB-LO. This is the only

configuration for which lateral data were obtained. The tests were made for the power-on condition with $C_D = 0$.

The data show that the model had only about neutral directional stability with the particular tails tested. The tail effectiveness was about constant over the angle-of-attack range, however, so it would seem that the directional stability could have been made adequate by the use of slightly larger vertical tails. It is also interesting to note that the directional stability was somewhat better with the simpler single vertical tail than with twin vertical tails of the same total area and the same aspect ratio. The difference in directional stability provided by the two vertical-tail configurations is not as great as might be expected from the difference in the geometric moment arms. Analysis of the data showed that the effective center of pressure of the twin tails was about where it would be expected to be, but that the effective center of pressure of the single tail was much farther forward than expected, that is, ahead of the leading edge of the root chord. This forward location of the center of pressure of side load caused by the tail evidently results from interference effects of the tail on the fuselage. A similar effect was noted in tests made on a tandem-helicopter fuselage as reported in reference 2. Detailed analysis of the data also showed that both the single and twin vertical tails were causing a much greater lateral force (40 and 60 percent, respectively) than would be expected on the basis of their areas and any normal estimate of their effective aspect ratios. In the case of the single tail, this greater lateral force is induced by the tail on the fuselage. This explanation is consistent with the forward center of pressure of the load caused by the tail. This explanation is not as satisfactory, however, in the case of the twin vertical tails. For the twin tails it seems more likely that the tails were in a favorable sidewash field, perhaps from tip vortices from the front ducts, or that the tails were in an area of increased dynamic pressure resulting from the slipstream from the front ducts which were operating with some appreciable thrust, since the tests were made for the zero drag condition. The data obtained in this investigation were not extensive enough to provide a complete explanation of the effectiveness of the vertical tails of a four-duct configuration such as that of the model. They do show, however, that the estimation of the tail effectiveness is not a straightforward procedure and that wind-tunnel tests of any such airplane design would be necessary to insure adequate directional stability.

The data of figure 41 also show that the values of C_{Y_β} for the model with the single vertical tail were very high. Actually they are about one-half as high as the slope of the lift curve C_{L_α} which was about 0.14; and if some allowance is made for the fact that a larger vertical tail is required for adequate directional stability, the value of C_{Y_β} would be an even larger percentage of C_{L_α}. These high values of C_{Y_β} indicate that riding in an airplane of this type could be unusually rough because of its high response to side gusts. For example, a standard side gust of 30 feet per second would give a sidewise acceleration one-half as great as the normal acceleration caused by a standard vertical gust of 30 feet per second; and sidewise accelerations are more objectionable than normal acceleration to the occupants of the airplane.

The effective dihedral of the model, as indicated by the parameter C_{l_β} in figure 41, seems fairly normal when allowance is made for the relatively small wing area on which C_l is based. A word of caution is in order in connection with these values of C_{l_β}, however. That is, the values were read from the very nonlinear curves of figure 36 in which C_l is plotted against β; these values are at best only a rough indication of the dihedral effect.

Static Stability in Transition

As previously pointed out, the IB-LO configuration is the only one for which data have been obtained in the transition range. In these tests, the blade angle and rotational speed of the front and rear propellers were the same and the incidence of the front and rear ducts was the same.

Longitudinal.- The results of the tests to determine the basic longitudinal-stability and trim characteristics of the IB-LO configuration in transition are shown in figure 34 and these data are summarized in figure 42. In these tests the wing was at an angle of incidence of -15° relative to the thrust axis of the rear duct for all values of rear-duct incidence. The data show that the untrimmed pitching moment was fairly small. At its maximum positive value M_Y is approximately 18 ft-lb, which corresponds to a center-of-pressure location of 0.15 propeller diameter behind the center of gravity. The data also show that there was a very low degree of static longitudinal instability M_{Y_α} throughout the transition range. Some idea of the significance of the magnitude of the values of M_{Y_α} shown can be gained by comparing them with those of other VTOL-aircraft configurations that have been flown. For example, the maximum unstable value shown $\left(M_{Y_\alpha} = 0.4\right)$ is less than that of a comparable model of a tilt-wing VTOL airplane that has been flown successfully.

The data of figure 43 summarize the effect of acceleration and deceleration on longitudinal stability and trim for the IB-LO configuration. In these tests, presented in figure 35, the incidence of the rear wing panel was 0° relative to the fuselage axis throughout the transition range. The condition for 0.25g acceleration shown in figure 43 can also be considered to represent a 14° climb and the condition for 0.25g deceleration corresponds to a 14° descent. The data of figure 43 show that there is essentially no difference in the maximum nose-up pitching moment that must be trimmed in the transition range for any of the three conditions of acceleration and that the model had a low degree of static longitudinal stability. In this respect, this four-duct configuration is different from many other VTOL-aircraft configurations for which the nose-up pitching moment is much greater for the condition of deceleration or descent than for the level flight condition of zero acceleration.

Lateral.- The lateral-stability characteristics of the model are presented in figure 44 for the IB-LO configuration. In these tests the front and rear ducts were set at the same incidence and the power was that required for zero drag at zero fuselage angle and zero sideslip. The data show that the model with the

single vertical tail was directionally stable to a slight degree and had a positive dihedral effect throughout the transition range.

SUMMARY OF RESULTS

The principal results of several wind-tunnel investigations conducted for the study of the aerodynamic characteristics of various four-duct tandem VTOL-aircraft configurations are as follows:

1. For the cruise condition, acceptable longitudinal stability could be obtained with either rear-duct-inboard or rear-duct-outboard configurations.

2. The slope of the lift curve for the cruise condition was higher and the induced drag was lower for the configuration with the rear ducts located outboard than for the configuration with the rear ducts located inboard, even though the wing span and total lifting area were approximately equal.

3. Throughout the transition range it was found that the change in longitudinal trim was small and the model had a low degree of static longitudinal stability. These results apply only to the configuration with the rear ducts inboard and the front ducts low because it was the only configuration for which longitudinal data were obtained in the transition range.

4. The model had about neutral directional stability in both the cruise and transition conditions for the configuration with the rear ducts inboard (the only configuration for which lateral data were obtained), but the vertical tails were effective, so the model could presumably have been made more stable by the use of larger tails.

5. The lateral tests also showed that in the cruise condition the model had a variation of lateral force with angle of sideslip that was abnormally high - about one-half as great as the slope of the lift curve.

Langley Research Center,
National Aeronautics and Space Administration,
Langley Station, Hampton, Va., October 8, 1962.

REFERENCES

1. Tosti, Louis P.: Force-Test Investigation of the Stability and Control Characteristics of a 1/8-Scale Model of a Tilt-Wing Vertical-Take-Off-and-Landing Airplane. NASA TN D-44, 1960.

2. Smith, Charles C., Jr.: Static Directional Stability of a Tandem-Helicopter Fuselage. NACA RM L50F29, 1950.

TABLE I.- DIMENSIONS OF MODEL

[All dimensions are in inches]

Body:		
Maximum height		15.4
Maximum width		15.4
Length		86
Distance of forward-duct pivot aft of nose		11
Distance between duct pivots		53.2
Distance of rear-duct pivot below top of fuselage		2.4
Distance of front-duct pivot below top of fuselage:		
High-duct location		2.4
Low-duct location		13
Wing:		
Span:		
Rear duct inboard		75.6
Rear duct outboard		78.6
Chord		12
Airfoil section		NACA 0015
Vertical tail:	Center	Twin (each)
Area	284	142
Height (from top of fuselage)	19.4	13.7
Root chord	19.4	13.7
Tip chord	9.8	6.9
Aspect ratio	1.3	1.3
Ducts:		
Outside diameter		17.25
Inside diameter		14
Exit diameter		15.96
Length		9
Pivot point, percent duct chord		50
Vane span		15.96
Vane chord		3.4
Airfoil section (maximum camber facing inward)		NACA 2418
Propeller:		
Diameter		13.75

TABLE II.- SUMMARY OF BASIC DATA FIGURES

Duct positions (rear-front)	Power condition	$i_{d,F}$, deg	$i_{d,R}$, deg	Vertical tail	Type of data	Figure
IB-HI	Windmilling and $T_c' = 0.5$	0 5 -5	0	Off	Longitudinal	2 3 4
IB-LO	Windmilling and $T_c' = 0.5$	0 5 -5	0	Off	Longitudinal	5 6 7
OB-HI	Windmilling and $T_c' = 0.5$	0 5 -5	0	Off	Longitudinal	8 9 10
OB-LO	Windmilling and $T_c' = 0.5$	0 5 -5	0	Off	Longitudinal	11 12 13
IB-HI	Off	0 2.5 5 -2.5 -5	0	Off	Longitudinal	14 15 16 17 18
IB-LO	Off	0 2.5 5 -2.5 -5	0	Off	Longitudinal	19 20 21 22 23
OB-HI	Off	0 2.5 5 -2.5 -5	0	Off	Longitudinal	24 25 26 27 28
OB-LO	Off	0 2.5 5 -2.5 -5	0	Off	Longitudinal	29 30 31 32 33
IB-LO	0g 0g 0.25g -0.25g 0g	15 to 75 0 15 to 60	15 to 75 0 15 to 60	Off Off Single Twin Off Single	Longitudinal Lateral	34 35(a) 35(b) 35(c) 36(a) 36(b) 36(c) 37(a) 37(b)

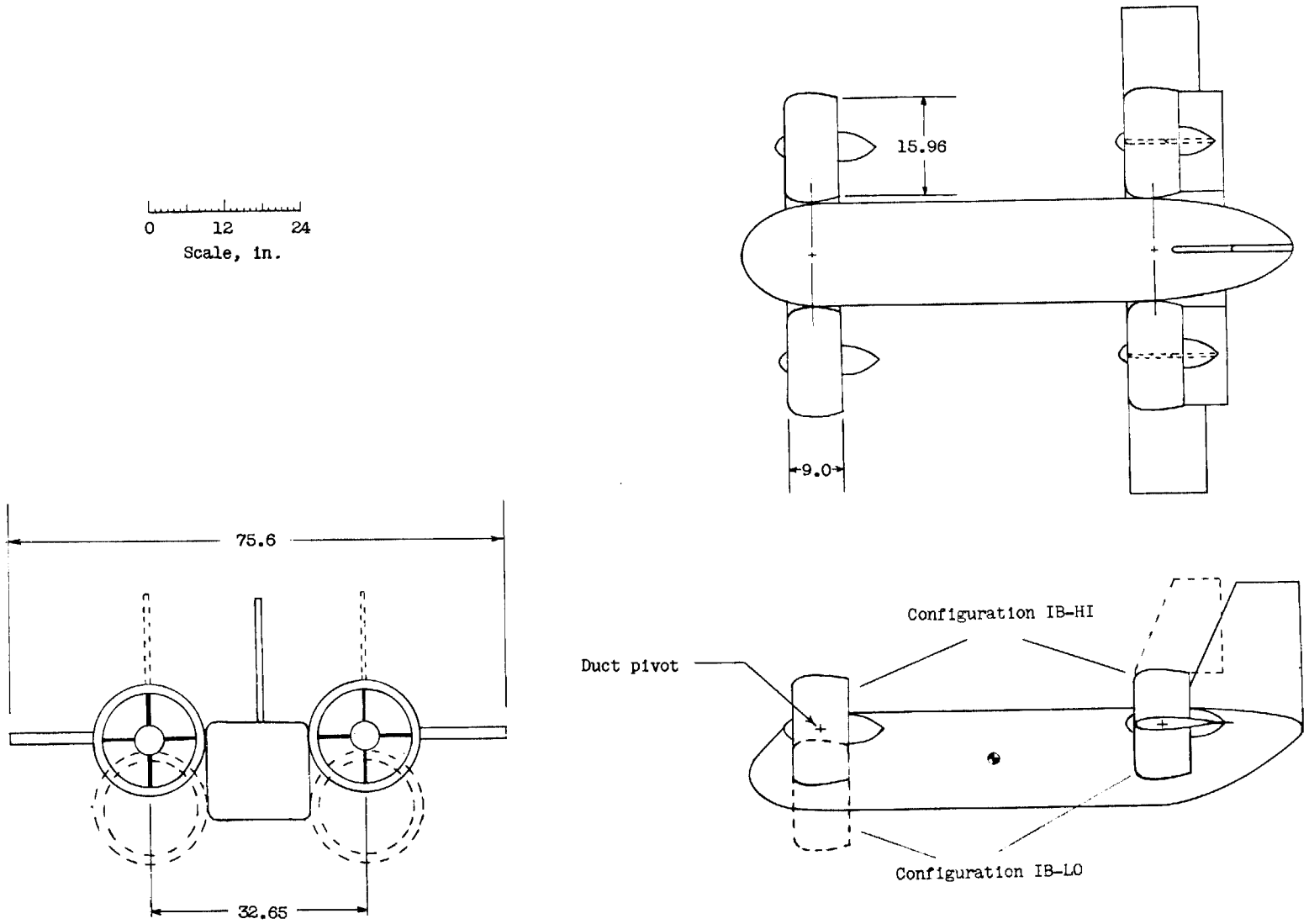

(a) Rear ducts inboard.

Figure 1.- Model used in tests.

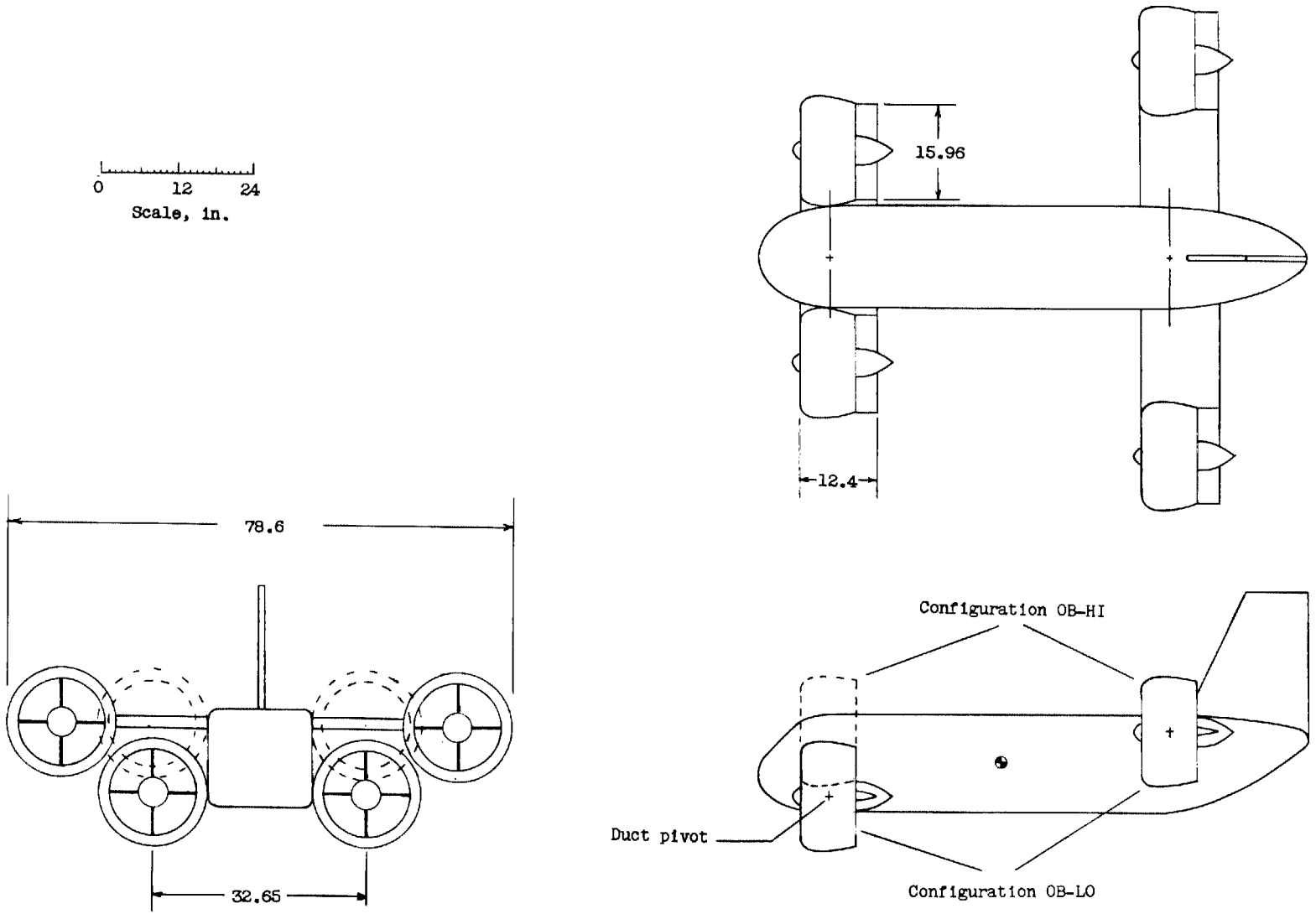

(b) Rear ducts outboard.

Figure 1.- Concluded.

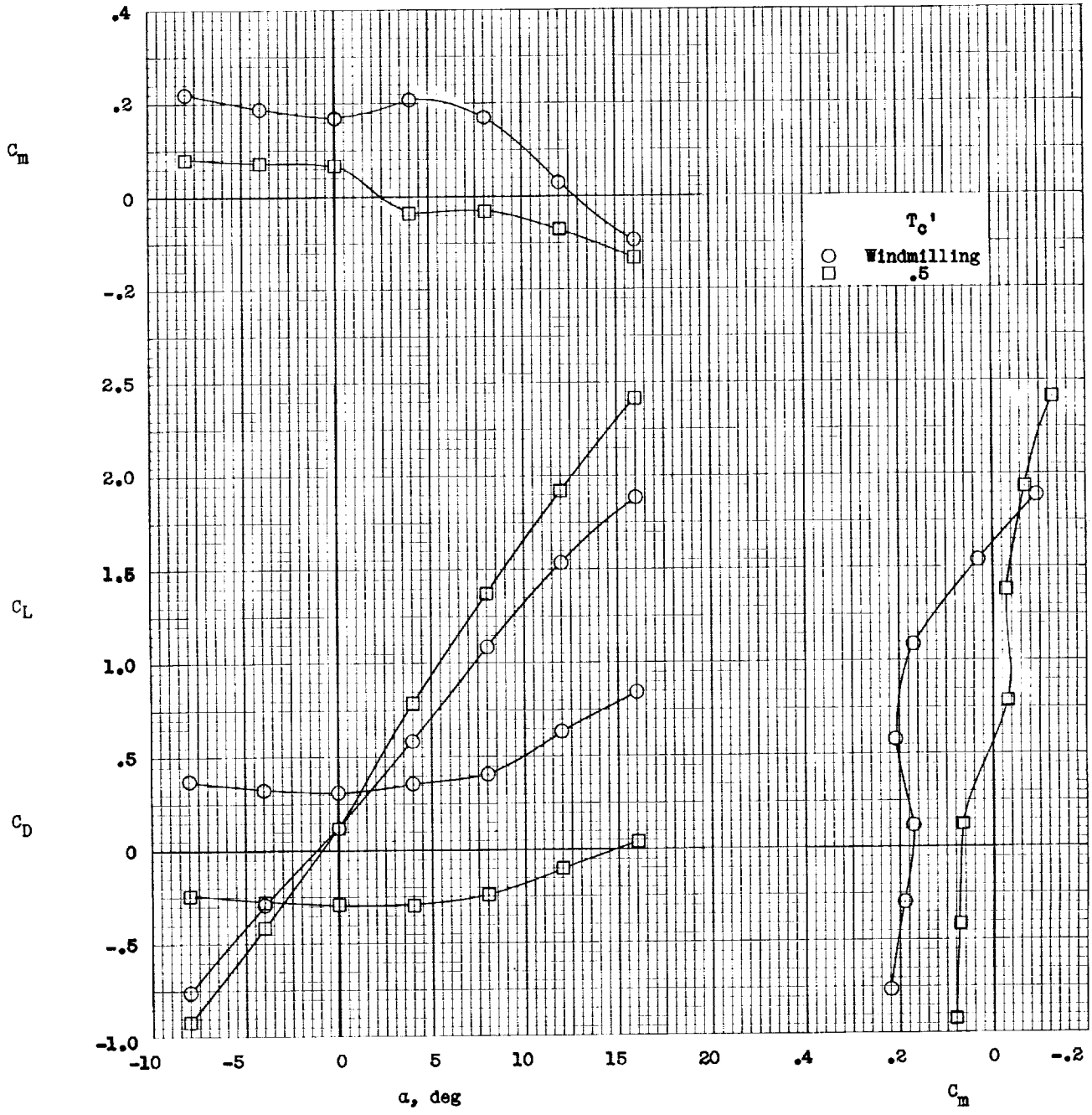

(a) $i_w = 0^o$.

Figure 2.- Longitudinal stability and trim characteristics of IB-HI configuration. $i_{d,F} = 0^o$; $q = 5.0$; gaps unsealed.

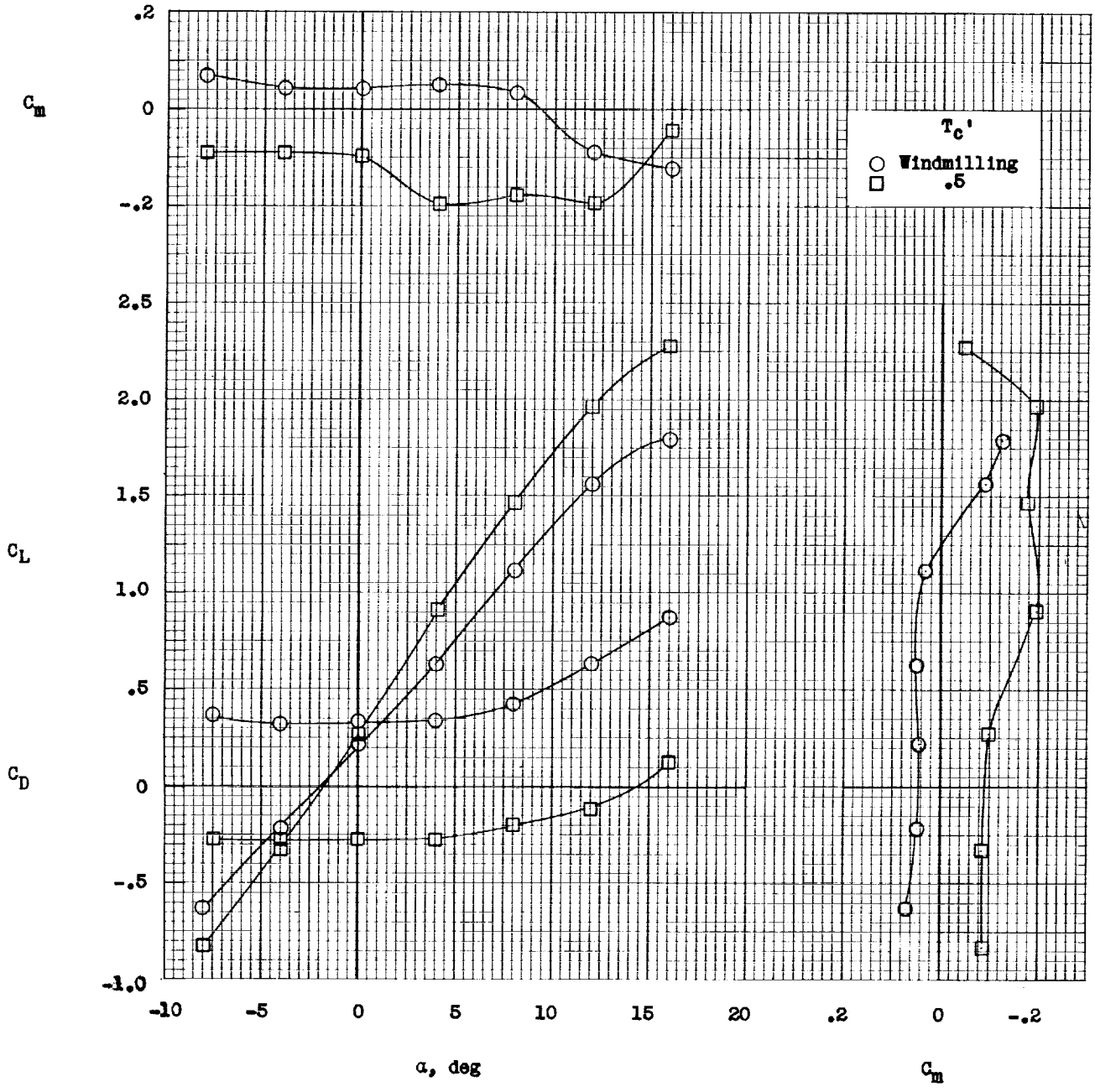

(b) $i_w = 5^\circ$.

Figure 2.- Continued.

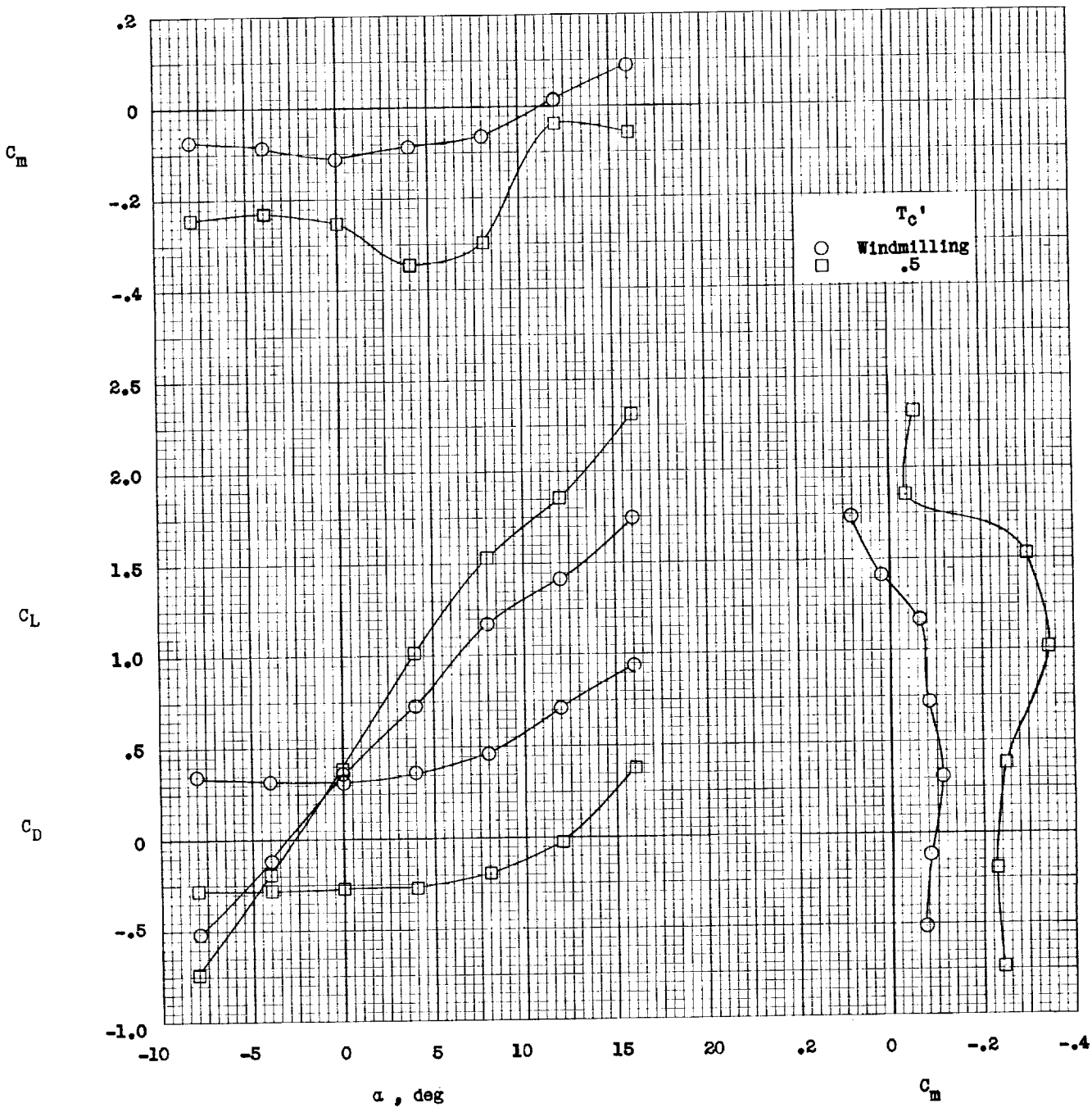

(c) $i_w = 10^o$.

Figure 2.- Continued.

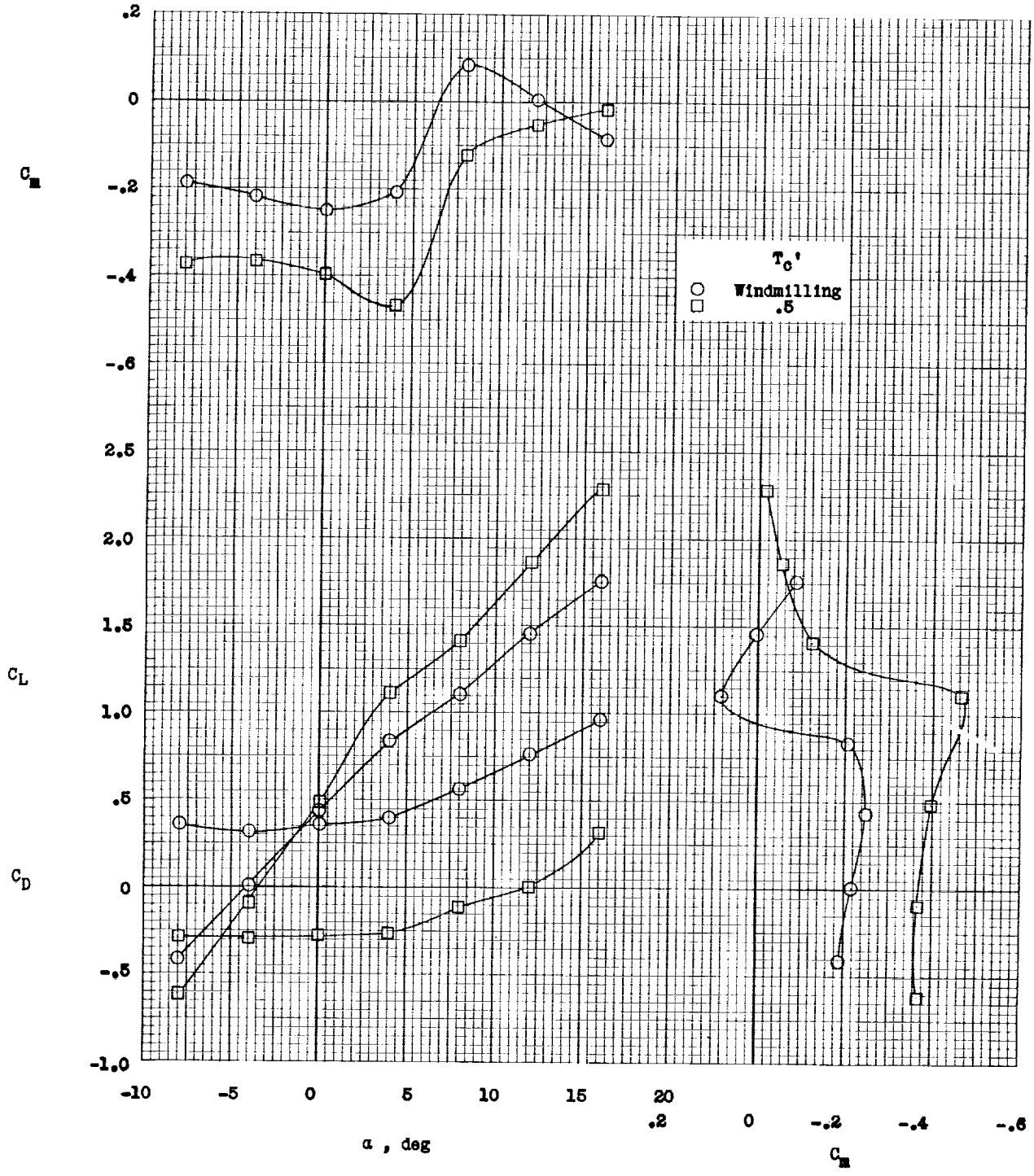

(d) $i_w = 15^\circ$.

Figure 2.- Continued.

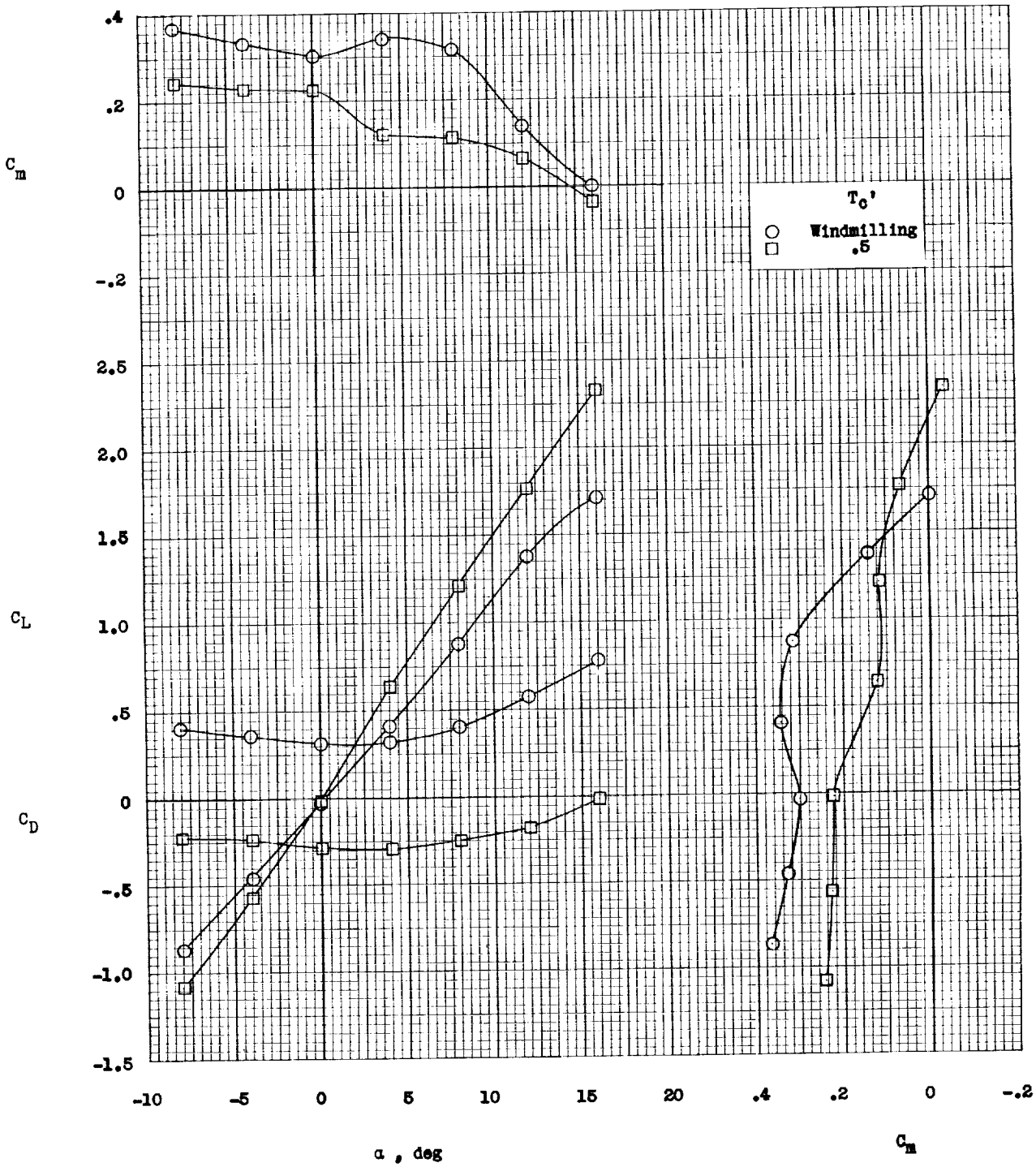

(e) $i_w = -5^\circ$.

Figure 2.- Continued.

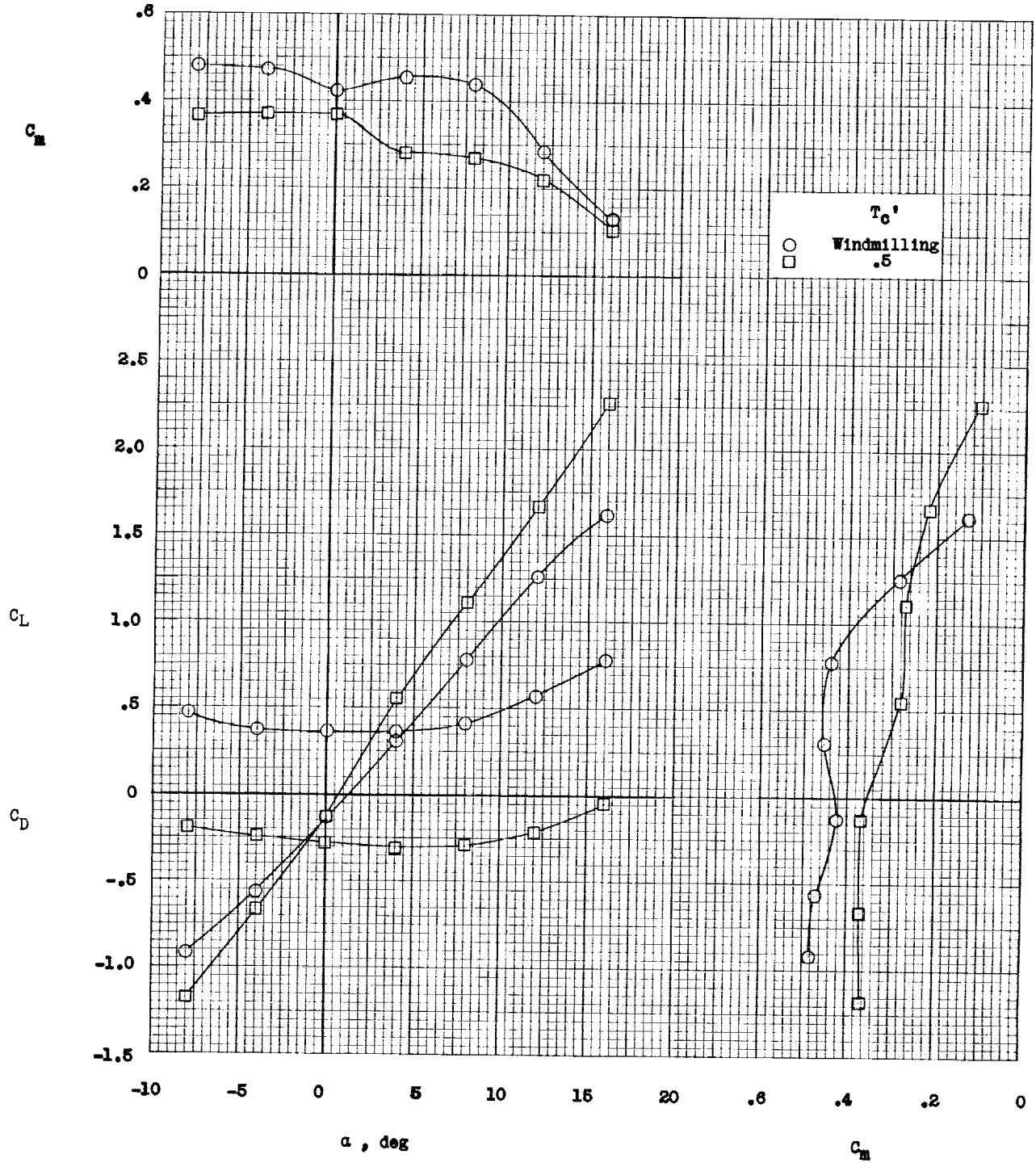

(f) $i_w = -10°$.

Figure 2.- Continued.

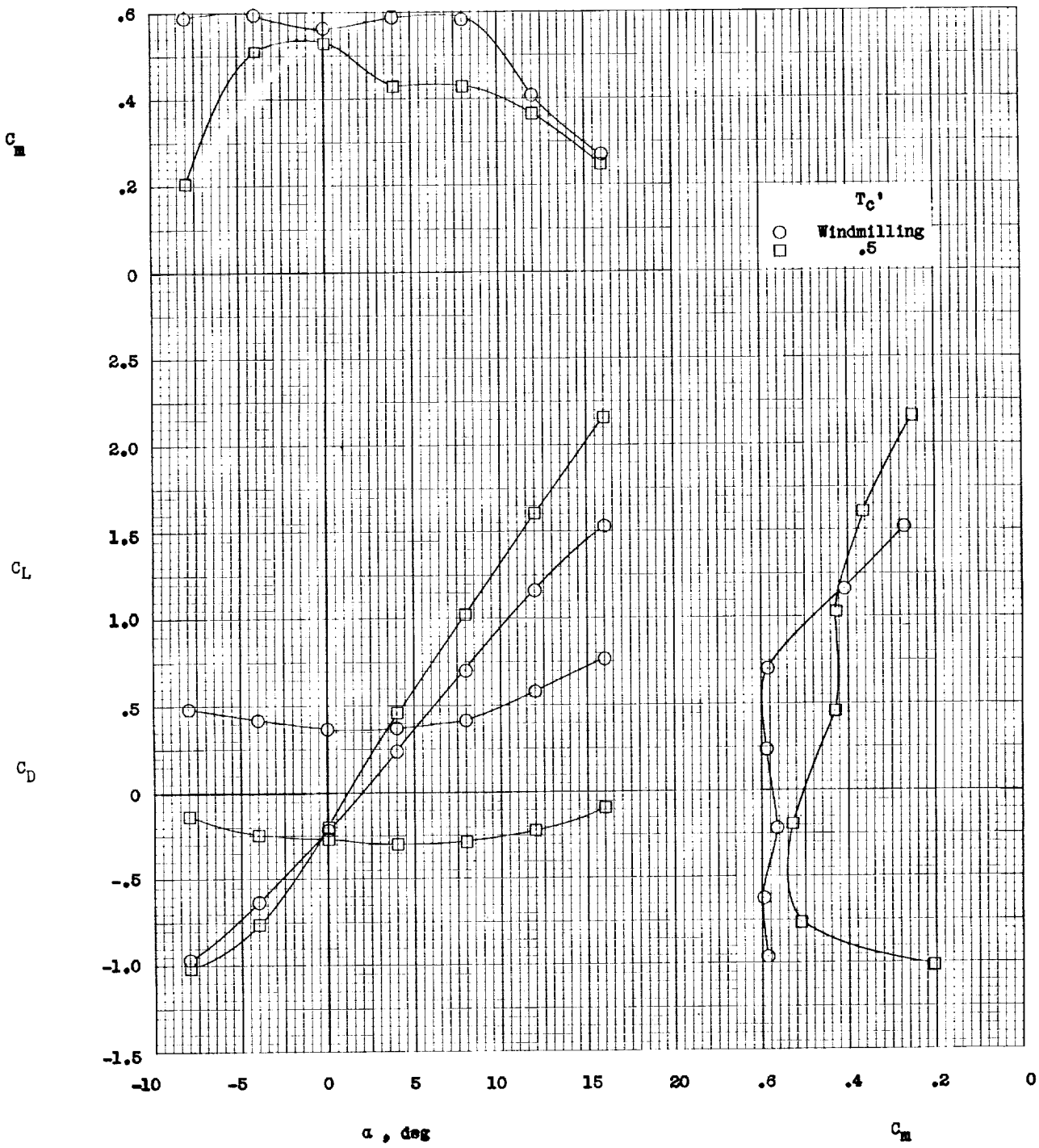

(g) $i_w = -15°$.

Figure 2.- Concluded.

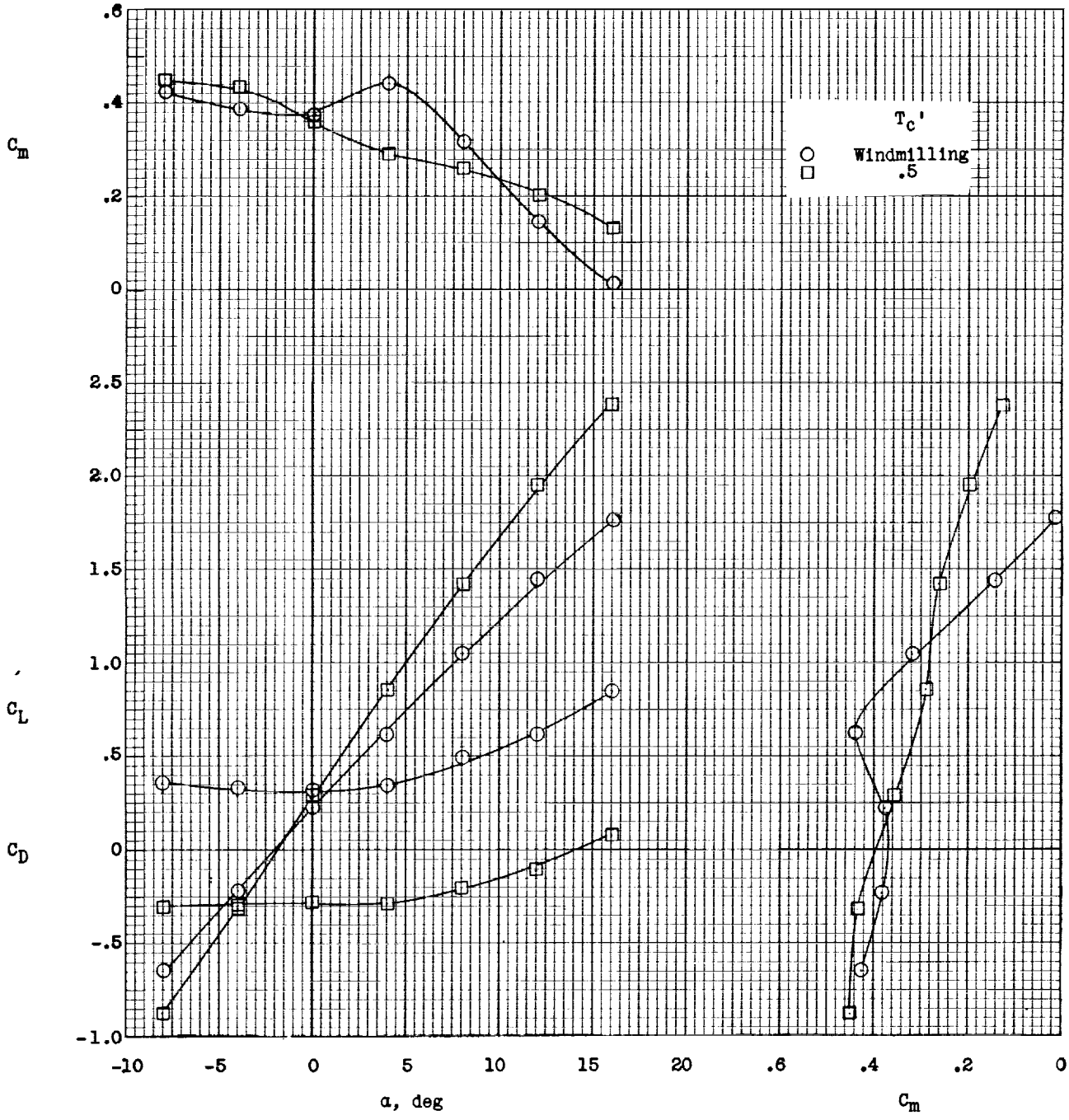

(a) $i_w = 0^\circ$.

Figure 3.- Longitudinal stability and trim characteristics of IB-HI configuration. $i_{d,F} = 5^\circ$; $q = 5.0$; gaps unsealed.

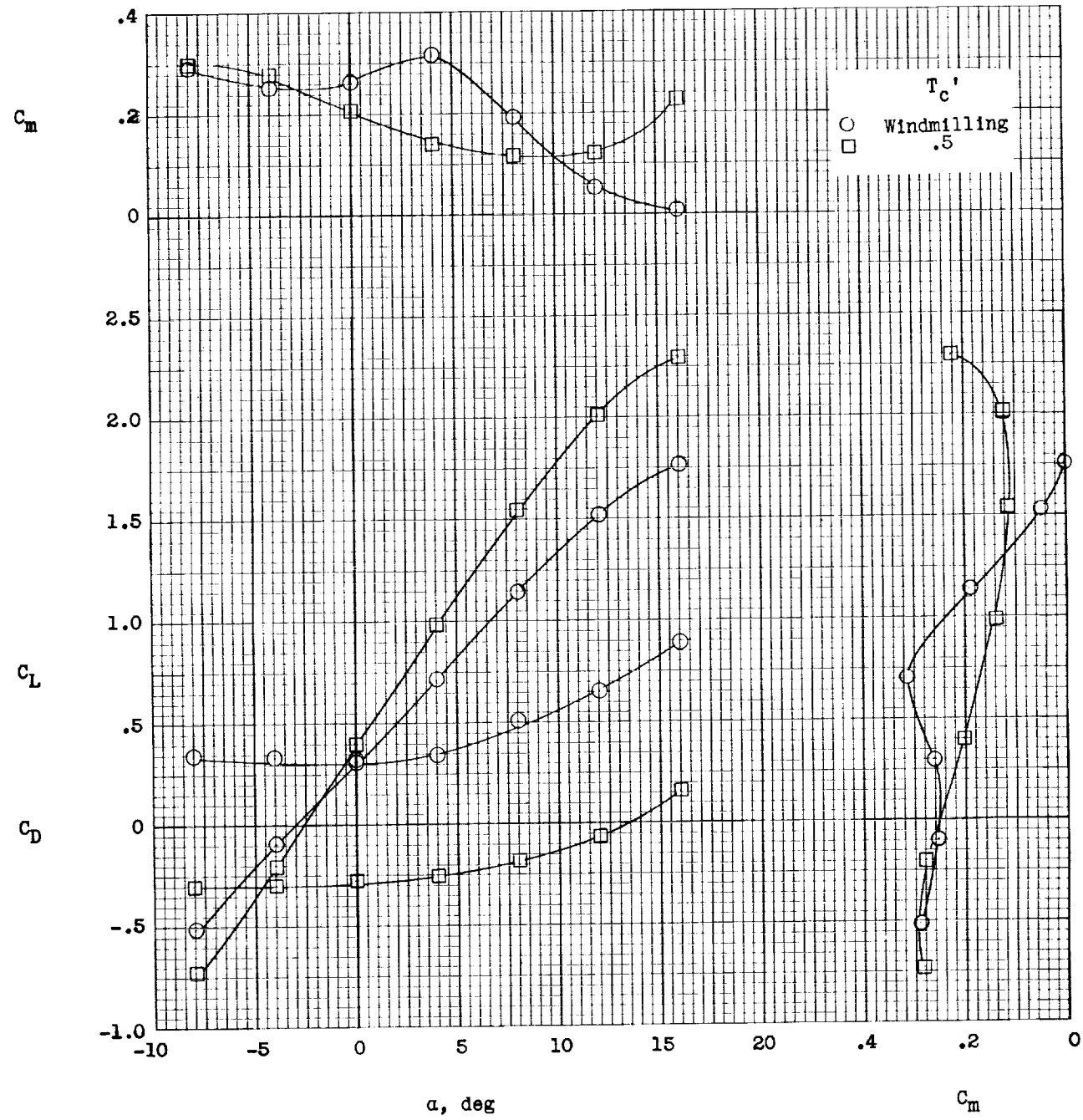

(b) $i_w = 5^\circ$.

Figure 3.- Continued.

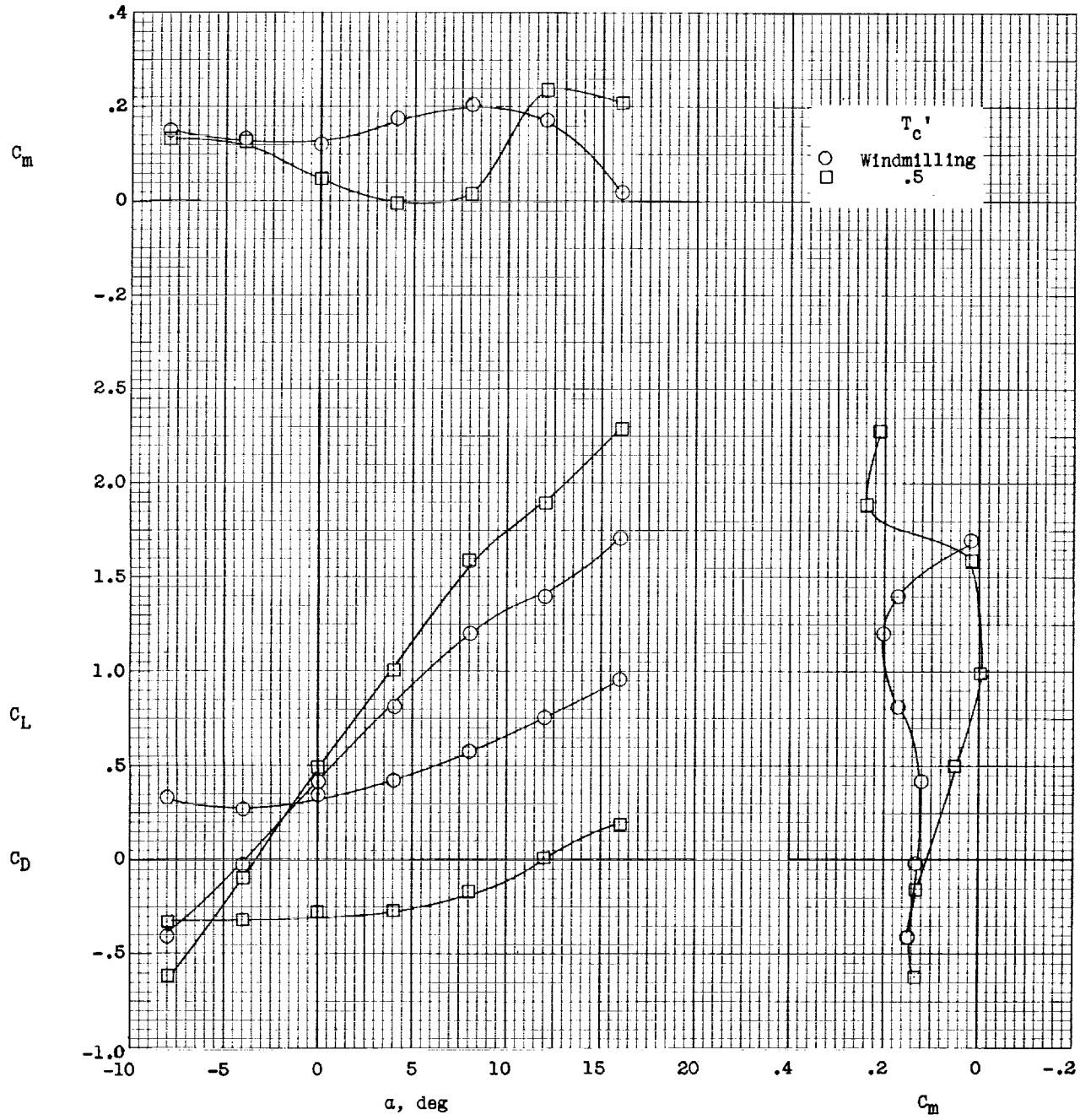

(c) $i_w = 10°$.

Figure 3.- Continued.

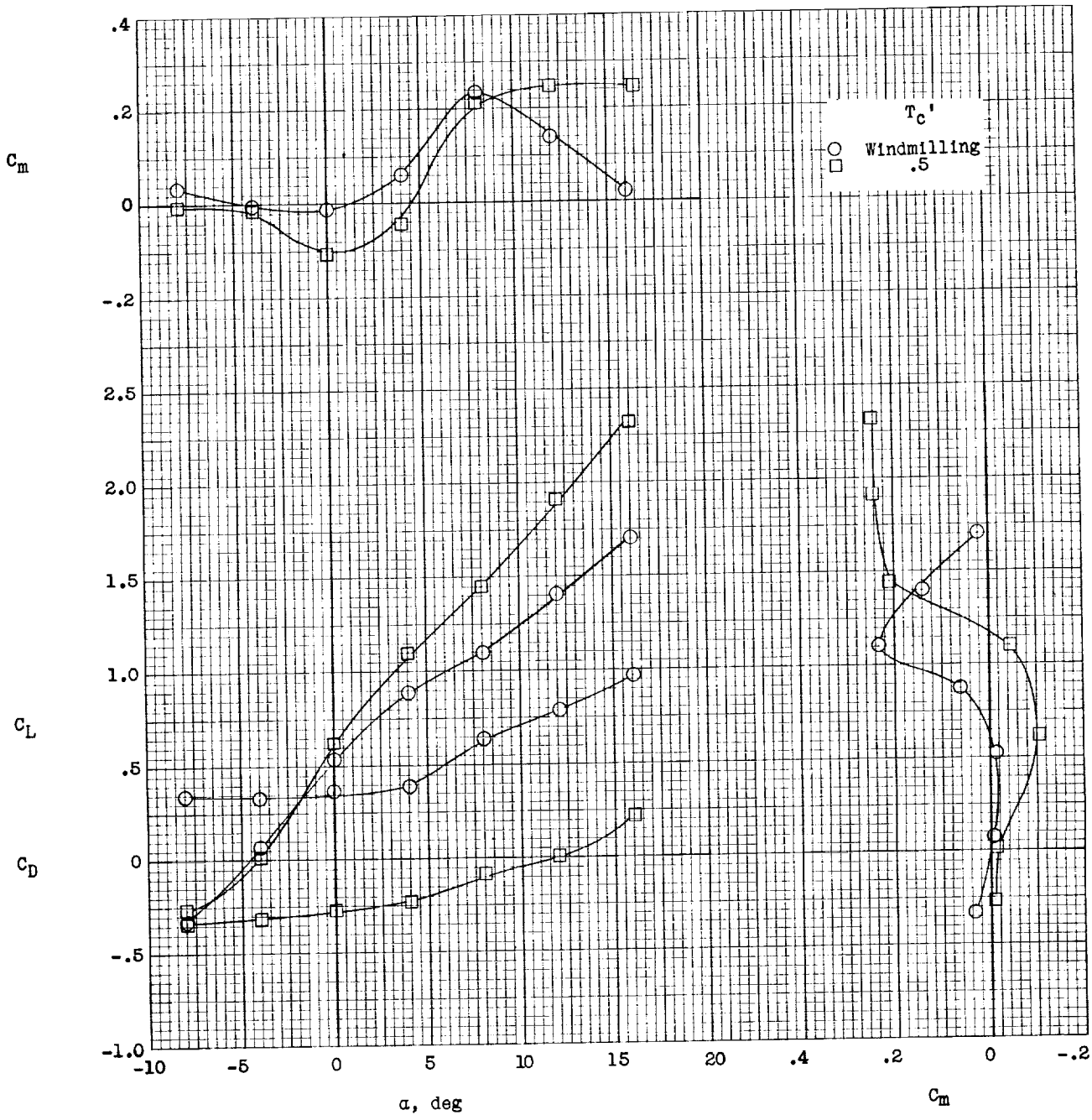

(d) $i_w = 15^\circ$.

Figure 3.- Continued.

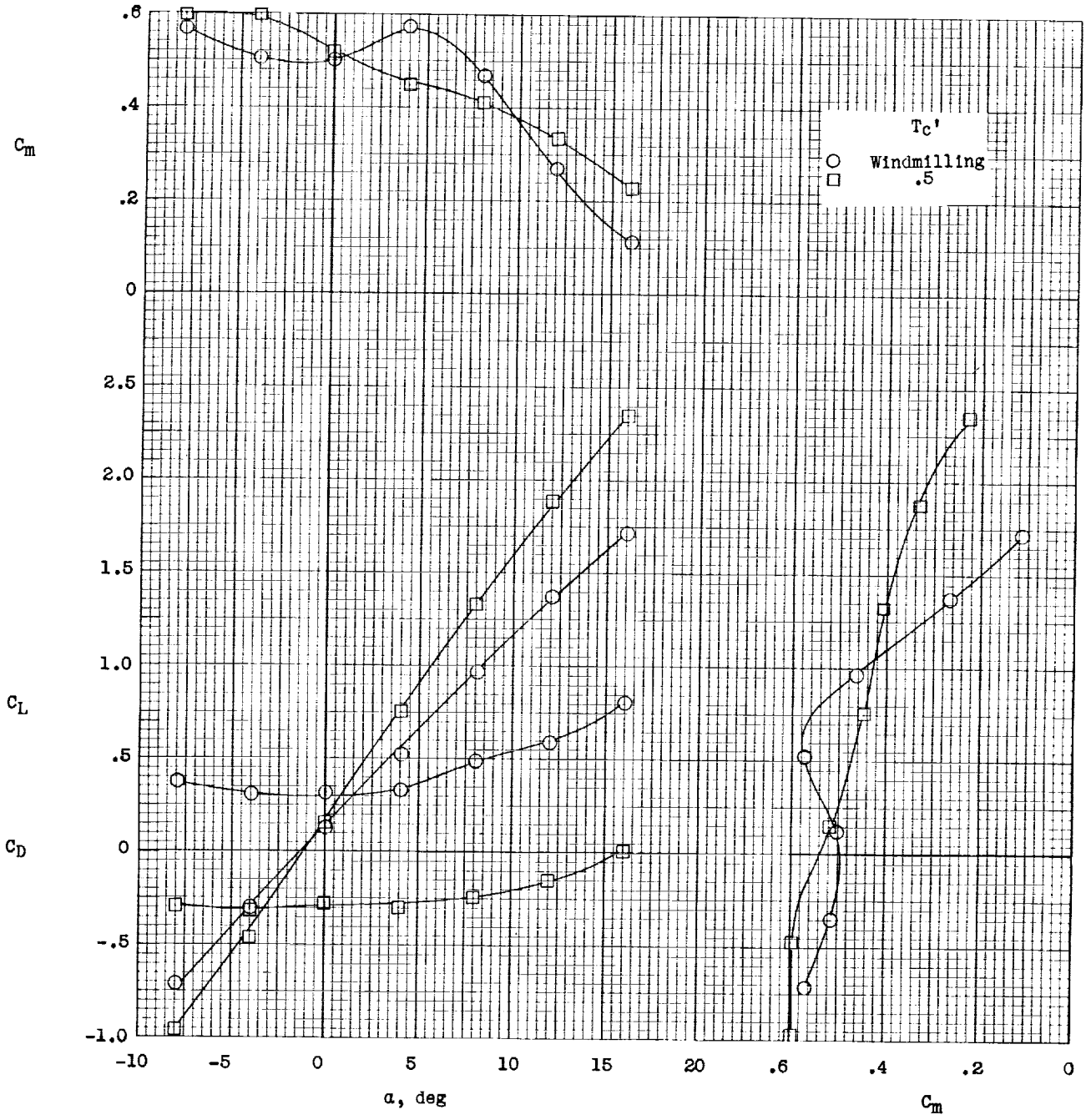

(e) $i_w = -5^\circ$.

Figure 3.- Continued.

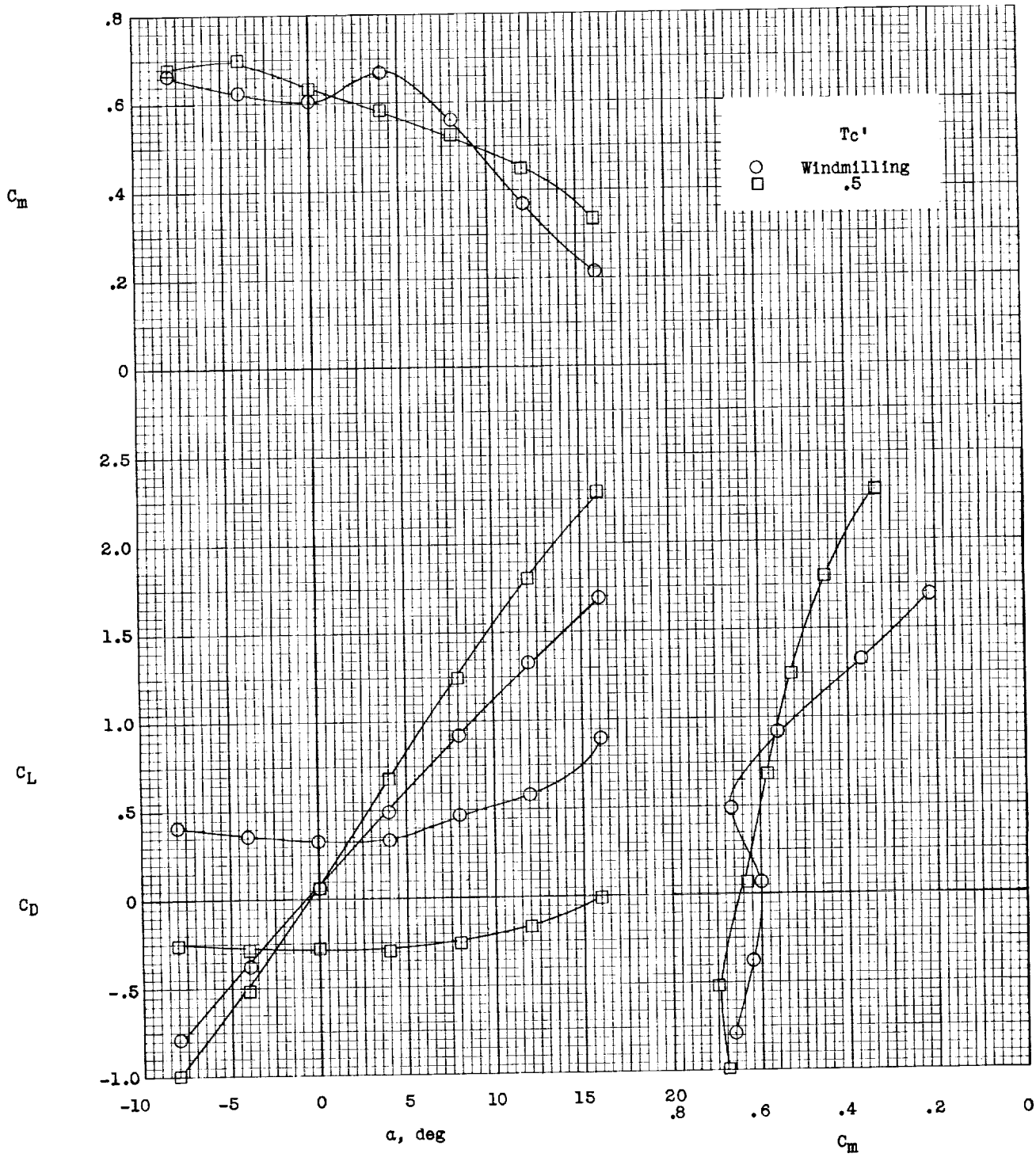

(f) $i_w = -10^o$.

Figure 3.- Concluded.

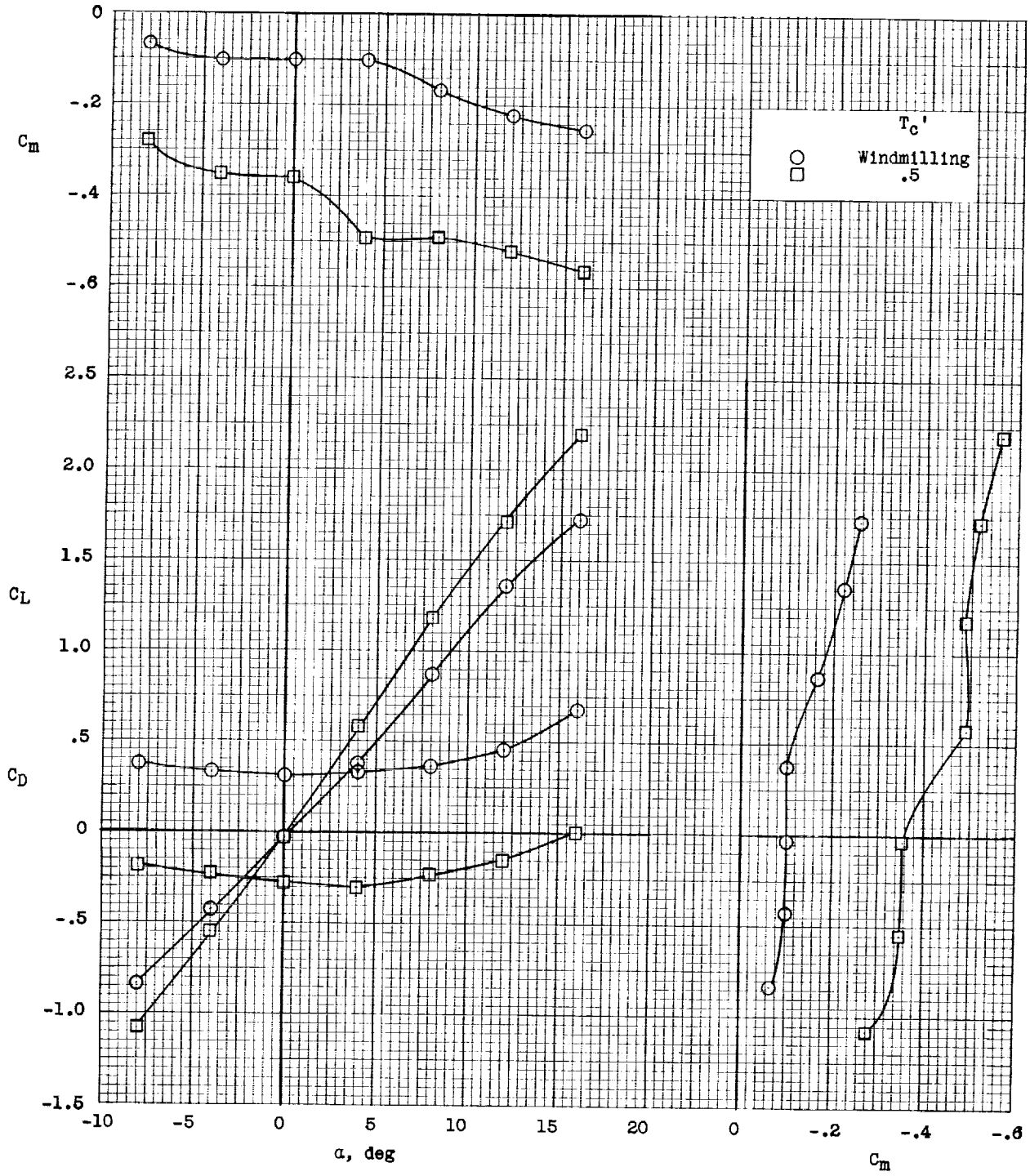

(a) $i_w = 0°$.

Figure 4.- Longitudinal stability and trim characteristics of IB-HI configuration. $i_{d,F} = -5°$; q = 5.0; gaps unsealed.

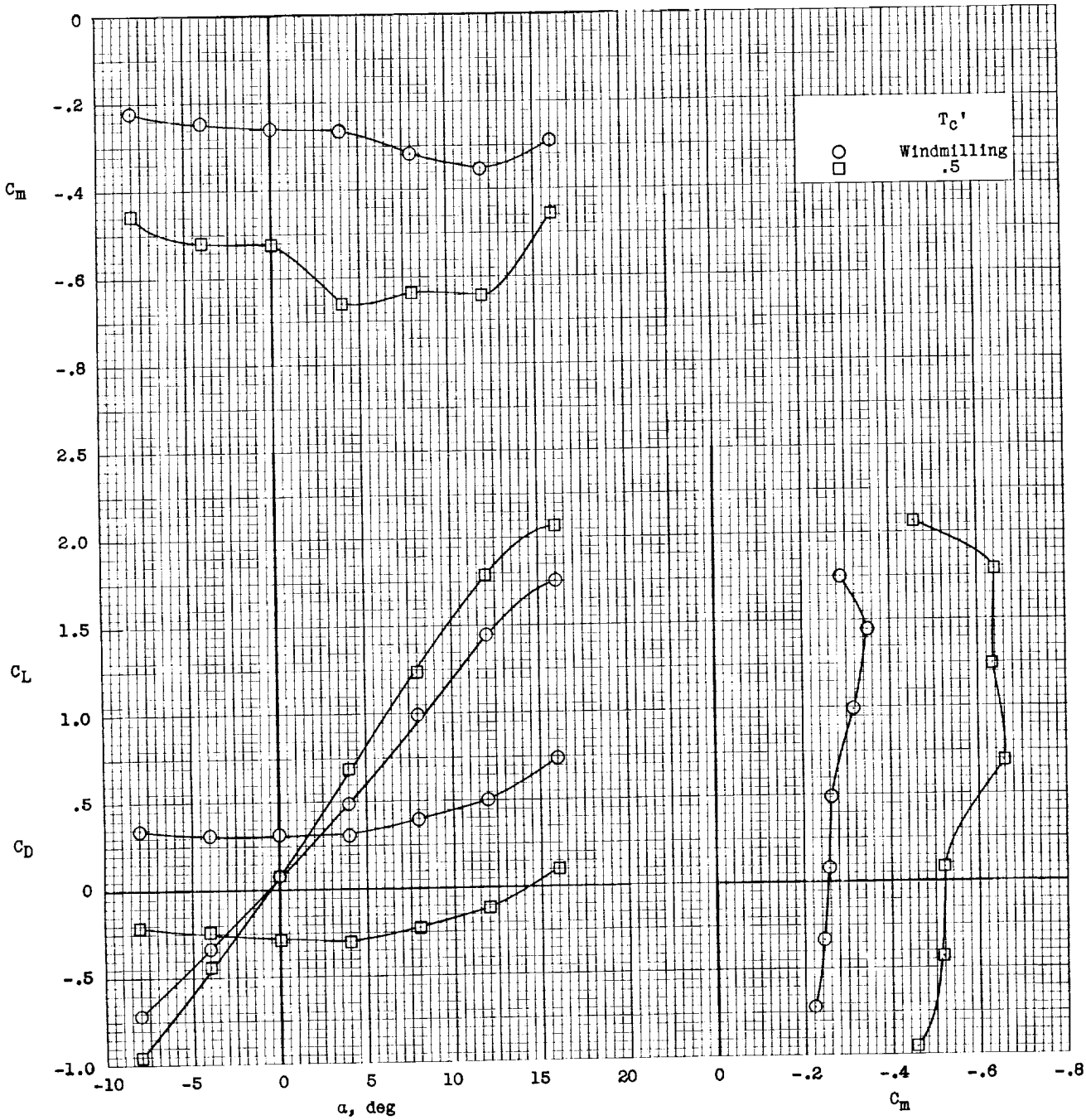

(b) $i_w = 5^o$.

Figure 4.- Continued.

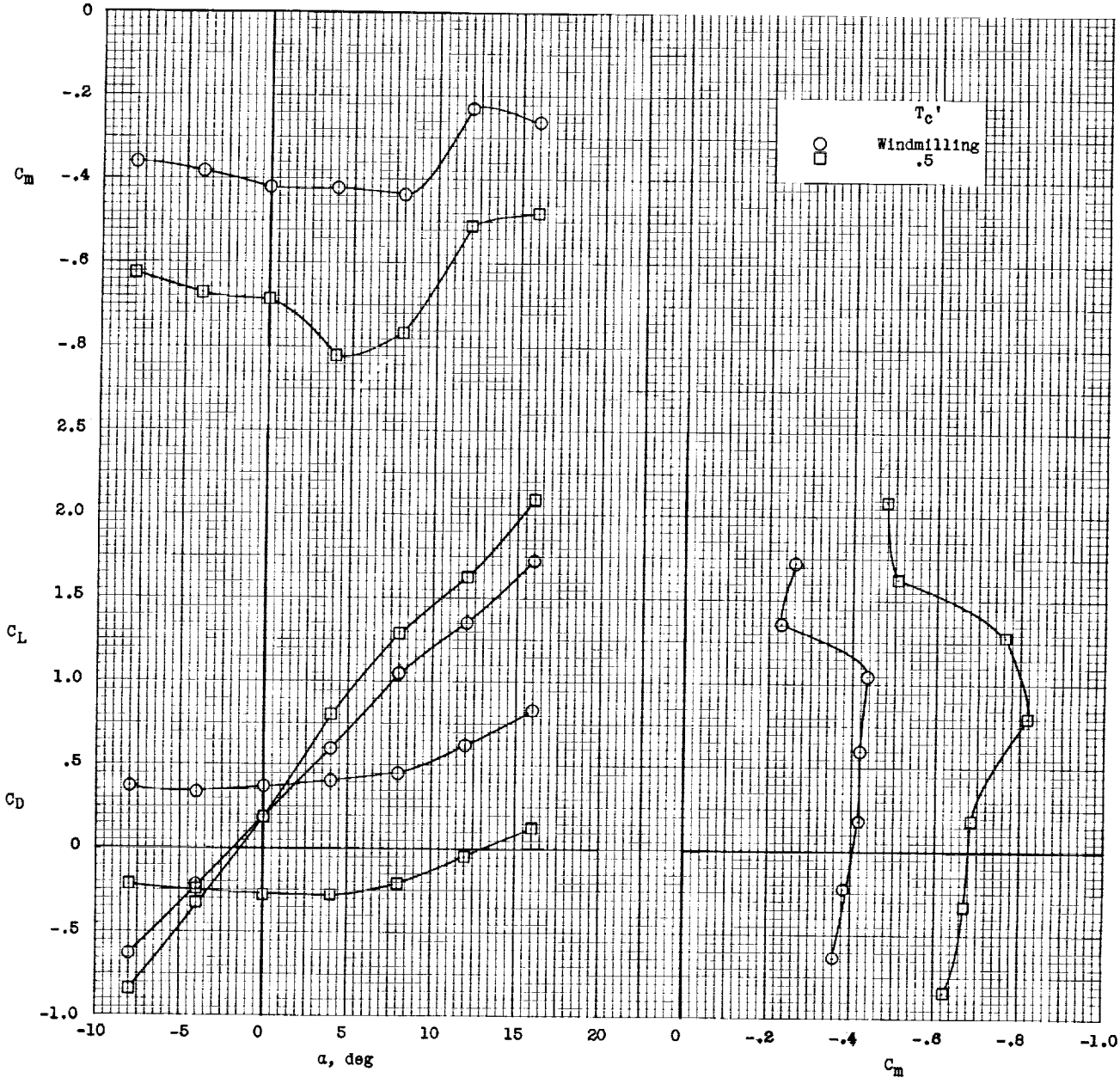

(c) $i_w = 10°$.

Figure 4.- Continued.

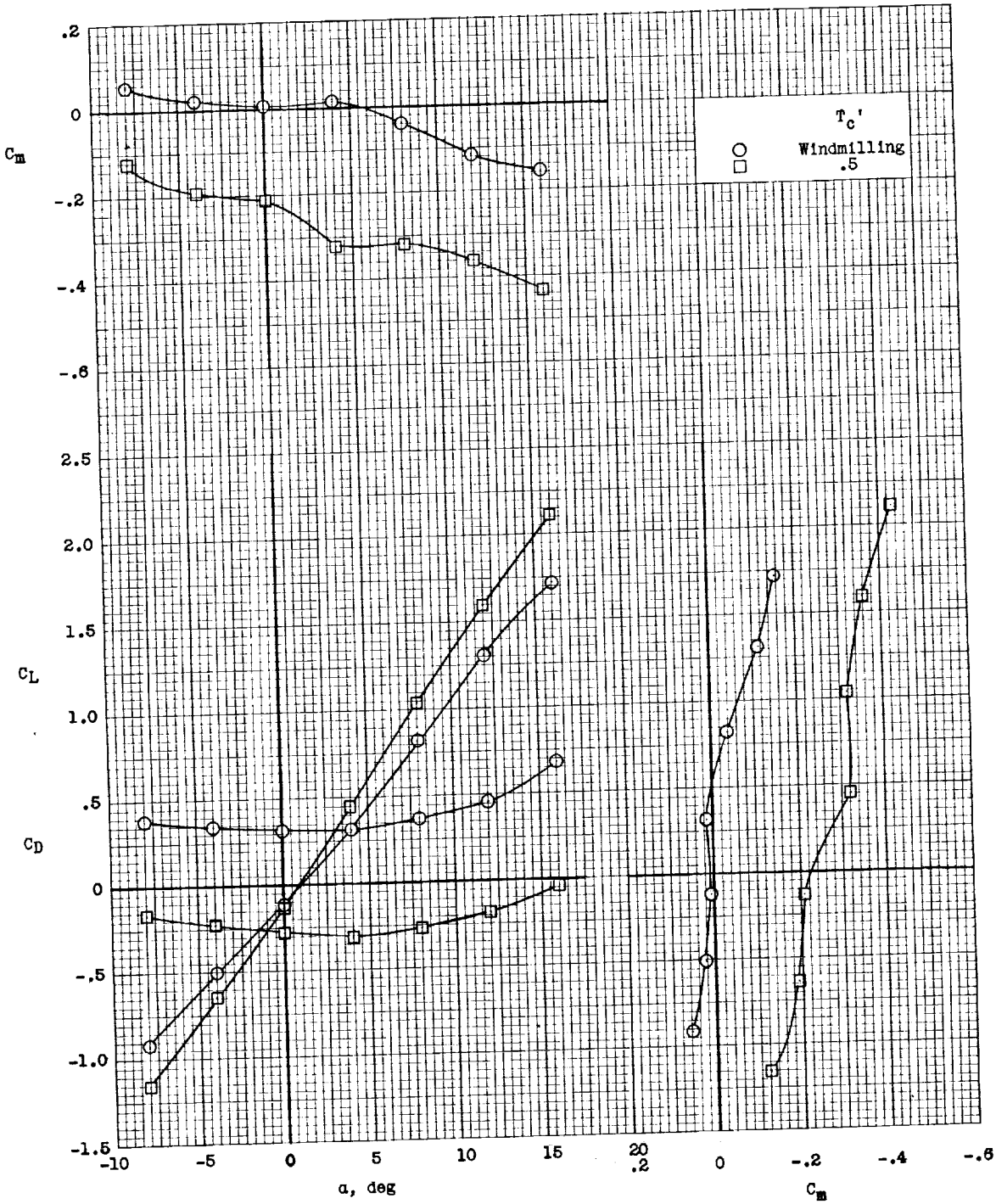

(d) $i_w = -5^\circ$.

Figure 4.- Continued.

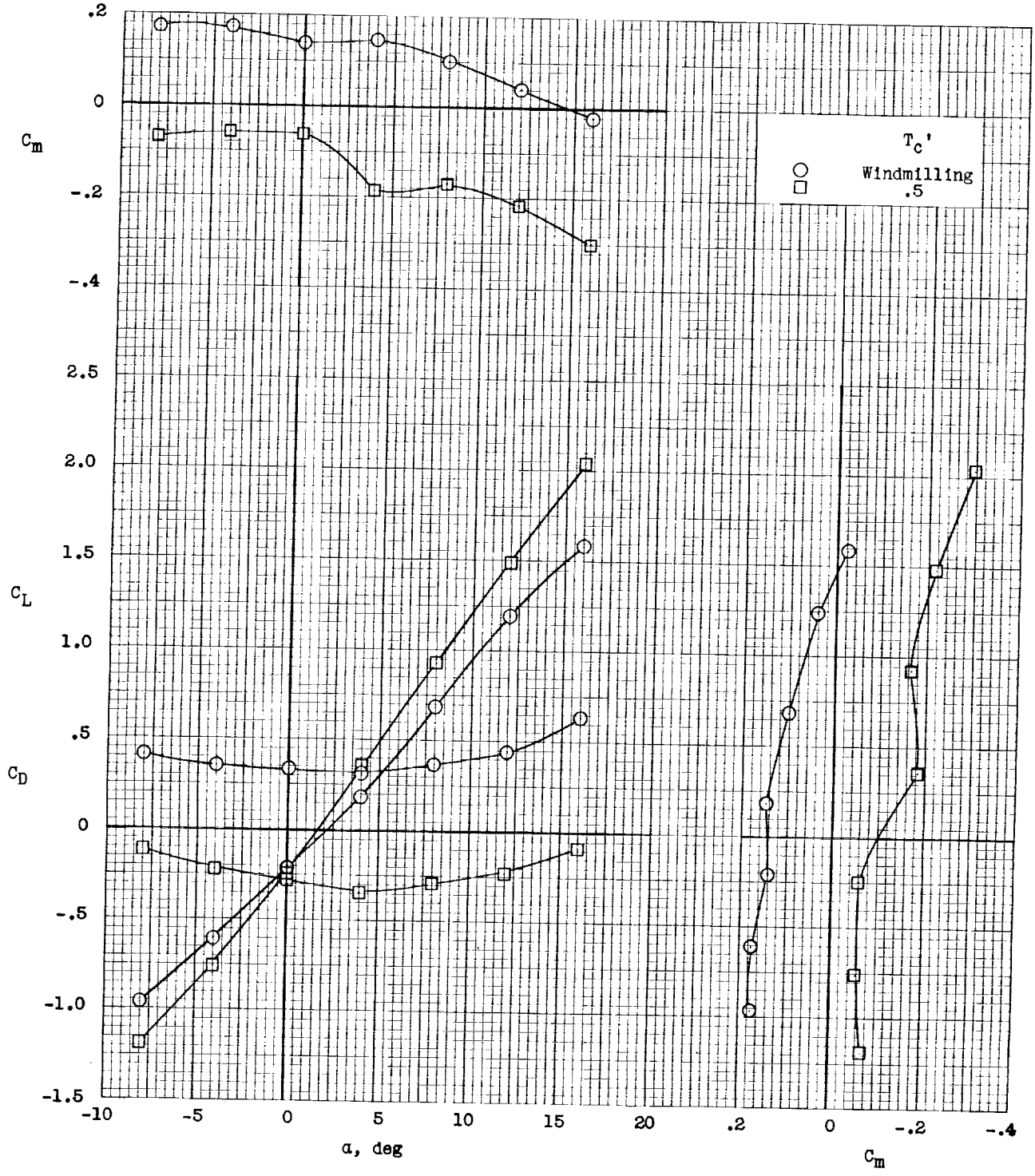

(e) $i_w = -10°$.

Figure 4.- Continued.

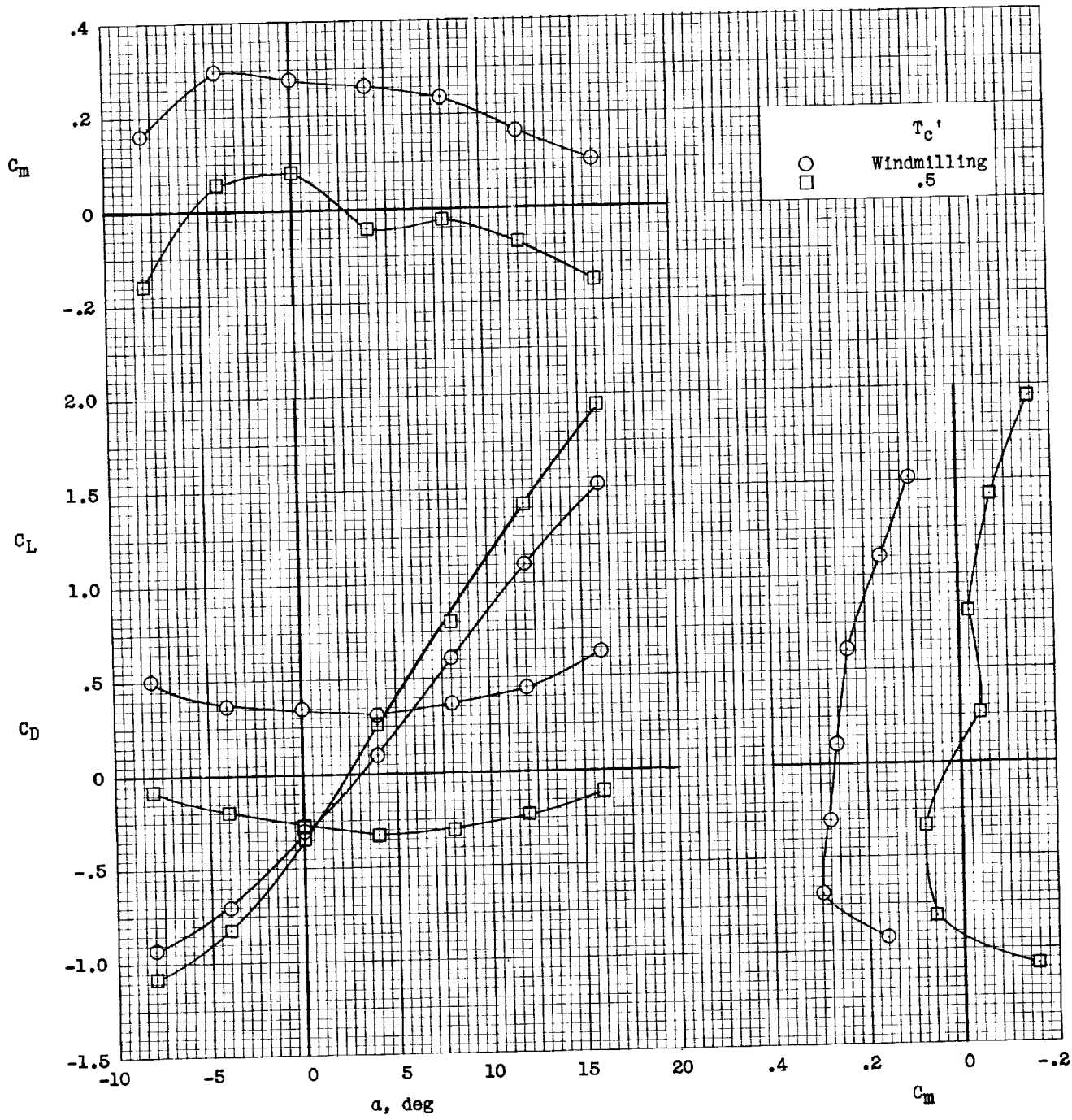

(f) $i_w = -15°$.

Figure 4.- Concluded.

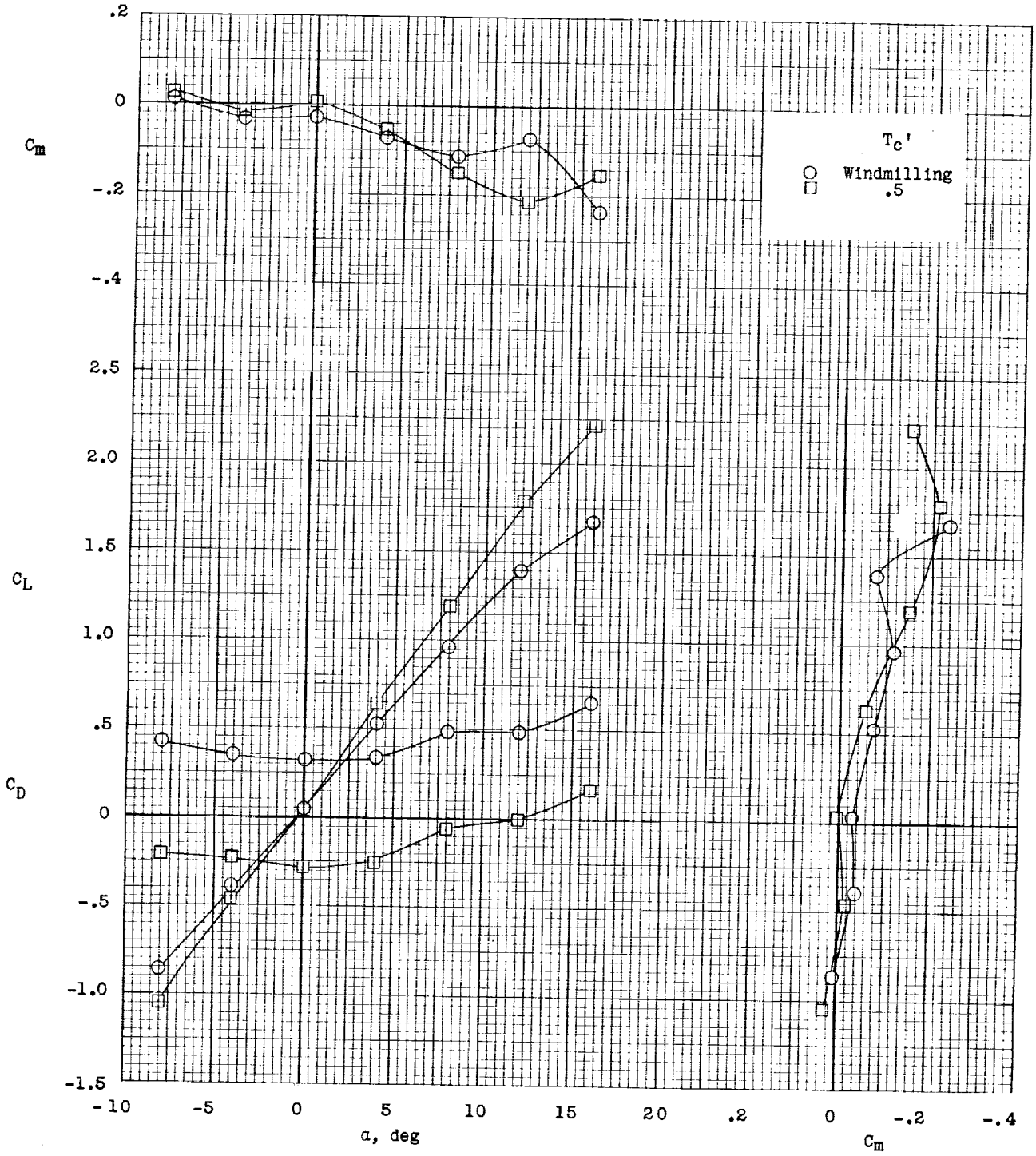

(a) $i_w = 0^o$.

Figure 5.- Longitudinal stability and trim characteristics of IB-LO configuration. $i_{d,F} = 0^o$; $q = 5.0$; gaps unsealed.

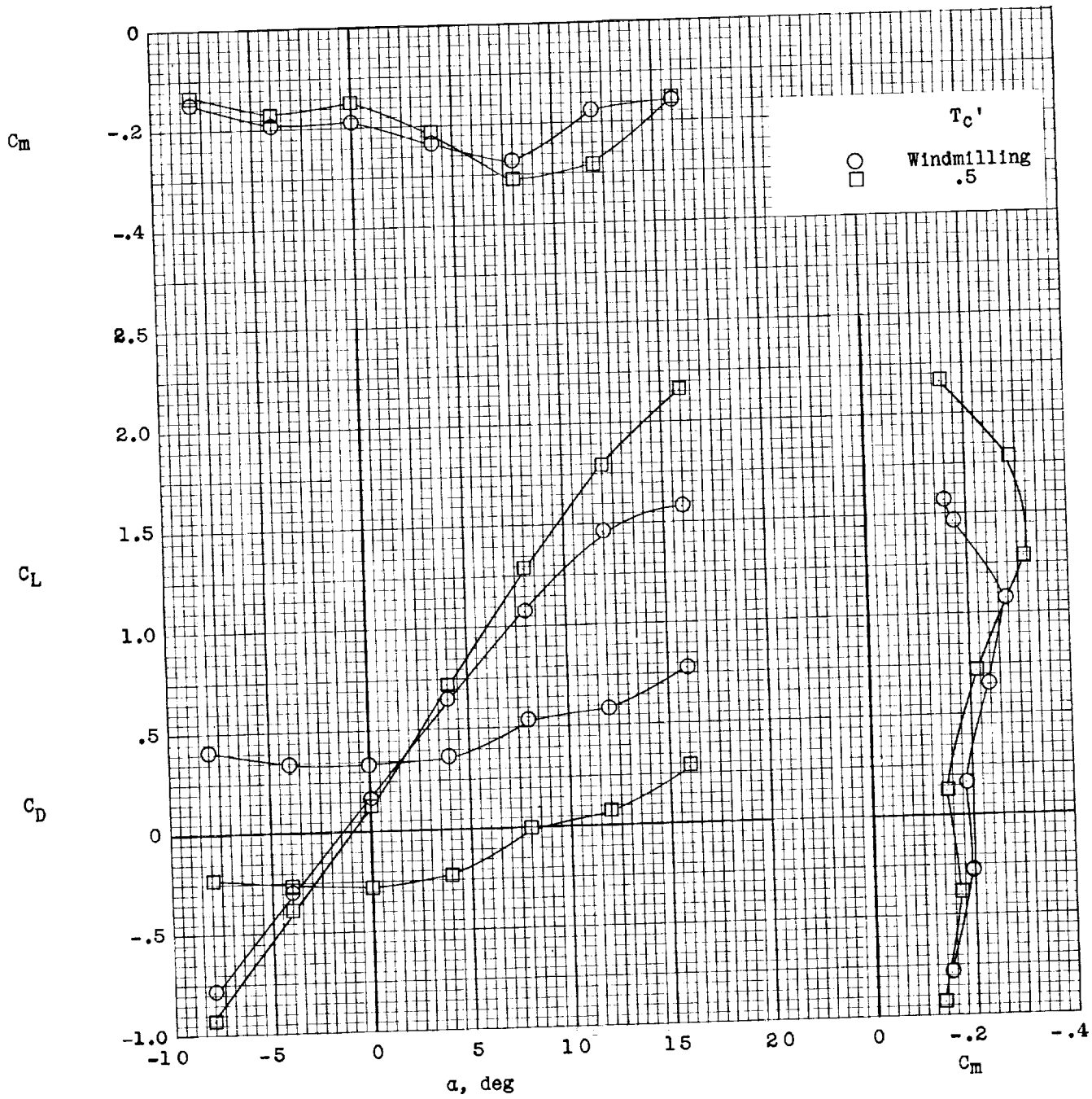

(b) $i_w = 5^\circ$.

Figure 5.- Continued.

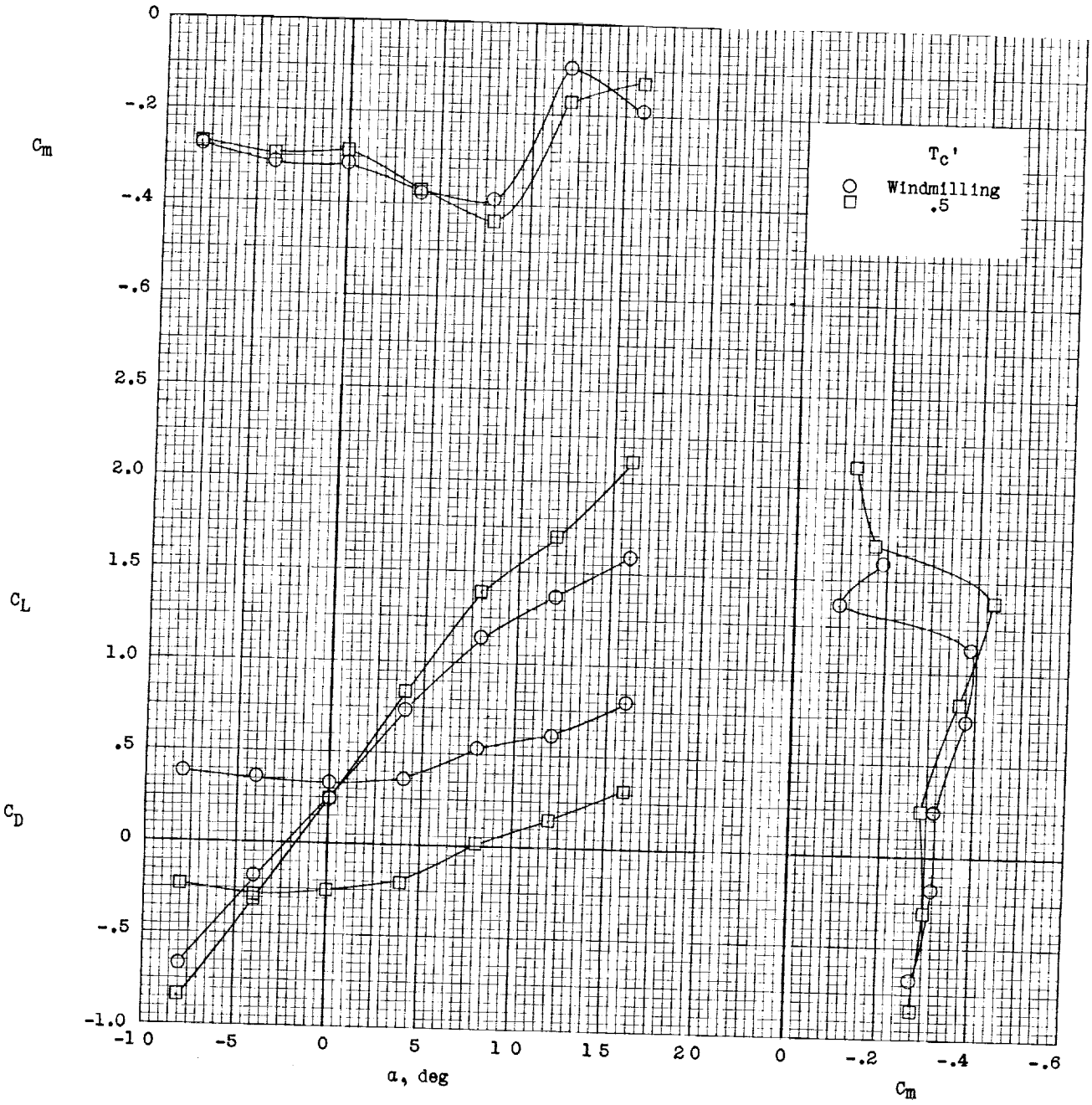

(c) $i_w = 10^o$.

Figure 5.- Continued.

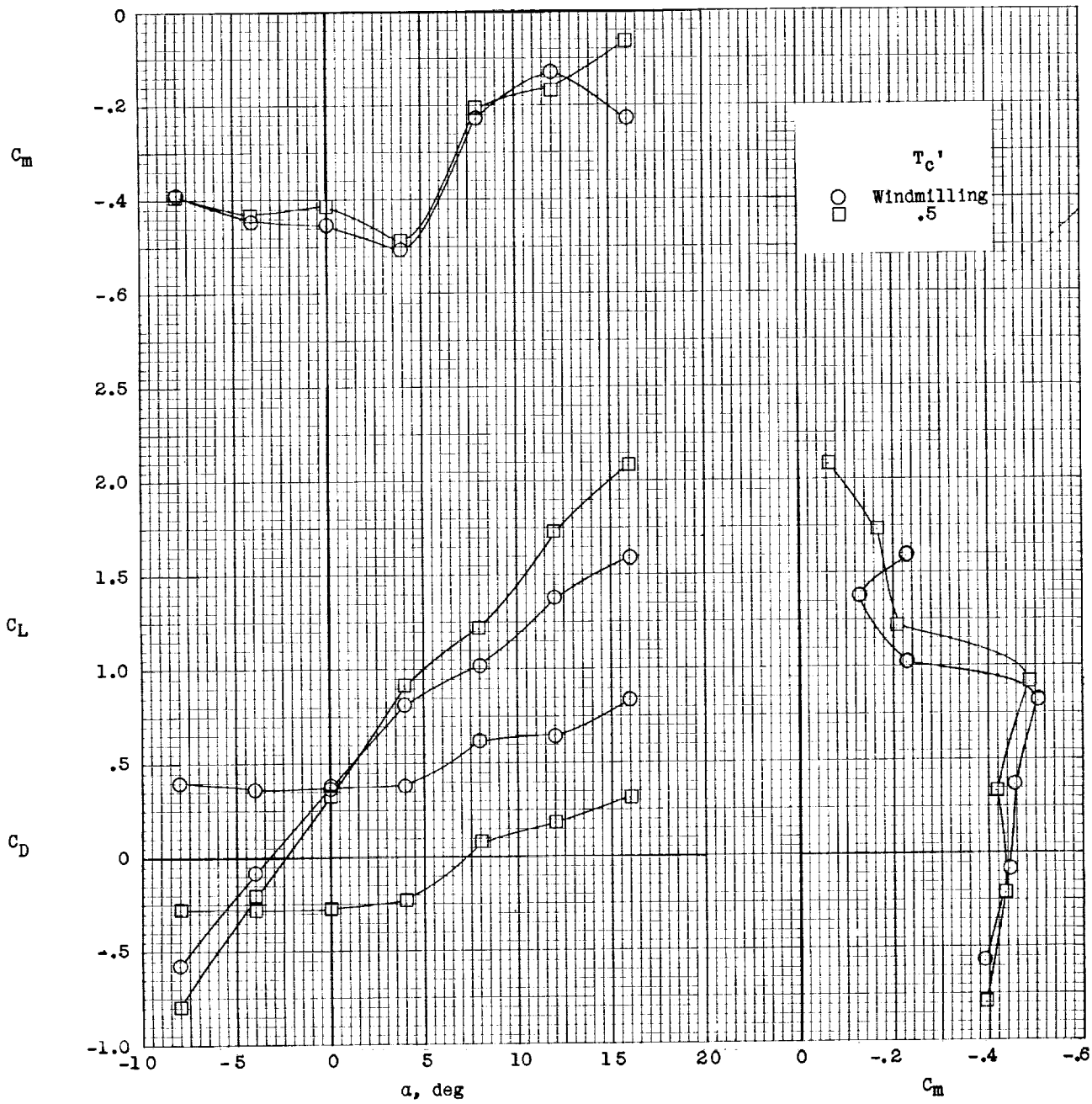

(d) $i_w = 15^\circ$.

Figure 5.- Continued.

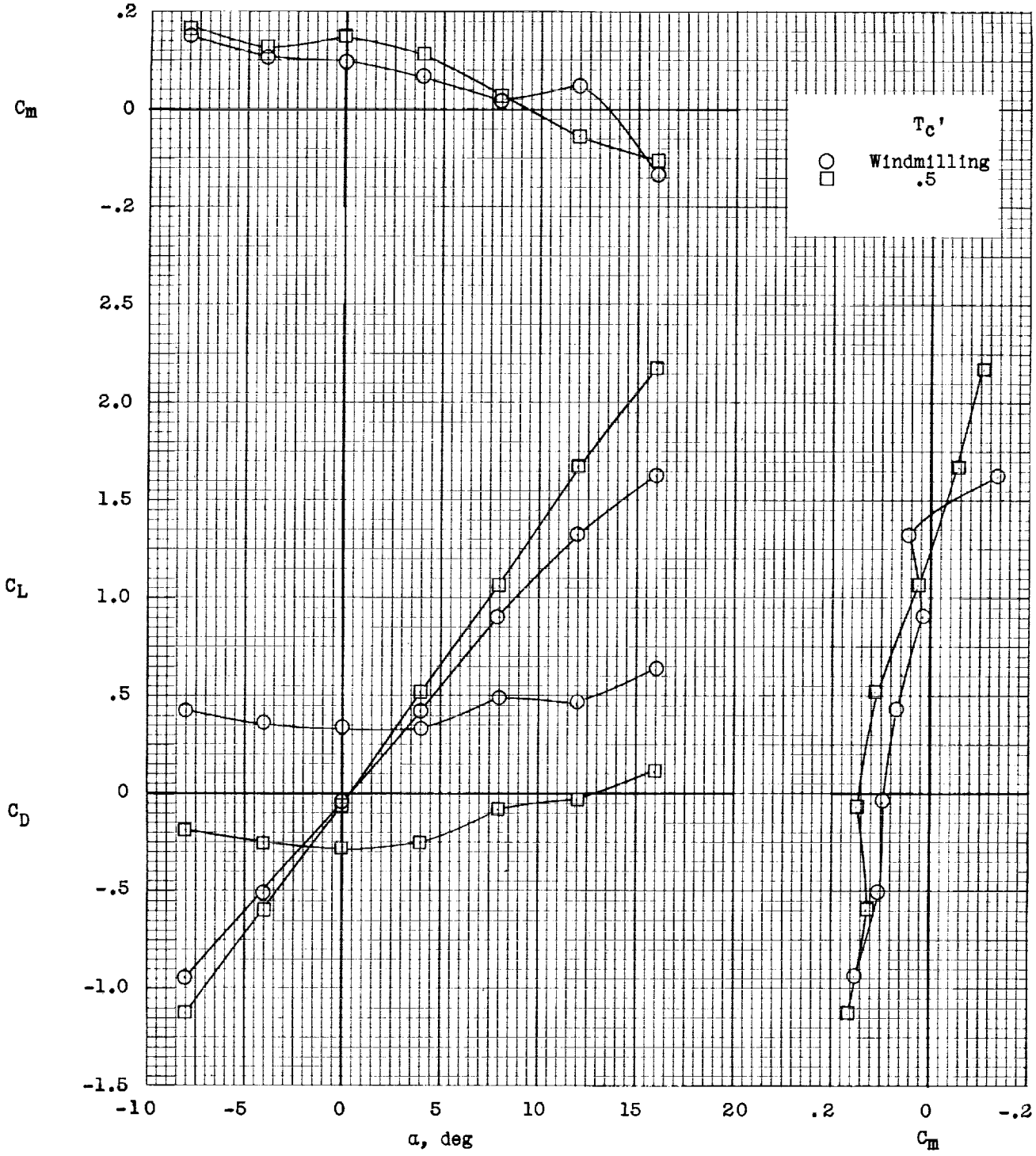

(e) $i_w = -5^o$.

Figure 5.- Continued.

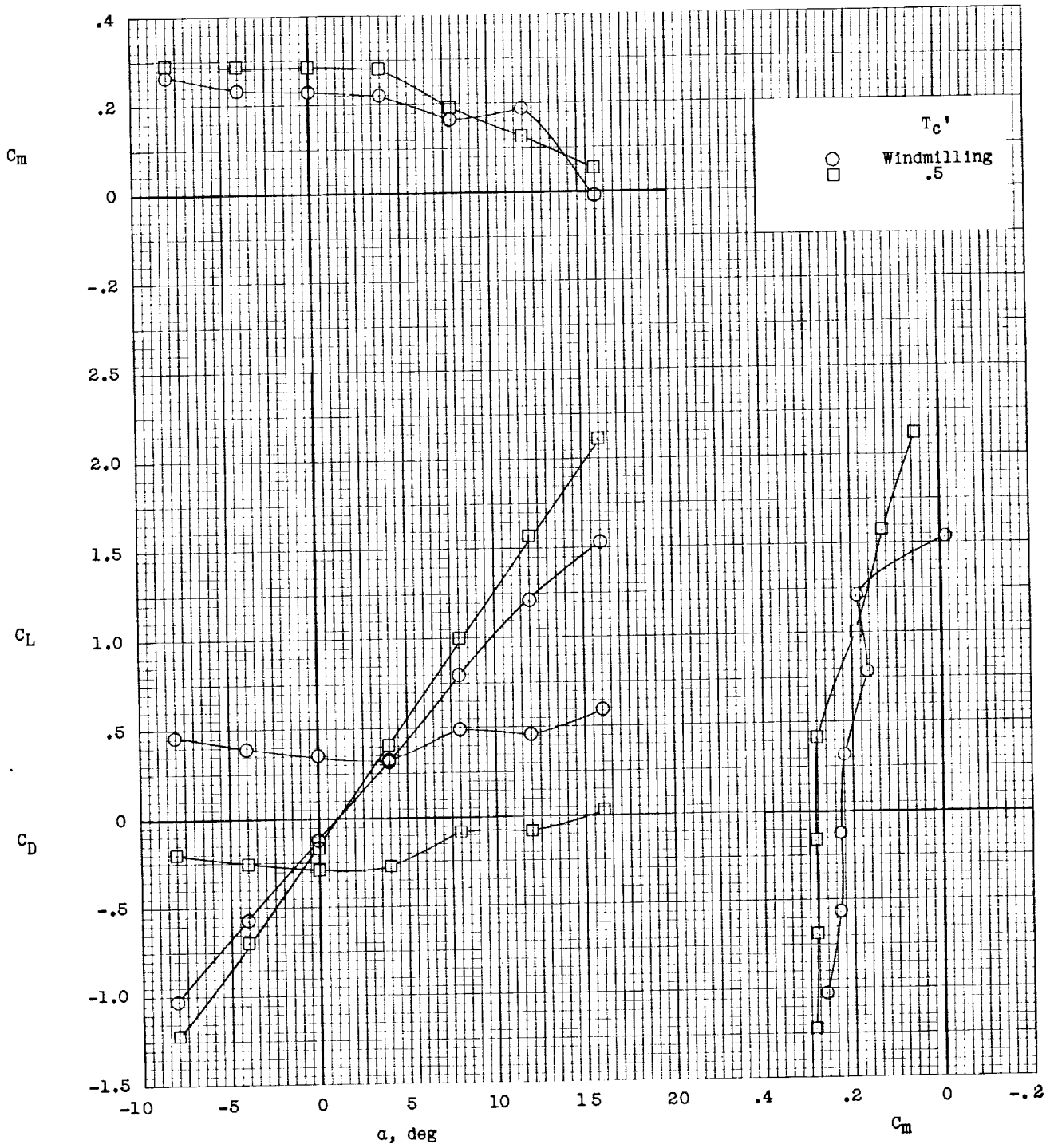

(f) $i_w = -10^o$.

Figure 5.- Continued.

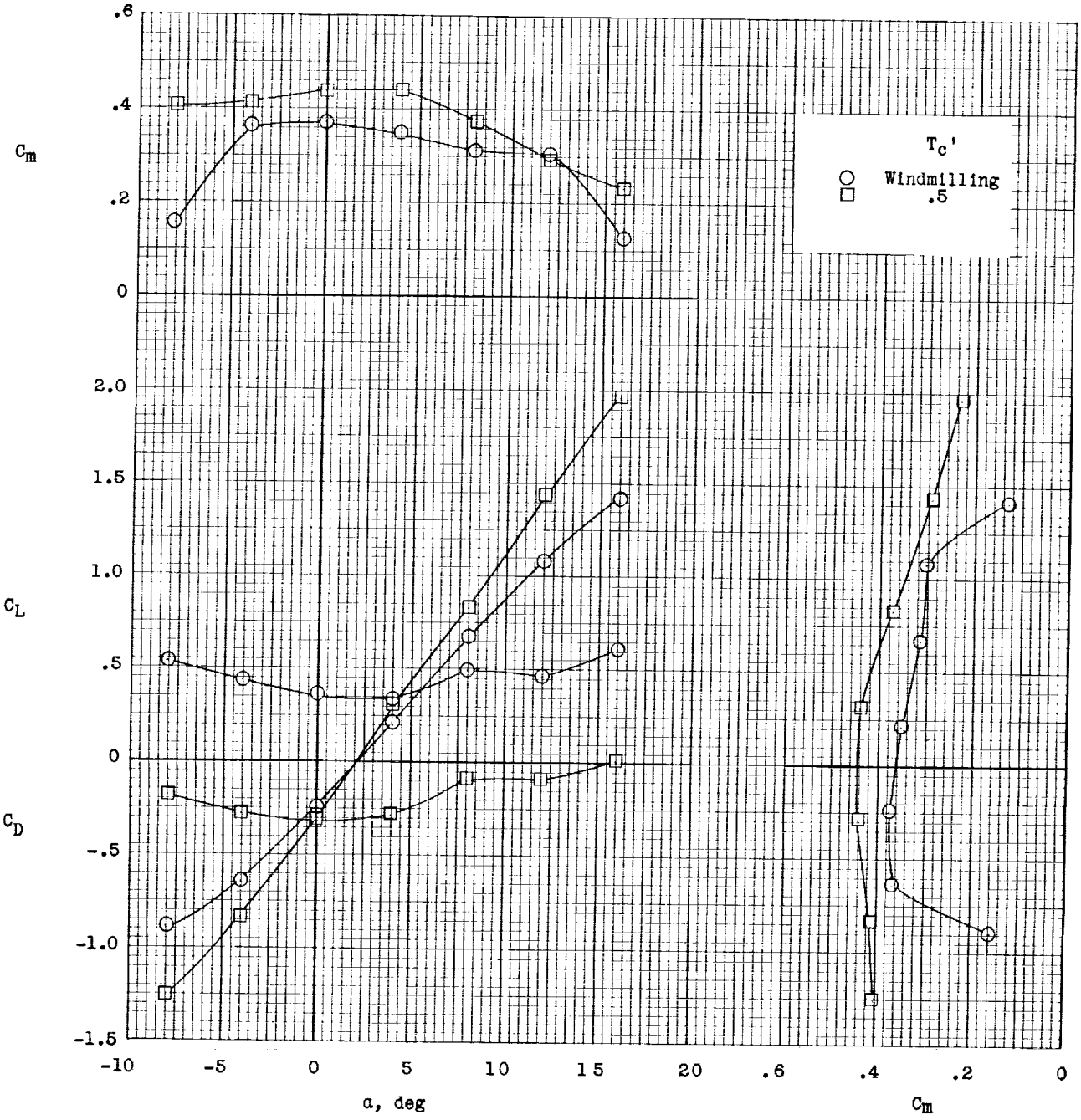

(g) $i_w = -15^\circ$.

Figure 5.- Concluded.

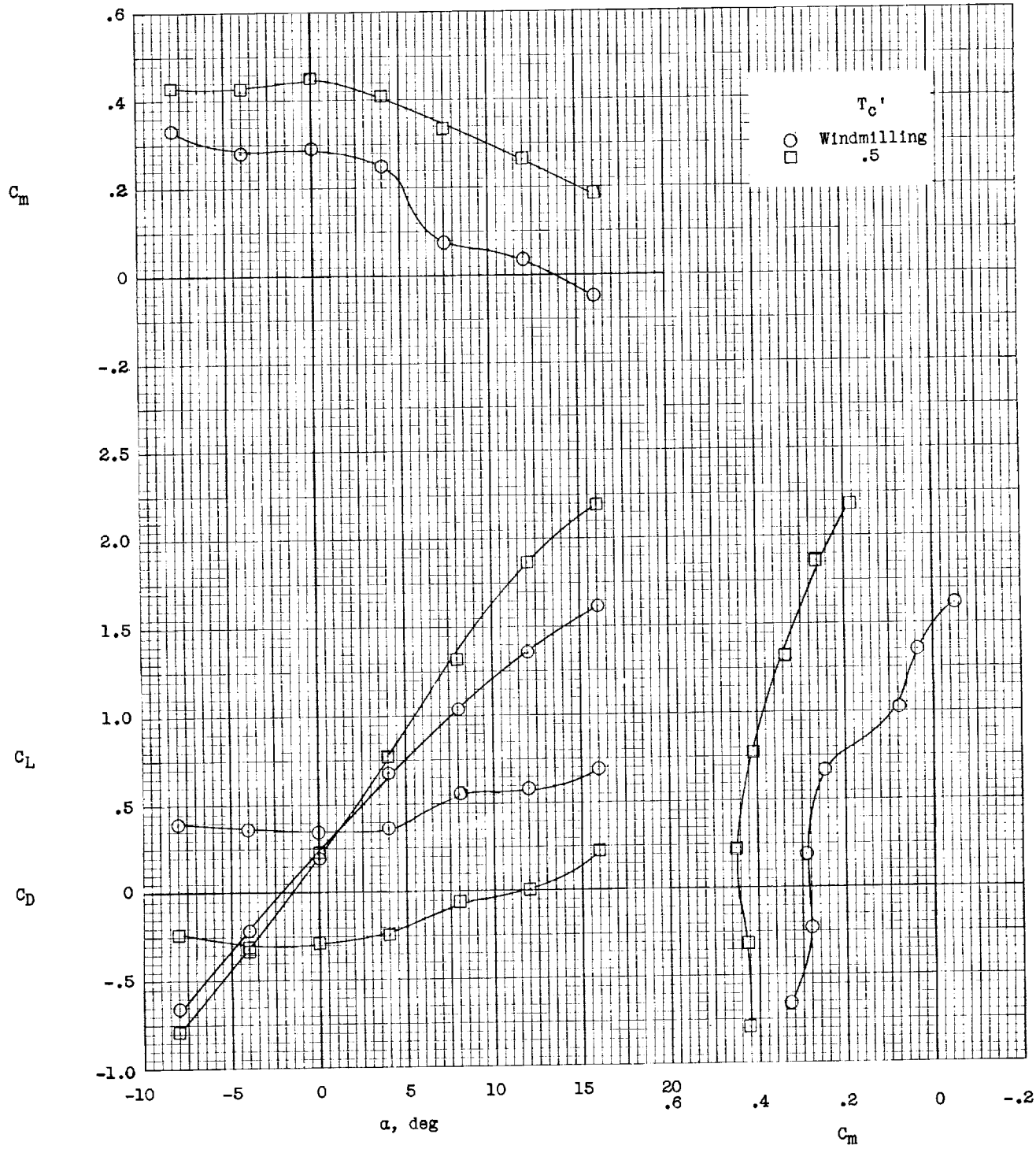

(a) $i_w = 0^o$.

Figure 6.- Longitudinal stability and trim characteristics of IB-LO configuration. $i_{d,F} = 5^o$; $q = 5.0$; gaps unsealed.

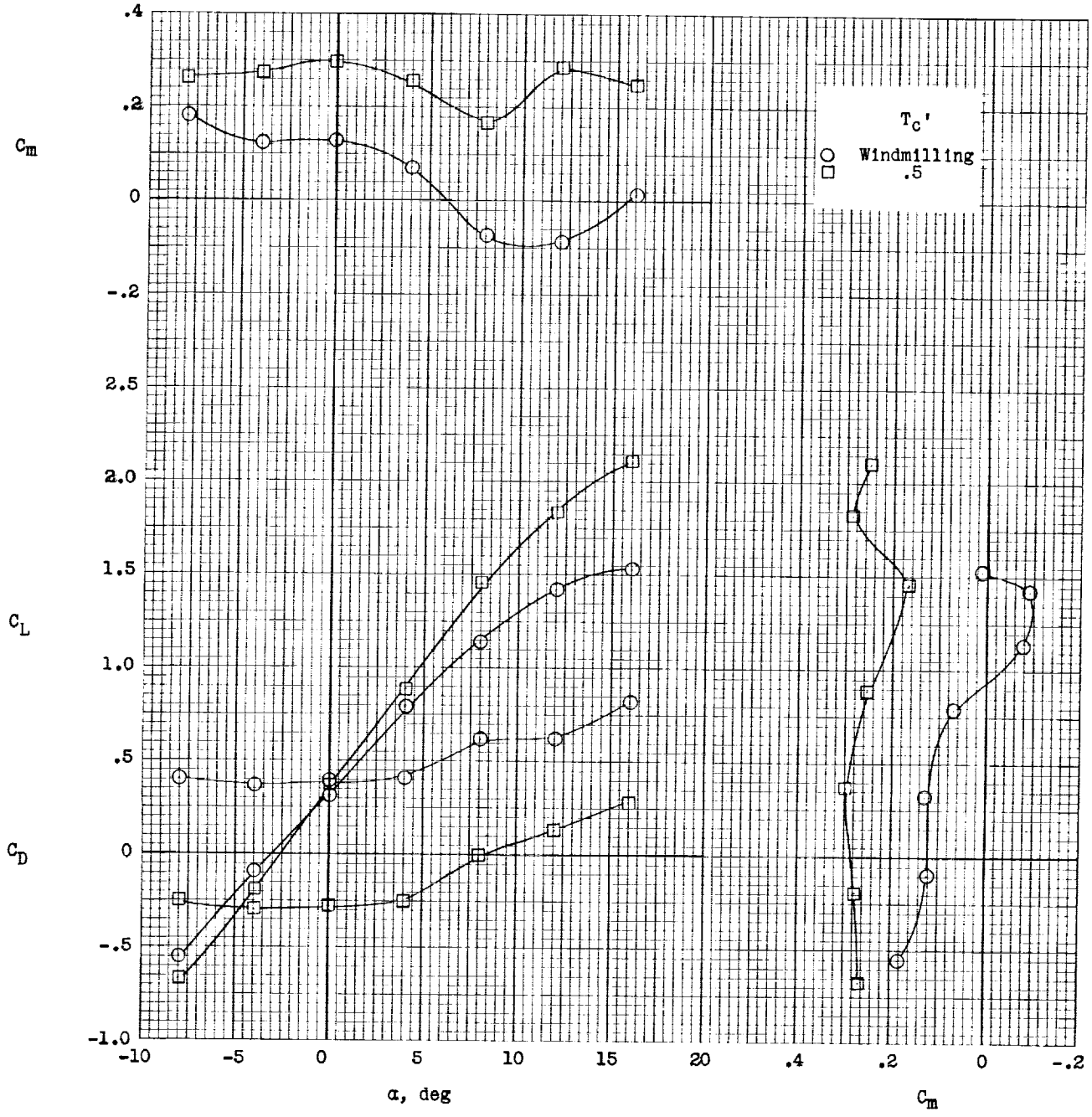

(b) $i_w = 5°$.

Figure 6.- Continued.

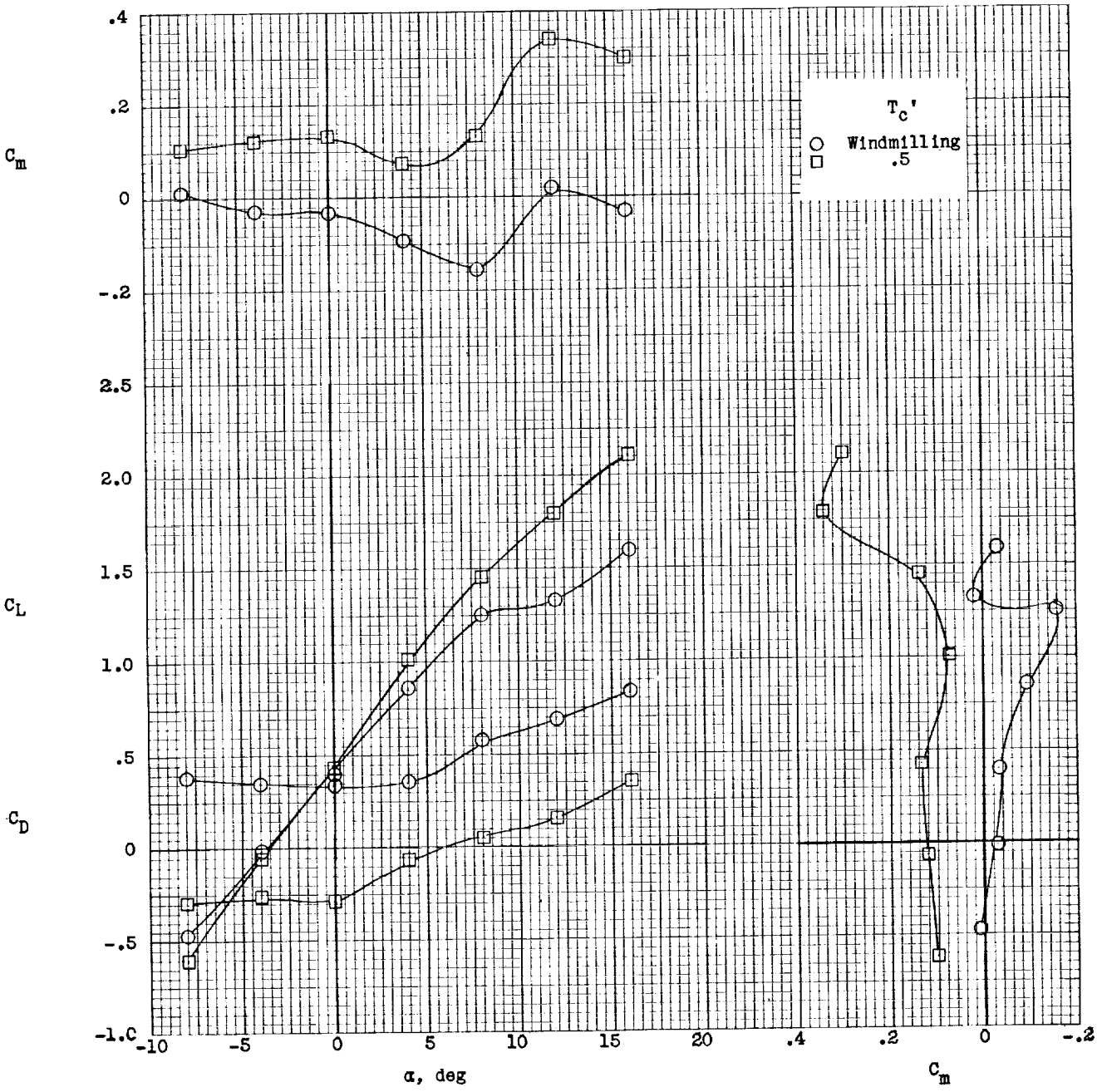

(c) $i_w = 10^o$.

Figure 6.- Continued.

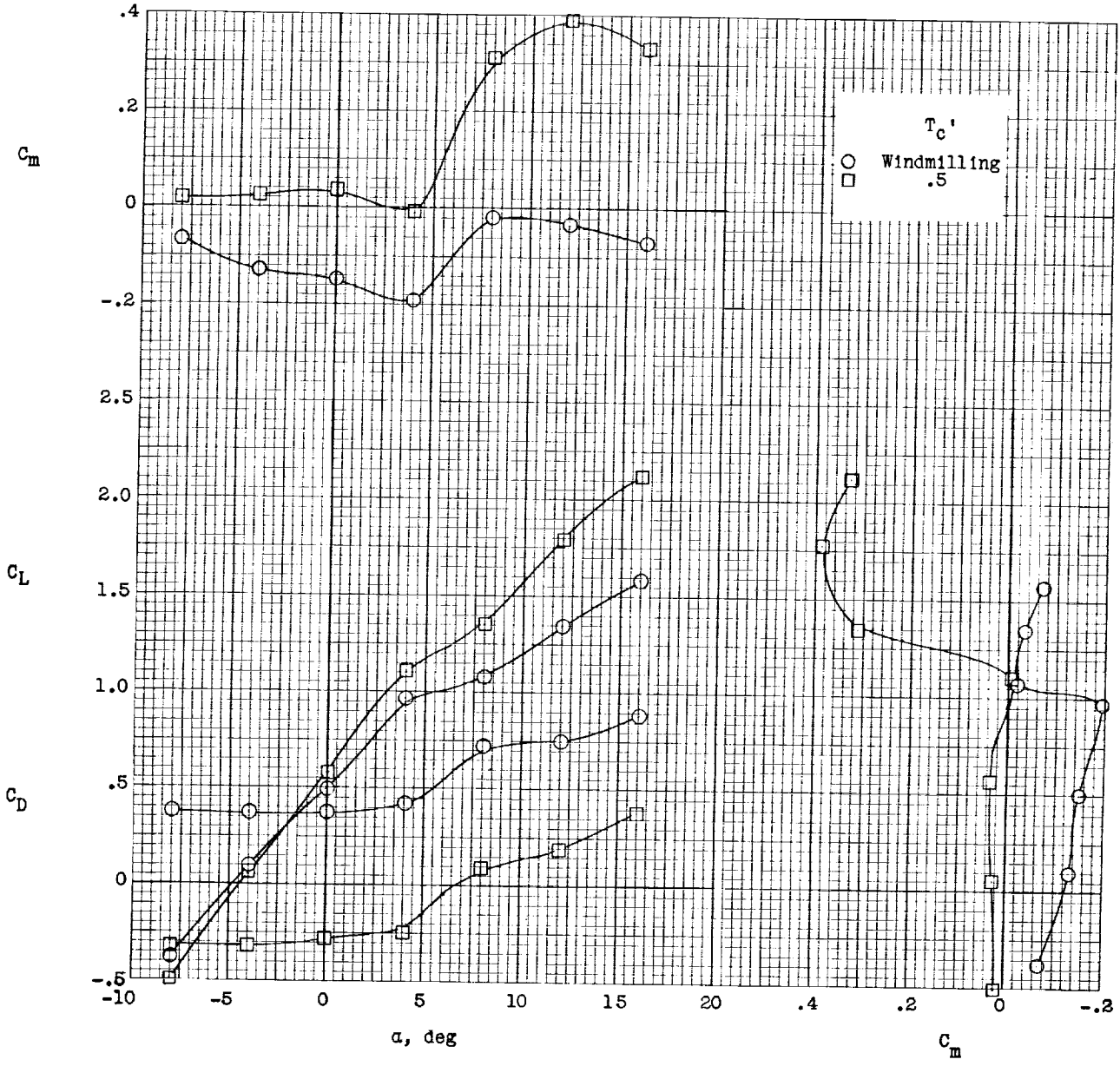

(d) $i_w = 15^\circ$.

Figure 6.- Continued.

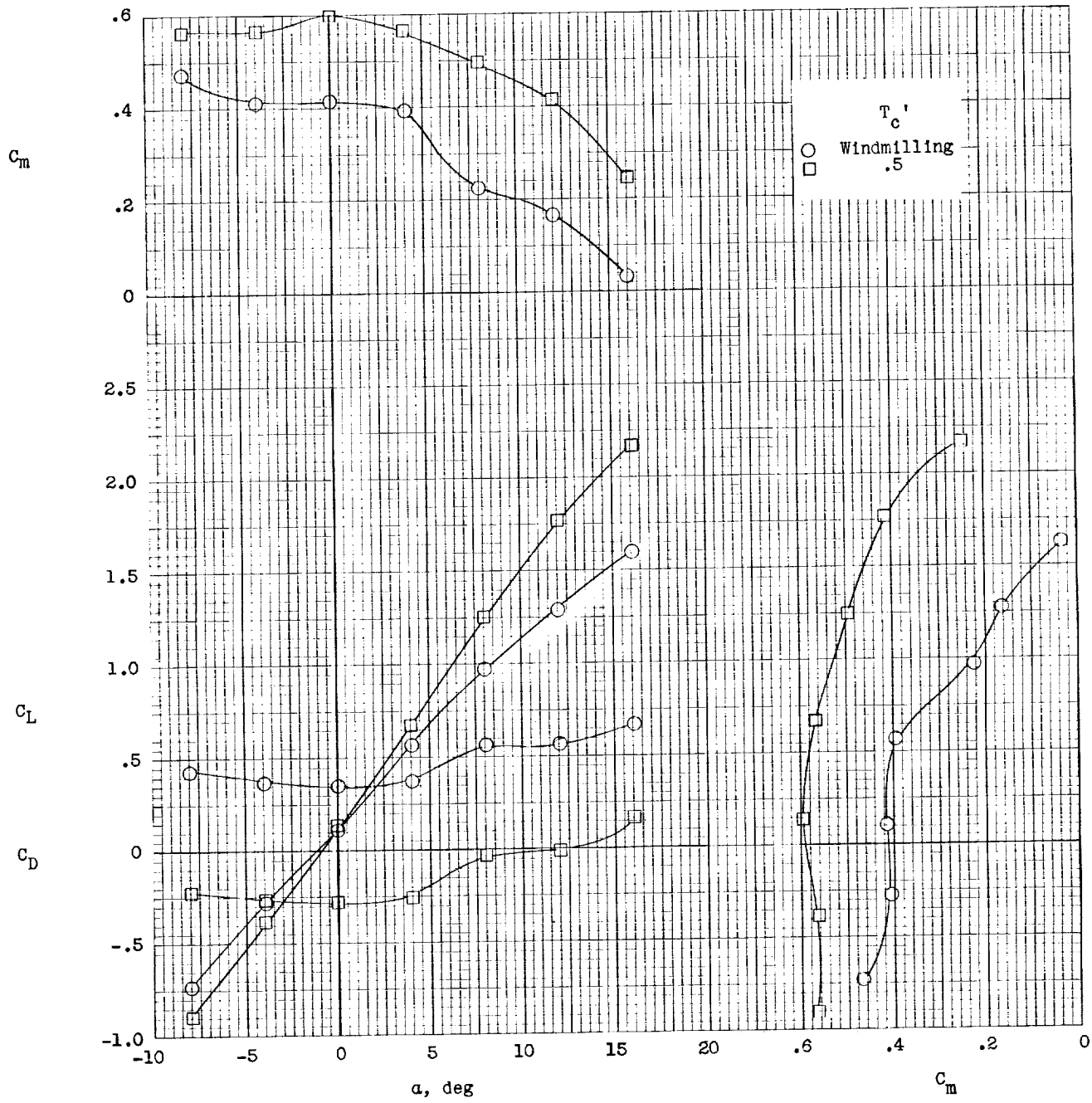

(e) $i_w = -5^o$.

Figure 6.- Continued.

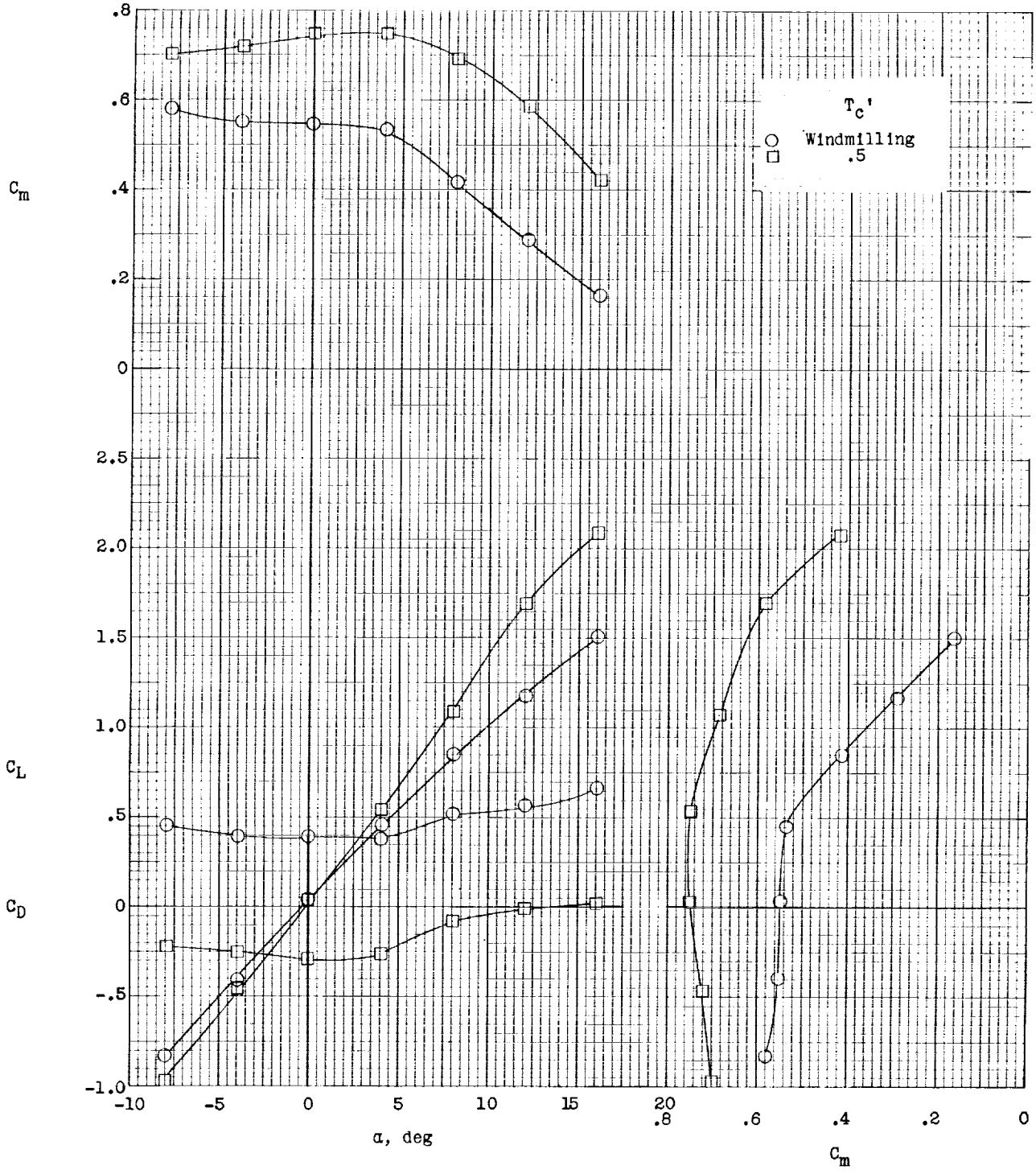

(f) $i_w = -10°$.

Figure 6.- Concluded.

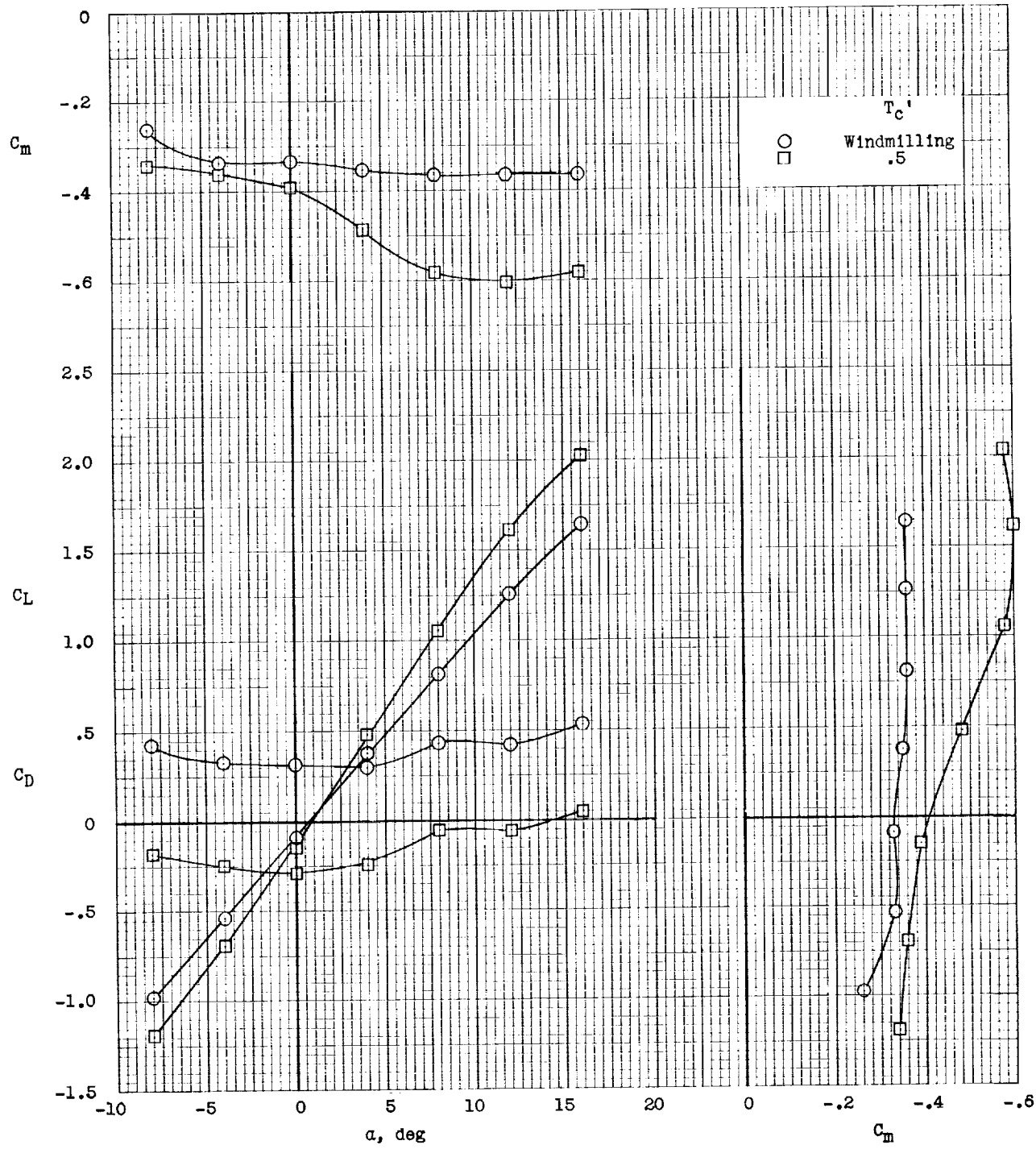

(a) $i_w = 0°$.

Figure 7.- Longitudinal stability and trim characteristics of IB-LO configuration. $i_{d,F} = -5°$; $q = 5.0$; gaps unsealed.

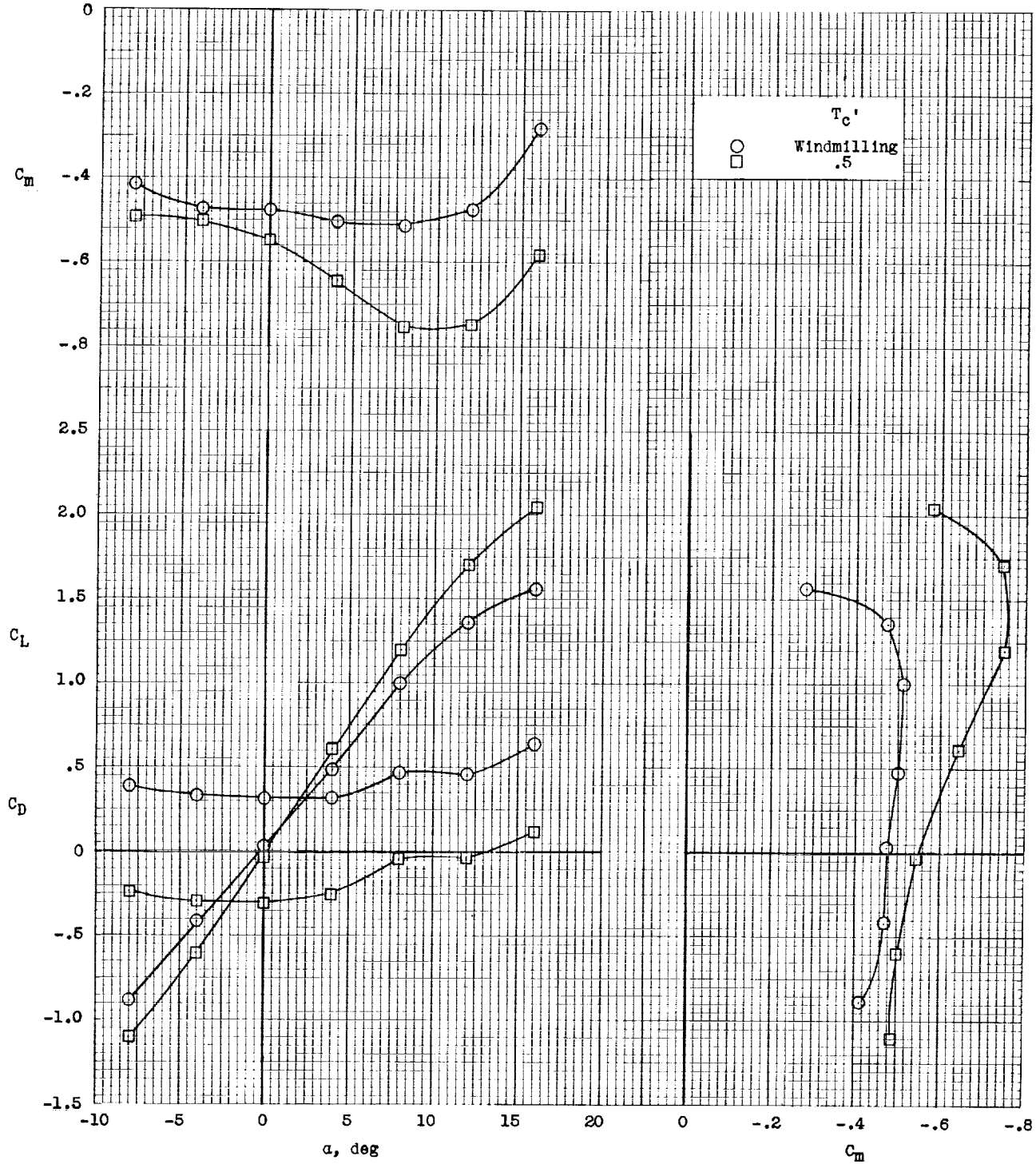

(b) $i_w = 5^\circ$.

Figure 7.- Continued.

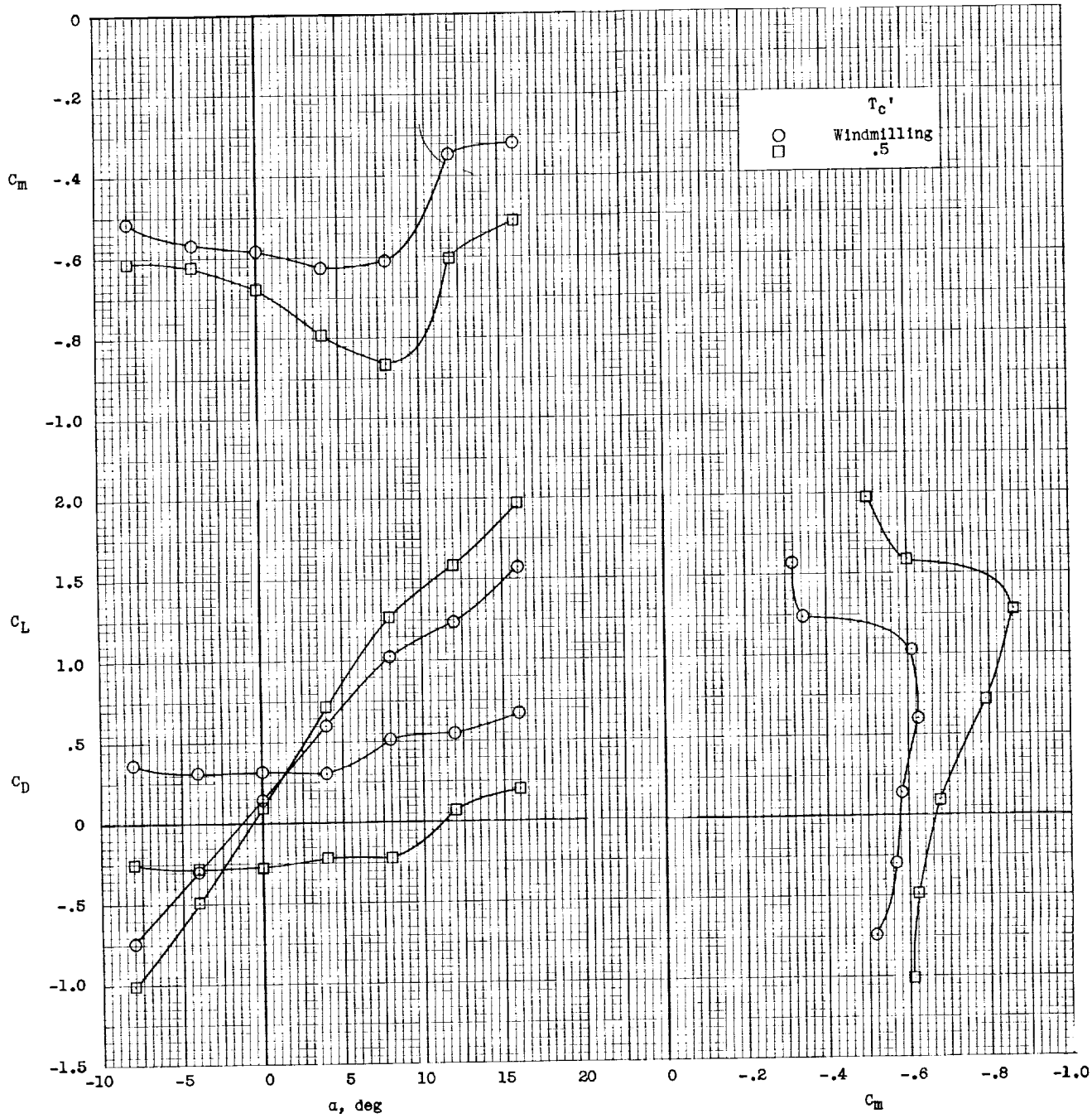

(c) $i_w = 10^o$.

Figure 7.- Continued.

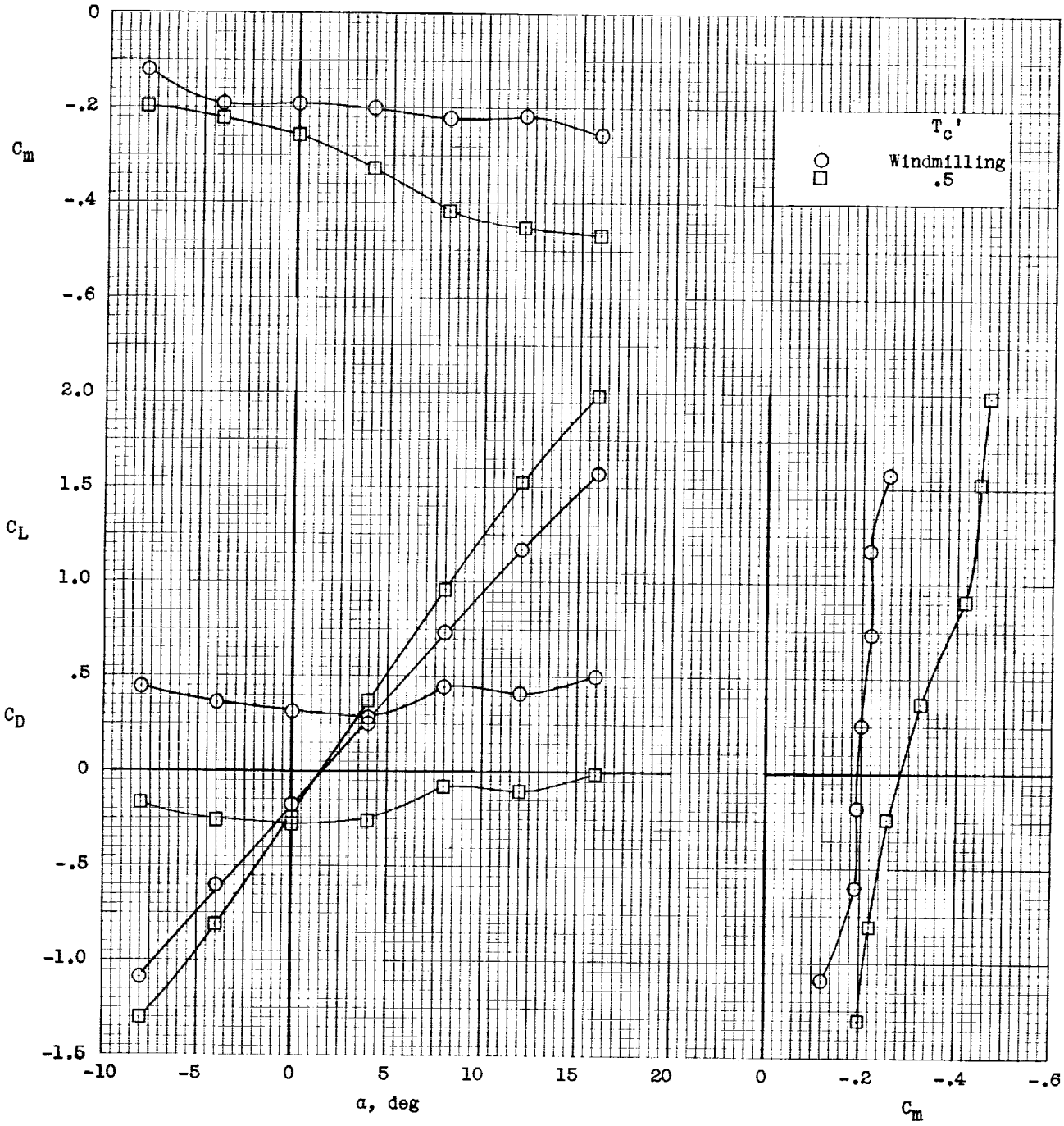

(d) $i_w = -5°$.

Figure 7.- Continued.

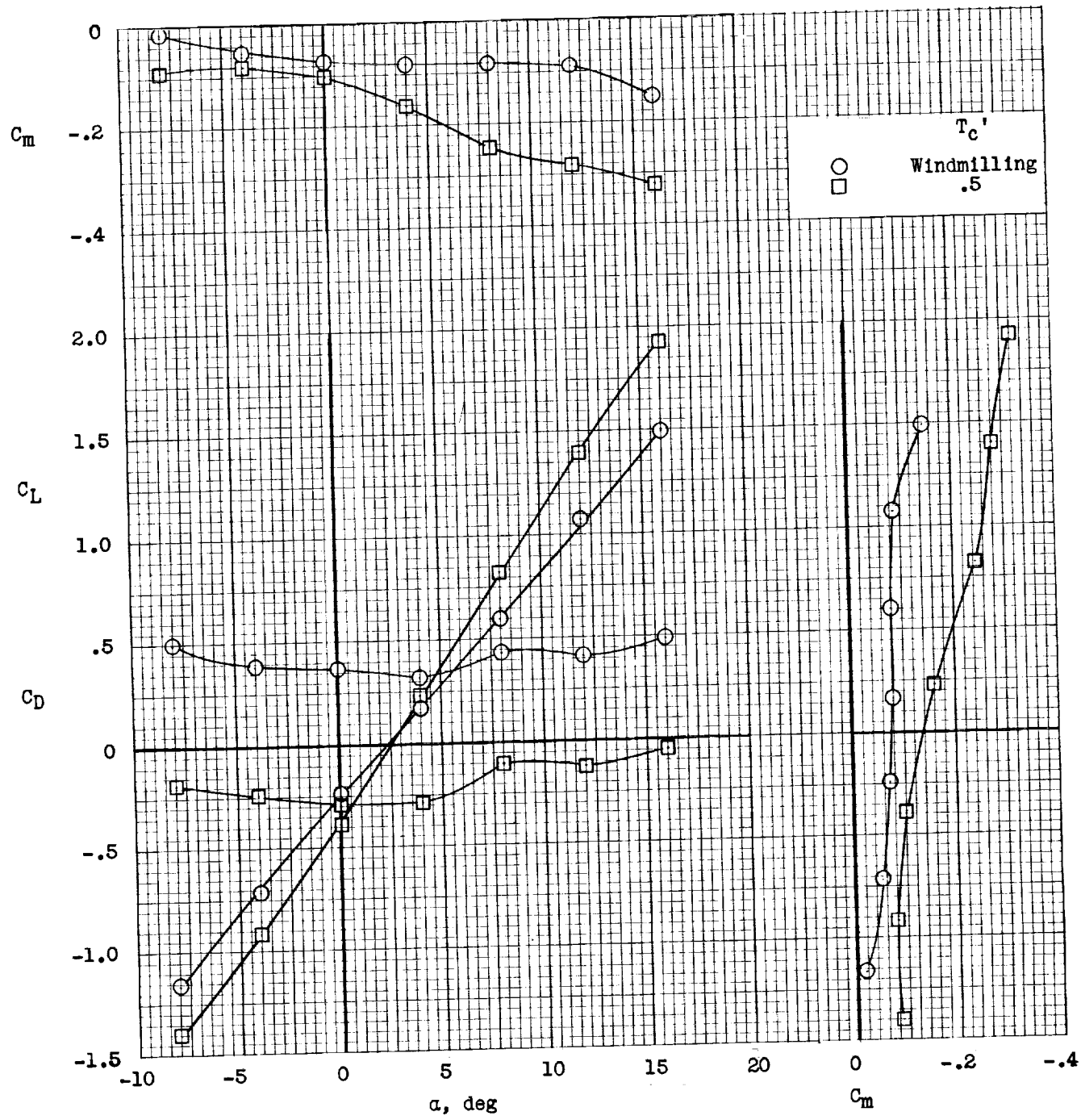

(e) $i_w = -10^o$.

Figure 7.- Continued.

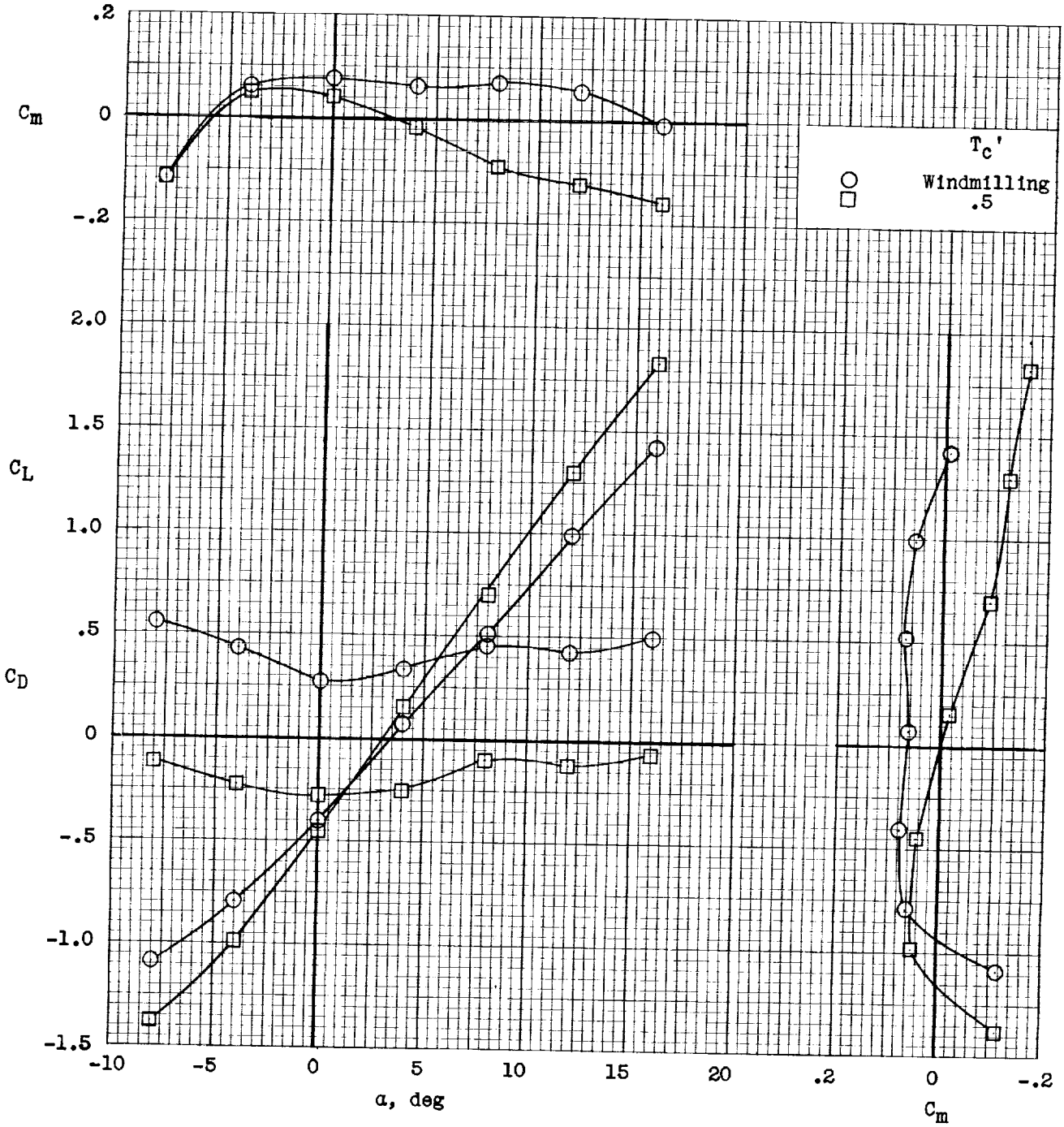

(f) $i_w = -15^\circ$.

Figure 7.- Concluded.

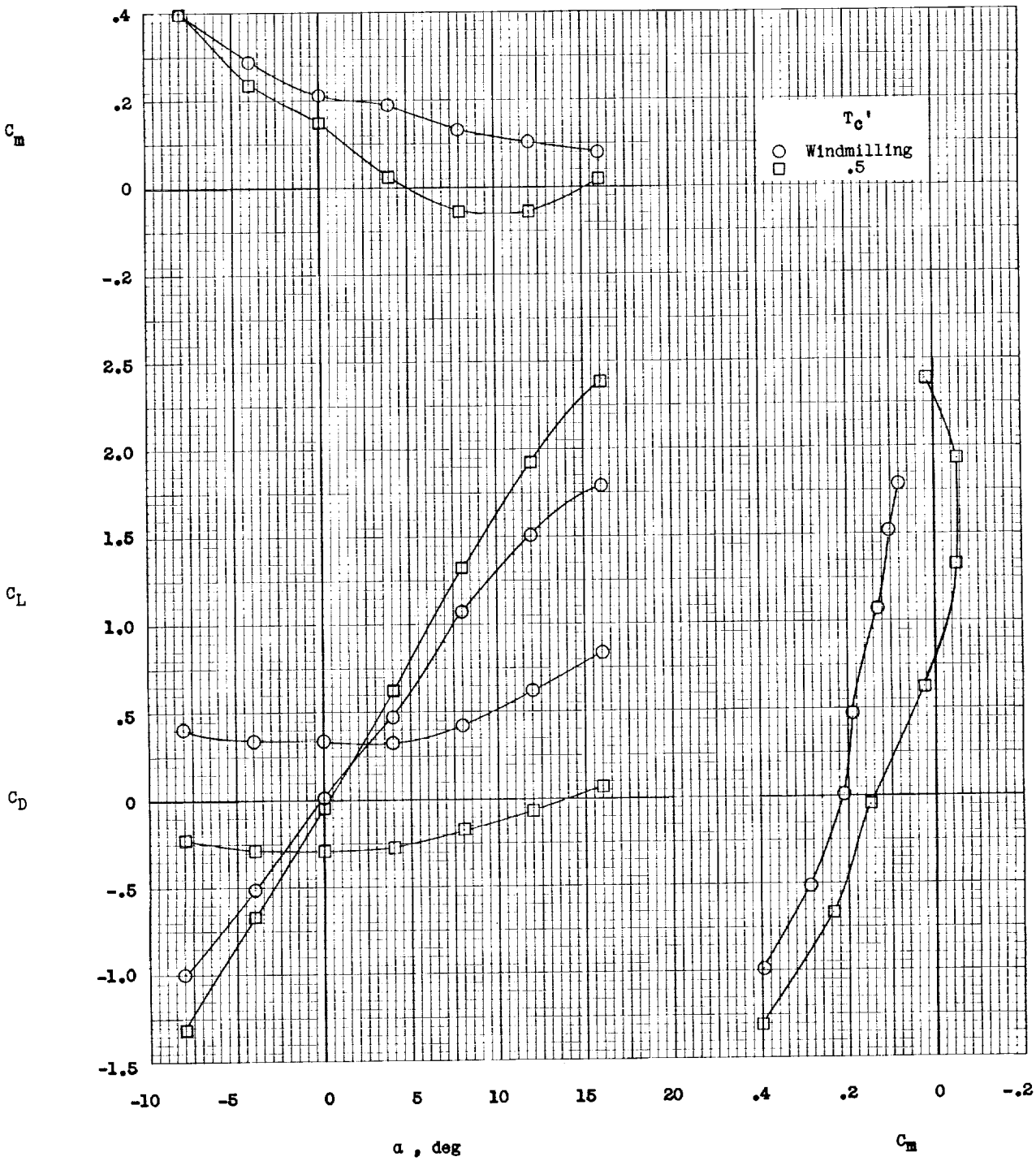

(a) $i_w = 0^o$.

Figure 8.- Longitudinal stability and trim characteristics of OB-HI configuration. $i_{d,F} = 0^o$; $q = 5.0$; gaps unsealed.

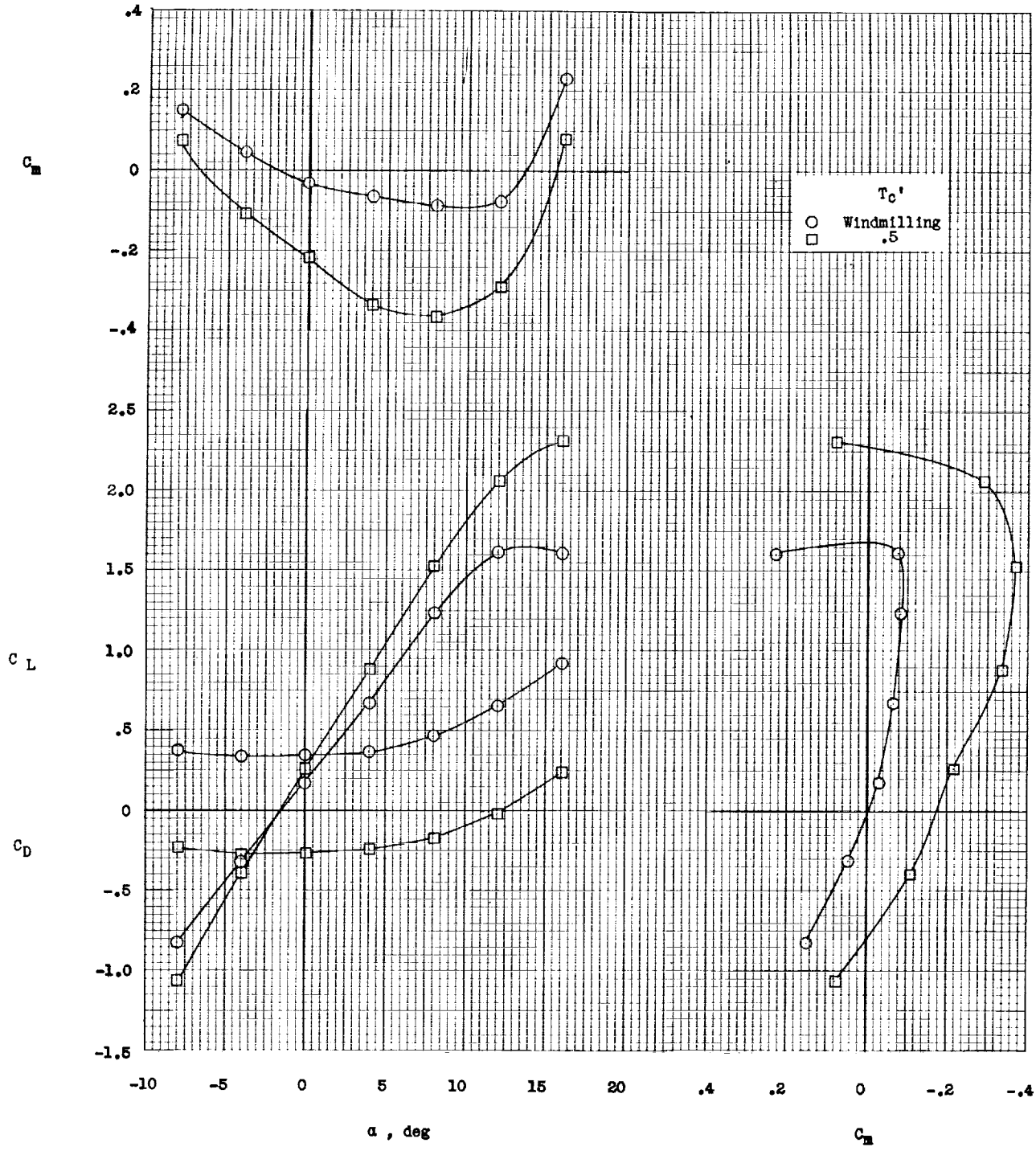

(b) $i_w = 5^o$.

Figure 8.- Continued.

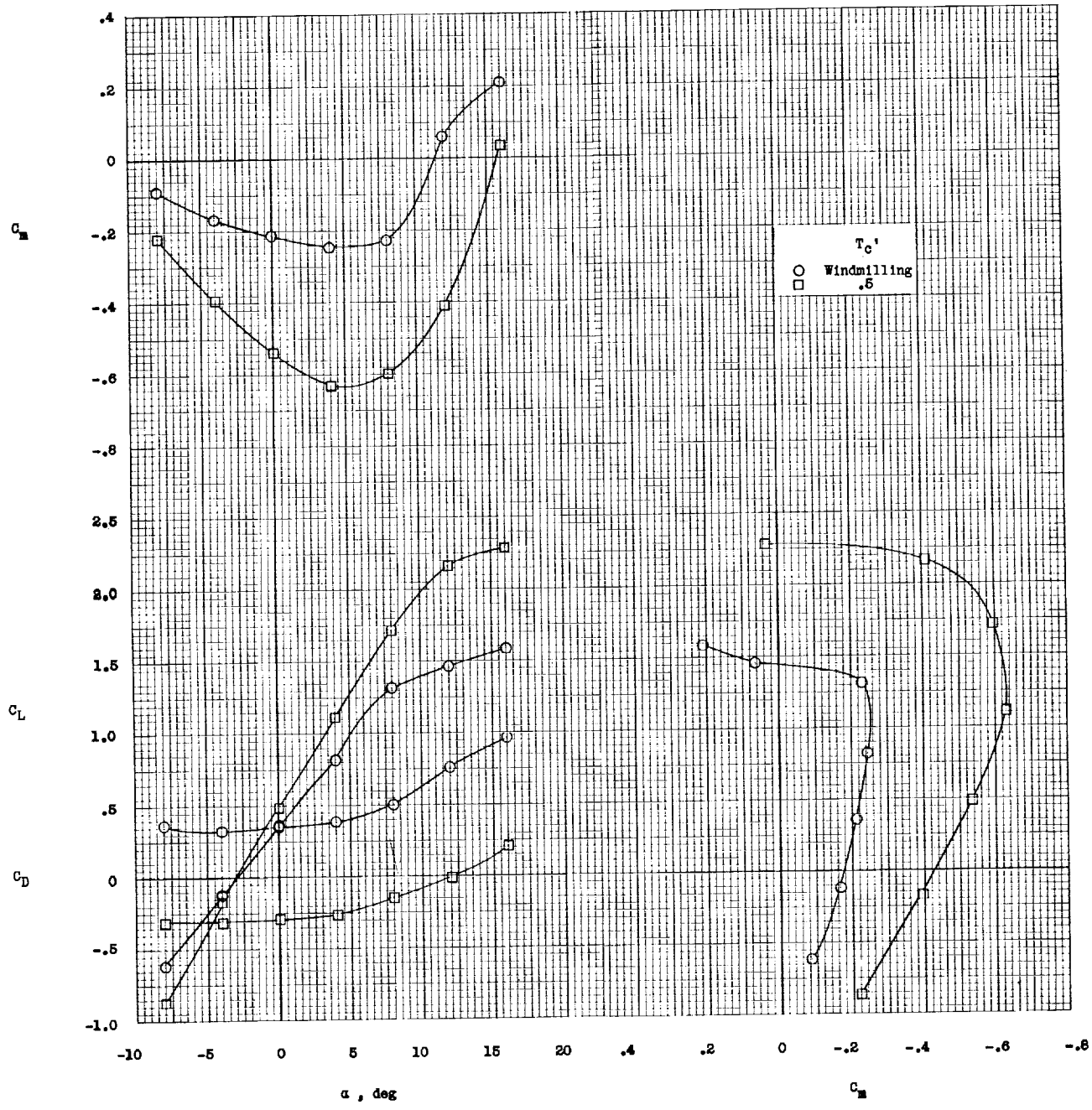

(c) $i_w = 10^o$.

Figure 8.- Continued.

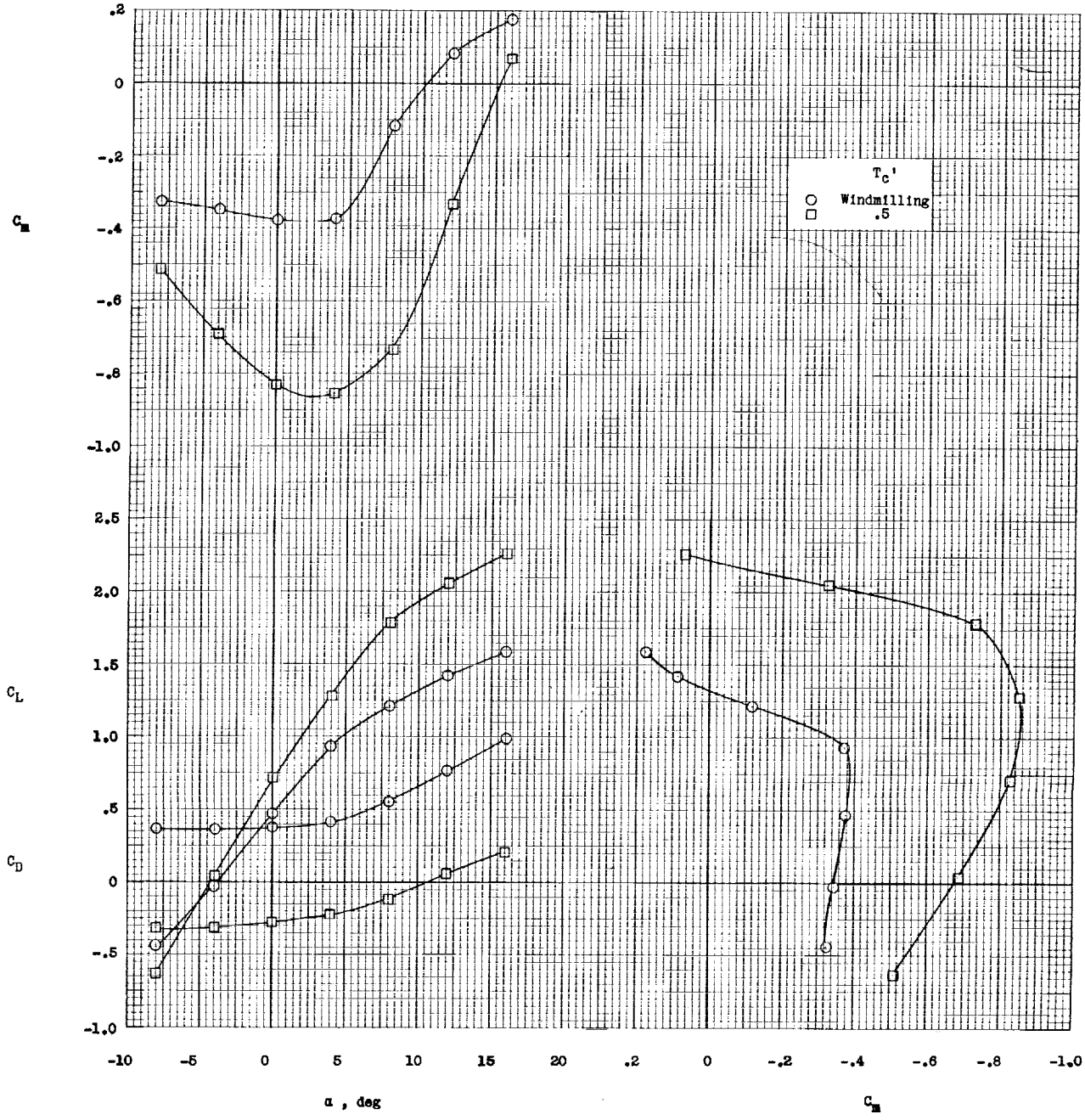

(d) $i_w = 15^\circ$.

Figure 8.- Continued.

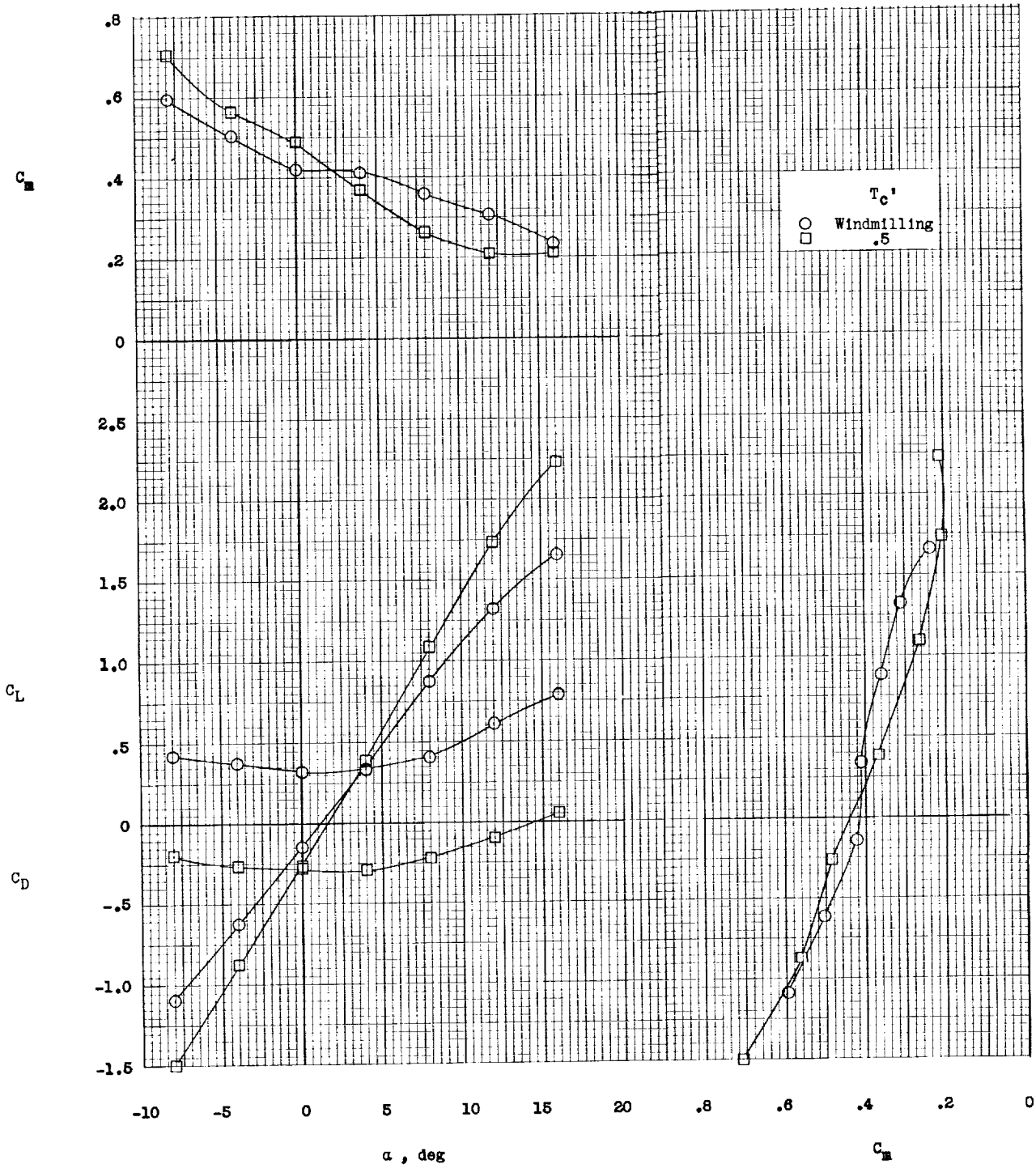

(e) $i_w = -5^o$.

Figure 8.- Continued.

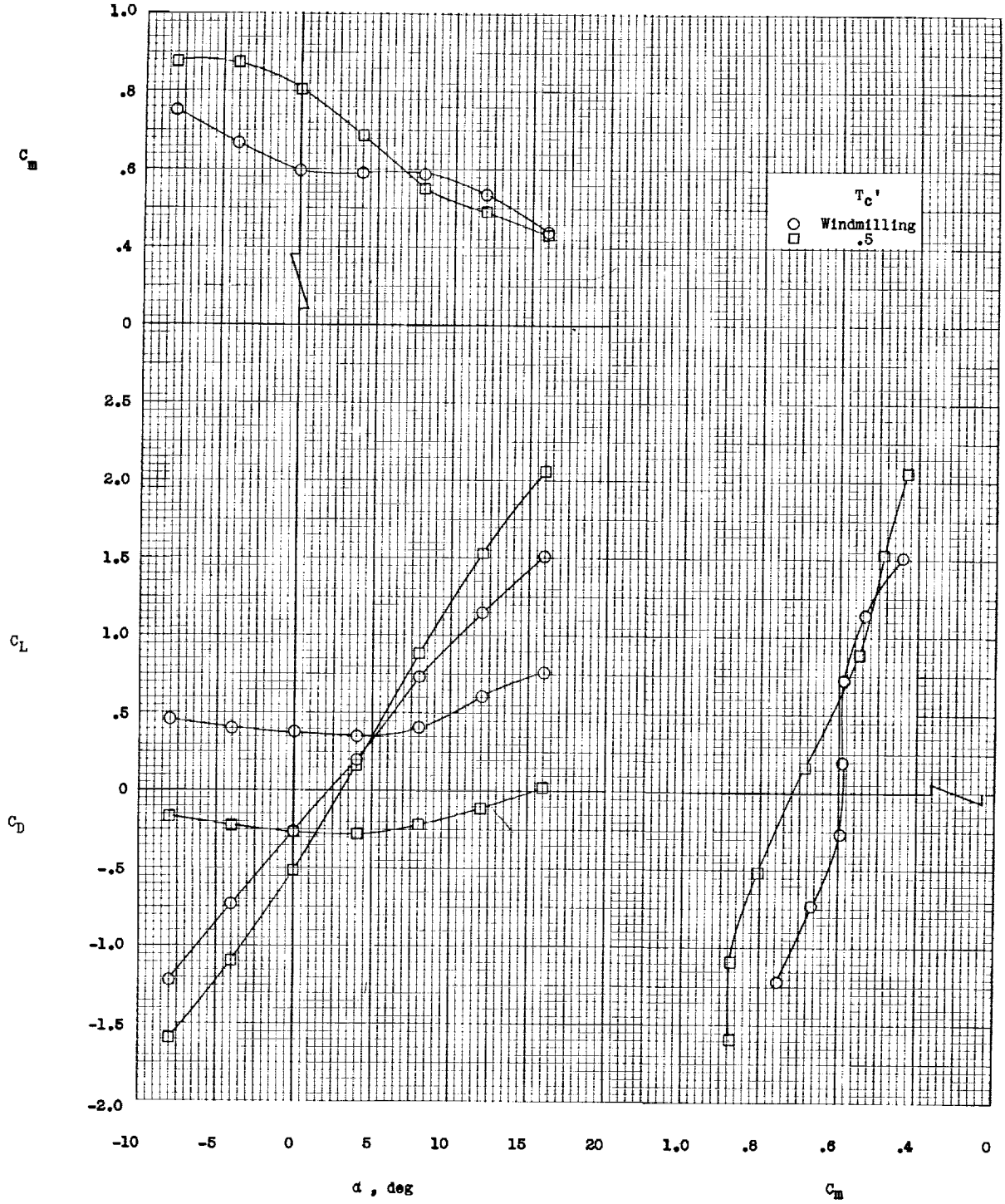

(f) $i_w = -10^\circ$.

Figure 8.- Continued.

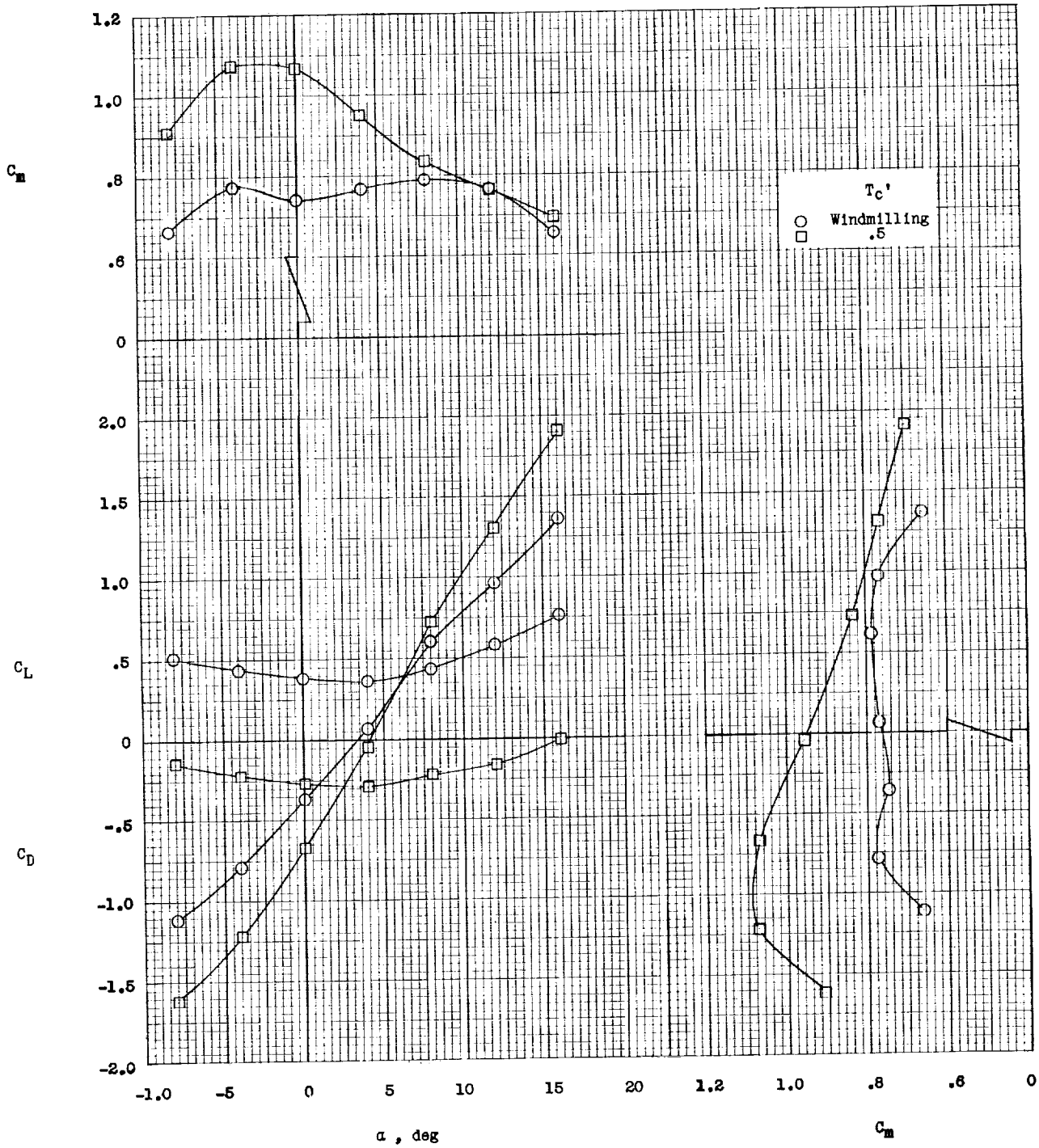

(g) $i_w = -15^\circ$.

Figure 8.- Concluded.

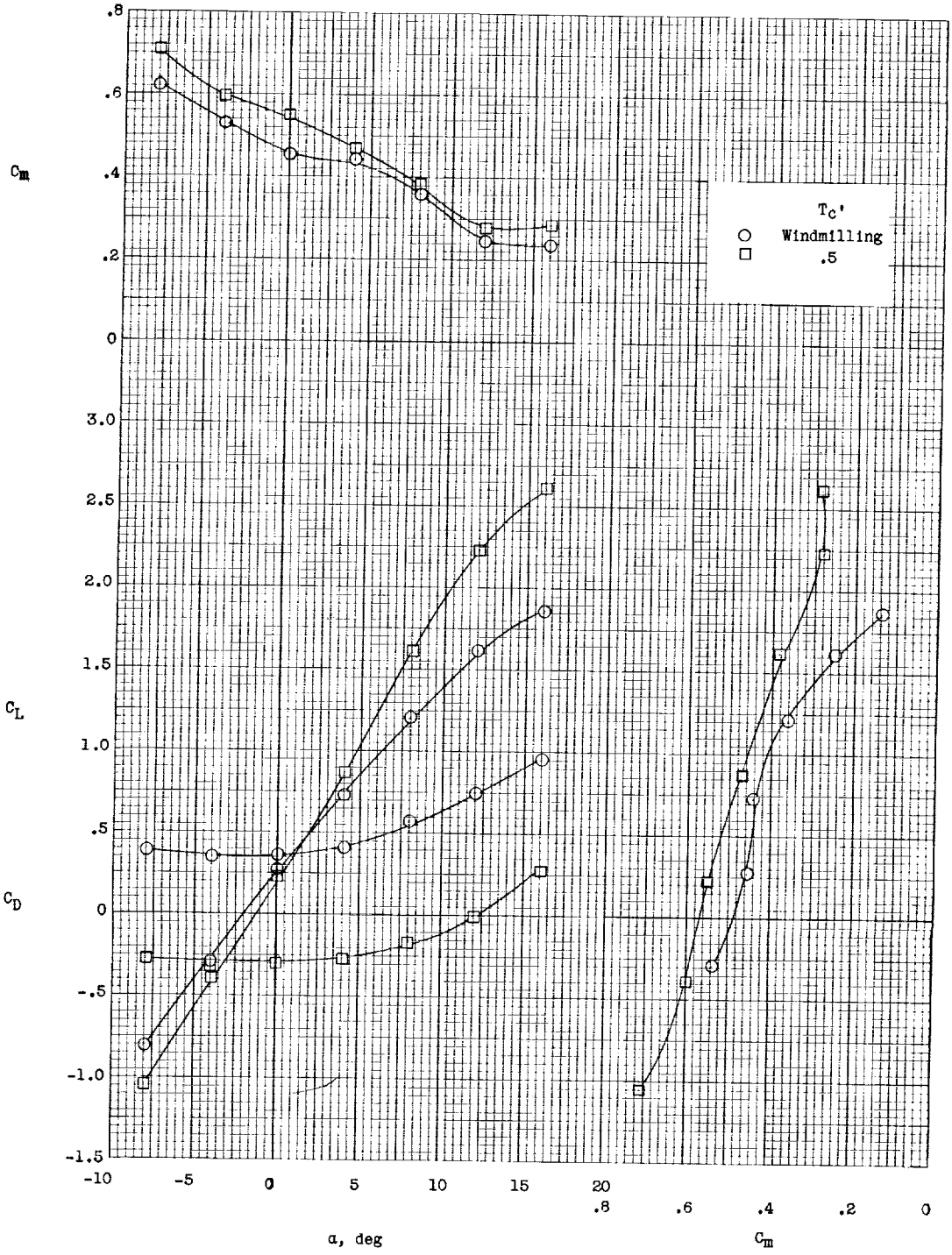

(a) $i_w = 0^o$.

Figure 9.- Longitudinal stability and trim characteristics of OB-HI configuration. $i_{d,F} = 5^o$; $q = 5.0$; gaps unsealed.

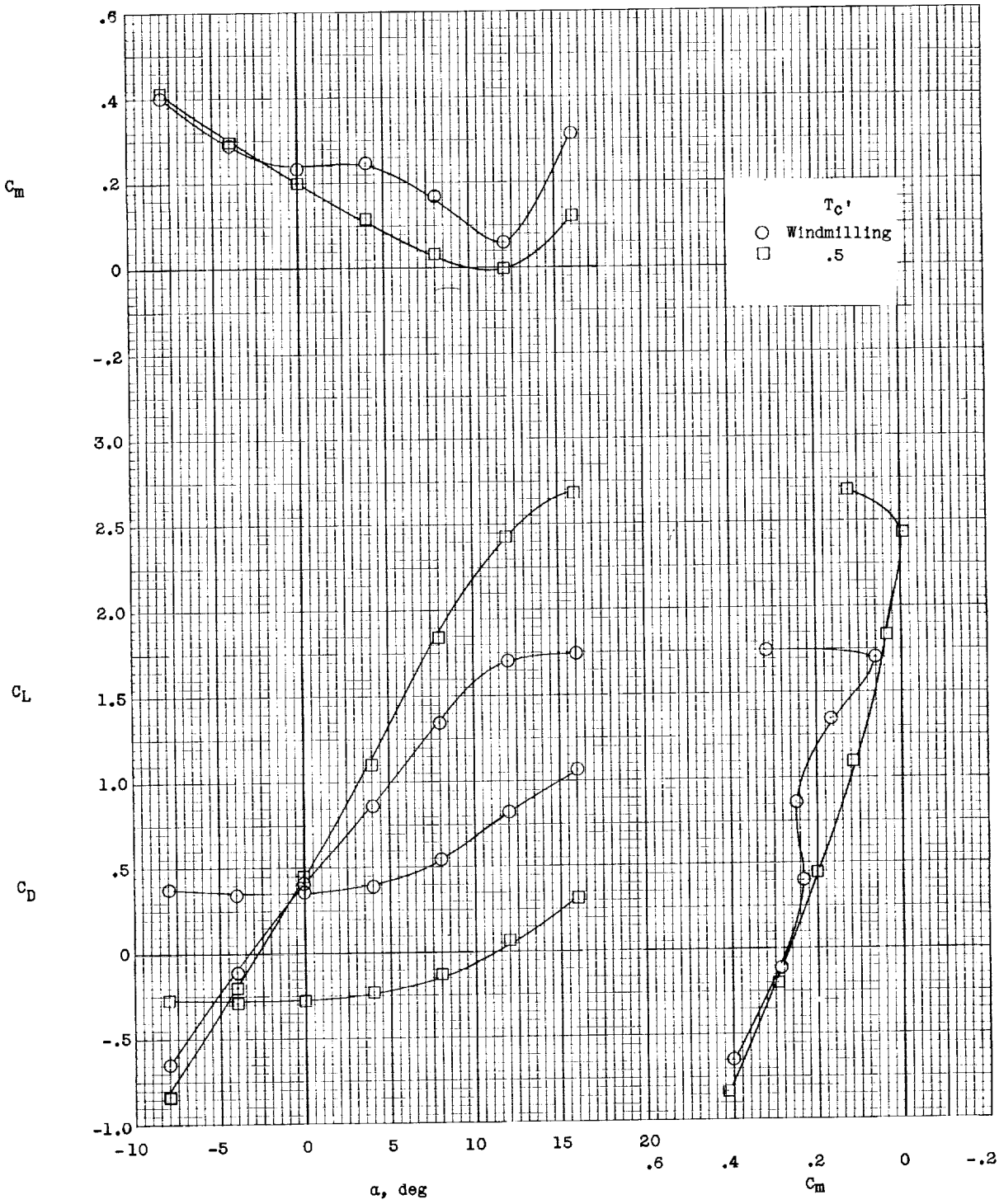

(b) $i_w = 5^o$.

Figure 9.- Continued.

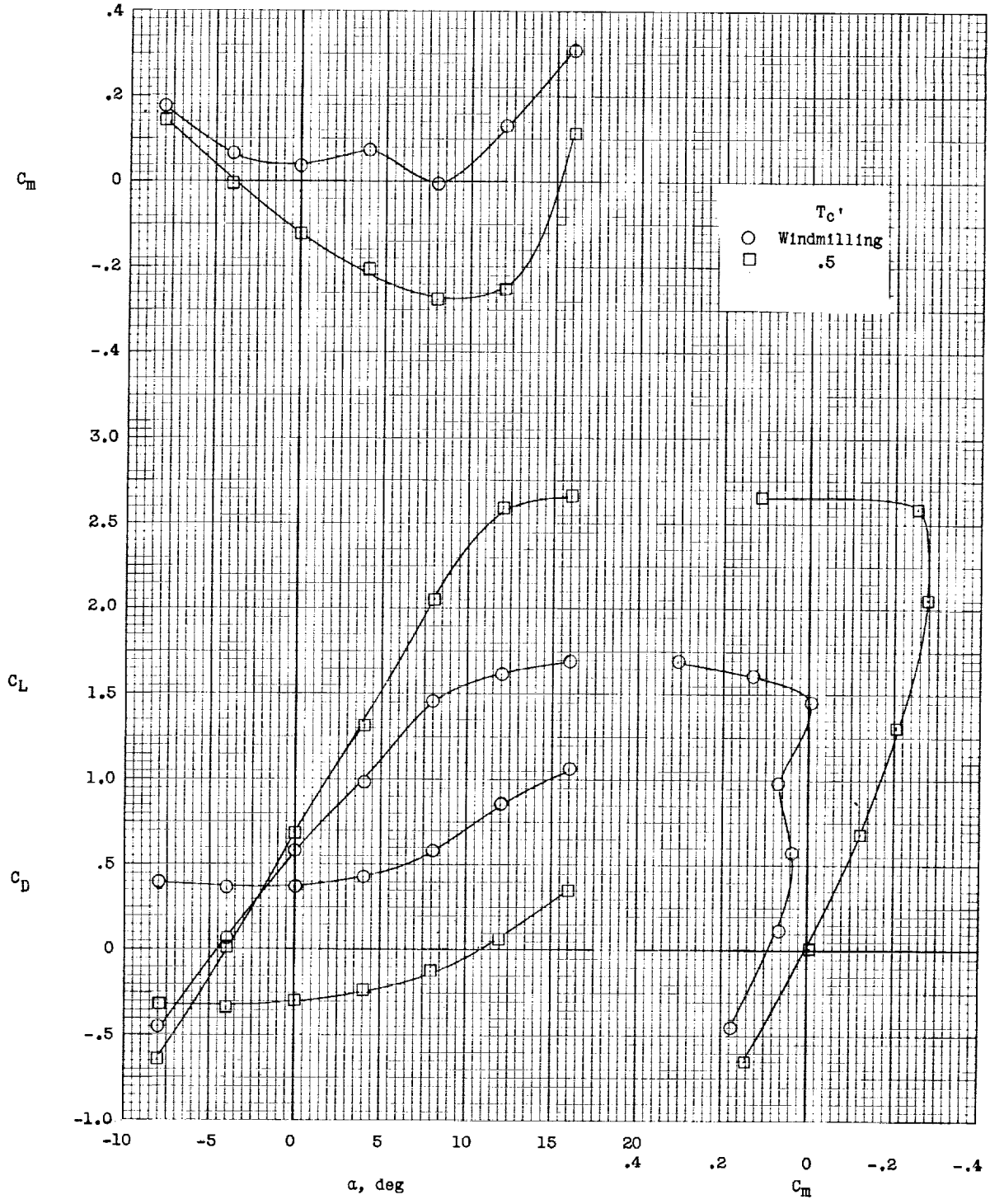

(c) $i_w = 10^o$.

Figure 9.- Continued.

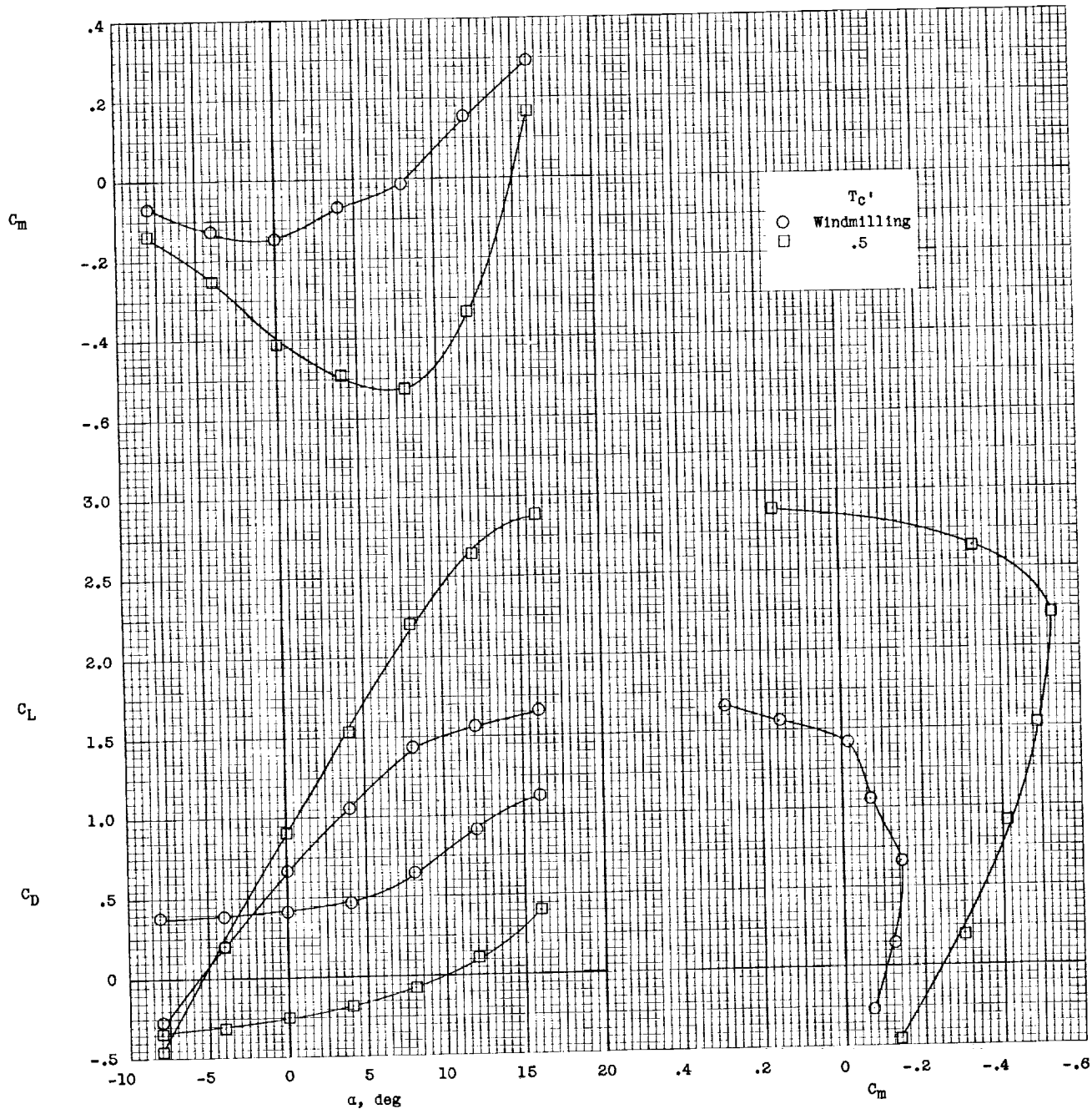

(d) $i_w = 15^\circ$.

Figure 9.- Continued.

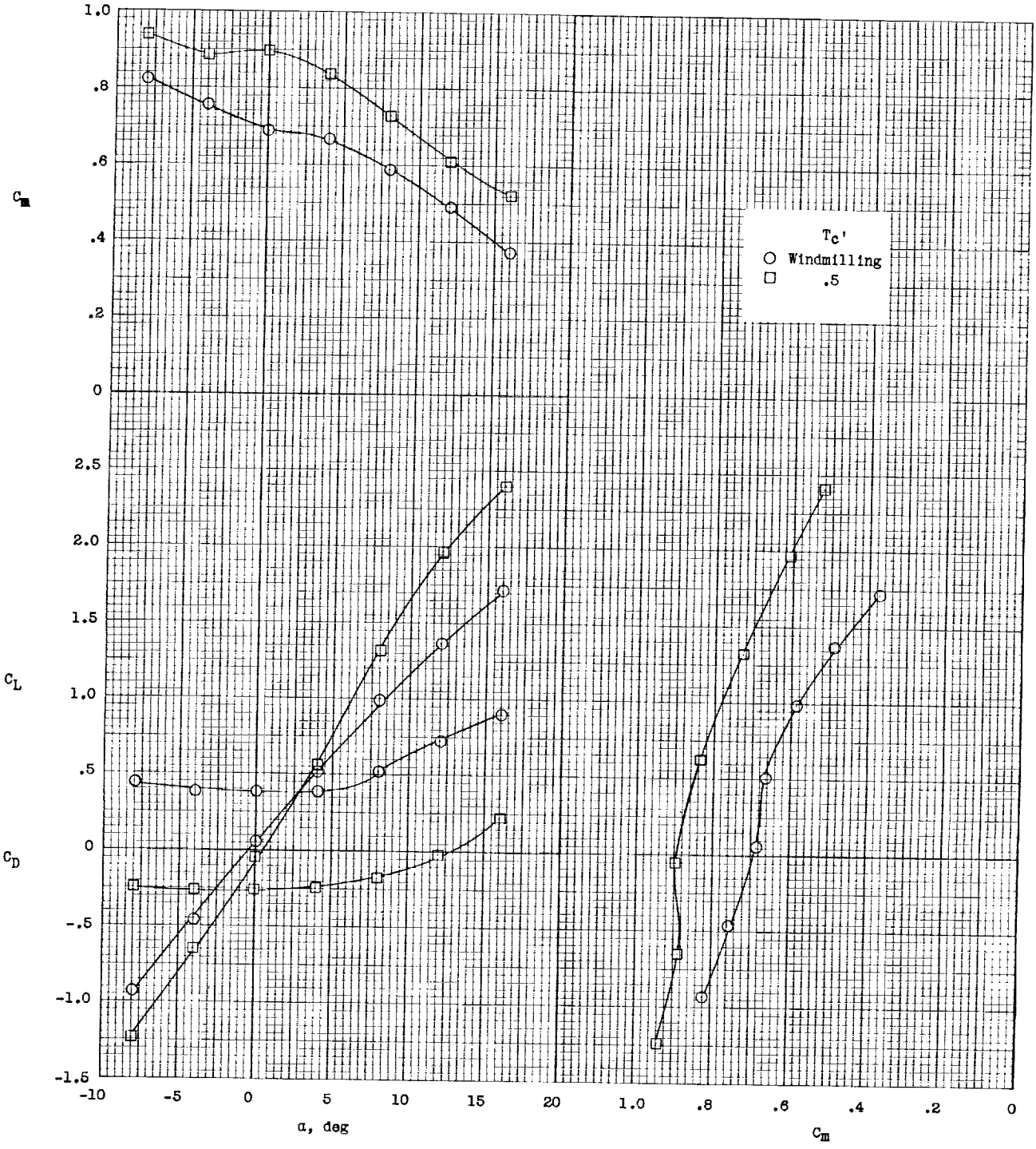

(e) $i_w = -5^\circ$.

Figure 9.- Continued.

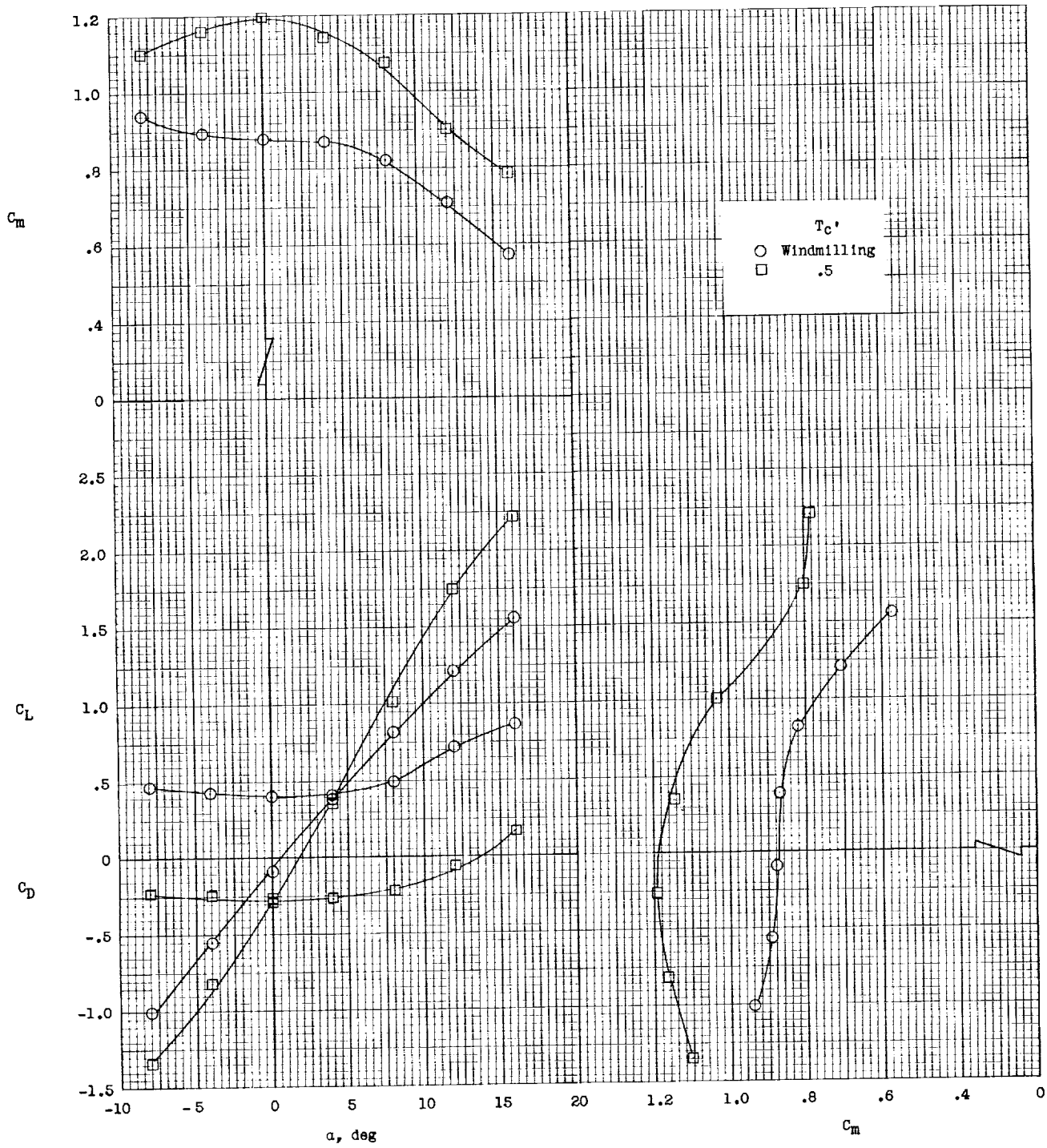

(f) $i_w = -10^\circ$.

Figure 9.- Continued.

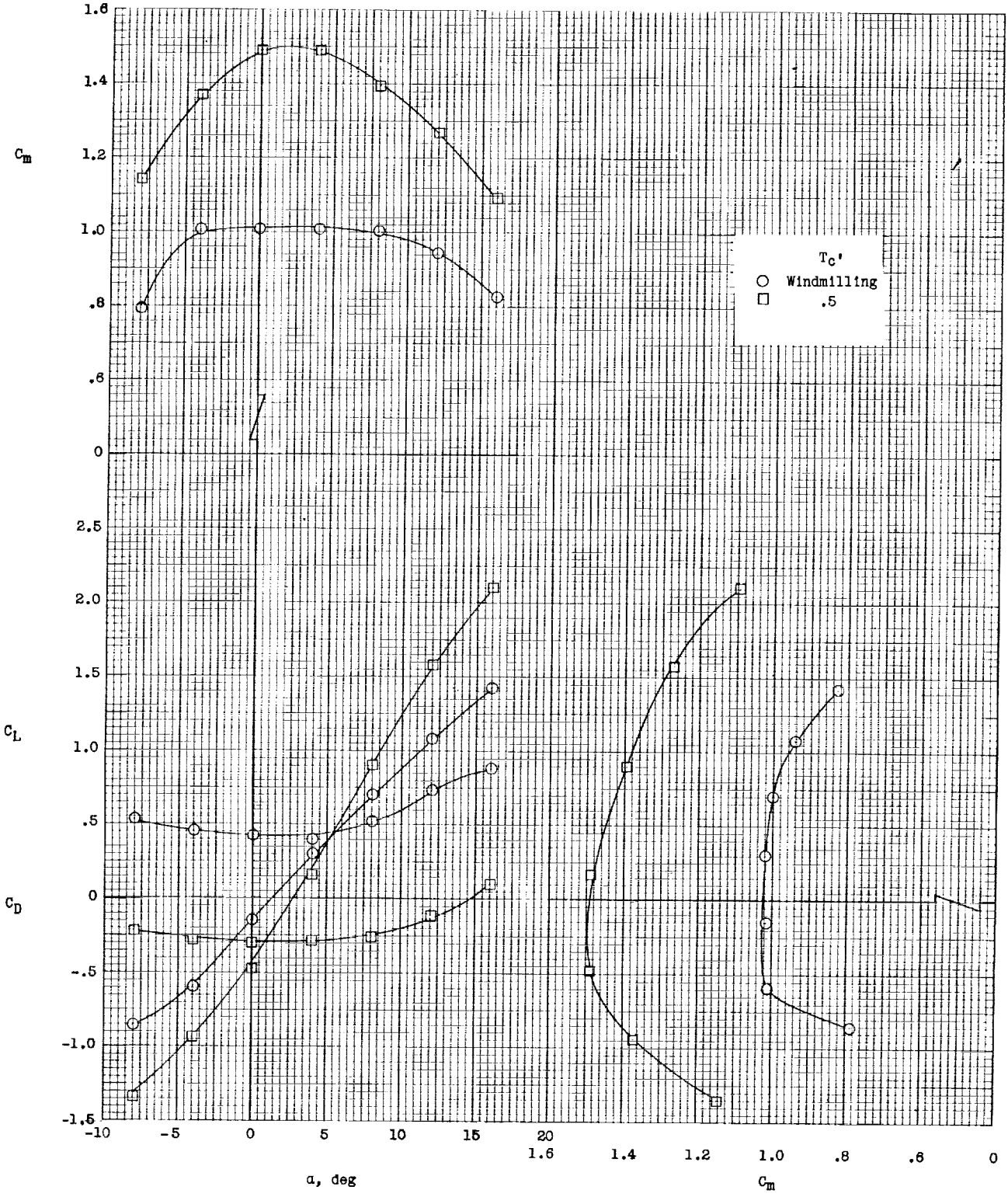

(g) $i_w = -15°$.

Figure 9.- Concluded.

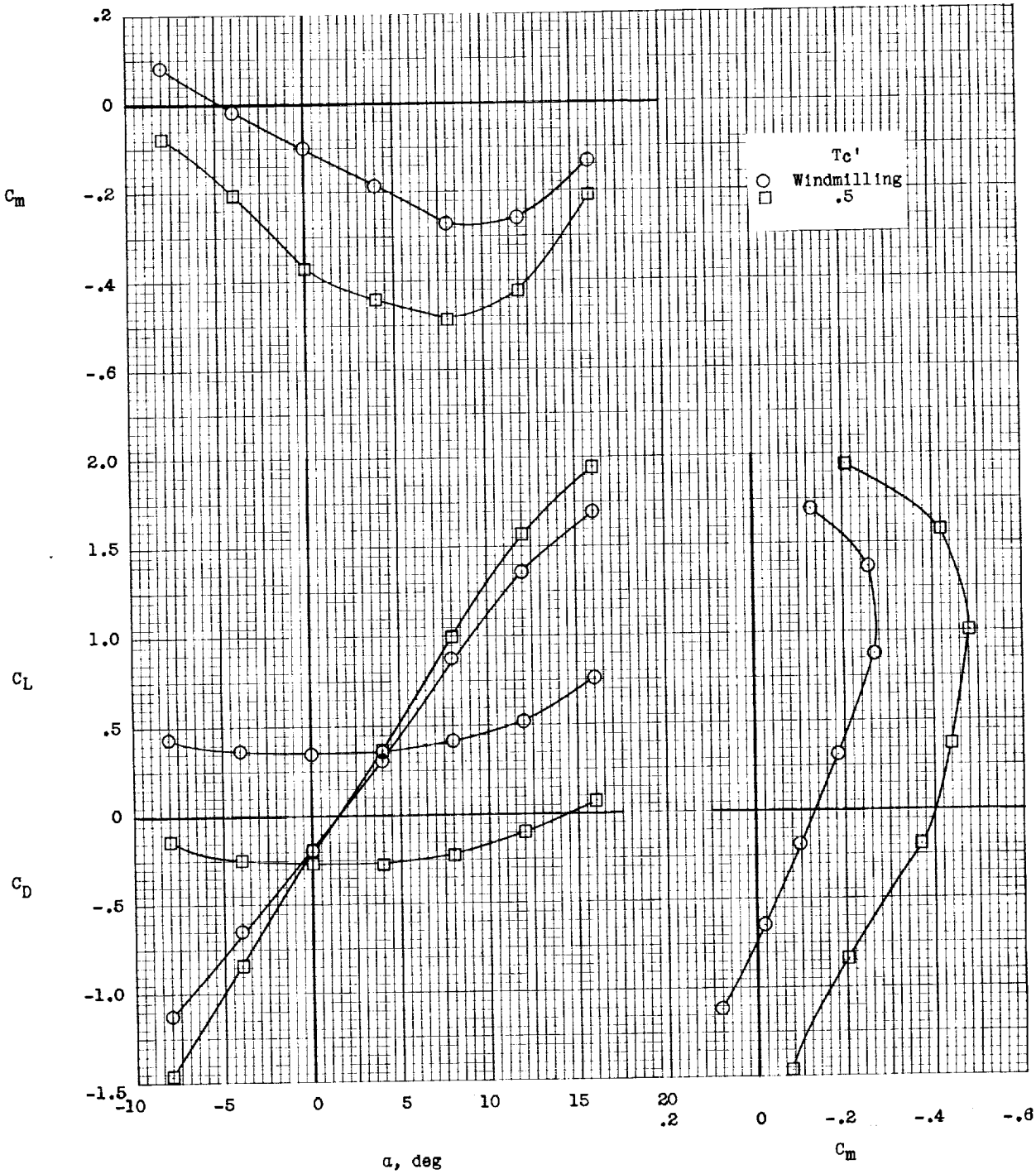

(a) $i_w = 0^o$.

Figure 10.- Longitudinal stability and trim characteristics of OB-HI configuration. $i_{d,F} = -5^o$; $q = 5.0$; gaps unsealed.

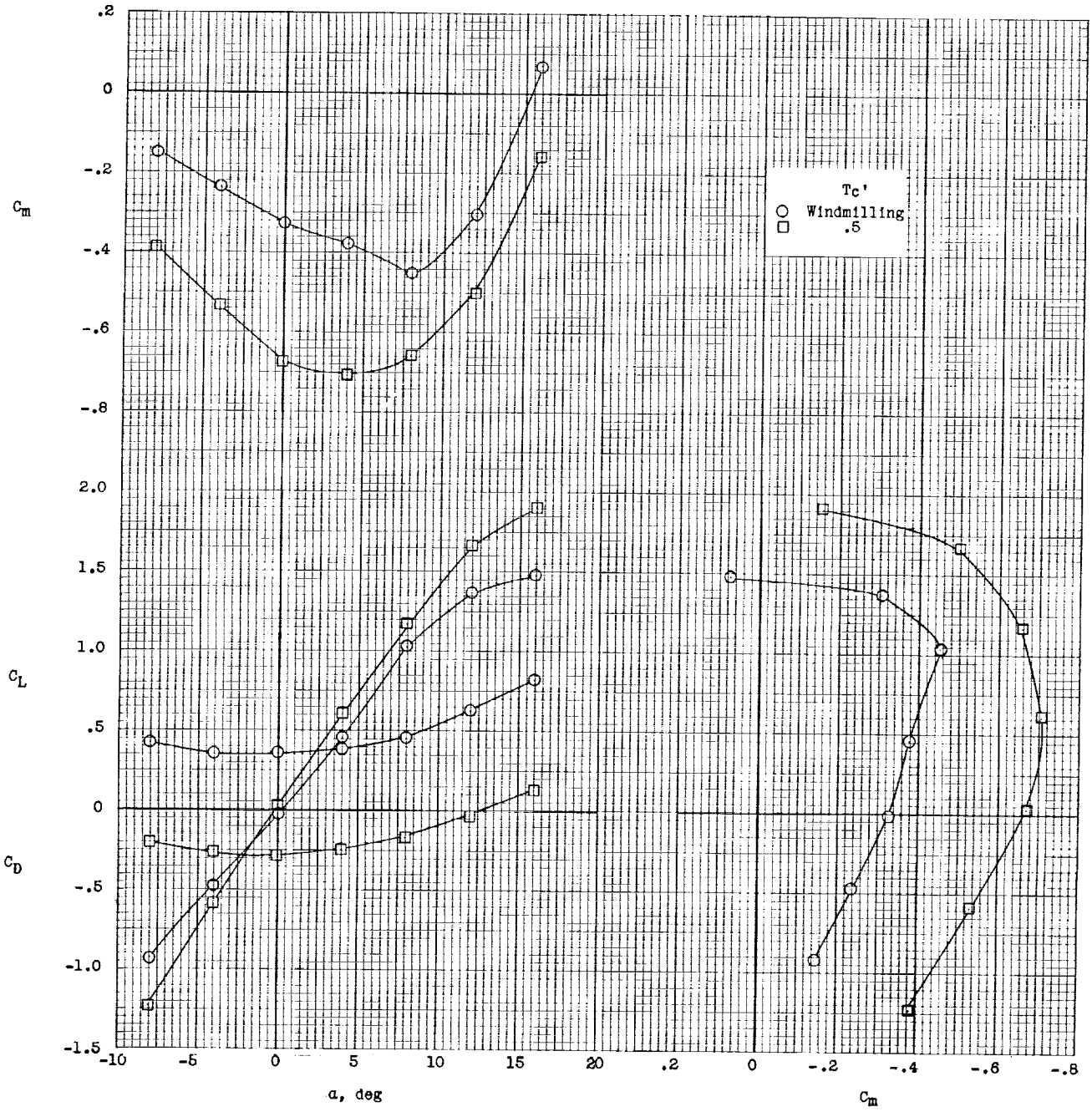

(b) $i_w = 5°$.

Figure 10.- Continued.

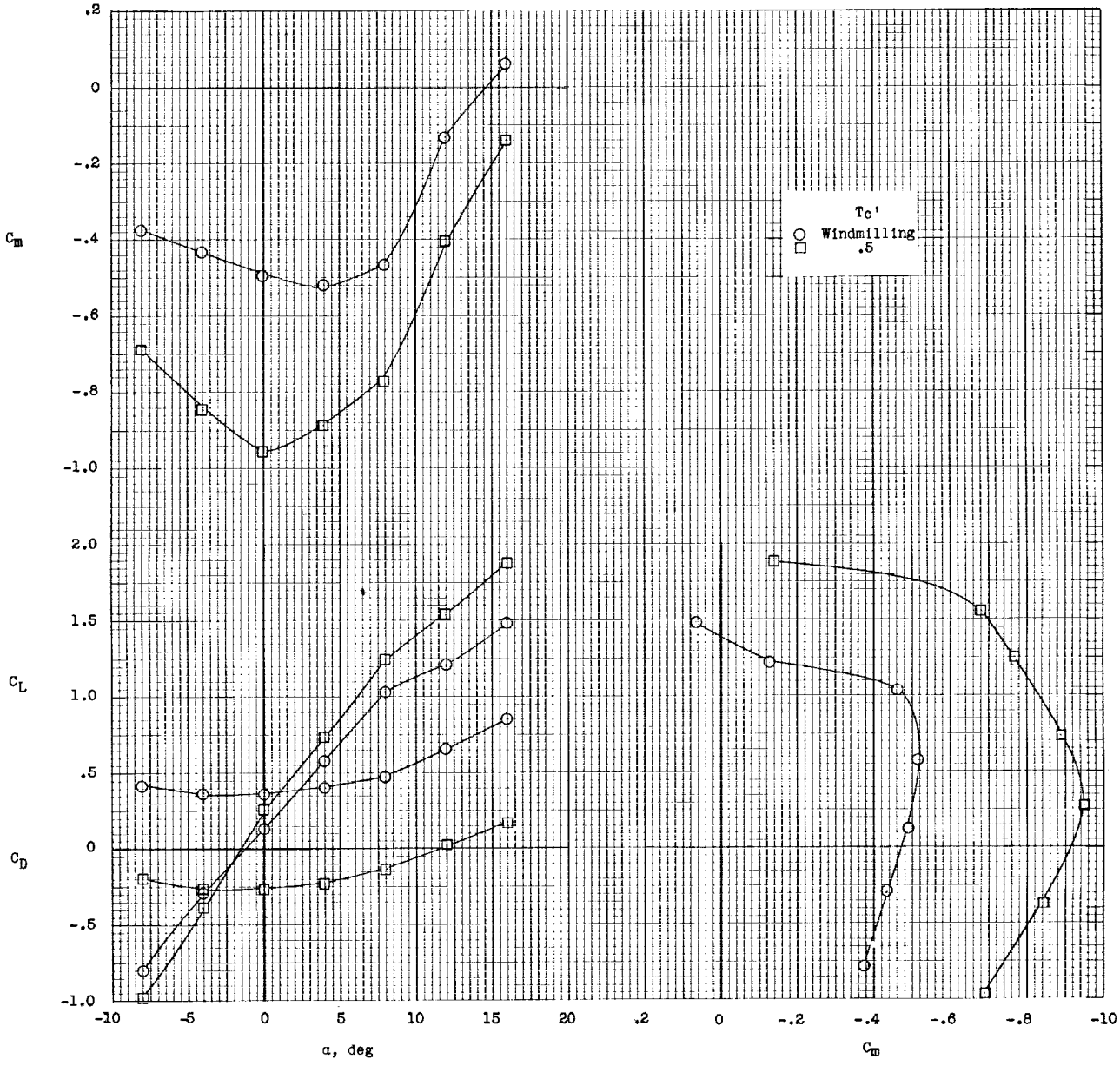

(c) $i_w = 10^o$.

Figure 10.- Continued.

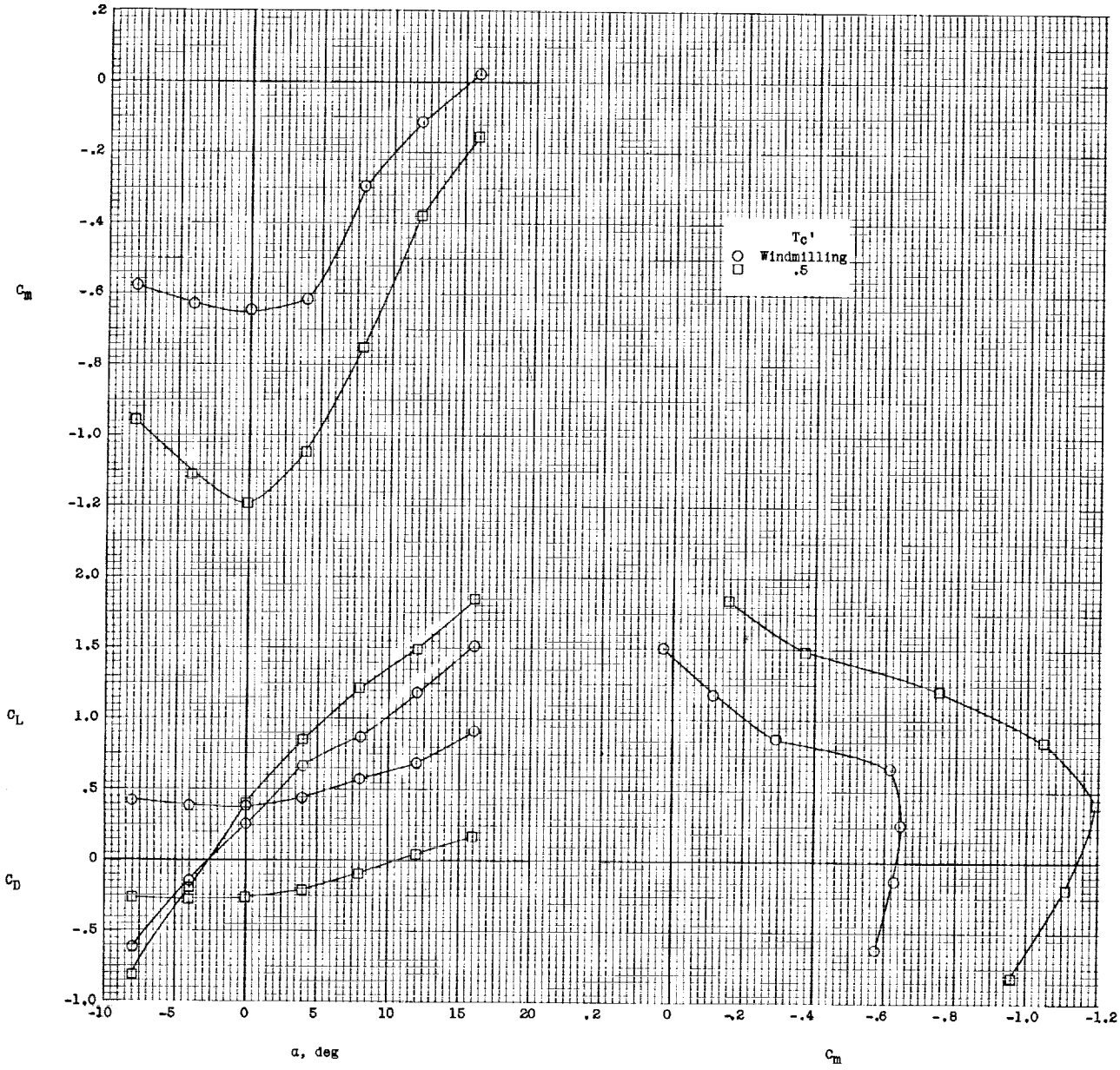

(d) $i_w = 15°$.

Figure 10.- Continued.

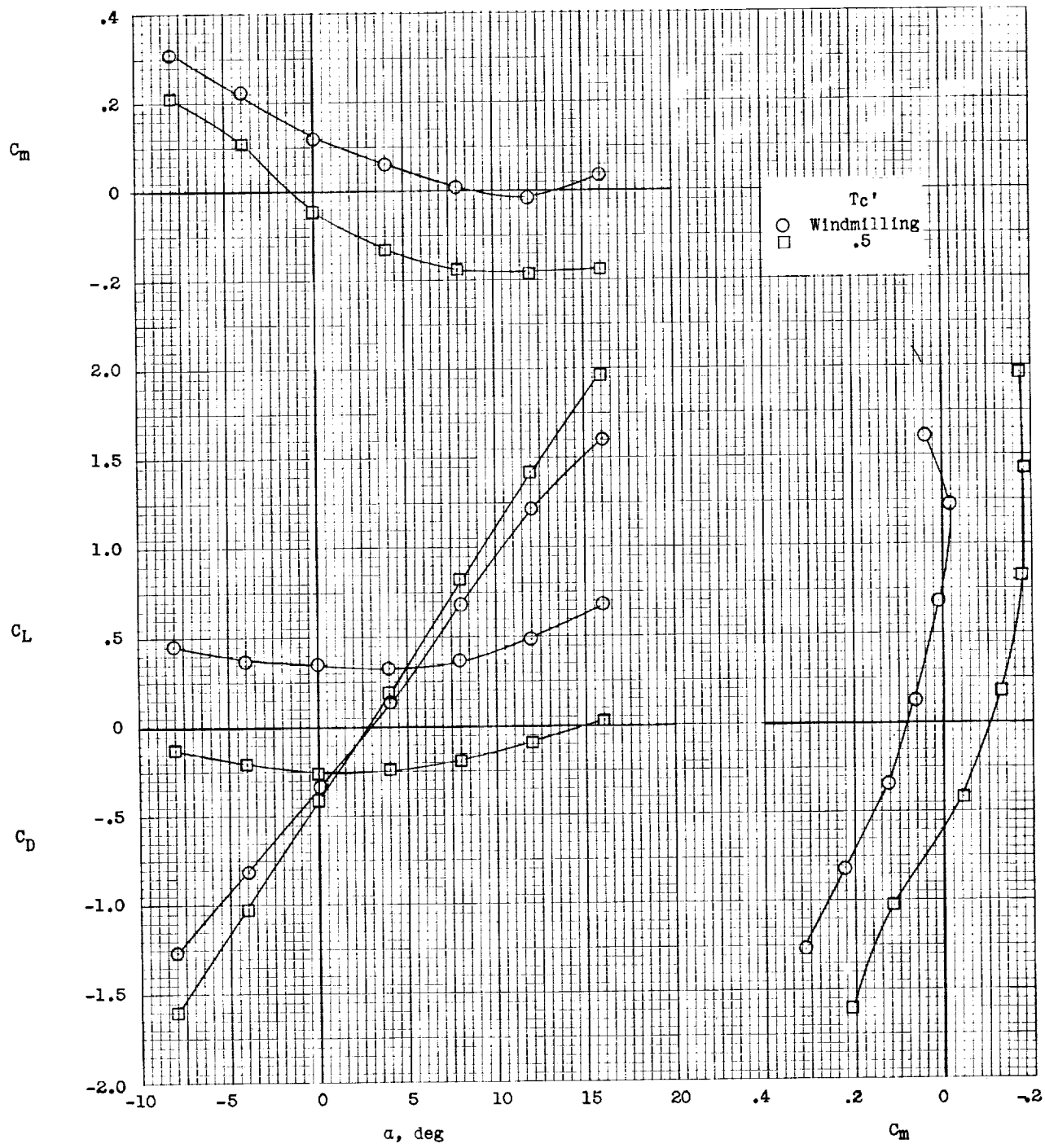

(e) $i_w = -5^\circ$.

Figure 10.- Continued.

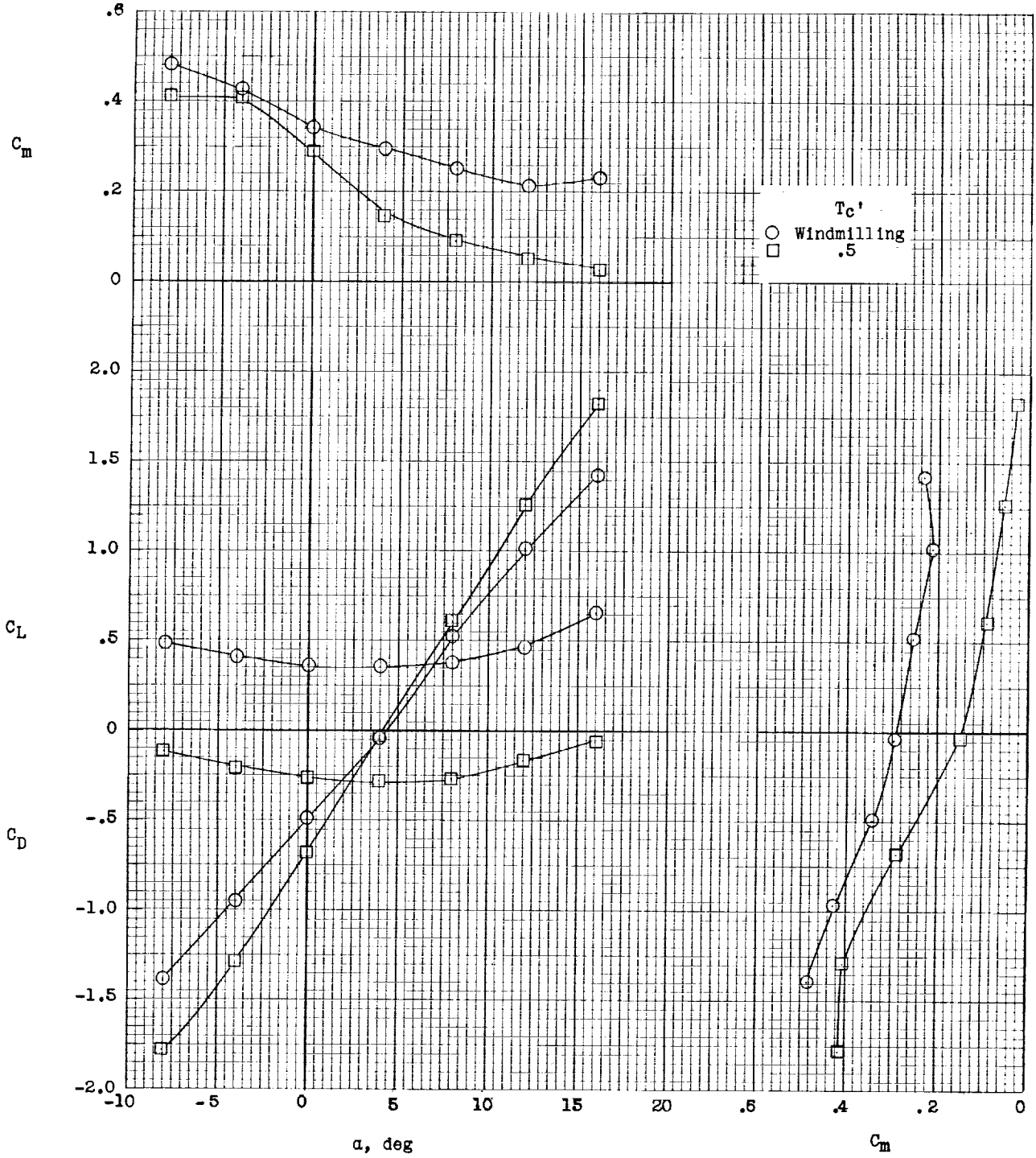

(f) $i_w = -10°$.

Figure 10.- Continued.

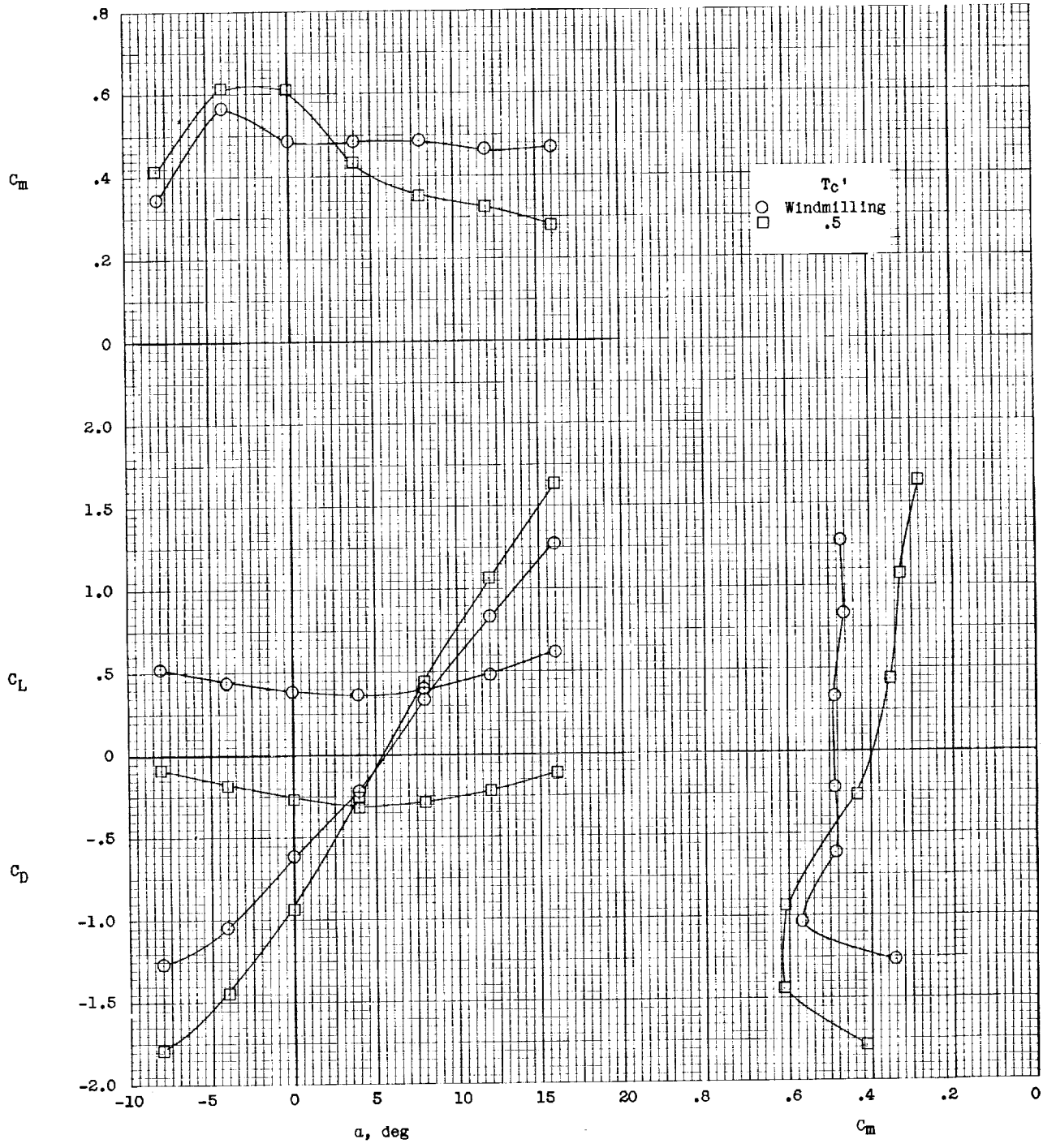

(g) $i_w = -15°$.

Figure 10.- Concluded.

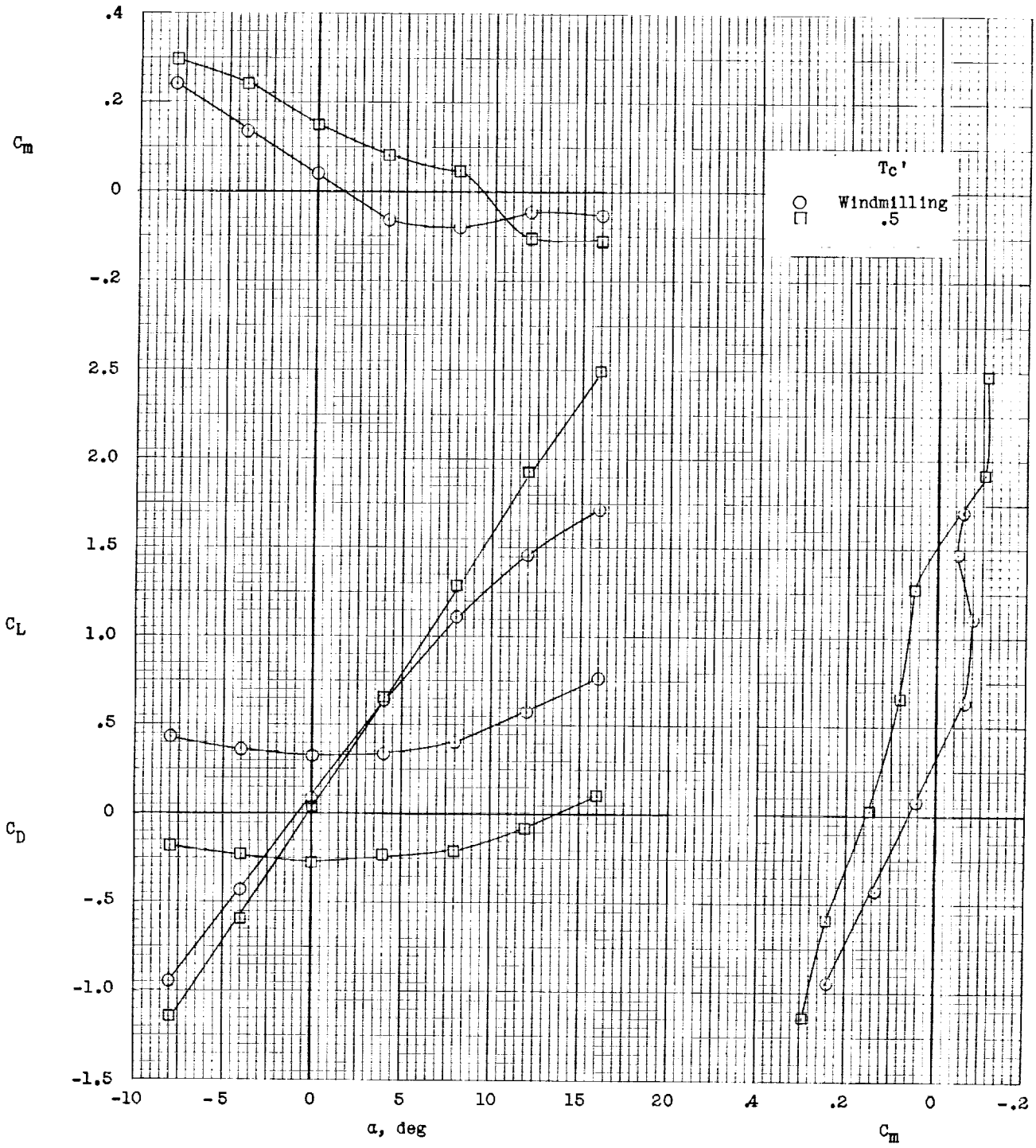

(a) $i_w = 0°$.

Figure 11.- Longitudinal stability and trim characteristics of OB-LO configuration. $i_{d,F} = 0°$; $q = 5.0$; gaps unsealed.

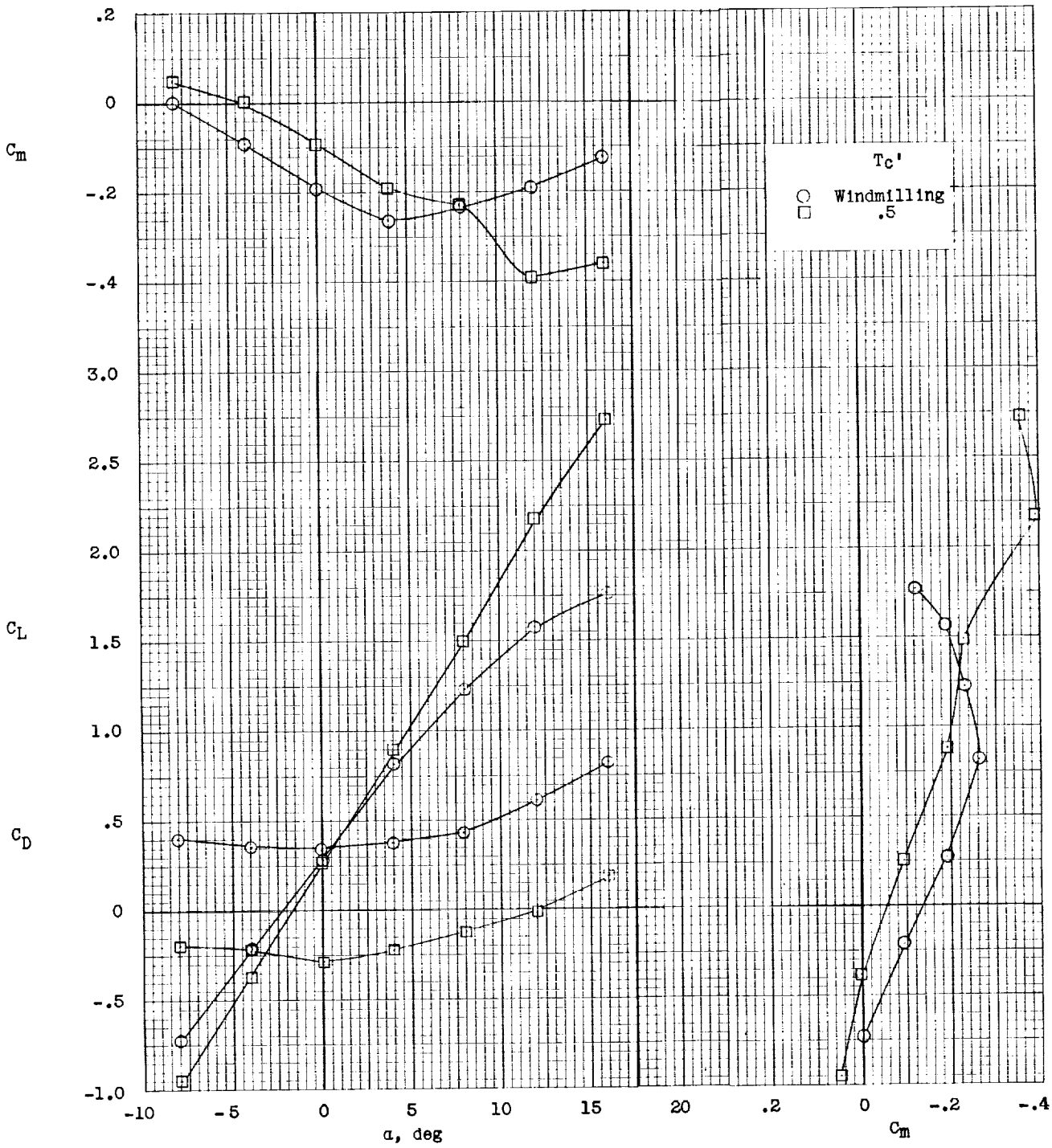

(b) $i_w = 5^o$.

Figure 11.- Continued.

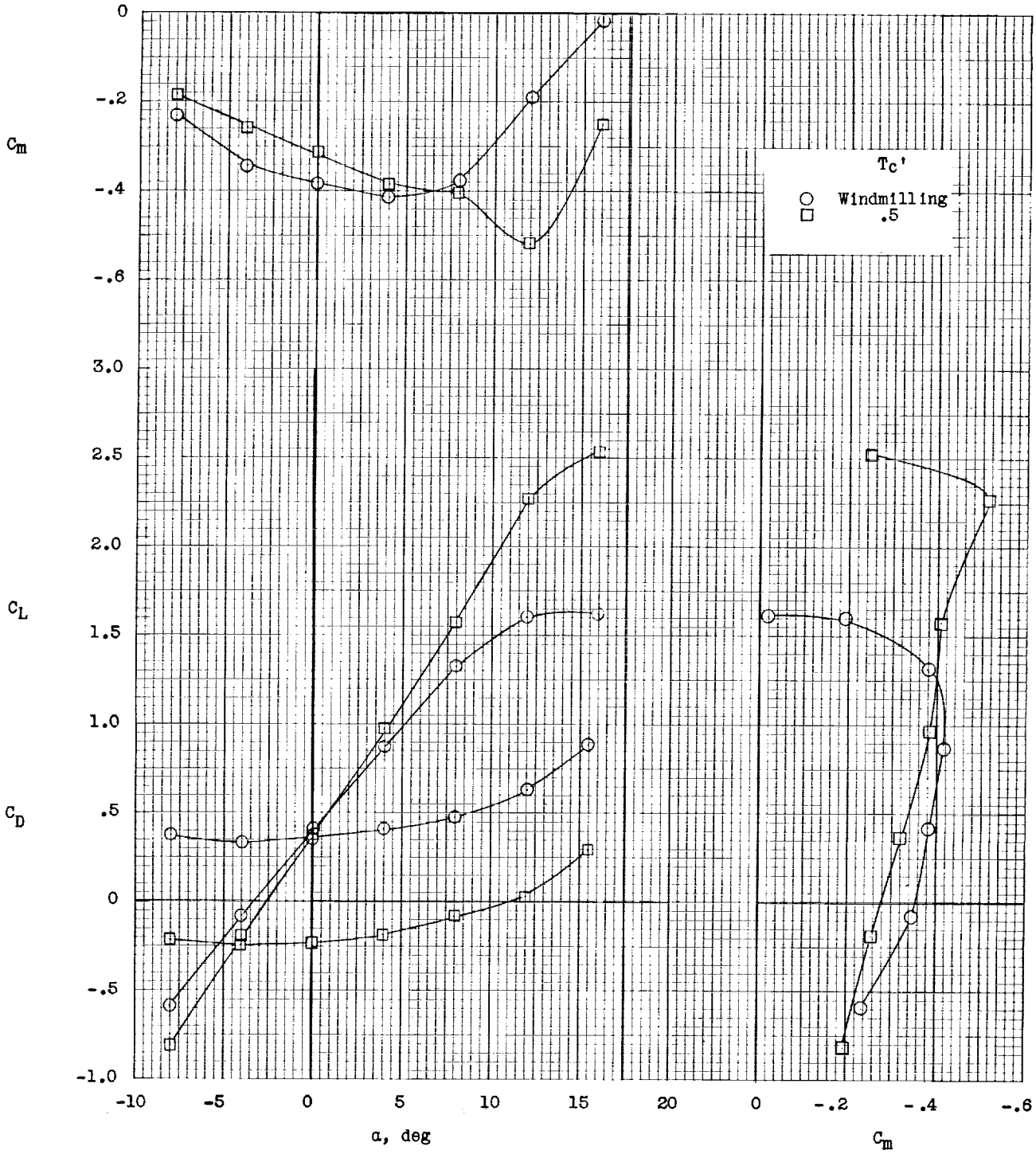

(c) $i_w = 10°$.

Figure 11.- Continued.

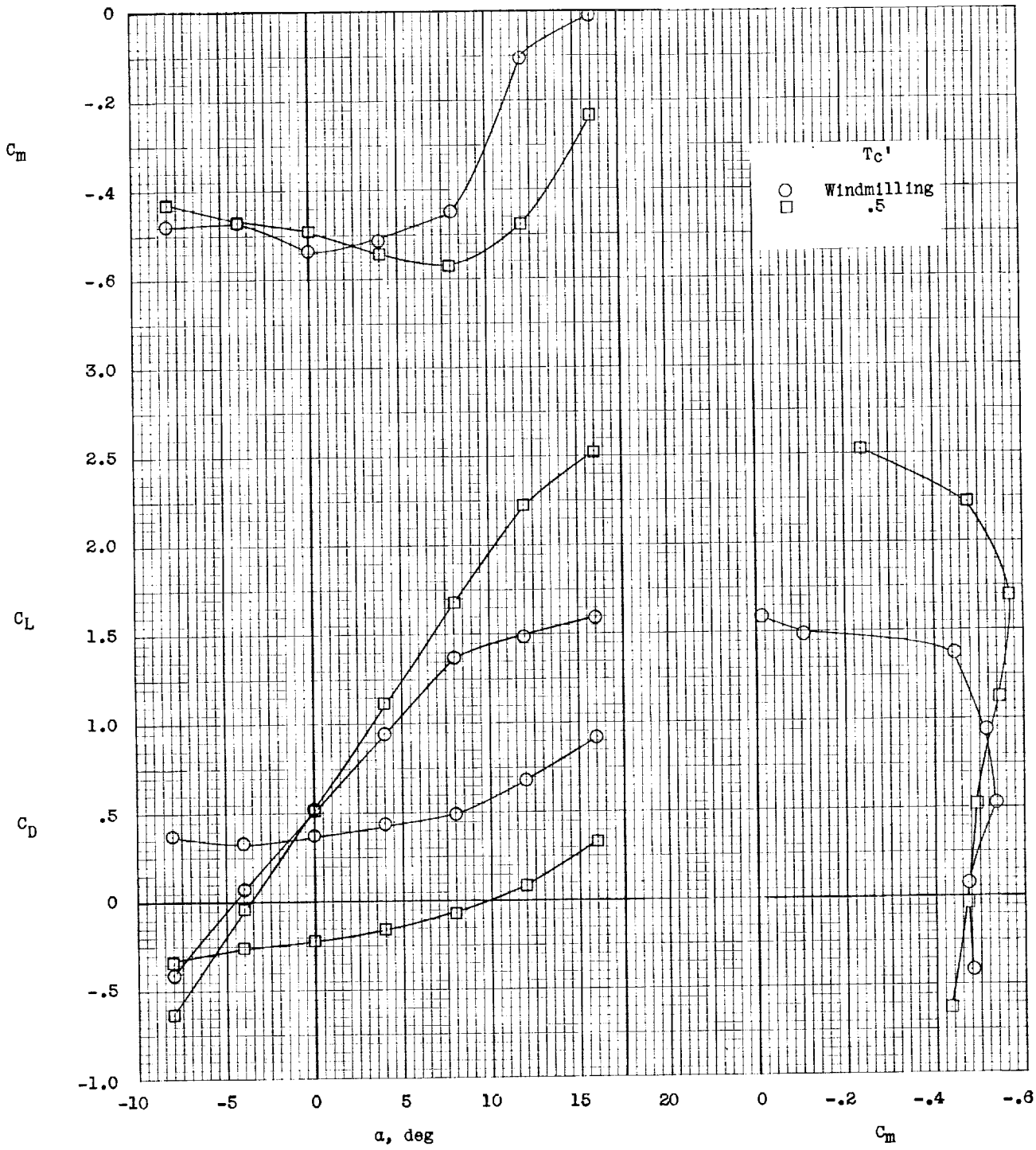

(d) $i_w = 15^\circ$.

Figure 11.- Continued.

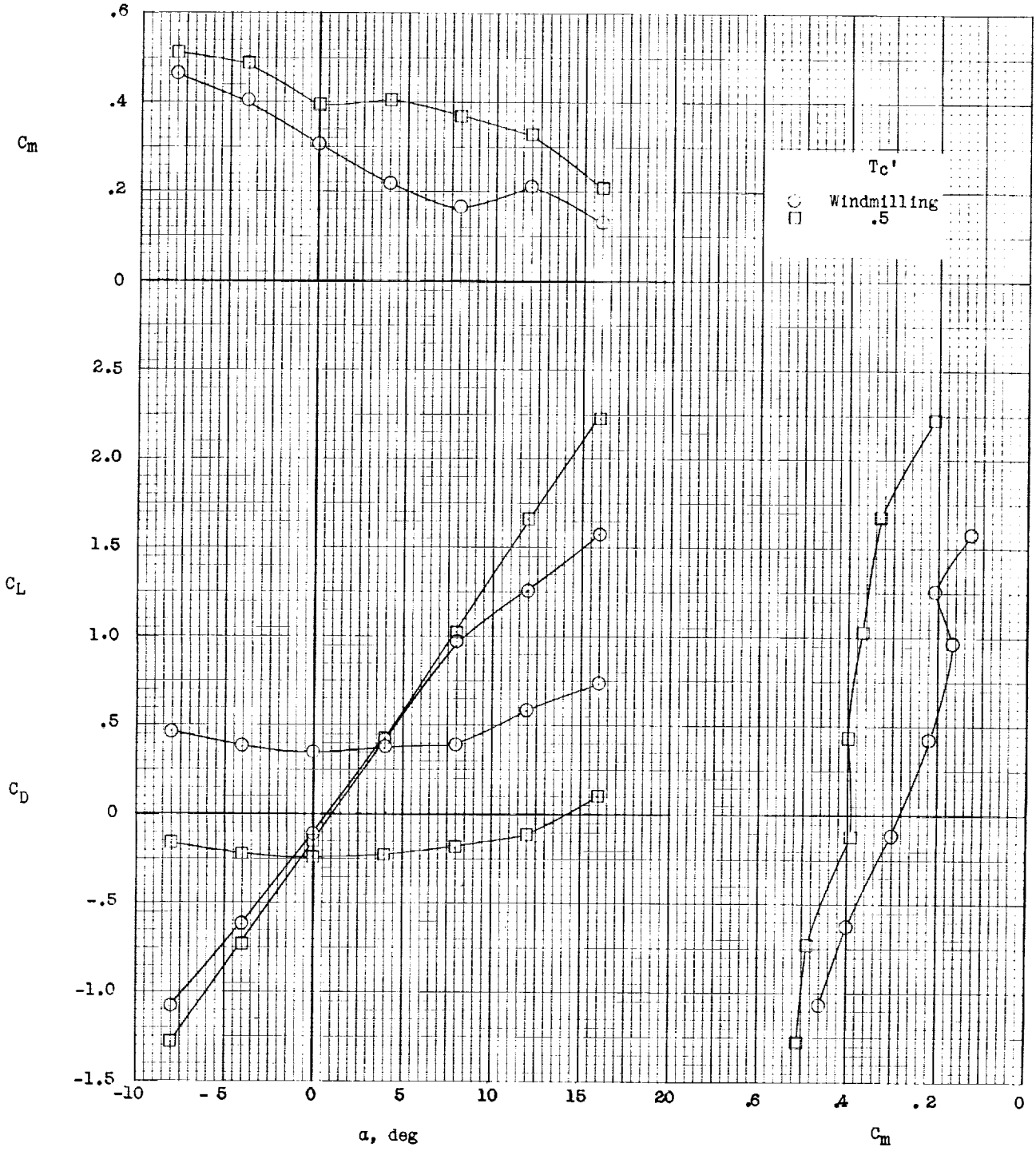

(e) $i_w = -5°$.

Figure 11.- Continued.

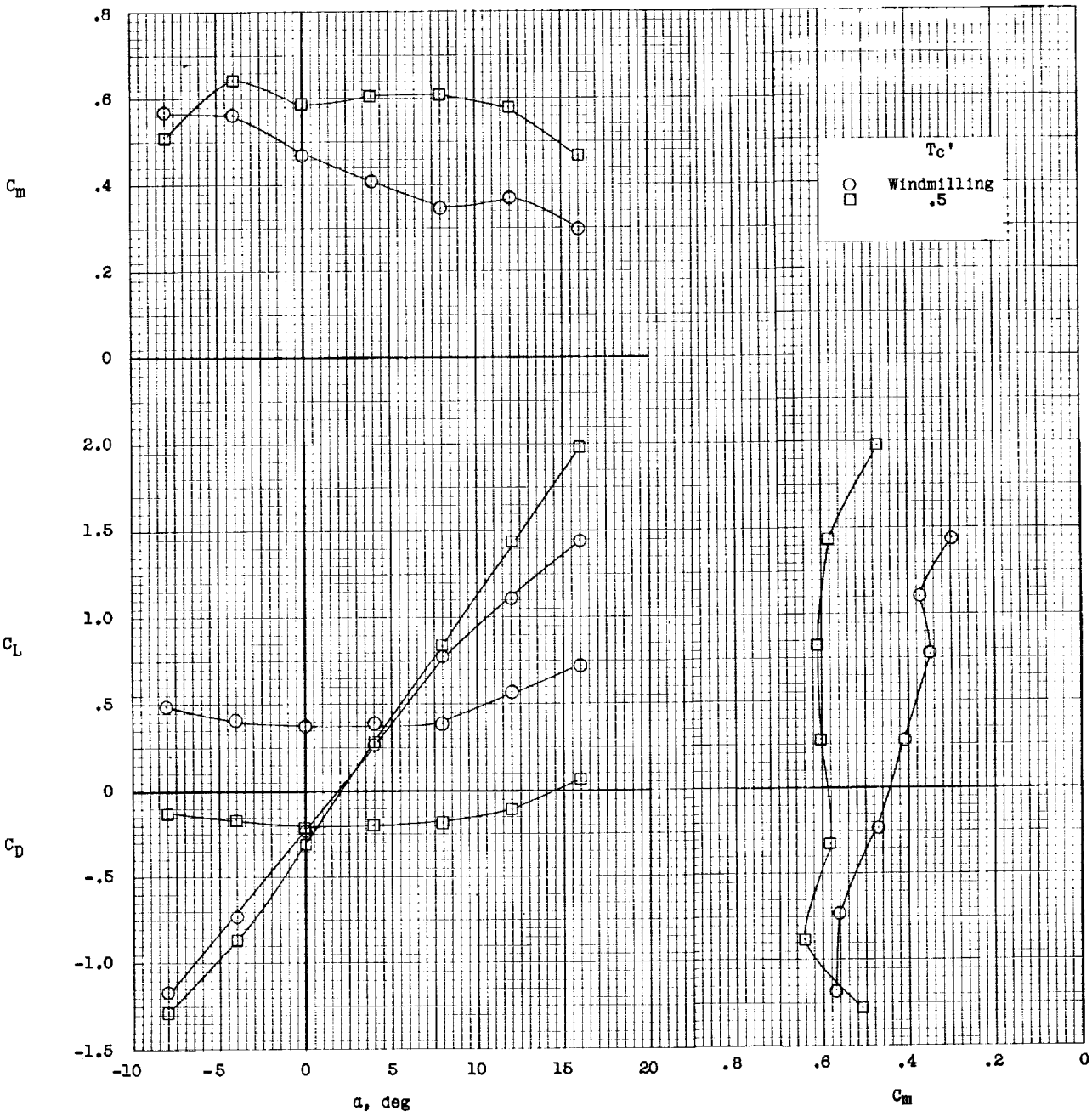

(f) $i_w = -10^\circ$.

Figure 11.- Continued.

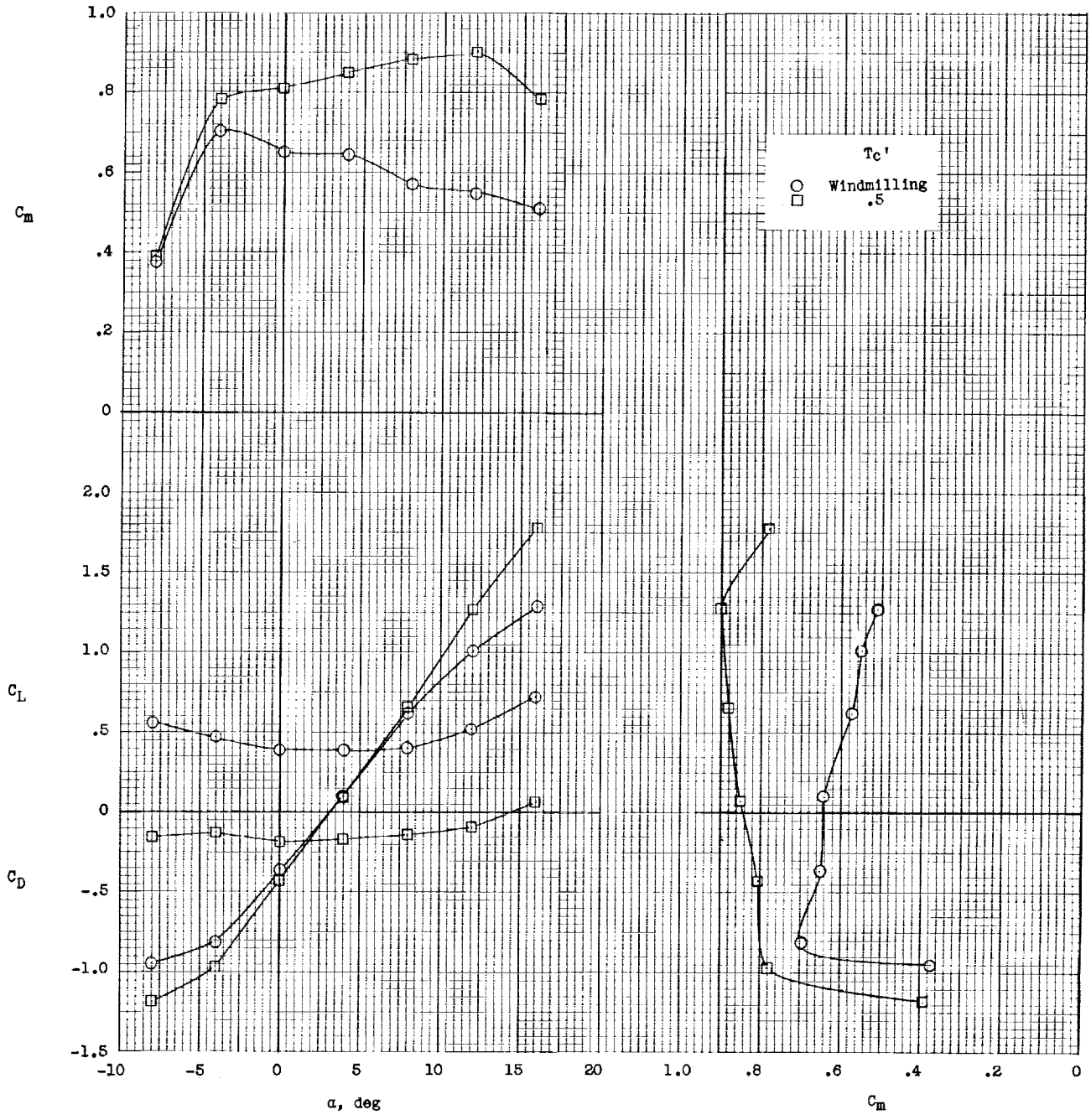

(g) $i_w = -15^\circ$.

Figure 11.- Concluded.

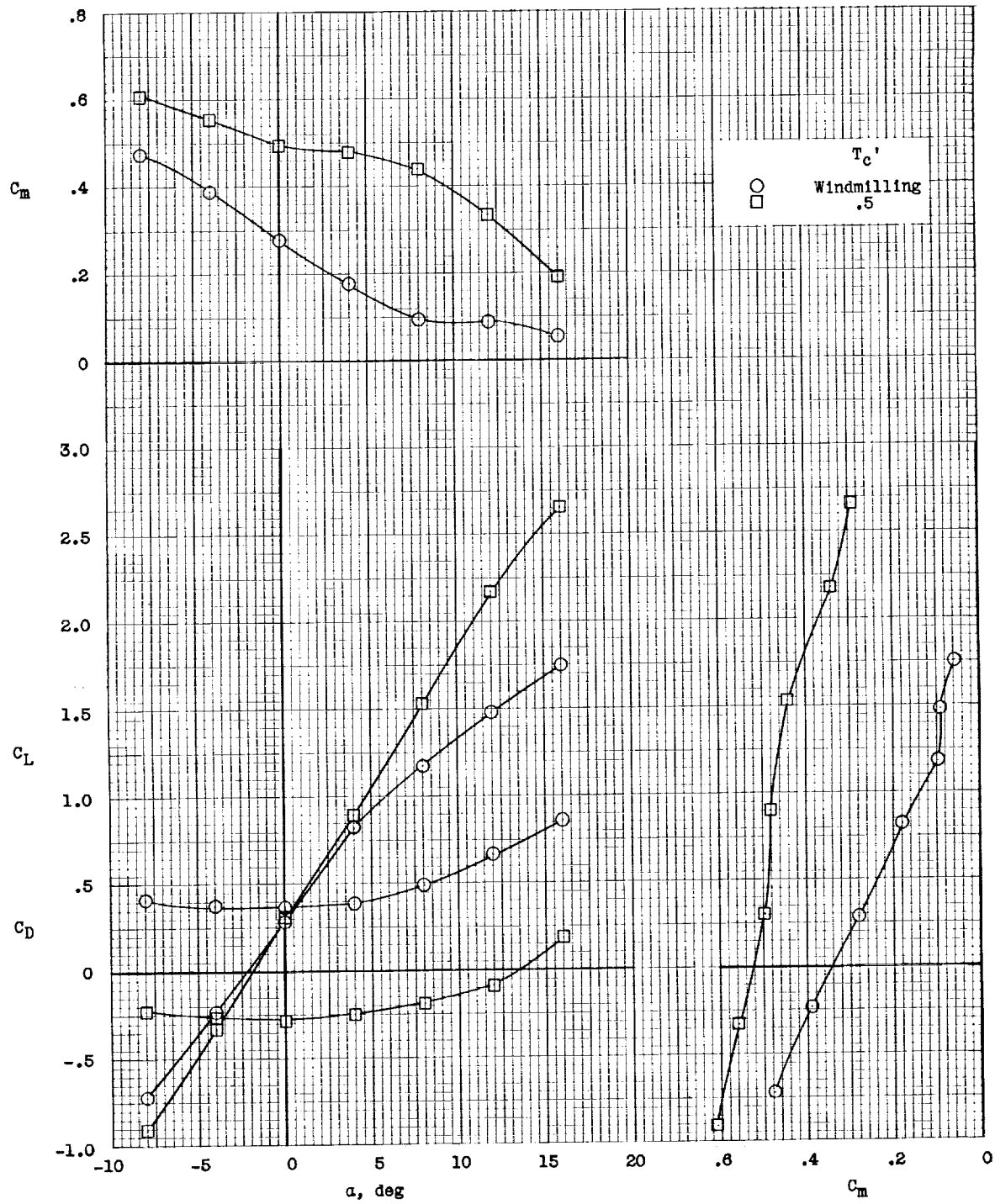

(a) $i_w = 0^o$.

Figure 12.- Longitudinal stability and trim characteristics of OB-LO configuration. $i_{d,F} = 5^o$; q = 5.0; gaps unsealed.

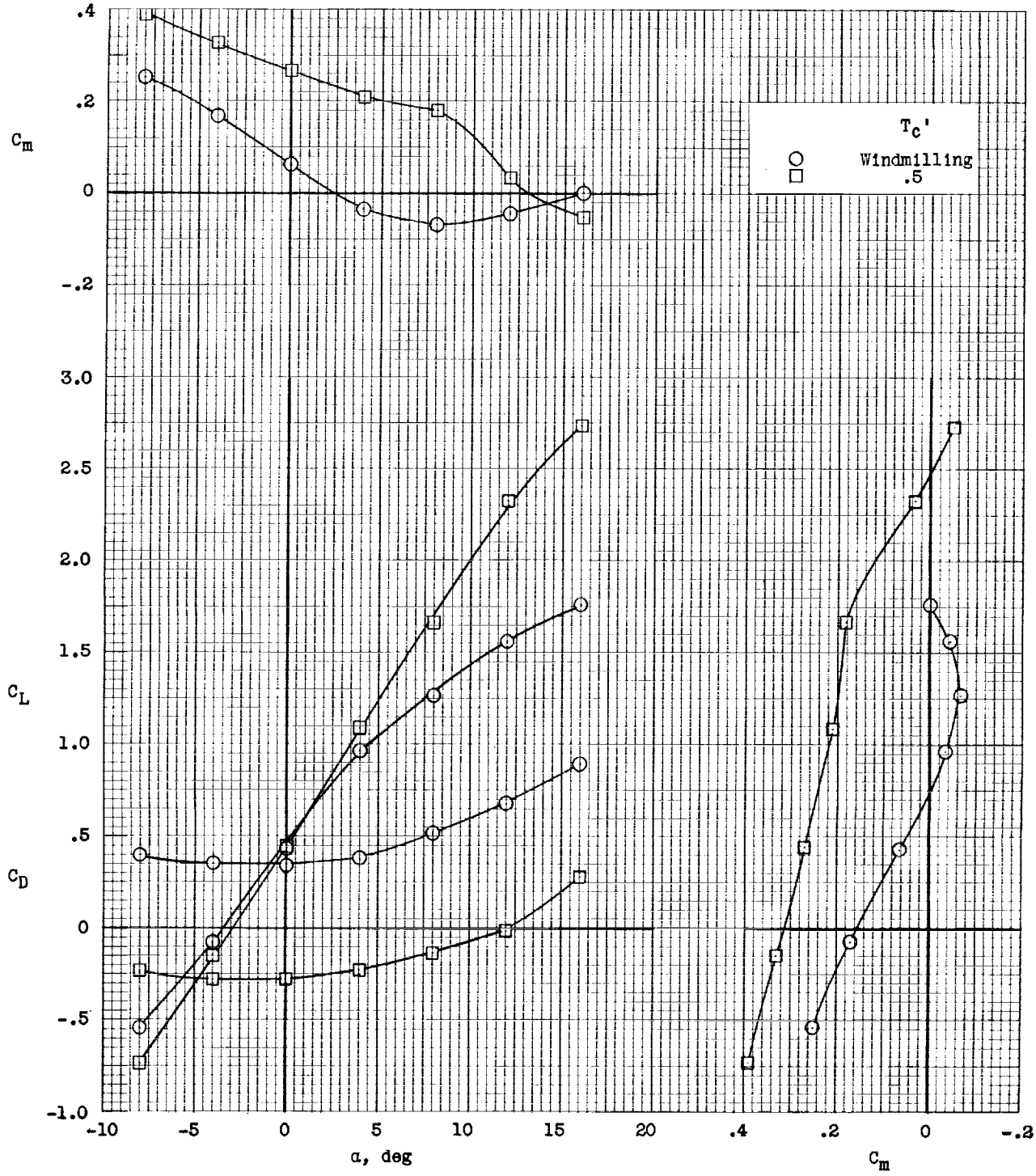

(b) $i_w = 5°$.

Figure 12.- Continued.

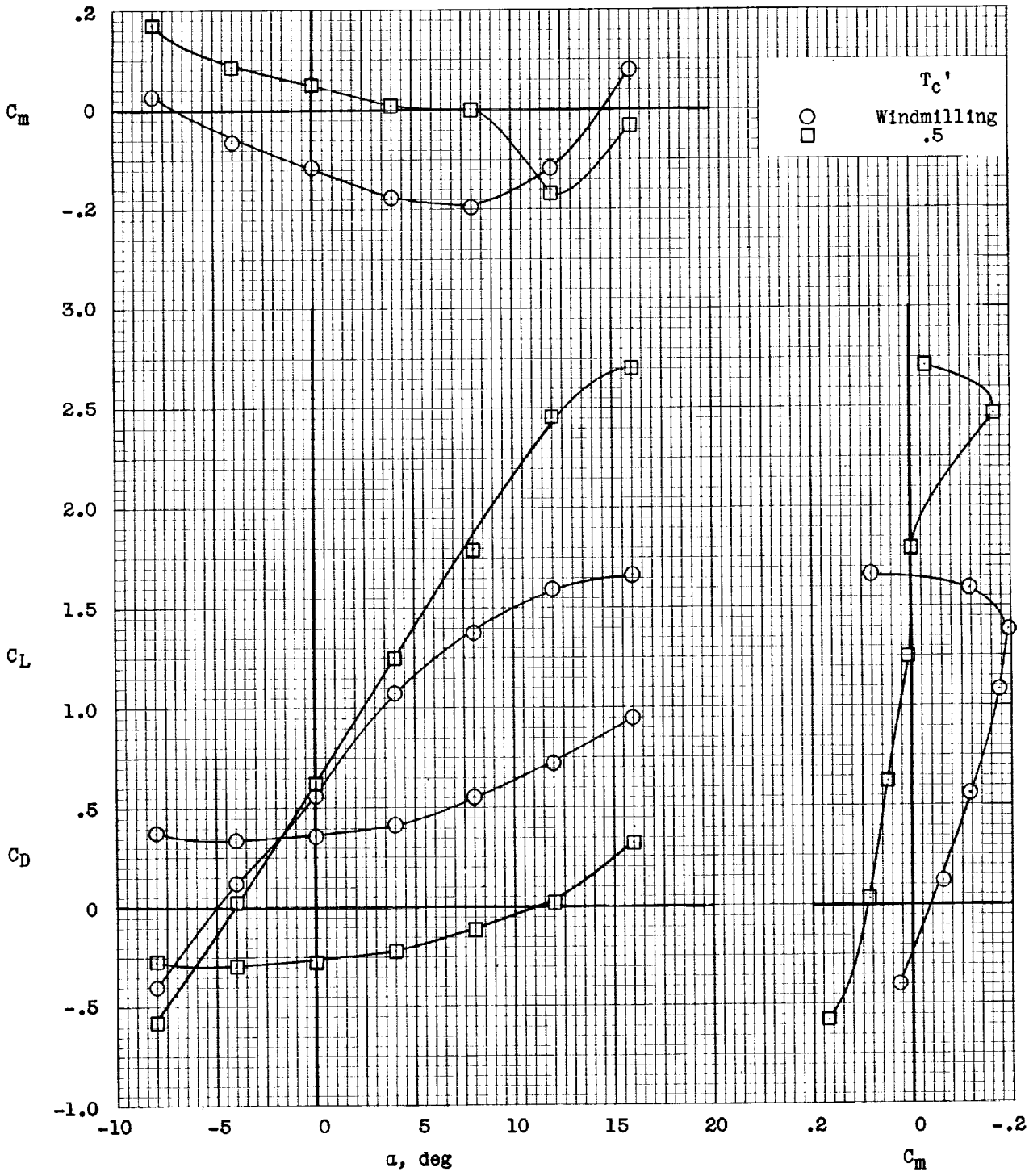

(c) $i_w = 10^o$.

Figure 12.- Continued.

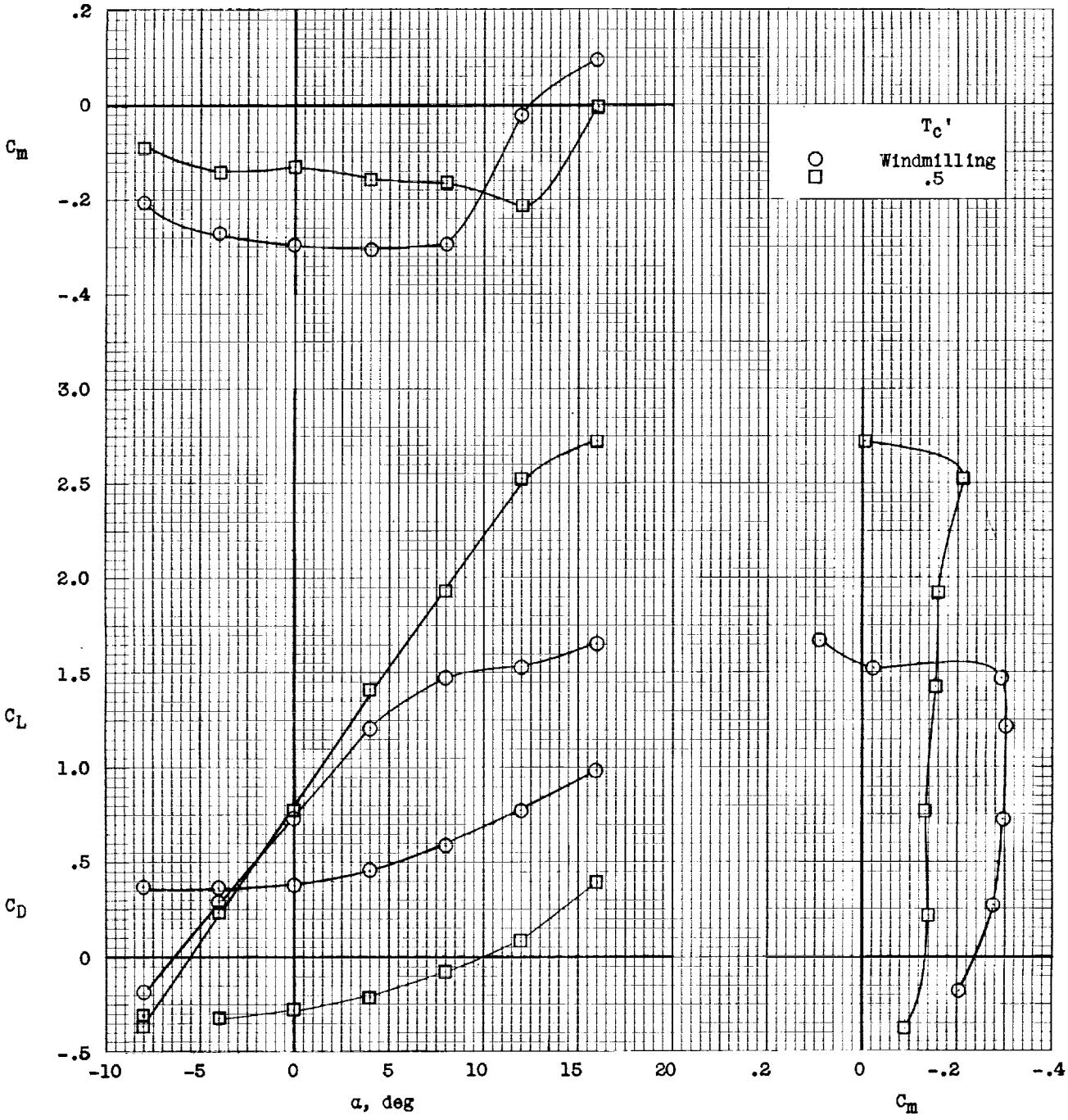

(d) $i_w = 15^o$.

Figure 12.- Continued.

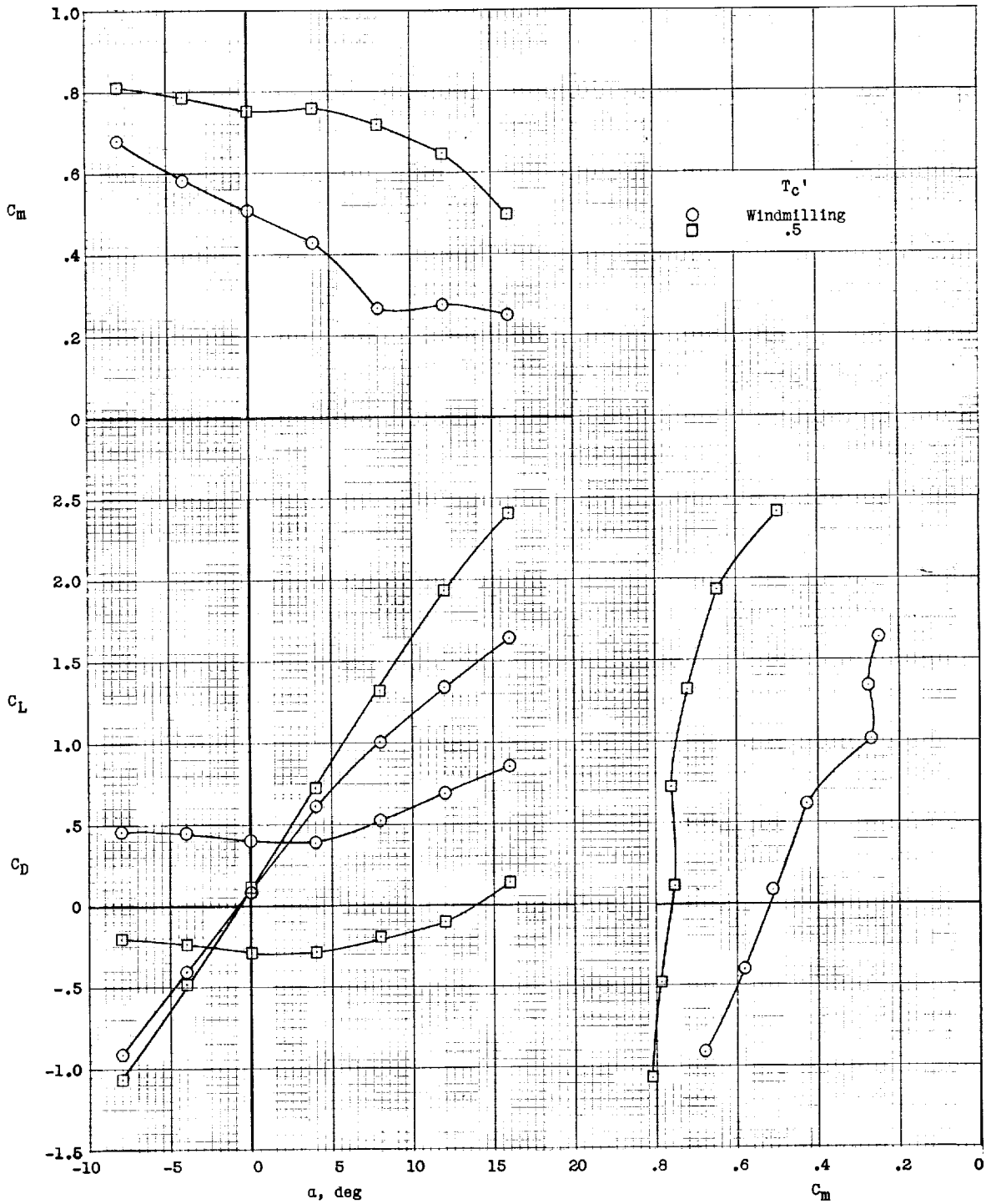

(e) $i_w = -5°$.

Figure 12.- Continued.

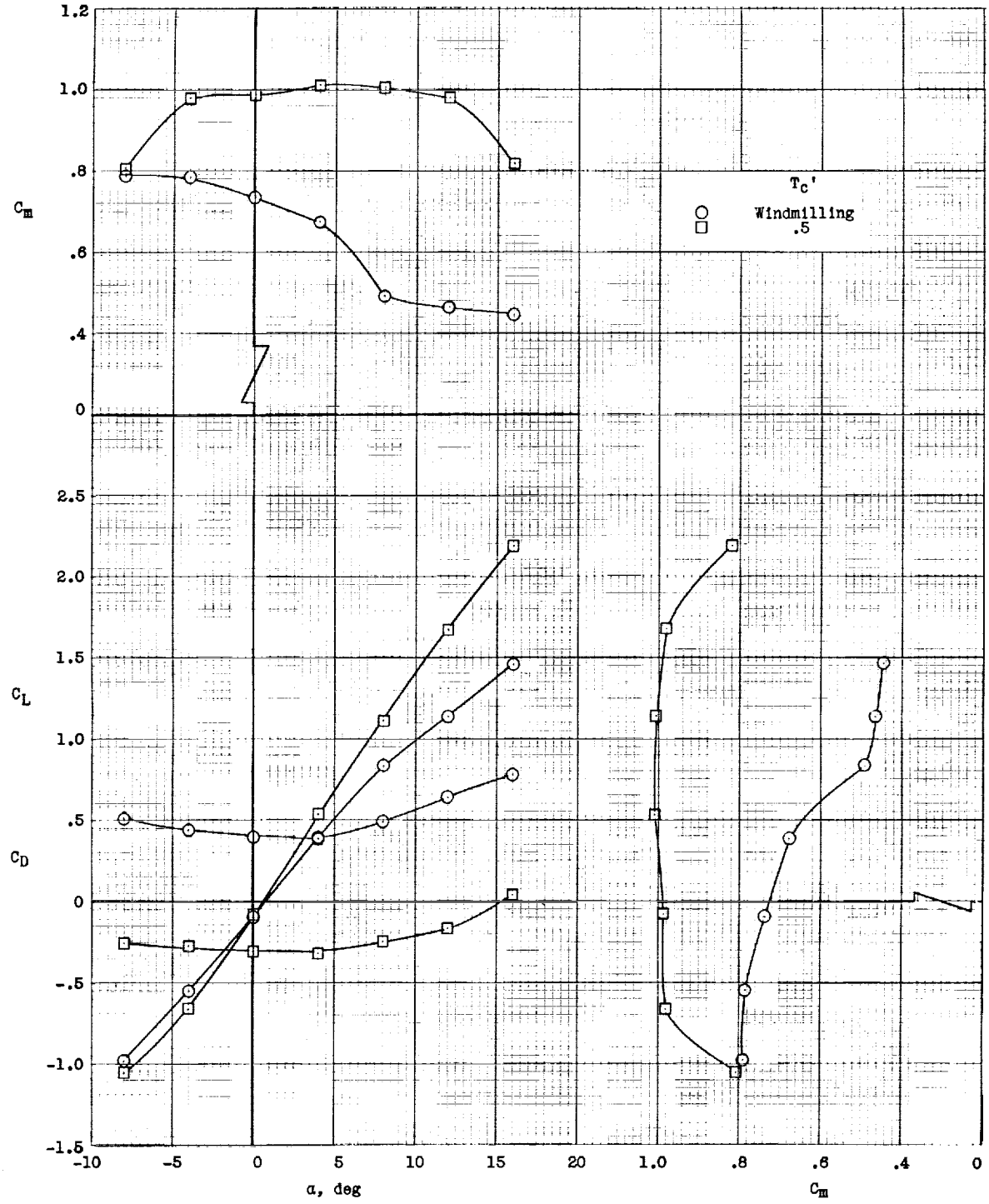

(f) $i_w = -10^\circ$.

Figure 12.- Continued.

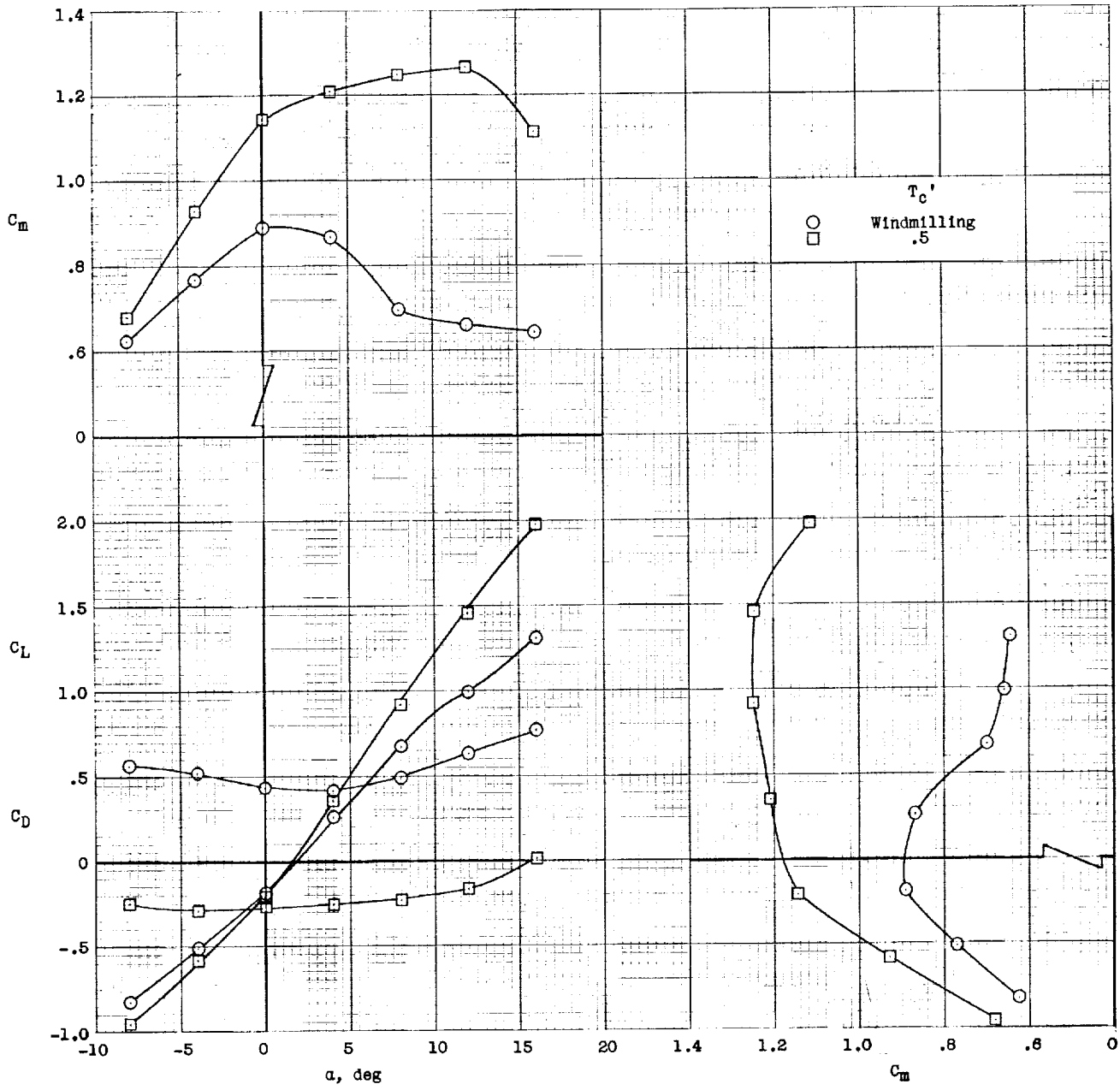

(g) $i_w = -15^\circ$.

Figure 12.- Concluded.

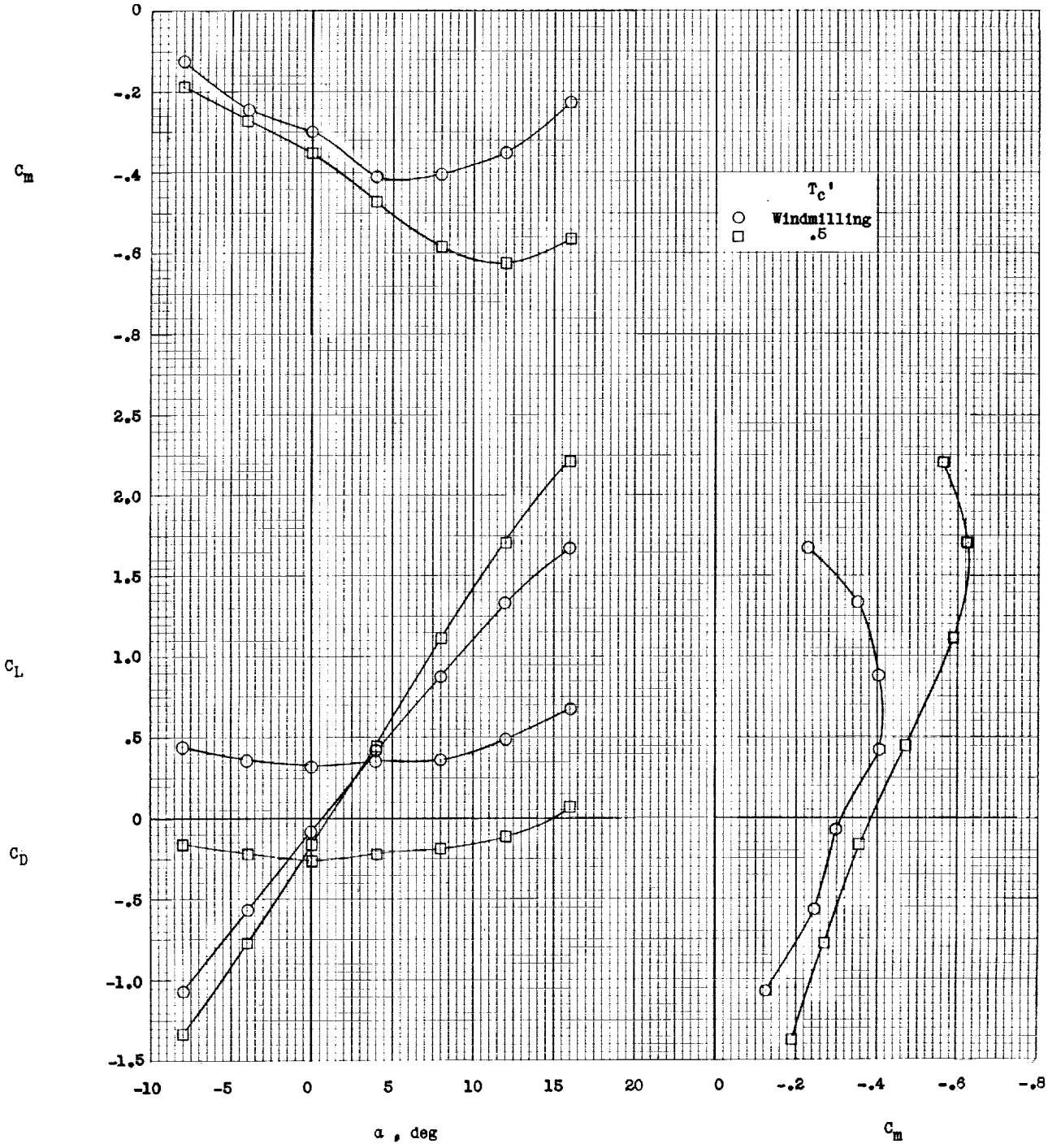

(a) $i_w = 0^o$.

Figure 13.- Longitudinal stability and trim characteristics of OB-LO configuration. $i_{d,F} = -5^o$; $q = 5.0$; gaps unsealed.

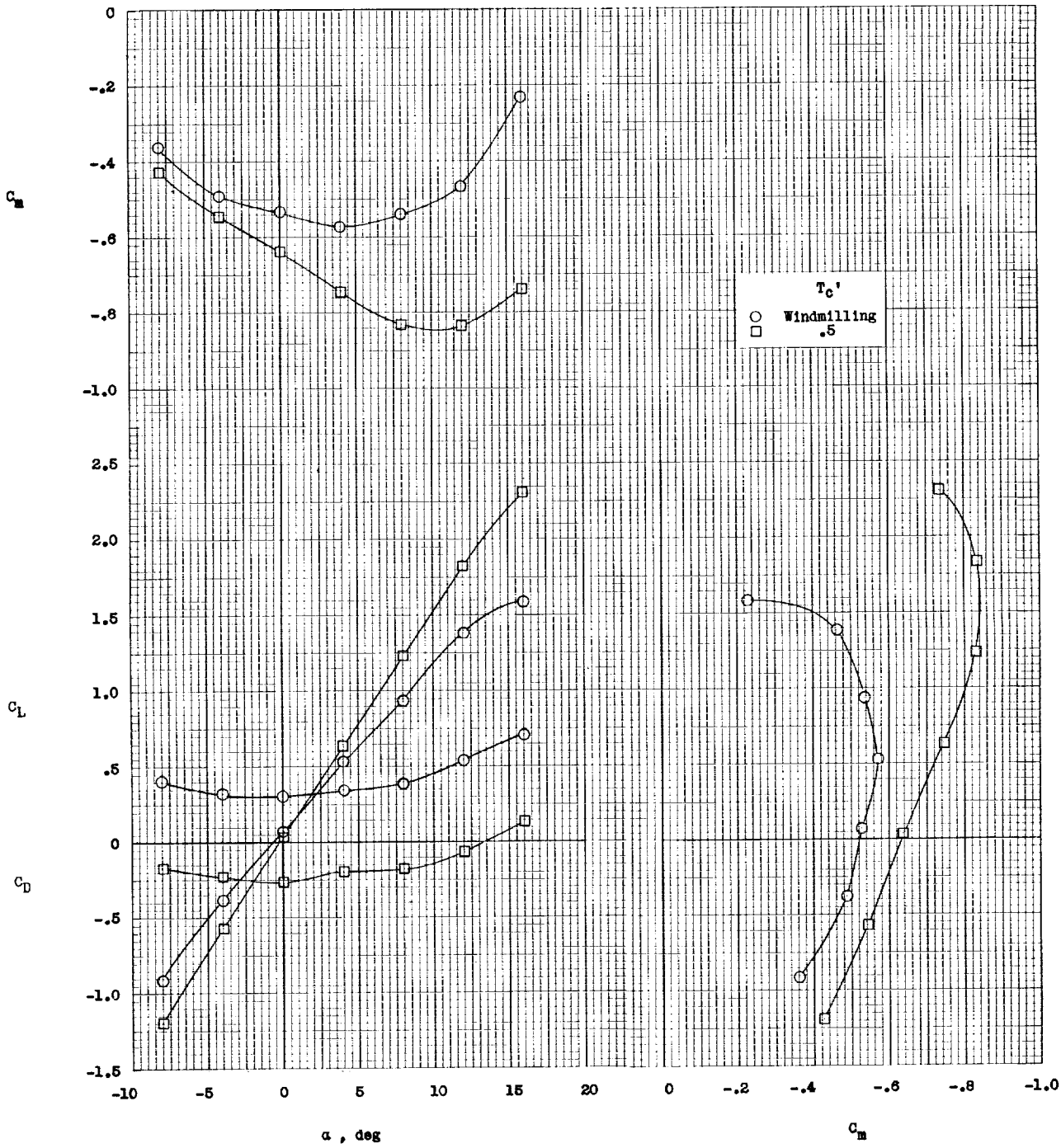

(b) $i_w = 5^\circ$.

Figure 13.- Continued.

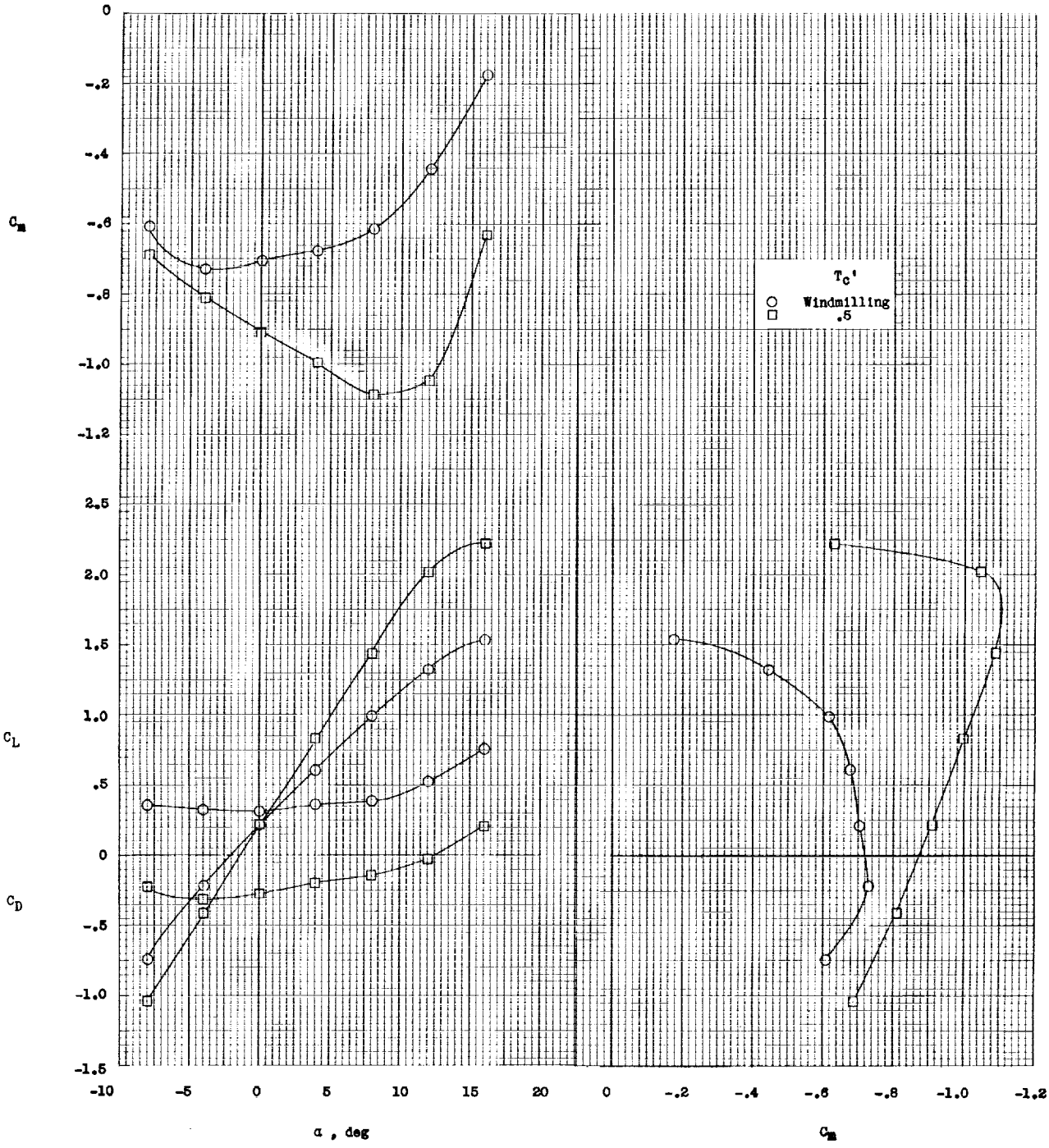

(c) $i_w = 10^o$.

Figure 13.- Continued.

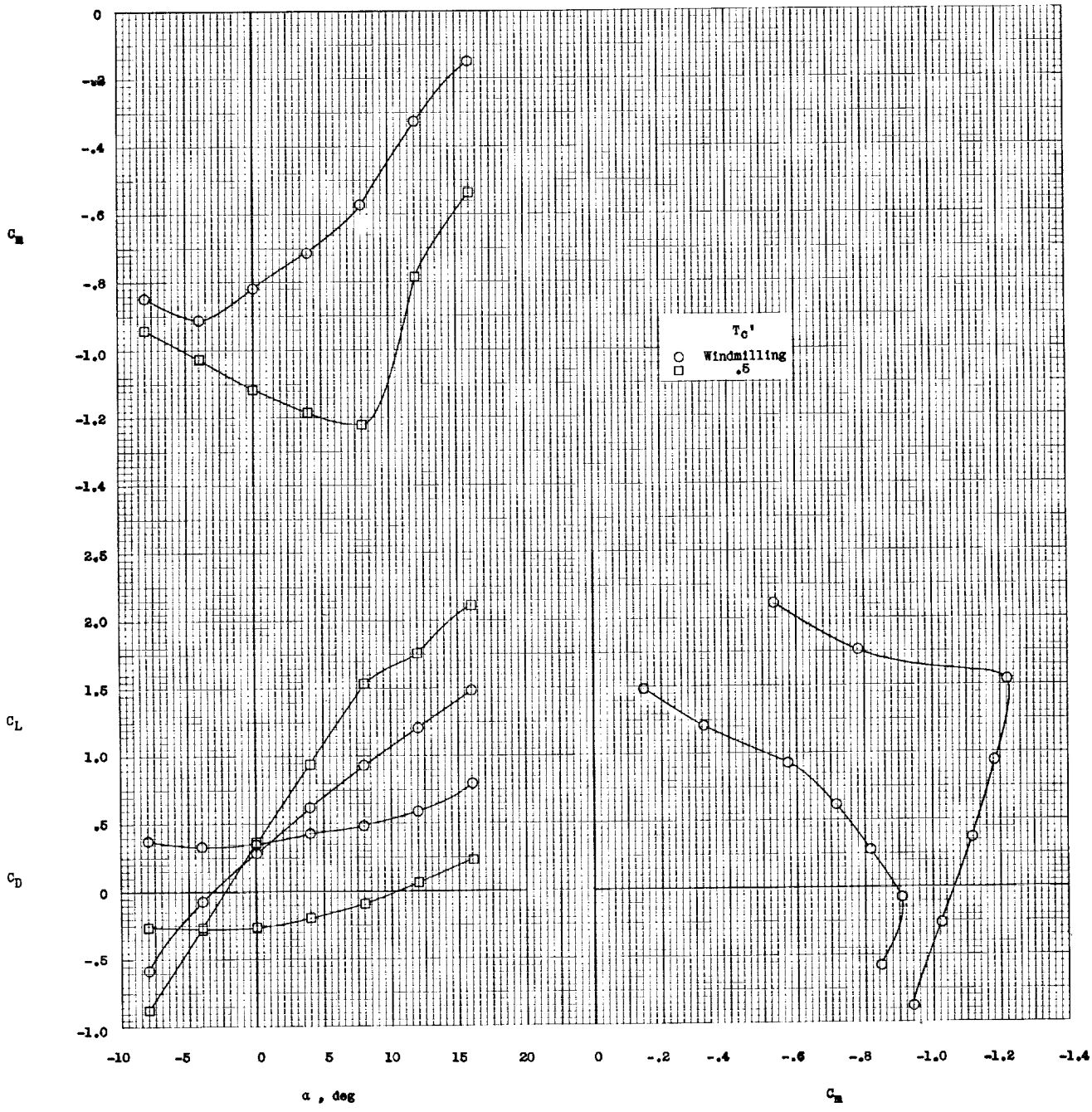

(d) $i_w = 15^\circ$.

Figure 13.- Continued.

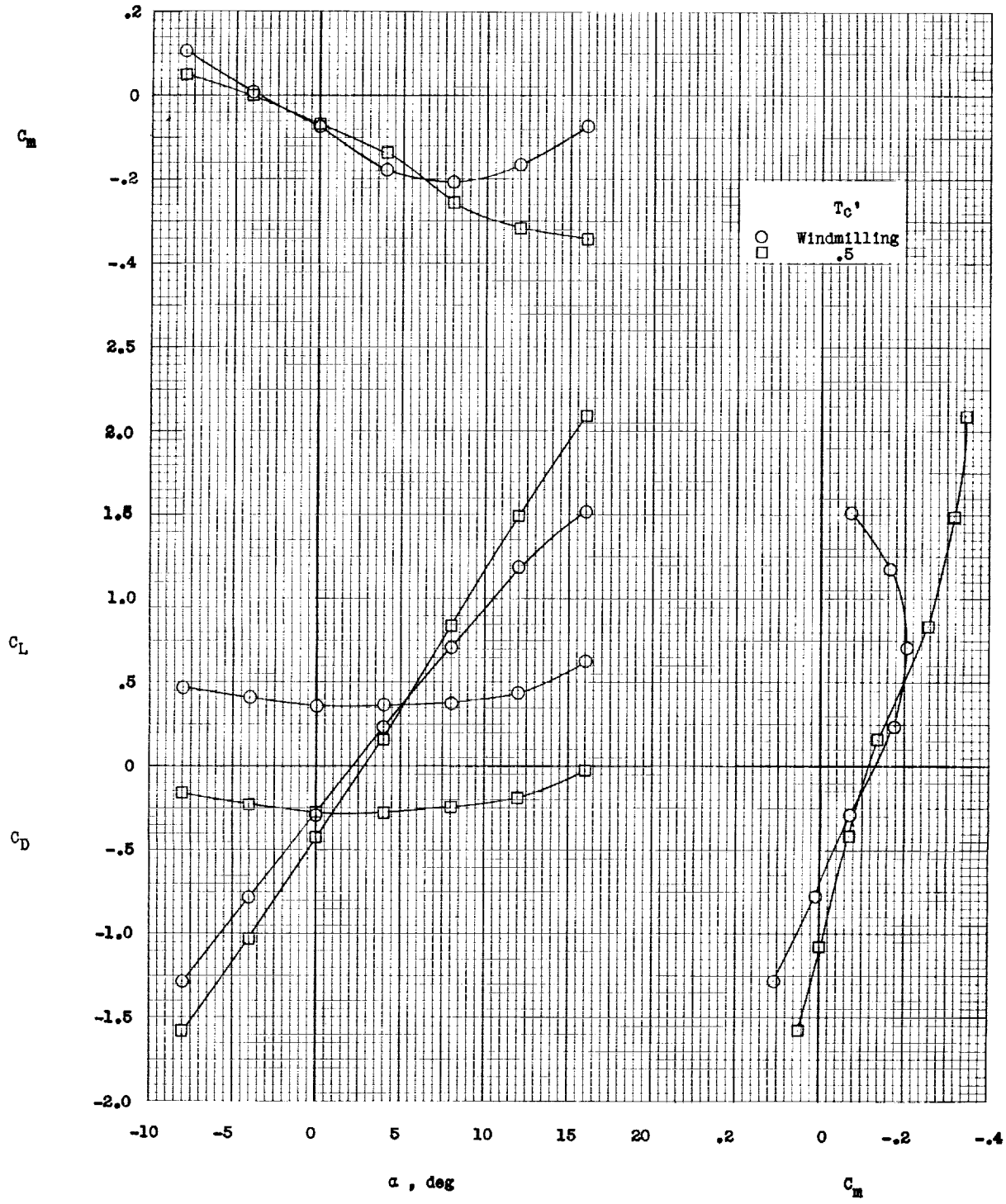

(e) $i_w = -5^\circ$.

Figure 13.- Continued.

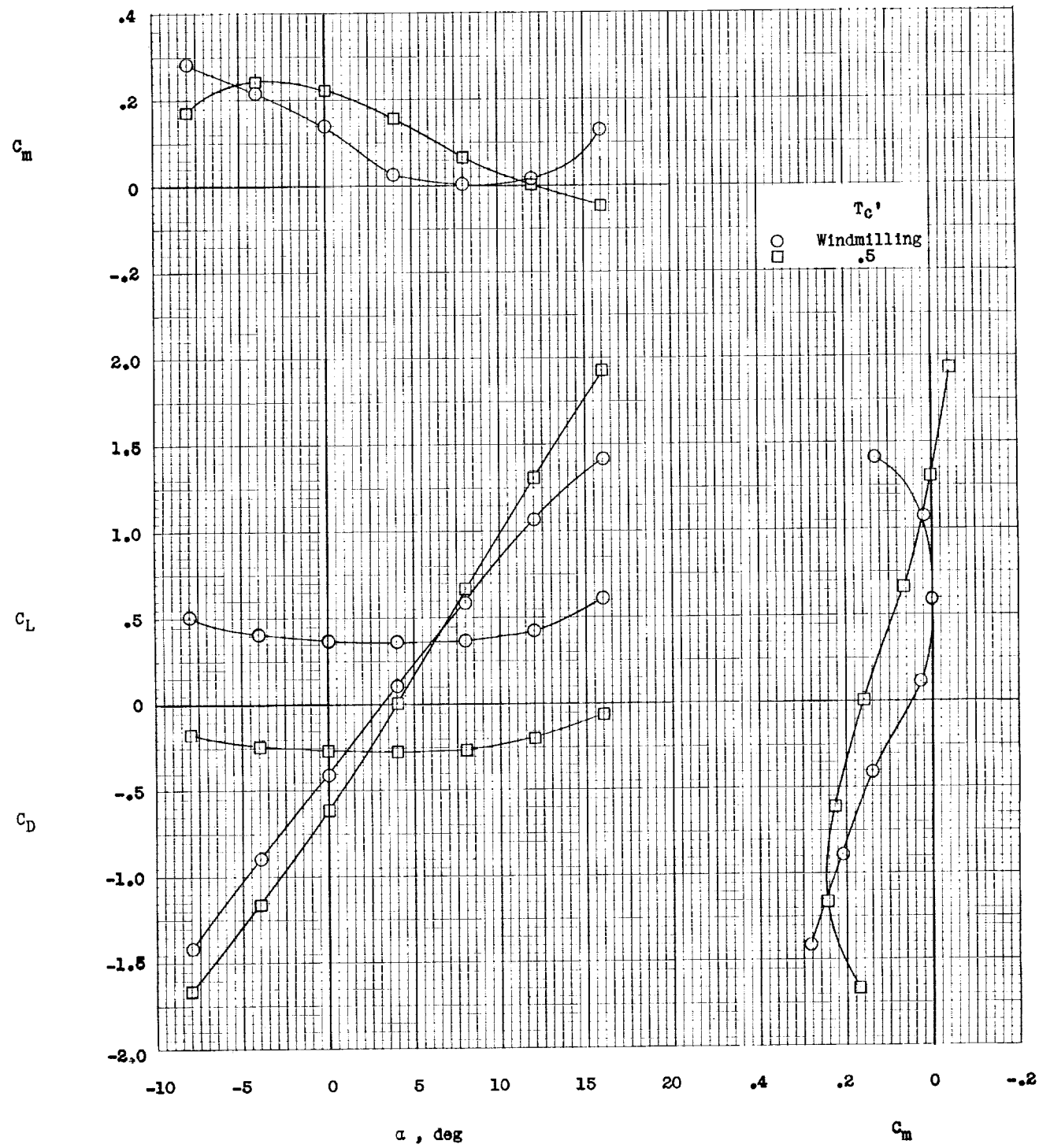

(f) $i_w = -10°$.

Figure 13.- Continued.

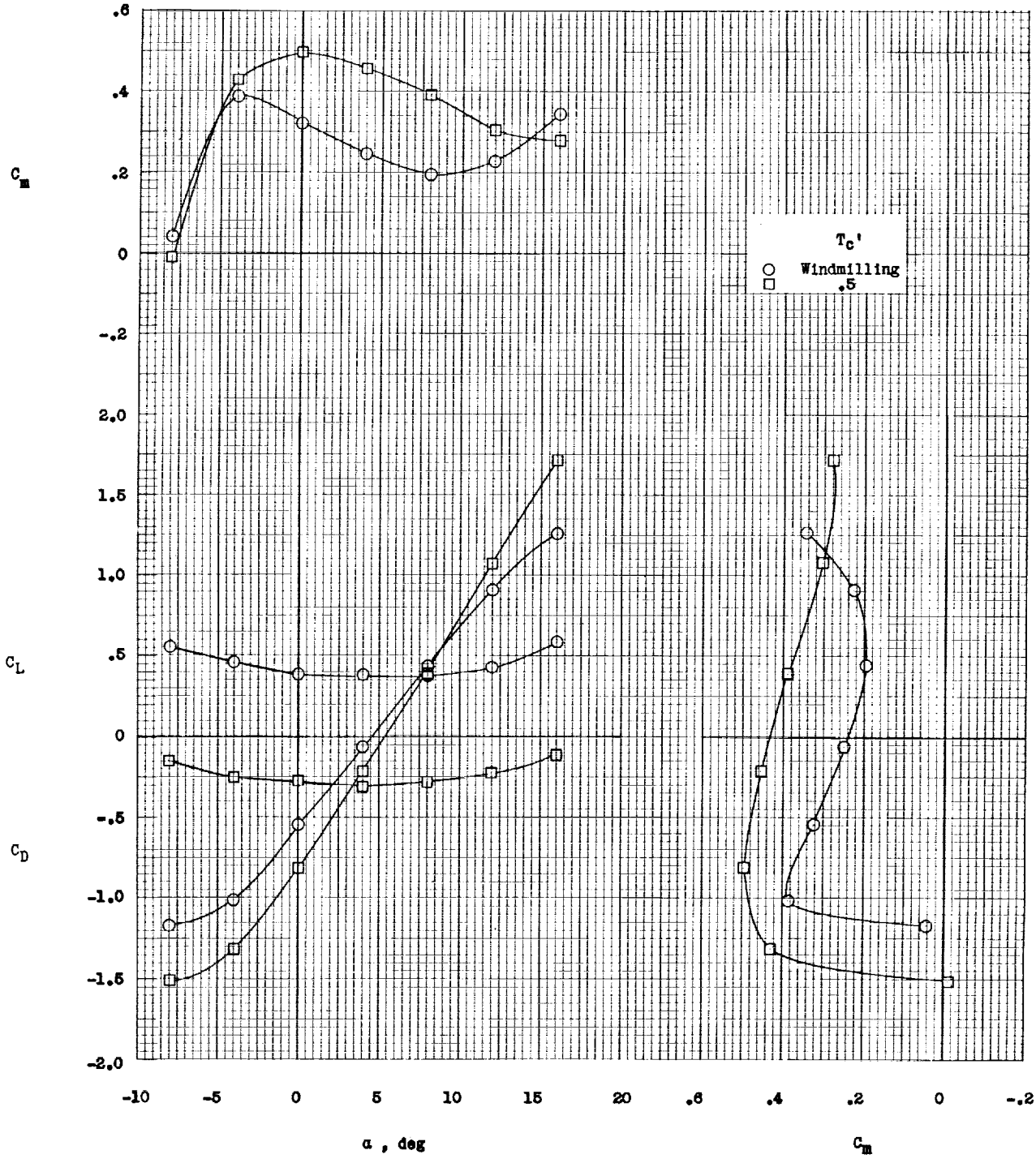

(g) $i_w = -15^\circ$.

Figure 13.- Concluded.

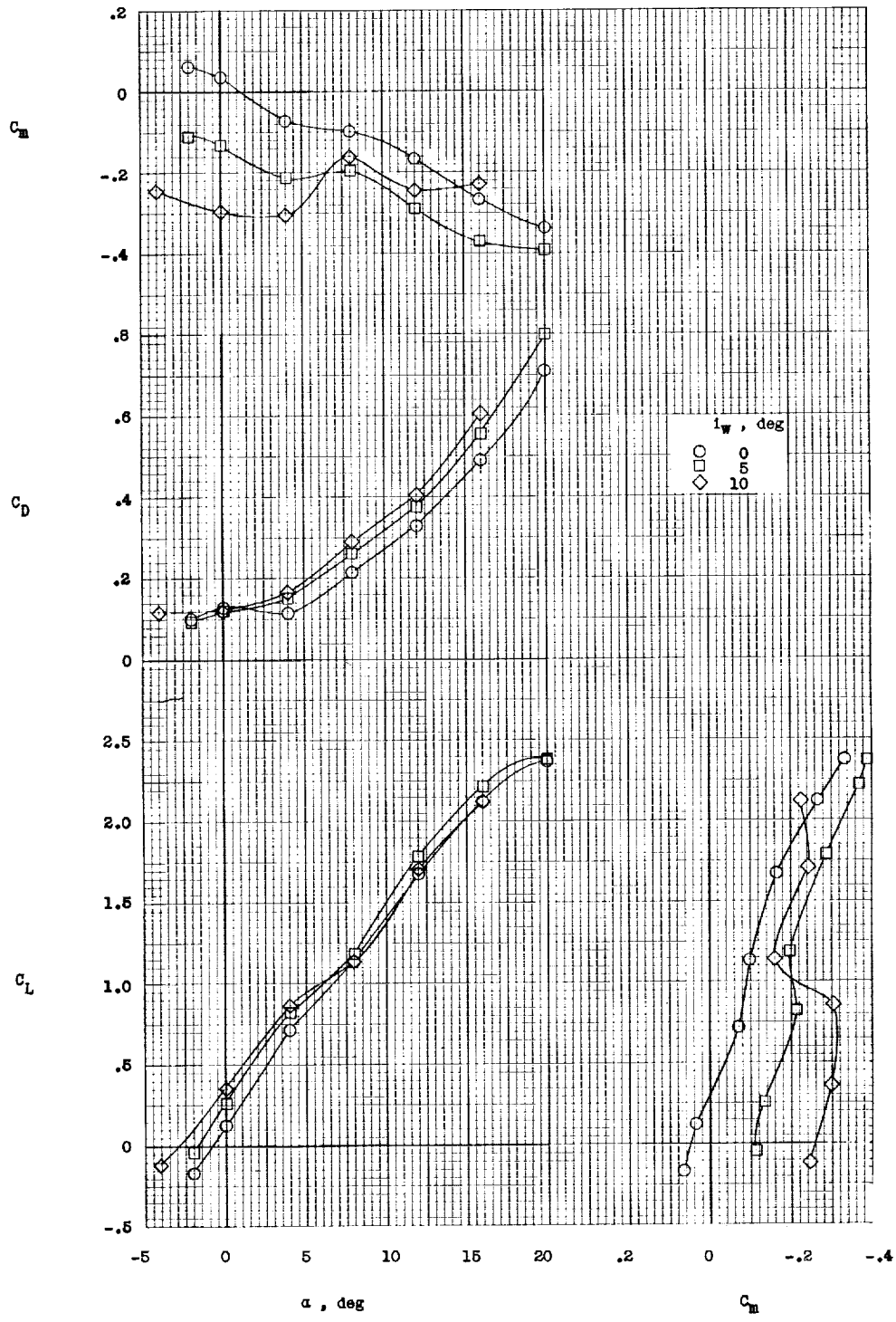

Figure 14.- Longitudinal stability and trim characteristics of IB-HI configuration. $i_{d,F} = 0^o$; $q = 5.0$; gaps sealed; ducts clean.

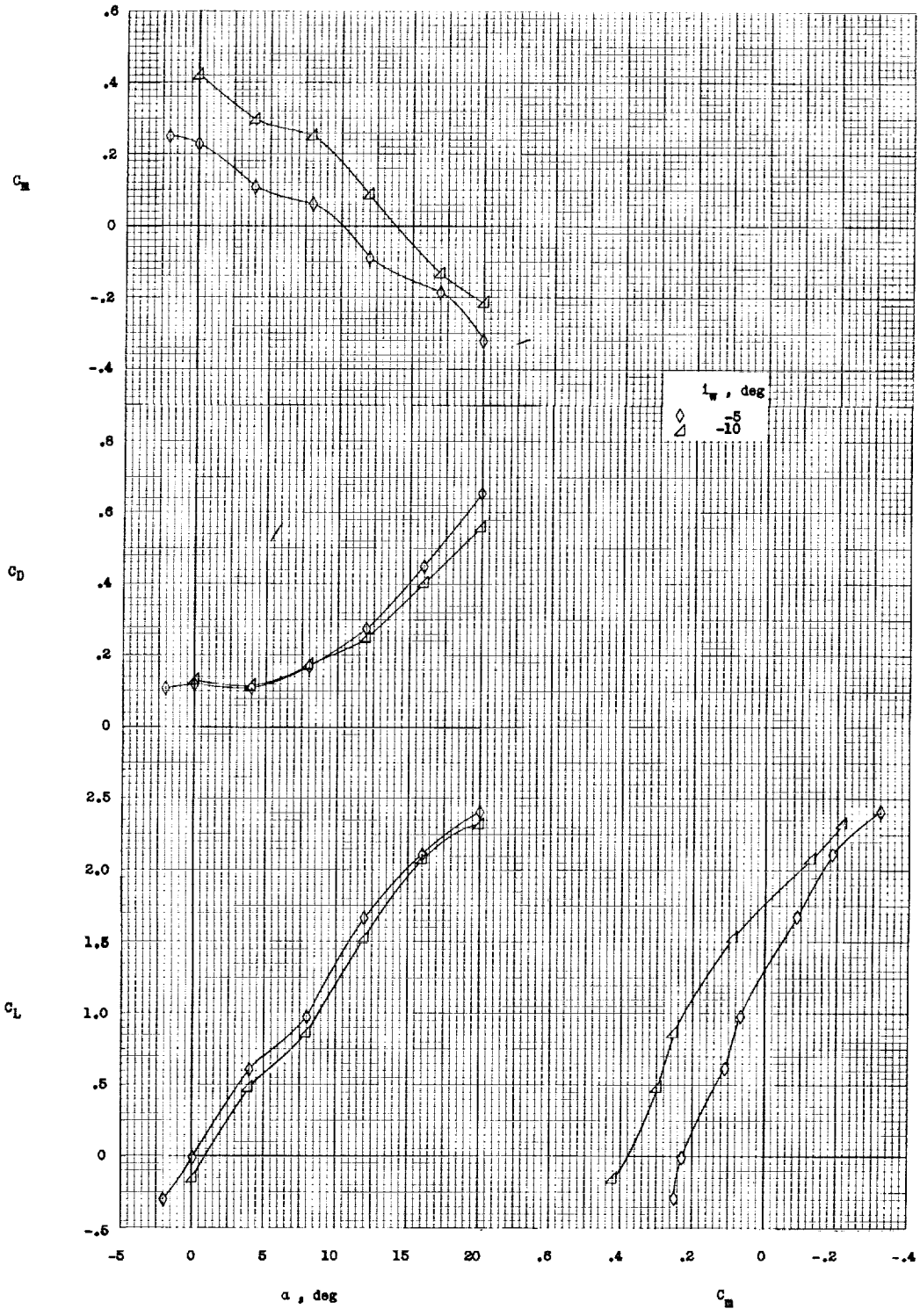

Figure 14.- Concluded.

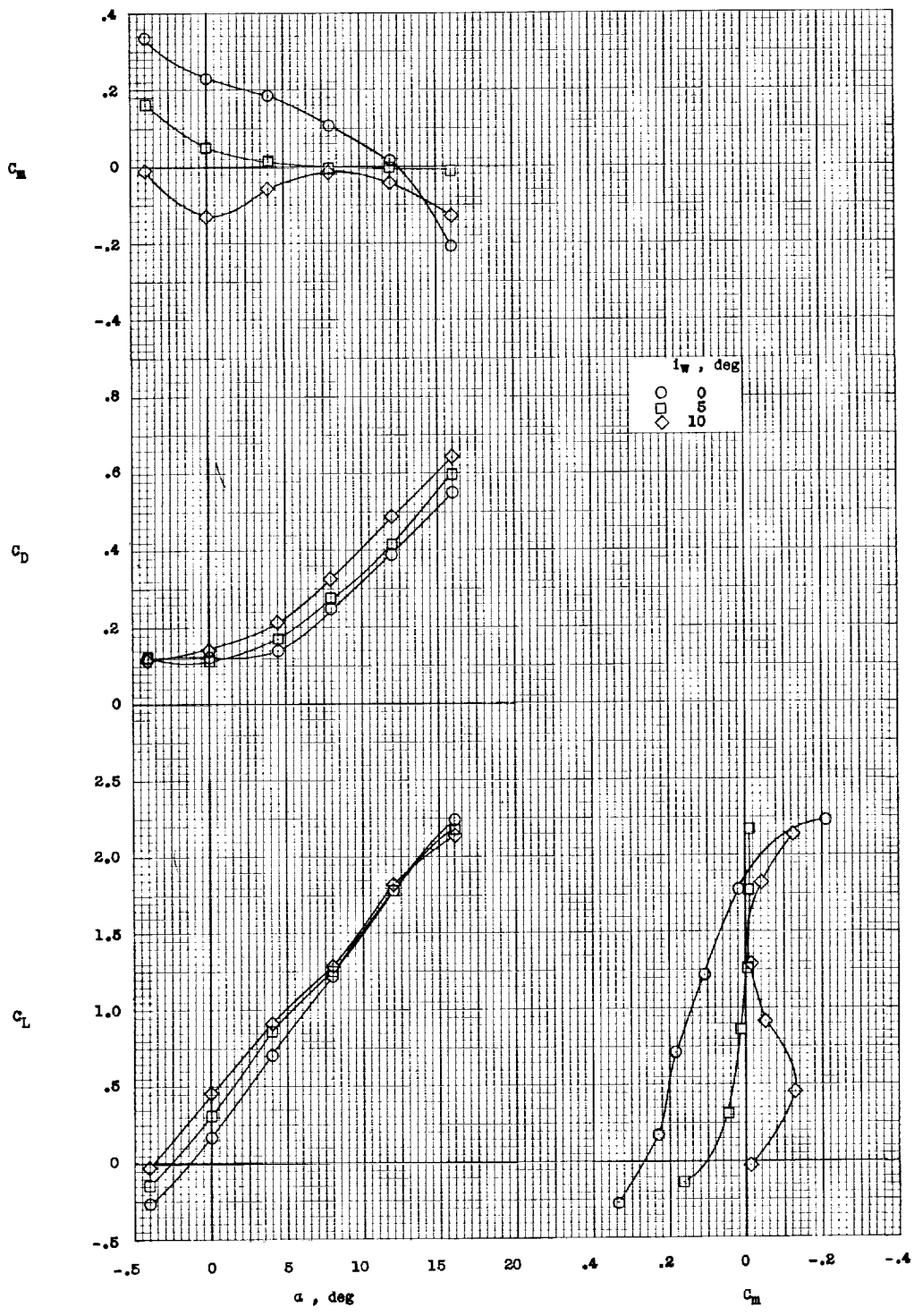

Figure 15.- Longitudinal stability and trim characteristics of IB-HI configuration. $i_{d,F} = 2.5^o$; q = 5.0; gaps sealed; ducts clean.

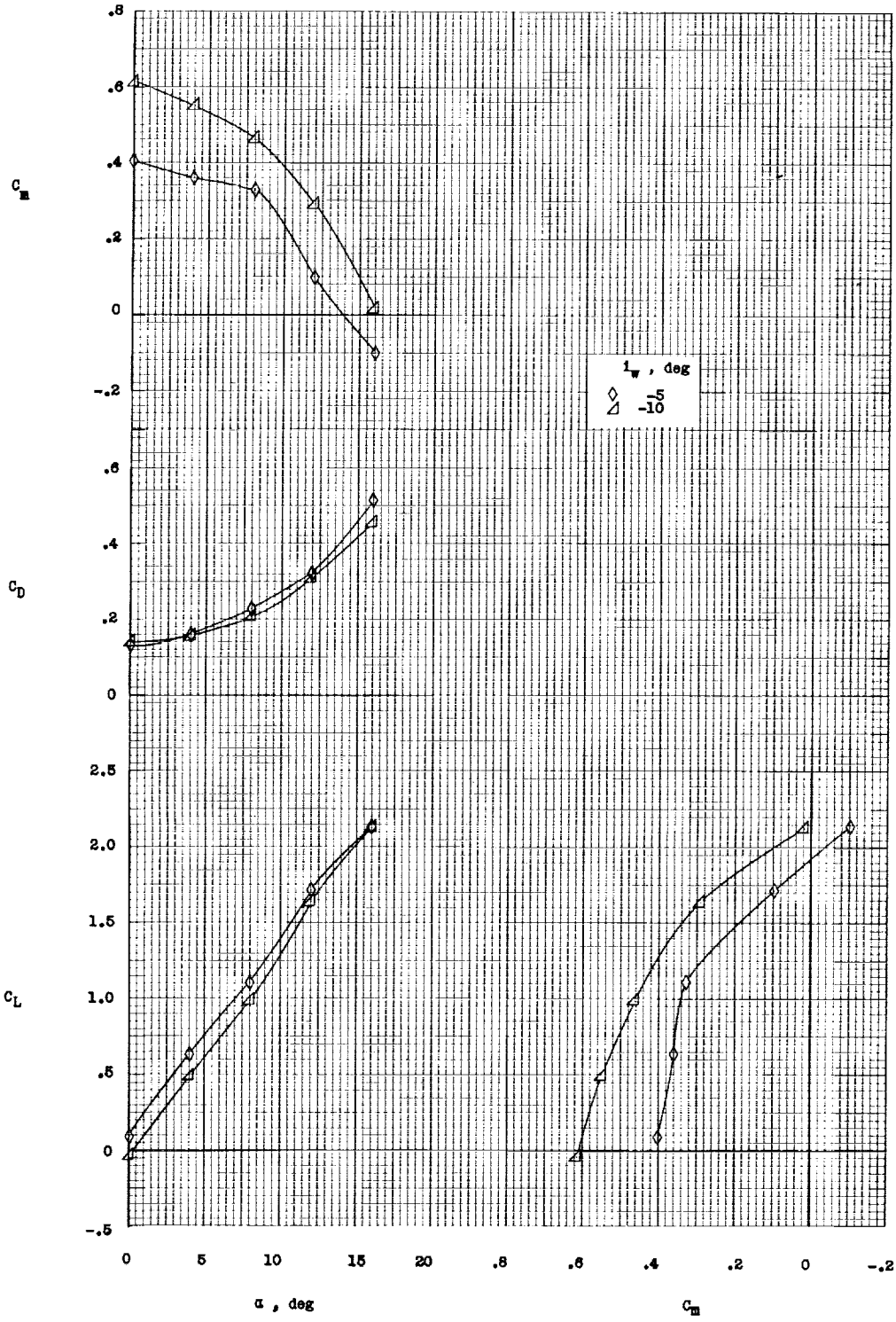

Figure 15.- Concluded.

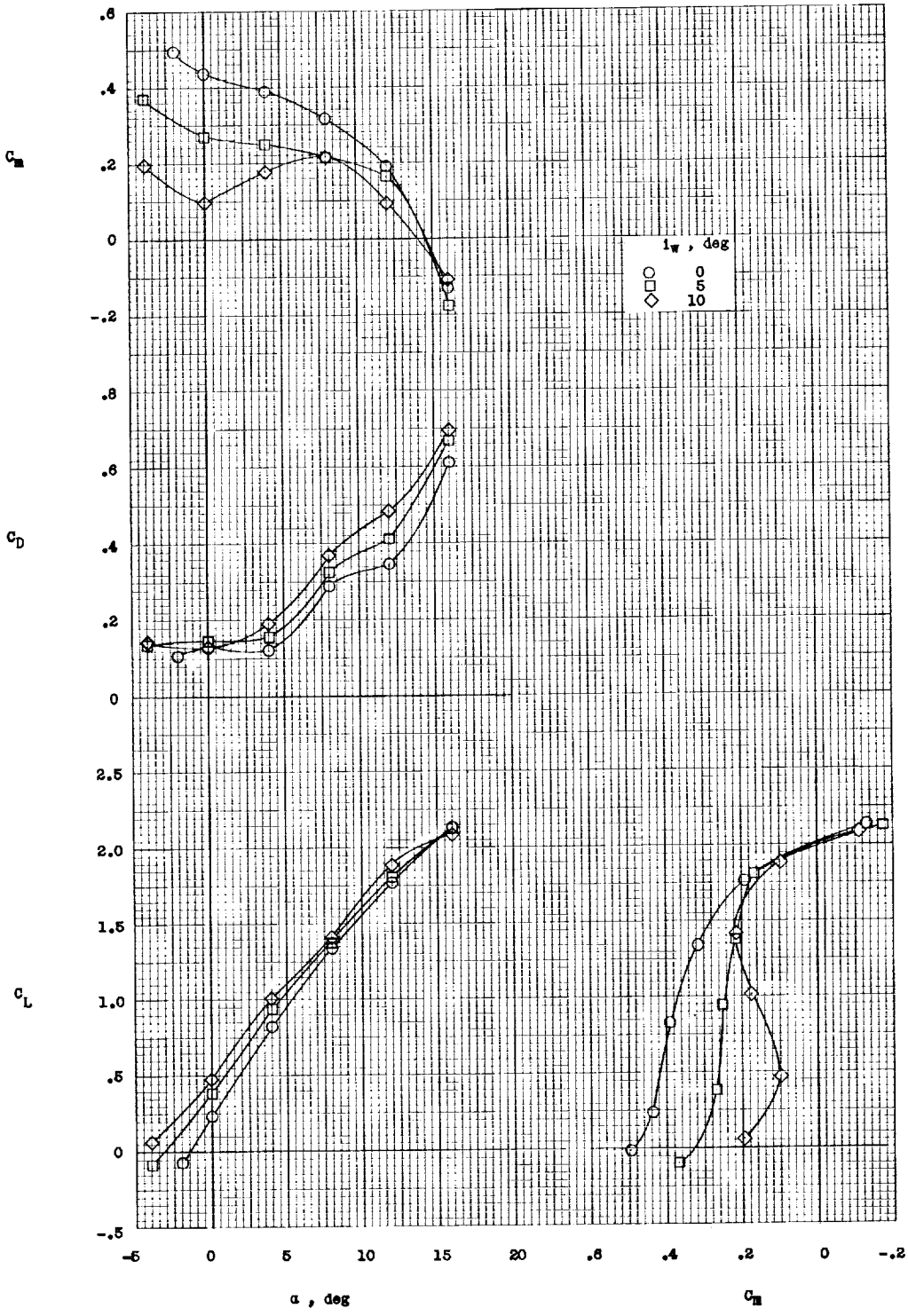

Figure 16.- Longitudinal stability and trim characteristics of IB-HI configuration. $i_{d,F} = 5^o$; q = 5.0; gaps sealed; ducts clean.

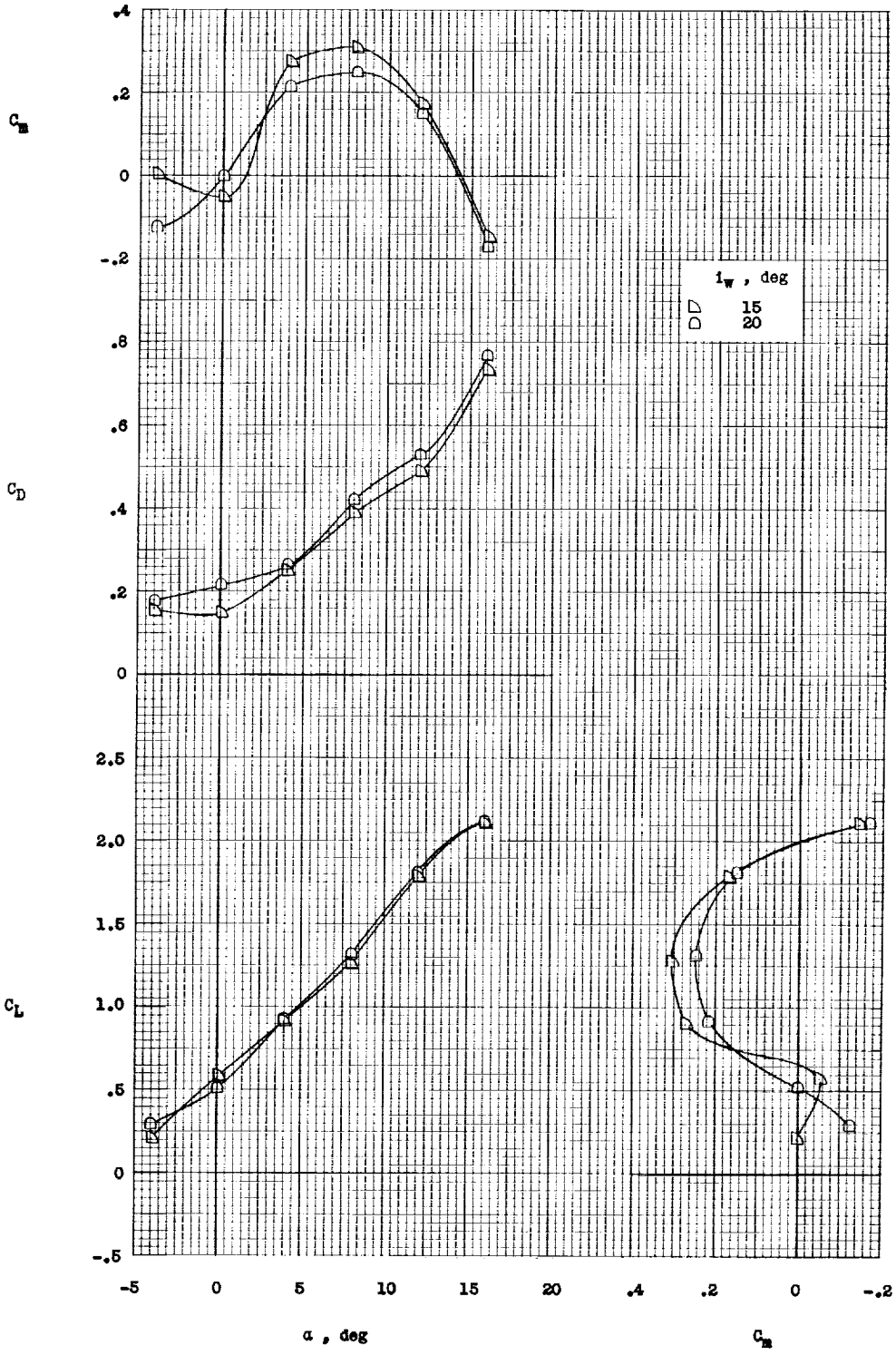

Figure 16.- Concluded.

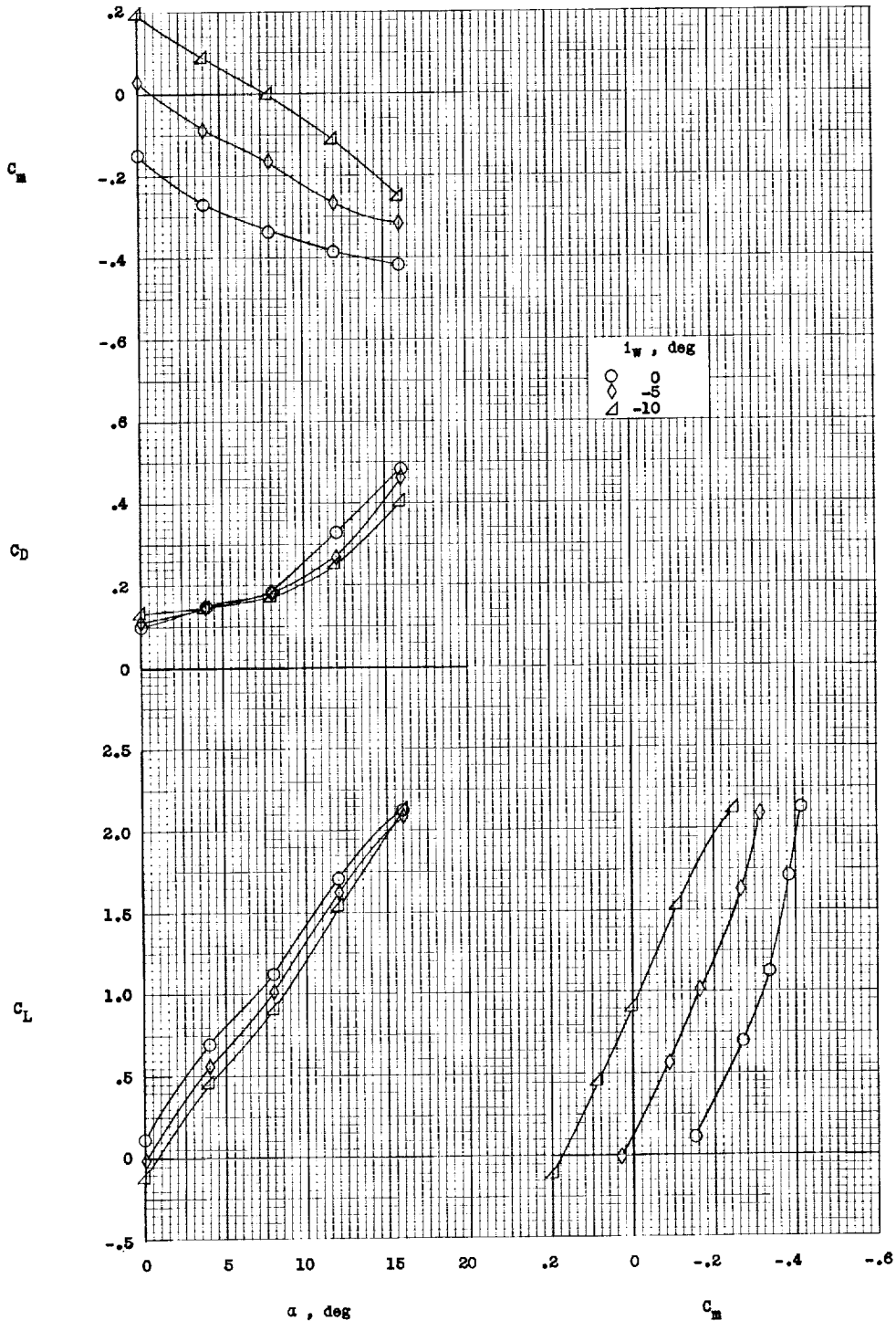

Figure 17.- Longitudinal stability and trim characteristics of IB-HI configuration. $i_{d,F} = -2.5^{\circ}$; $q = 5.0$; gaps sealed; ducts clean.

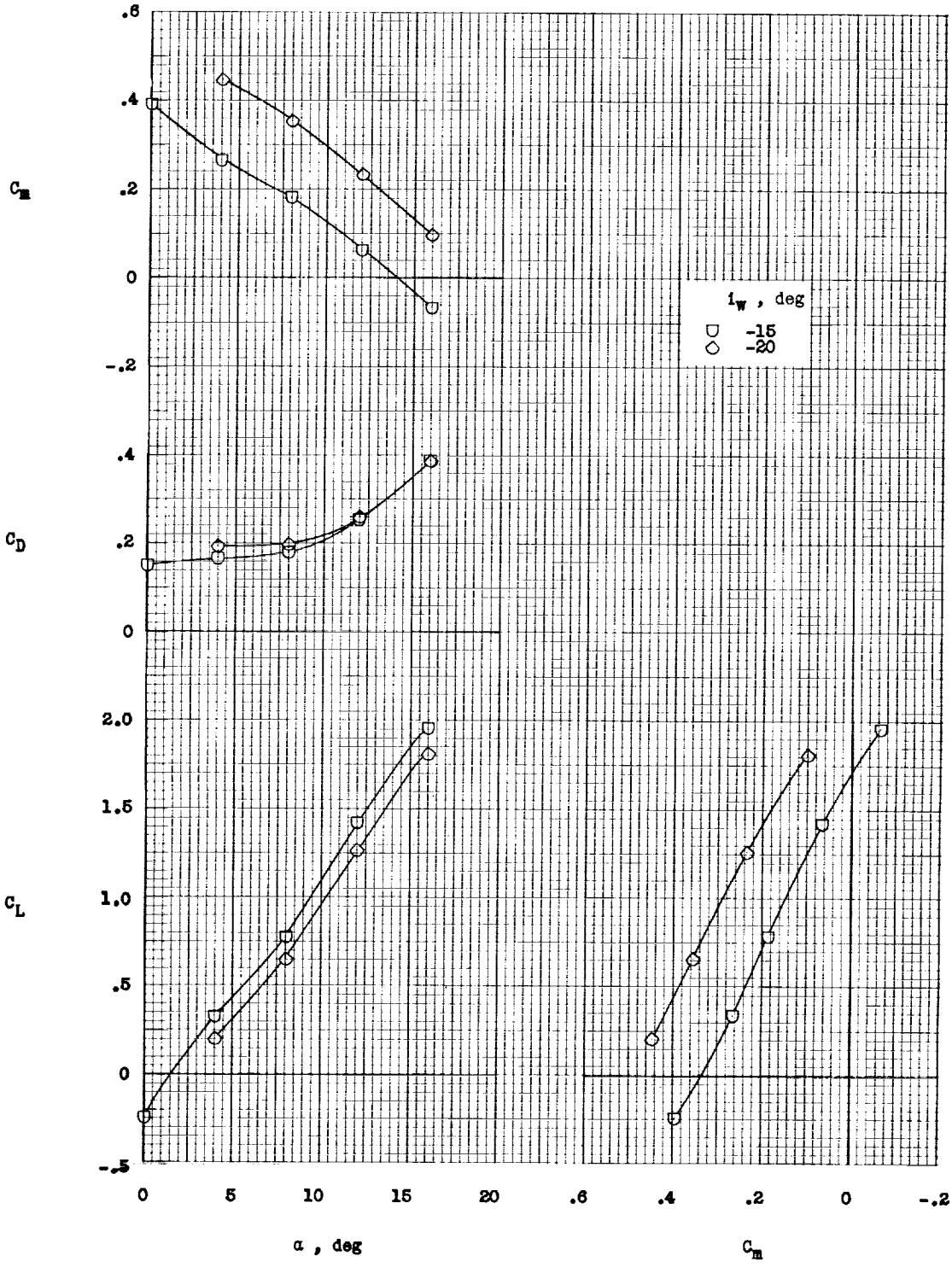

Figure 17.- Concluded.

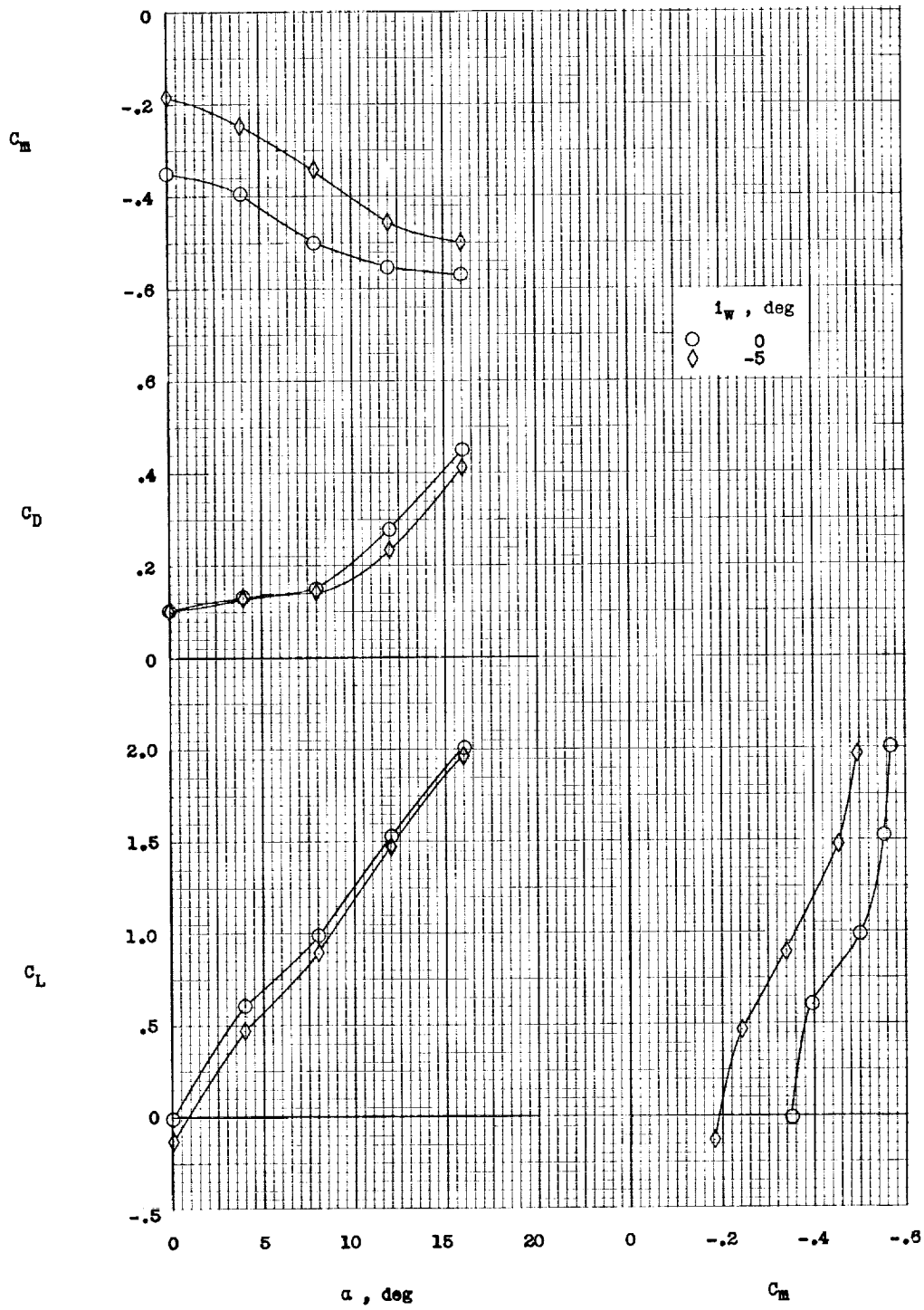

Figure 18.- Longitudinal stability and trim characteristics of IB-HI configuration. $i_{d,F} = -5^{\circ}$; $q = 5.0$; gaps sealed; ducts clean.

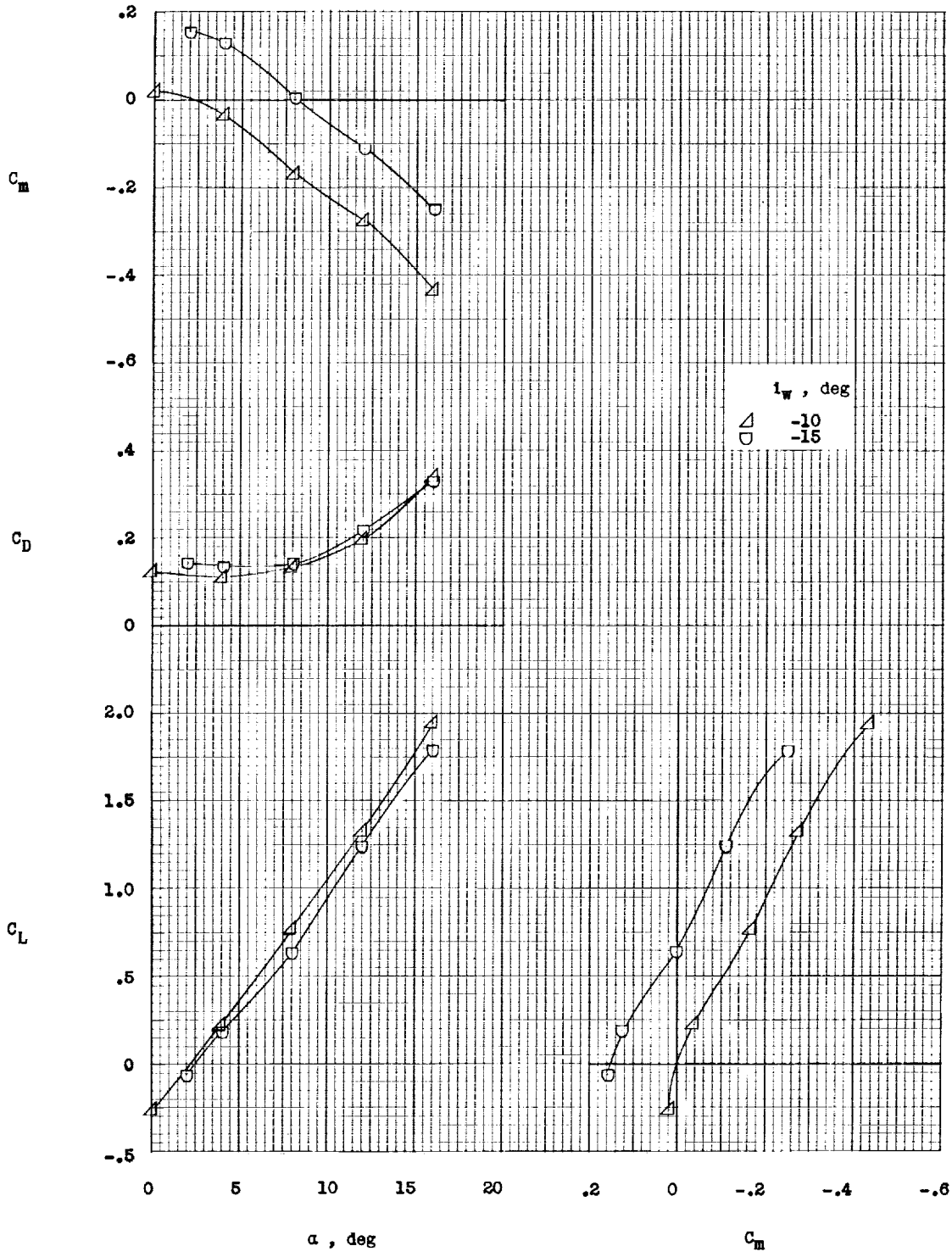

Figure 18.- Concluded.

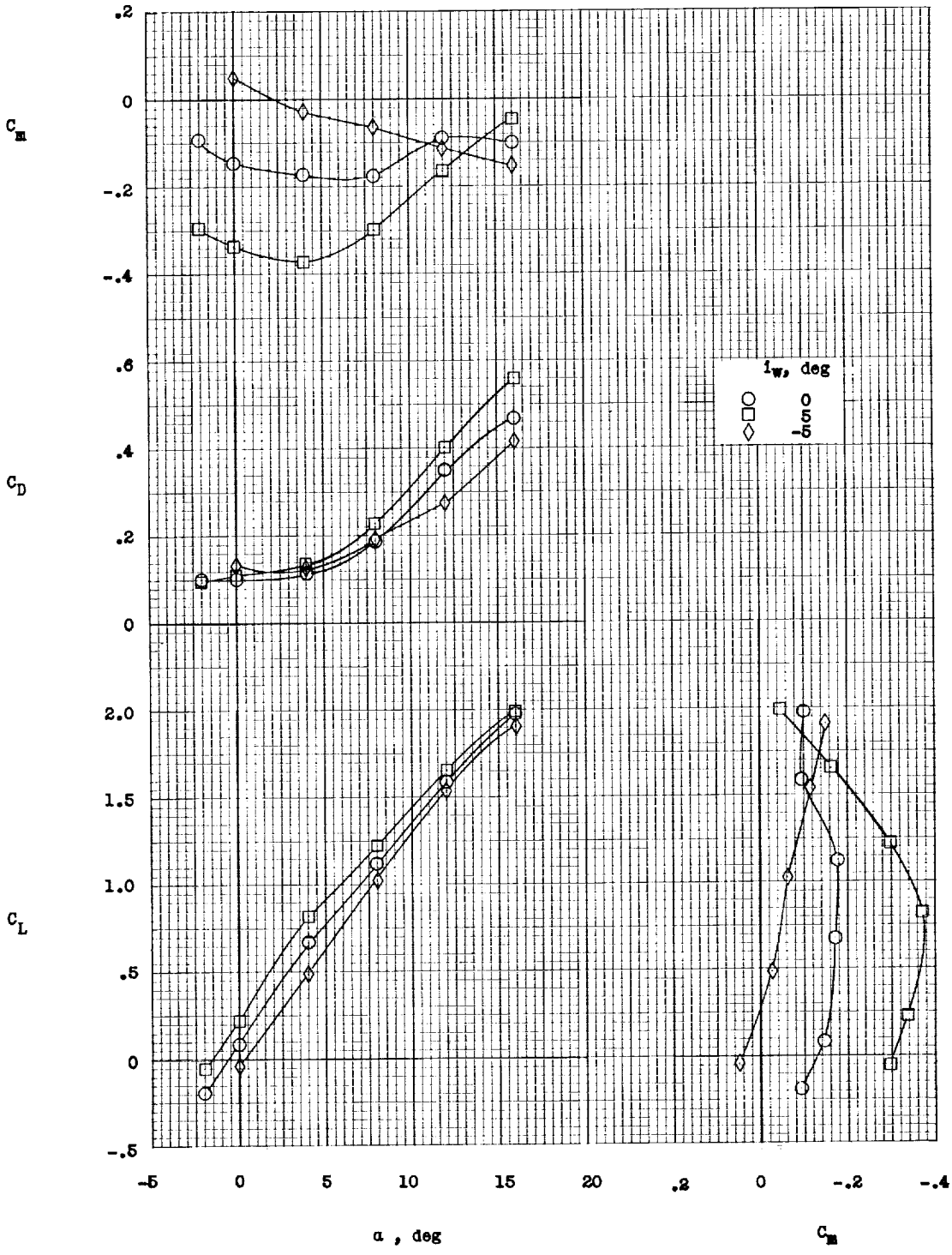

Figure 19.- Longitudinal stability and trim characteristics of IB-LO configuration. $i_{d,F} = 0^{o}$; $q = 5.0$; gaps sealed; ducts clean.

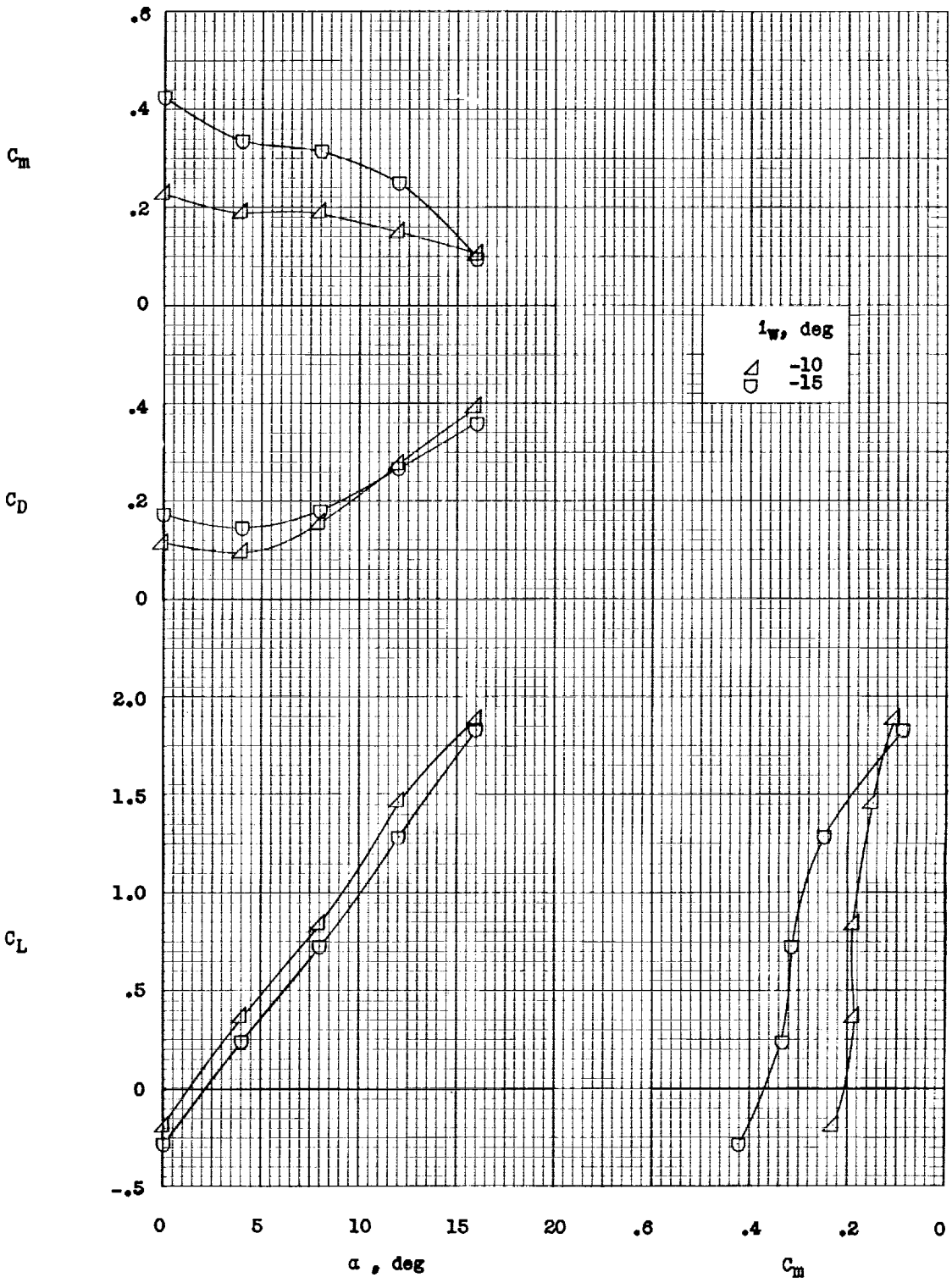

Figure 19.- Concluded.

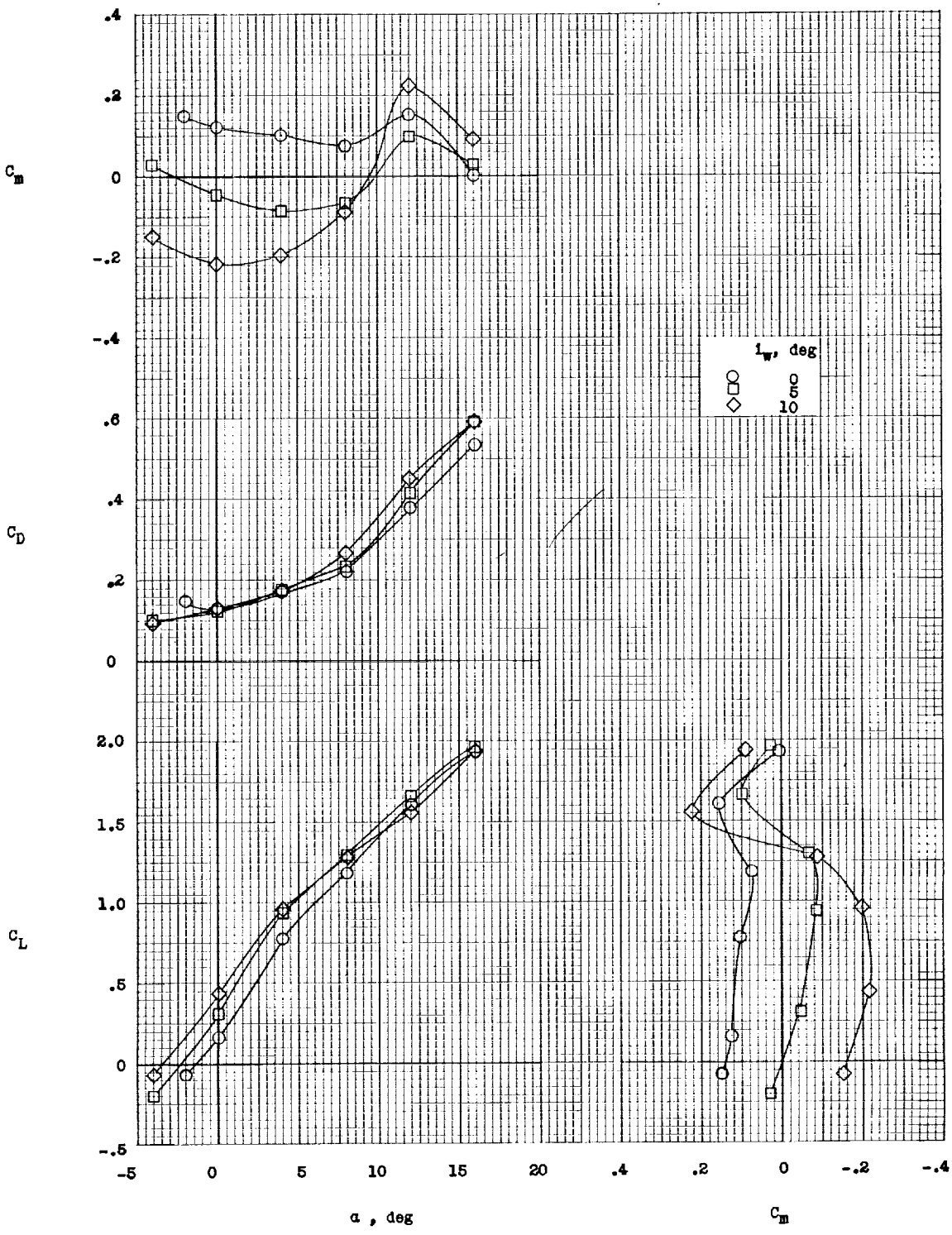

Figure 20.- Longitudinal stability and trim characteristics of IB-LO configuration. $i_{d,F} = 2.5^o$; q = 5.0; gaps sealed; ducts clean.

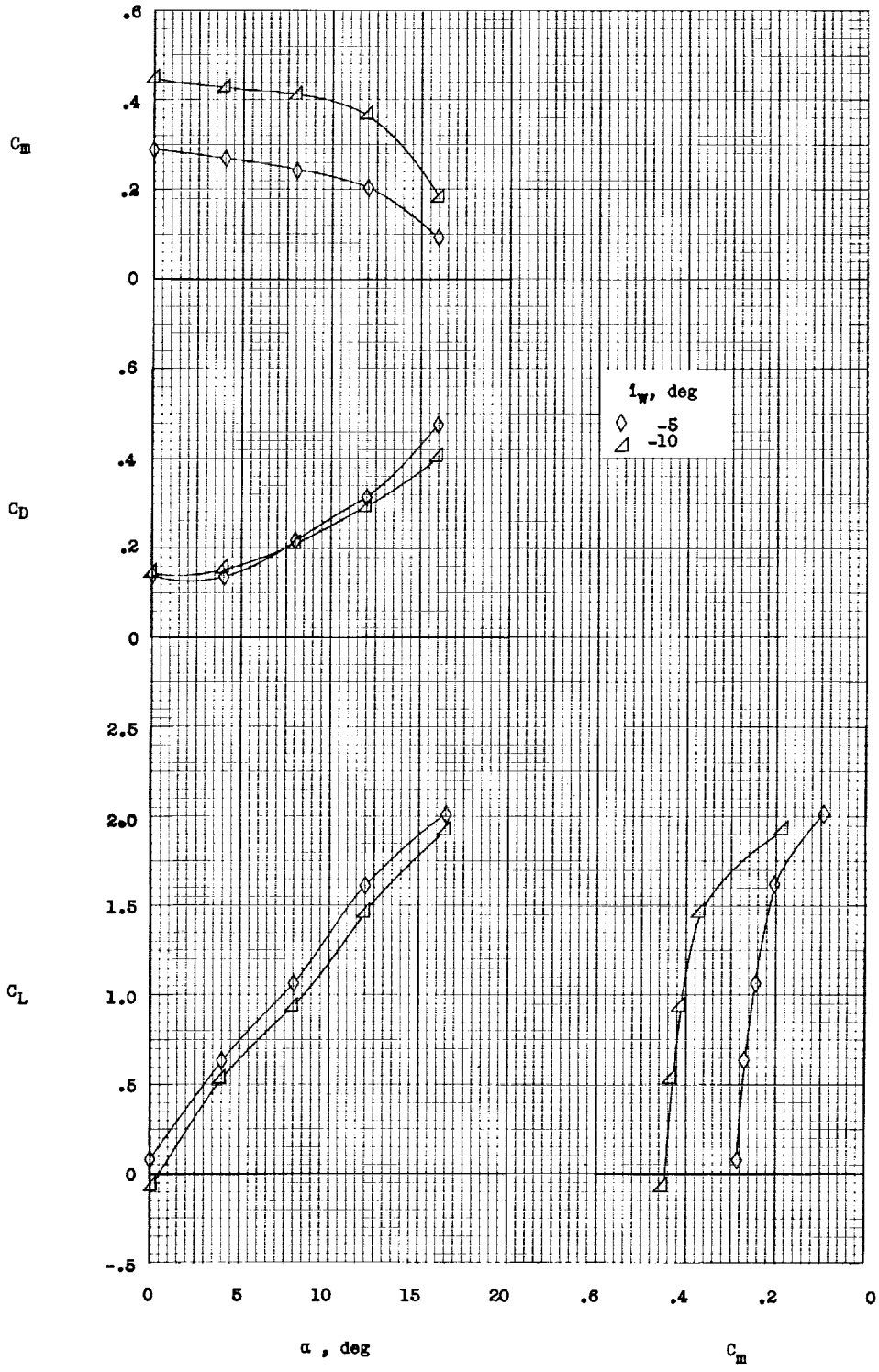

Figure 20.- Concluded.

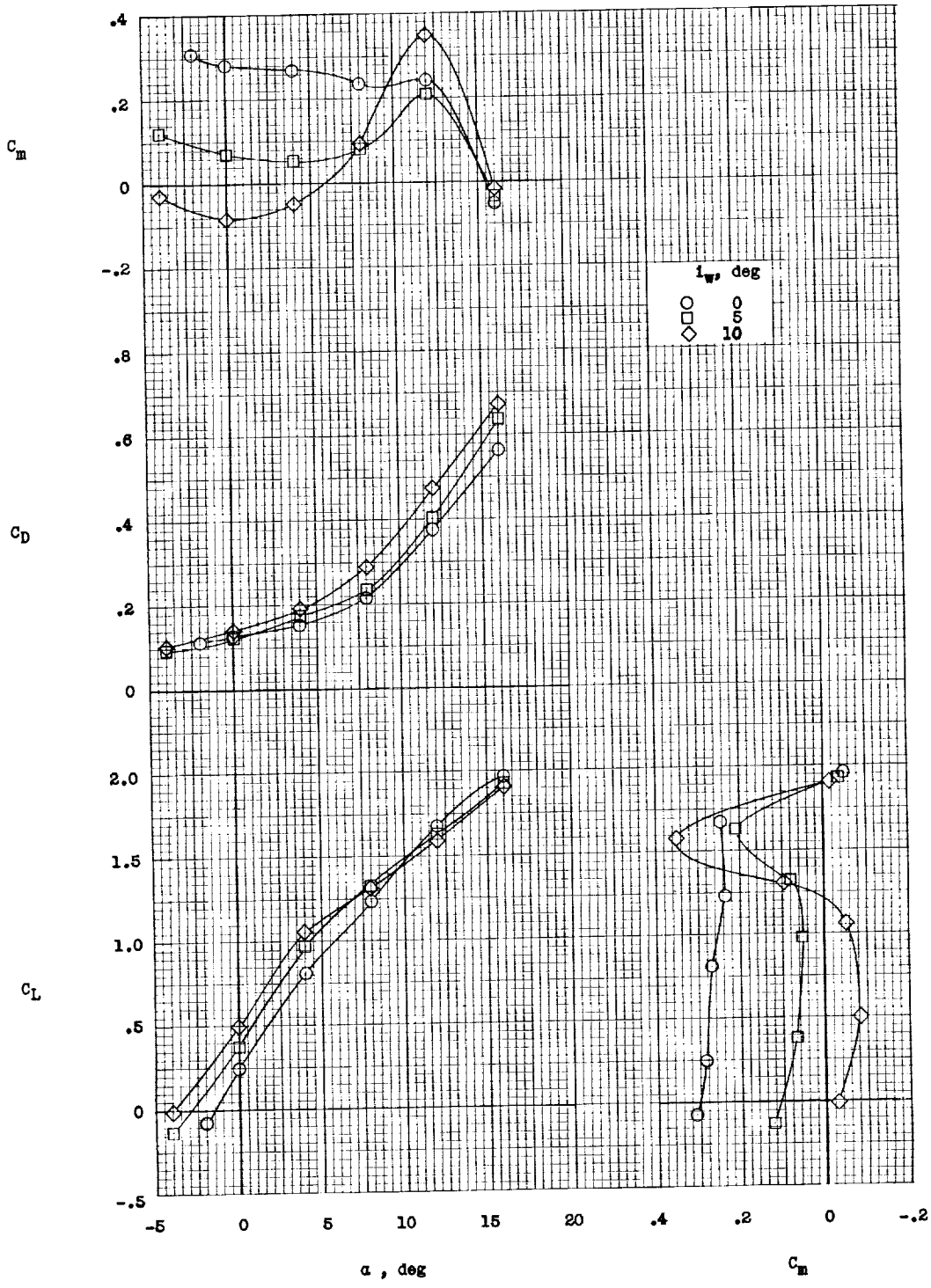

Figure 21.- Longitudinal stability and trim characteristics of IB-LO configuration. $i_{d,F} = 5^{\circ}$; q = 5.0; gaps sealed; ducts clean.

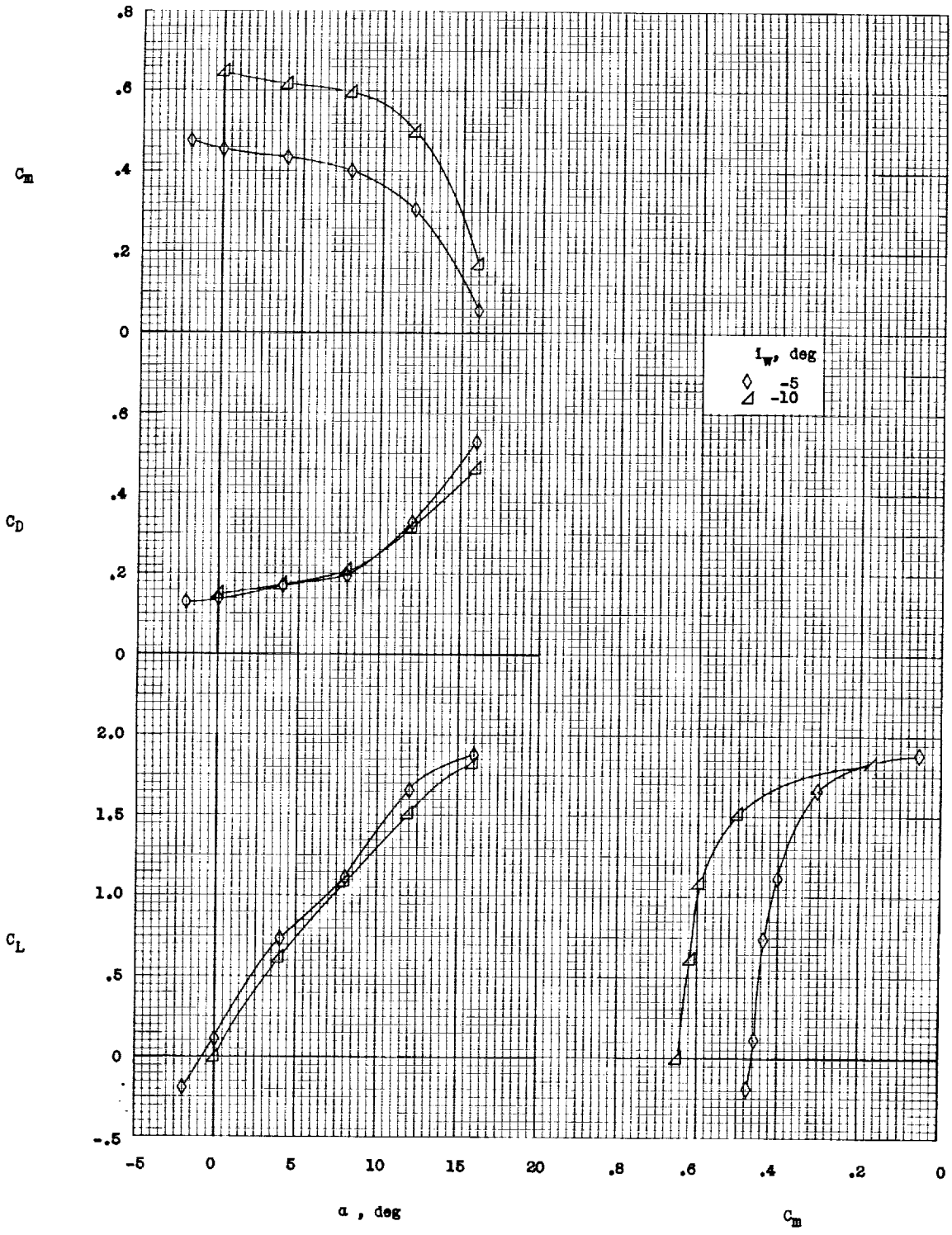

Figure 21.- Concluded.

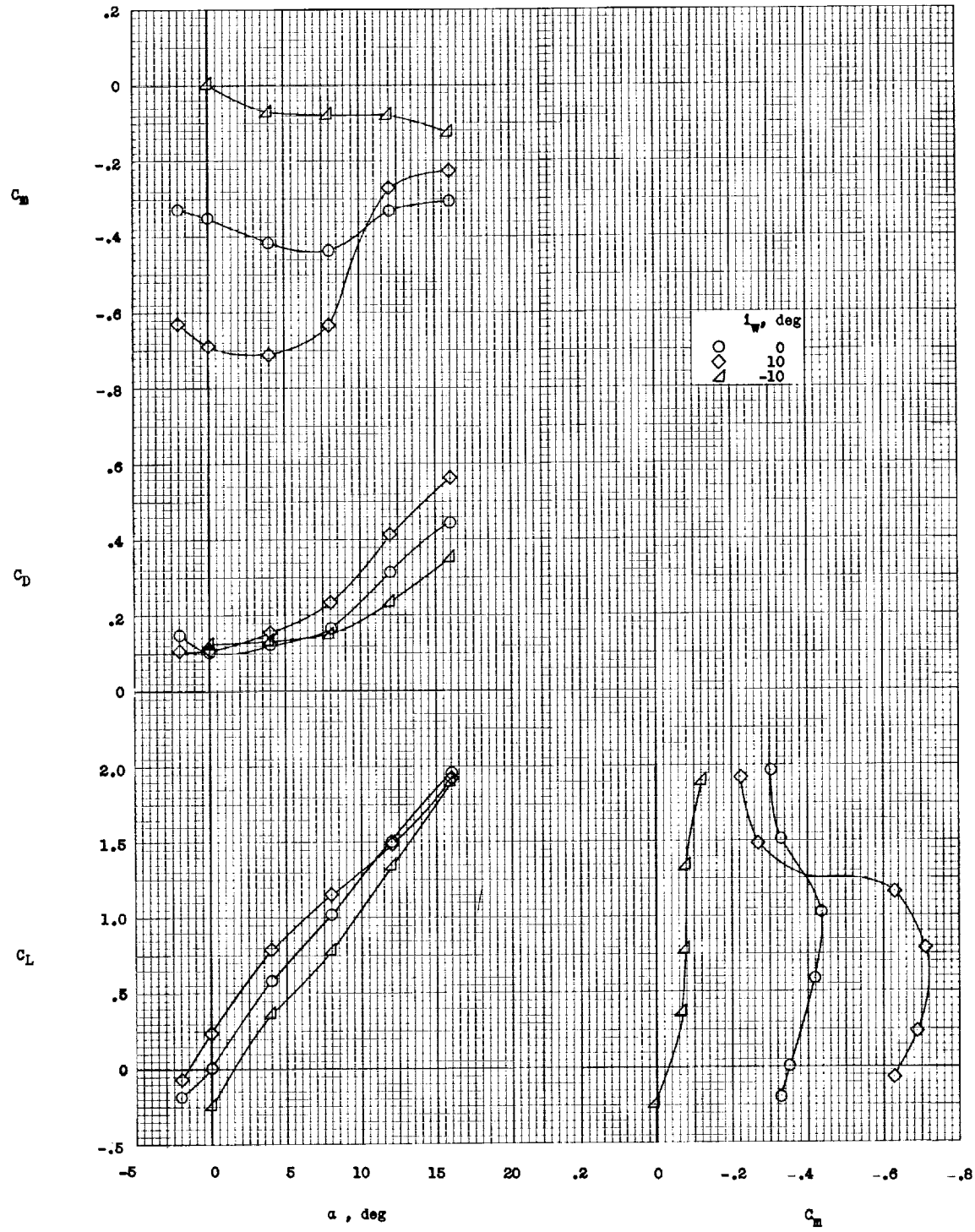

Figure 22.- Longitudinal stability and trim characteristics of IB-LO configuration. $i_{d,F} = -2.5^{o}$; $q = 5.0$; gaps sealed; ducts clean.

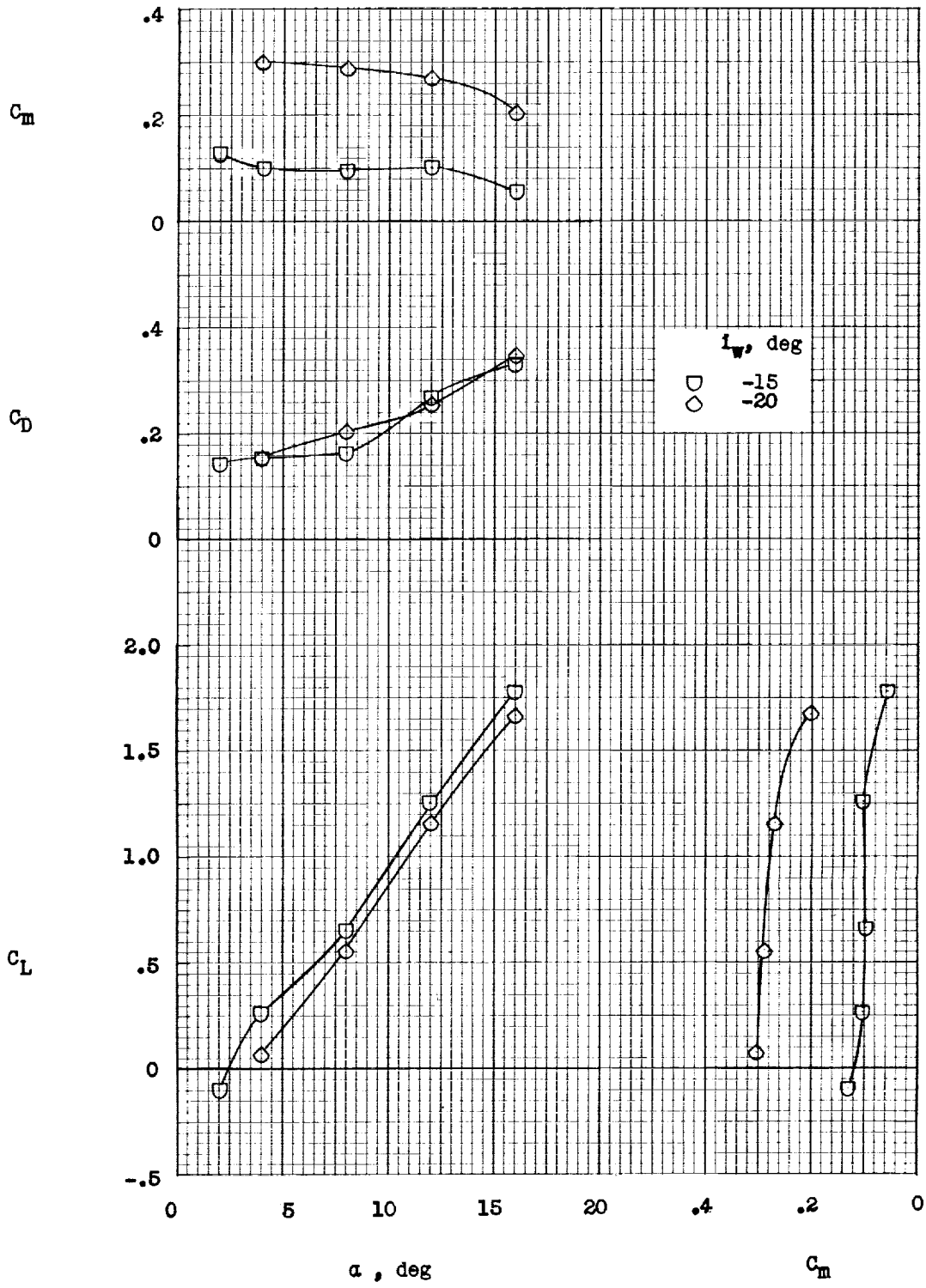

Figure 22.- Concluded.

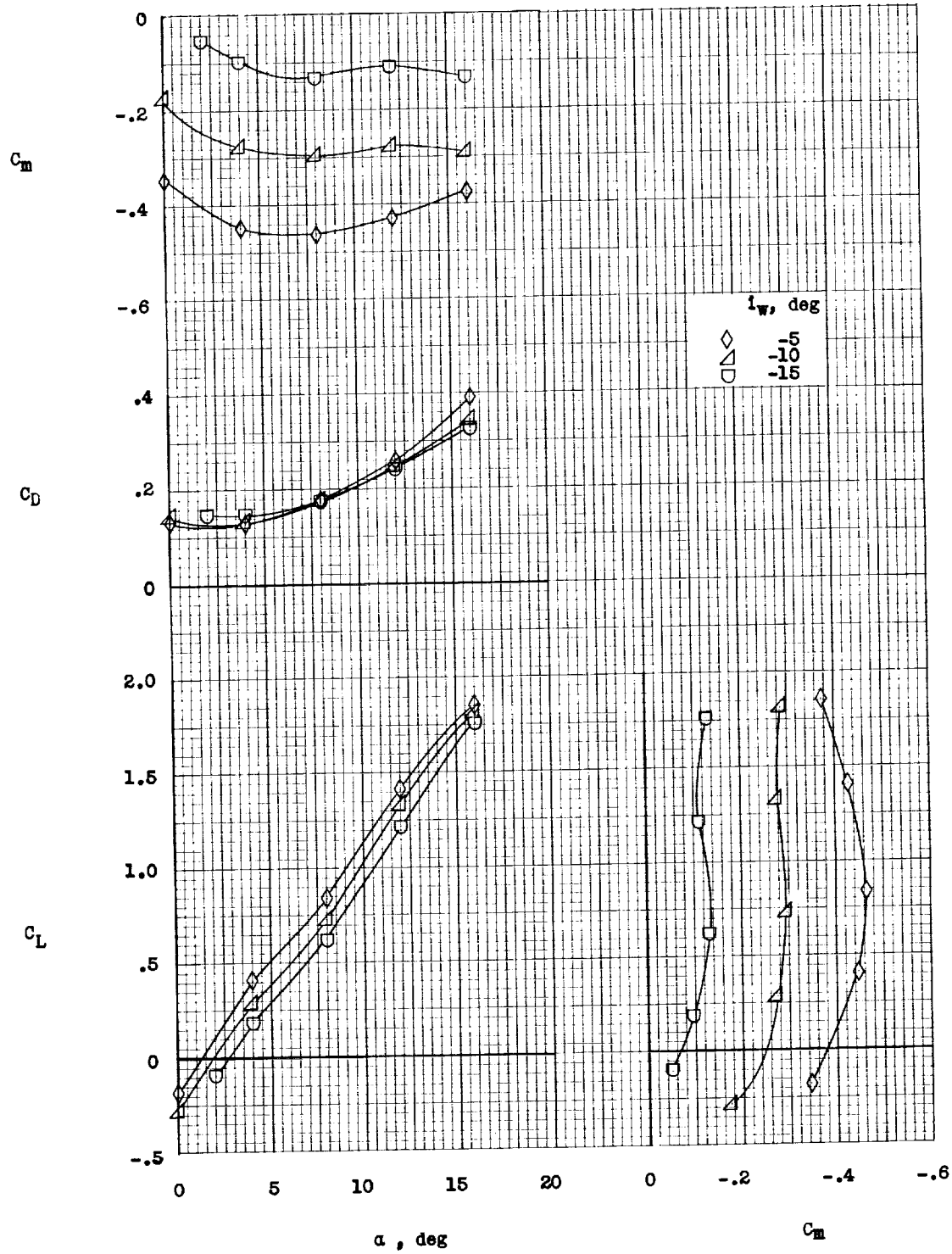

Figure 23.- Longitudinal stability and trim characteristics of IB-LO configuration. $i_{d,F} = -5^{o}$; $q = 5.0$; gaps sealed; ducts clean.

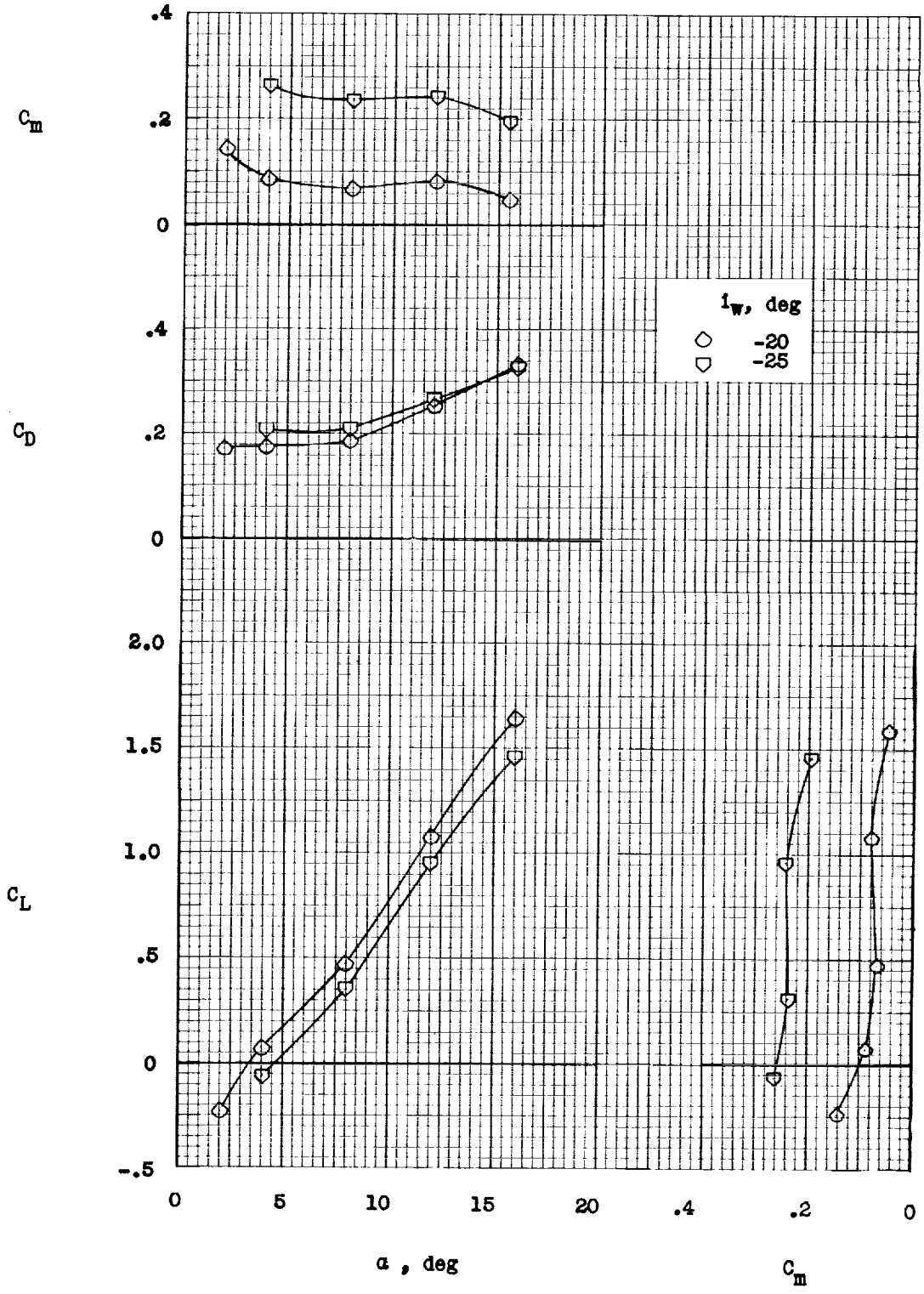

Figure 23.- Concluded.

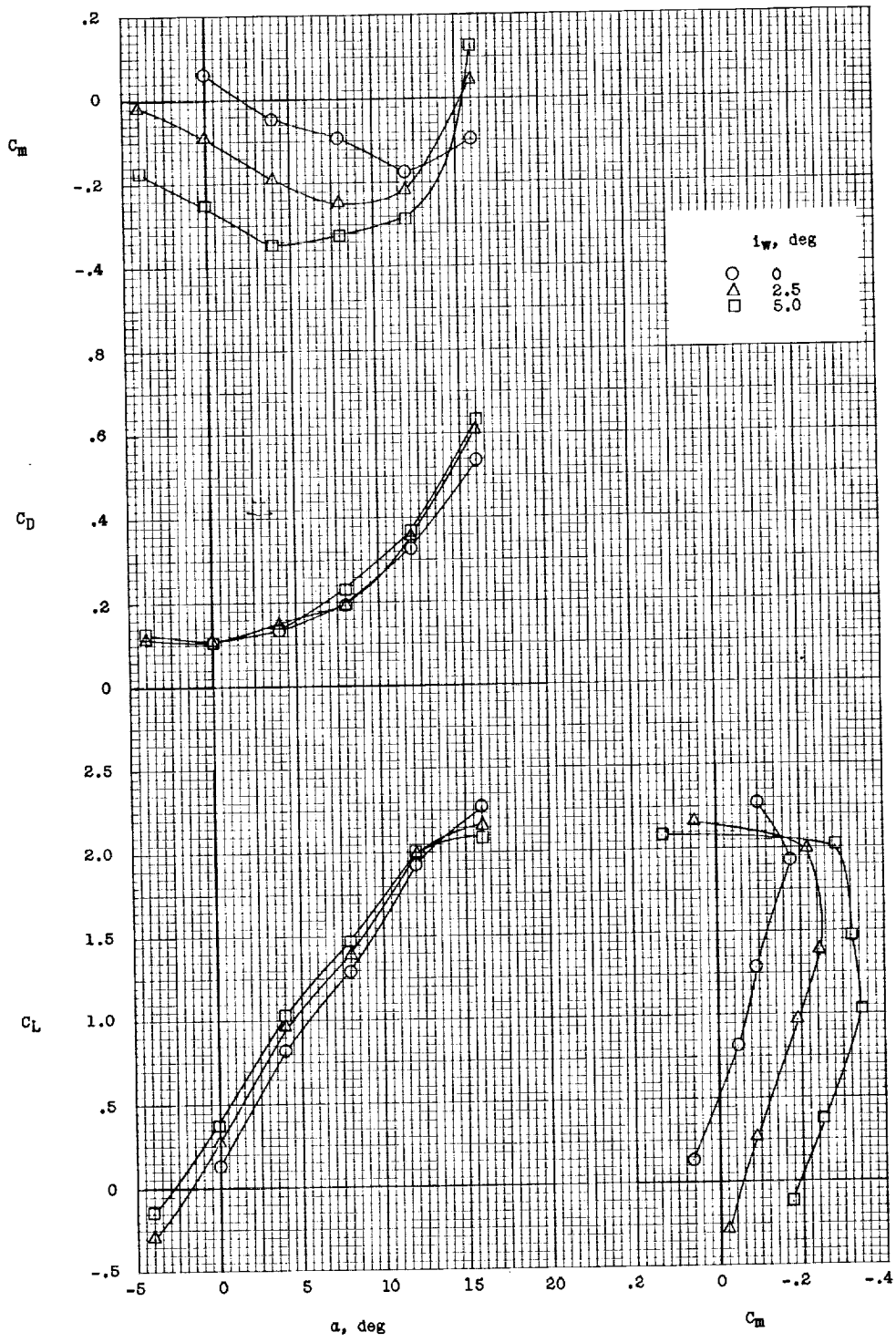

Figure 24.- Longitudinal stability and trim characteristics of OB-HI configuration. $i_{d,F} = 0^o$; q = 5.0; gaps sealed; ducts clean.

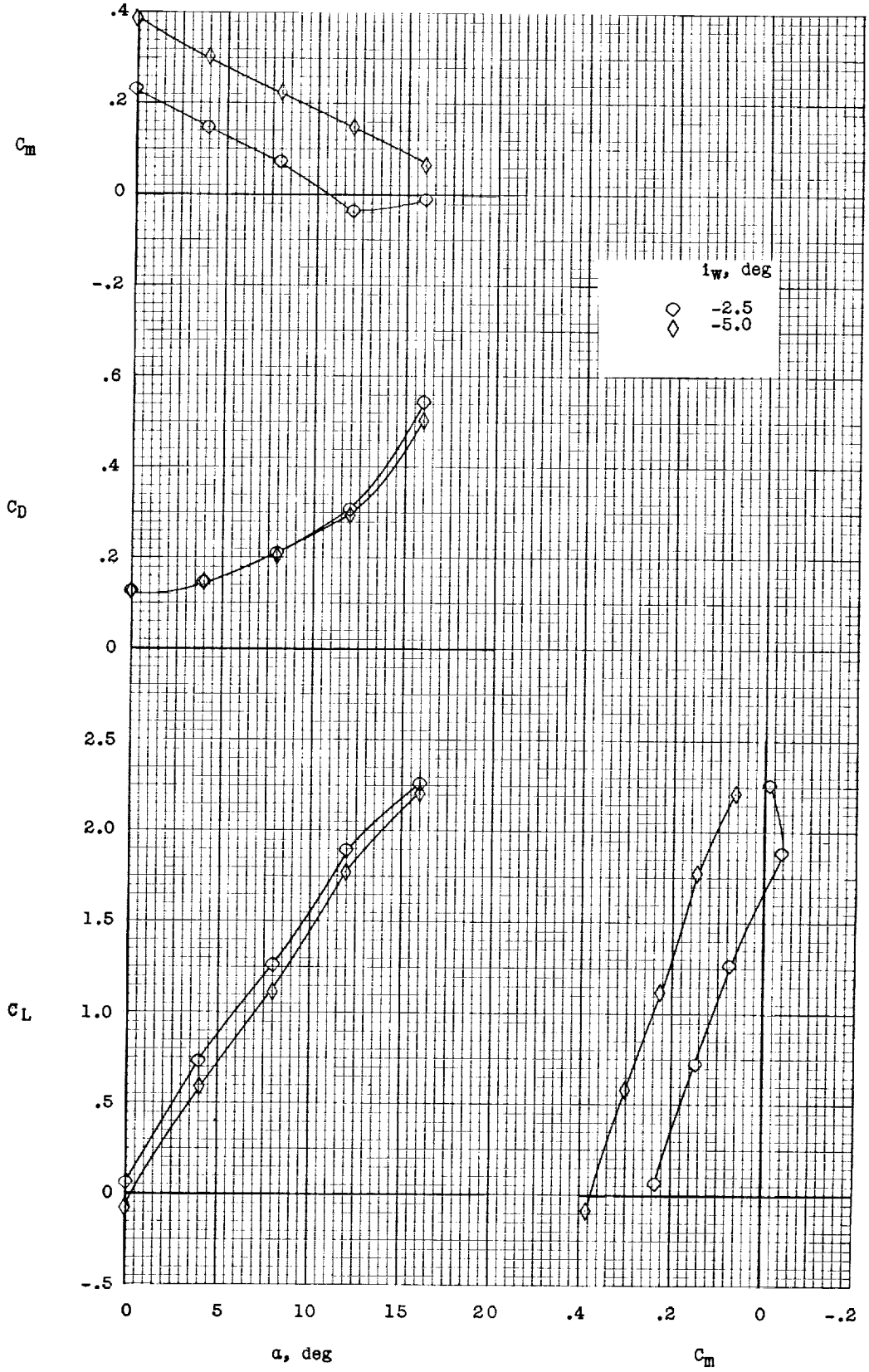

Figure 24.- Concluded.

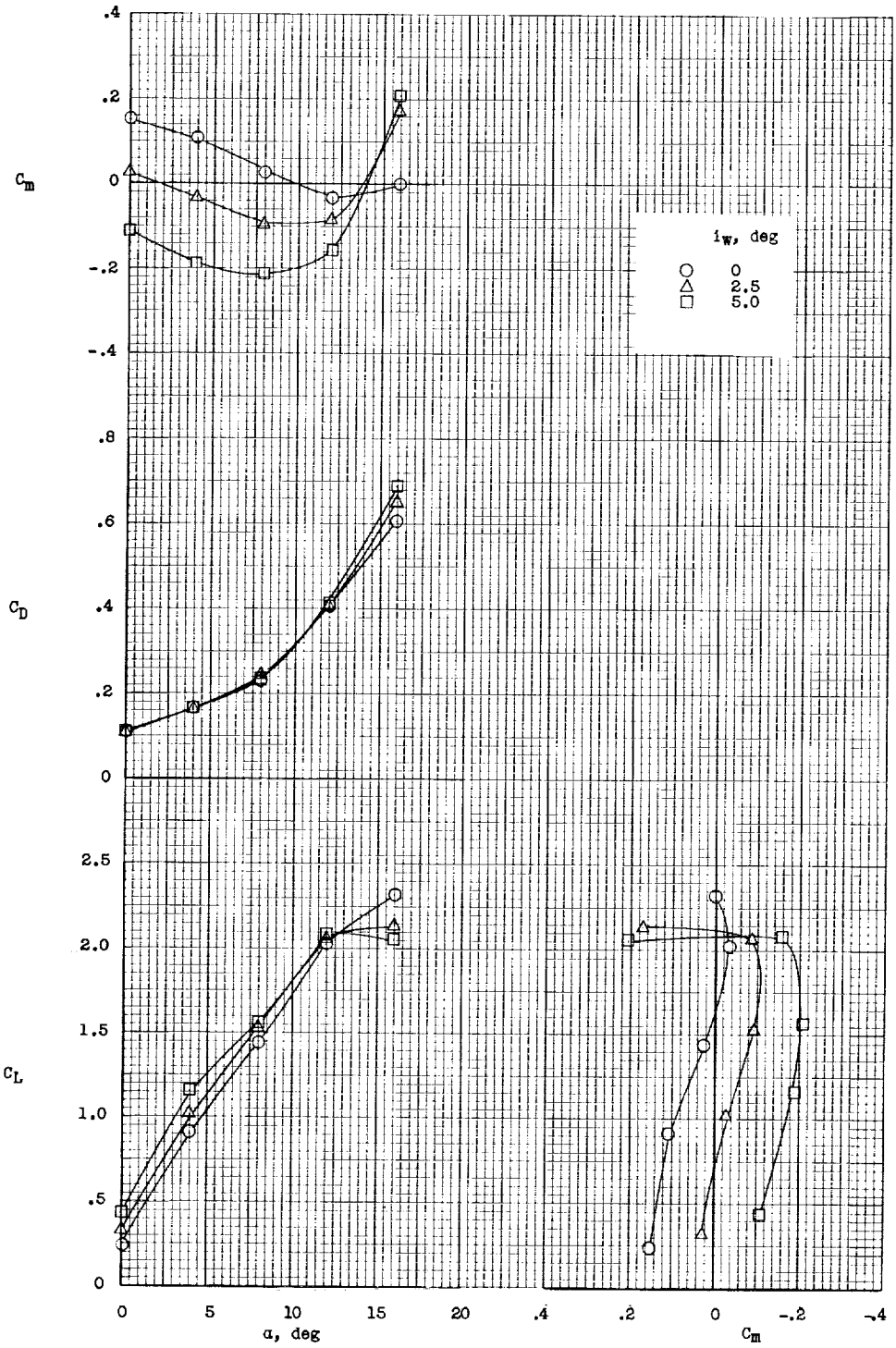

Figure 25.- Longitudinal stability and trim characteristics of OB-HI configuration. $i_{d,F} = 2.5°$; $q = 5.0$; gaps sealed; ducts clean.

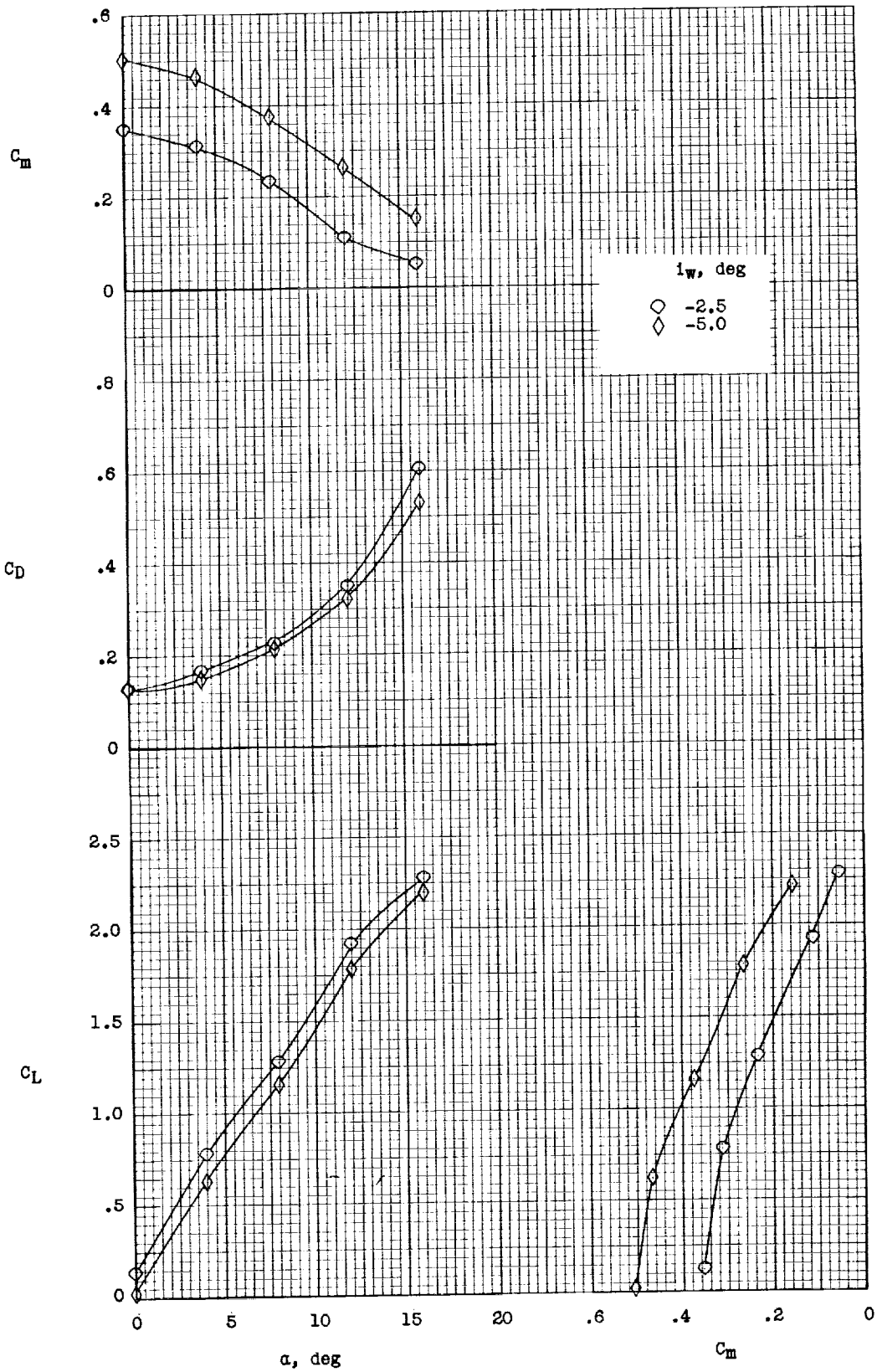

Figure 25.- Concluded.

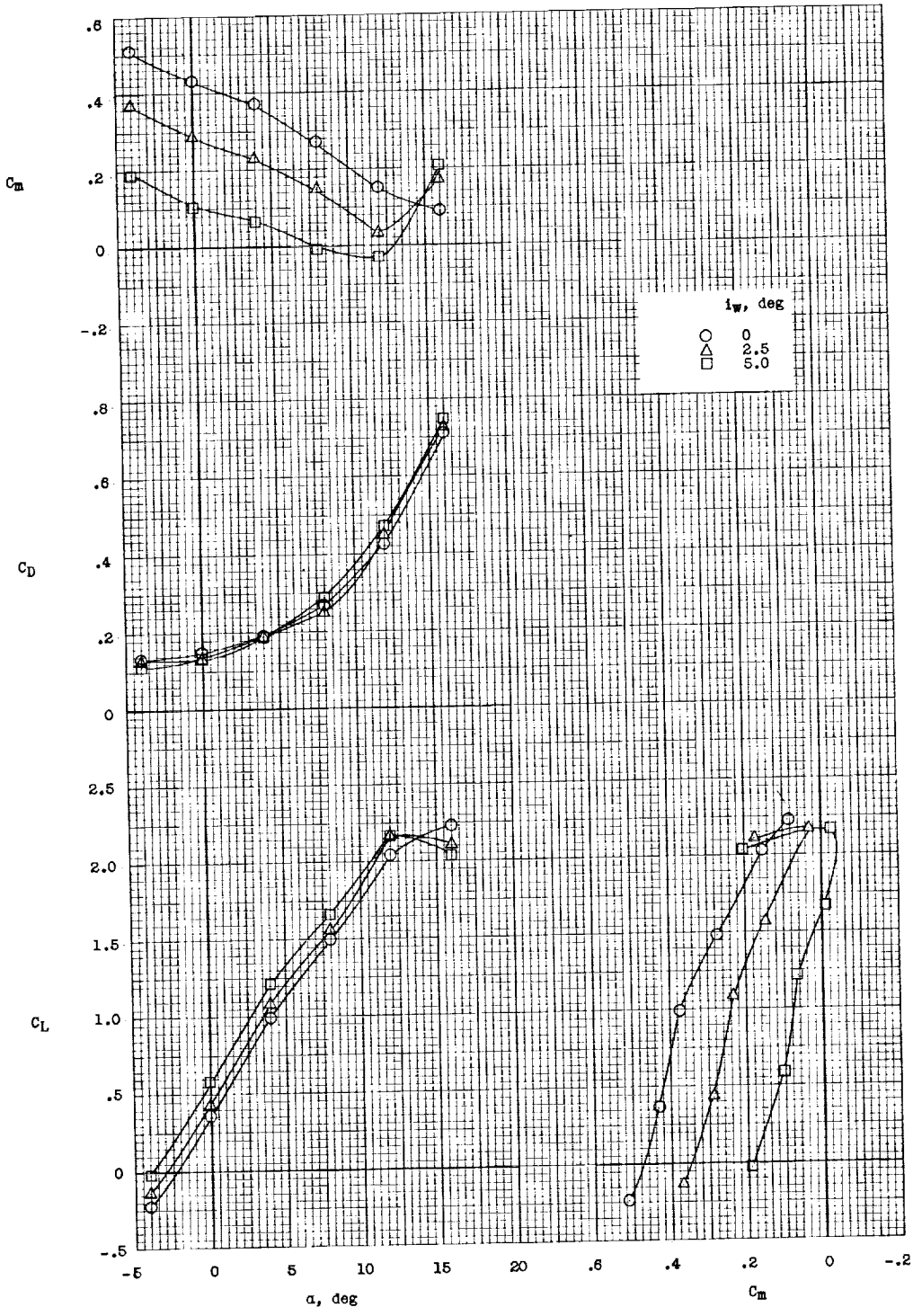

Figure 26.- Longitudinal stability and trim characteristics of OB-HI configuration. $i_{d,F} = 5^o$; q = 5.0; gaps sealed; ducts clean.

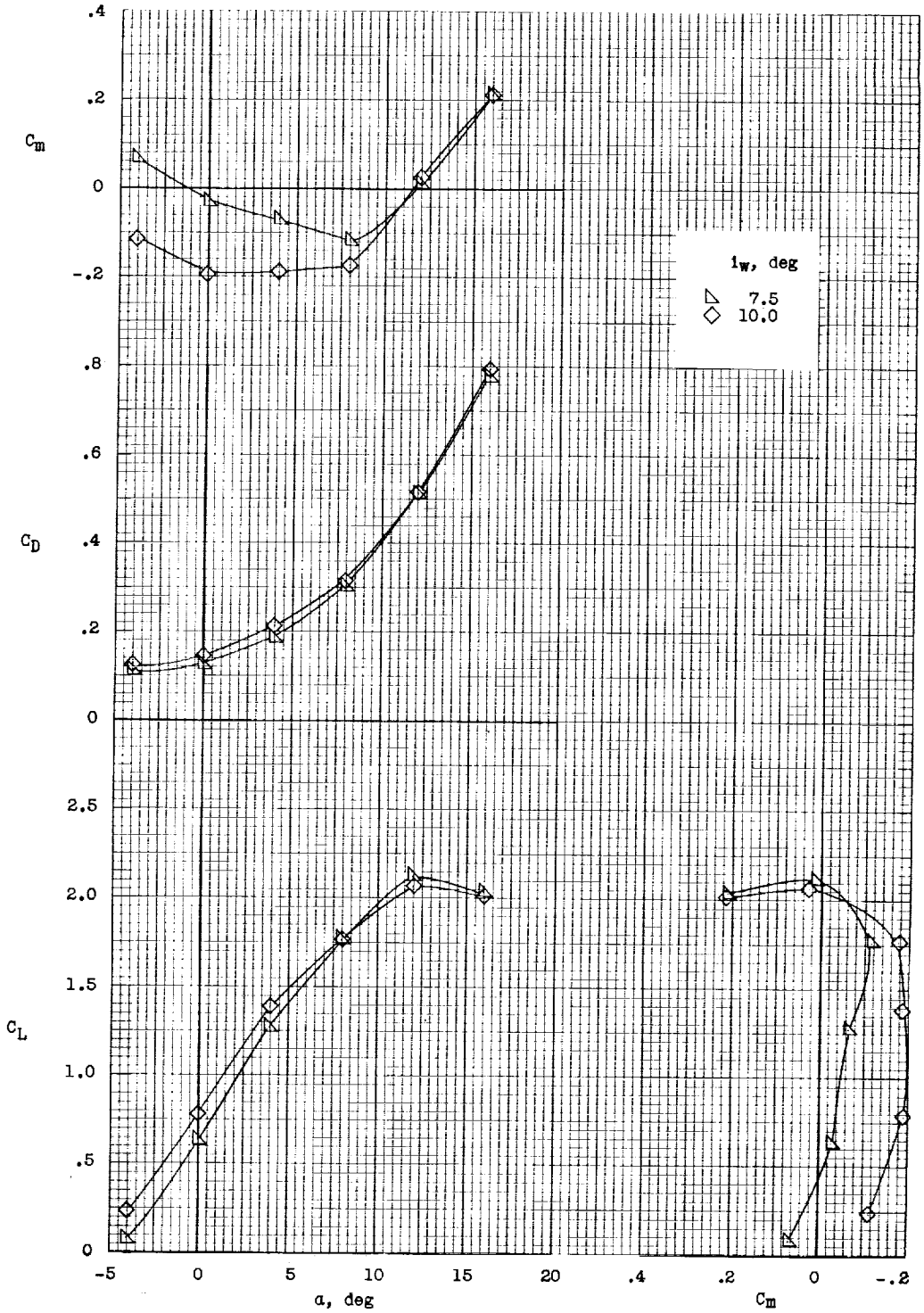

Figure 26.- Concluded.

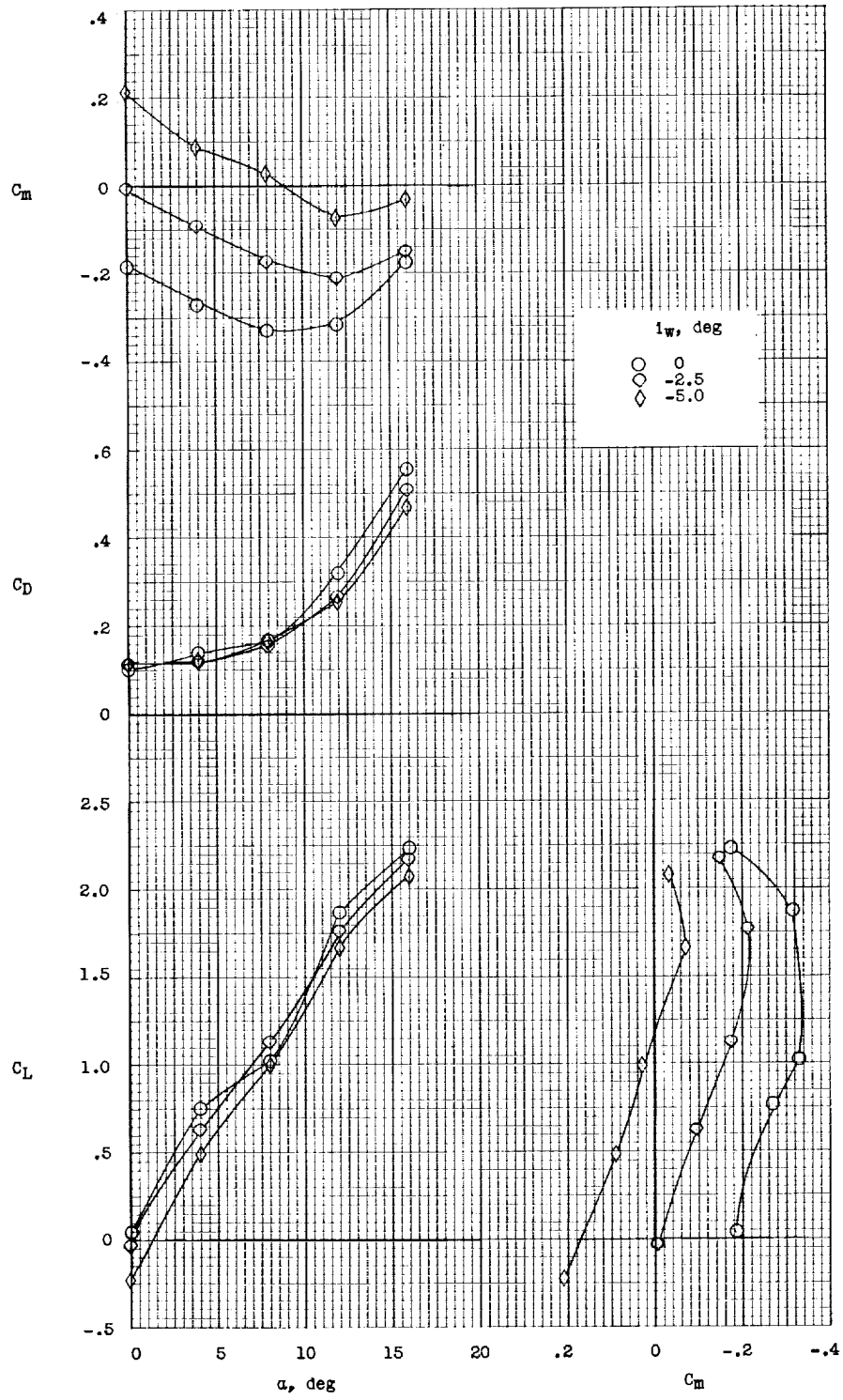

Figure 27.- Longitudinal stability and trim characteristics of OB-HI configuration. $i_{d,F}$ = -2.5°; q = 5.0; gaps sealed; ducts clean.

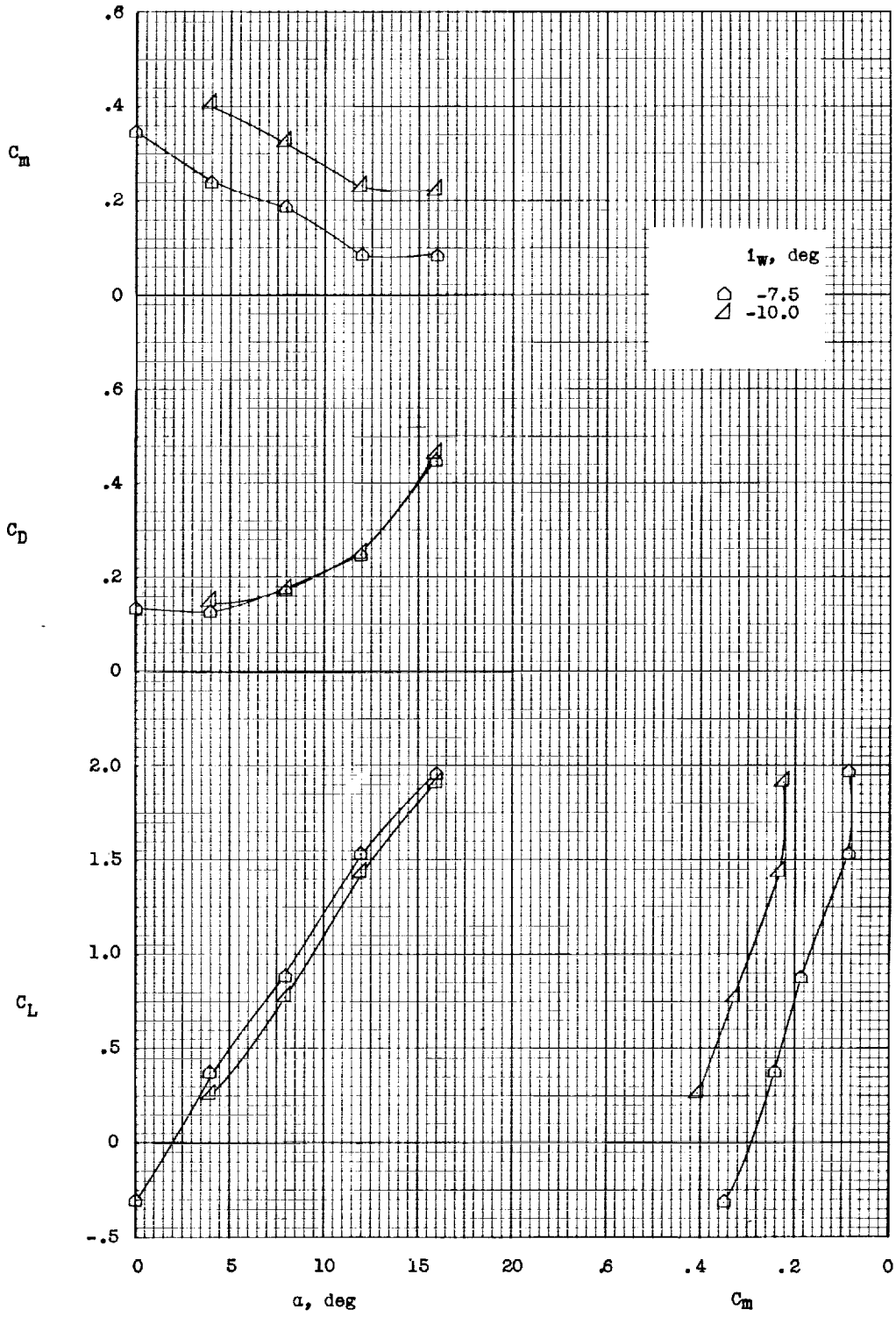

Figure 27.- Concluded.

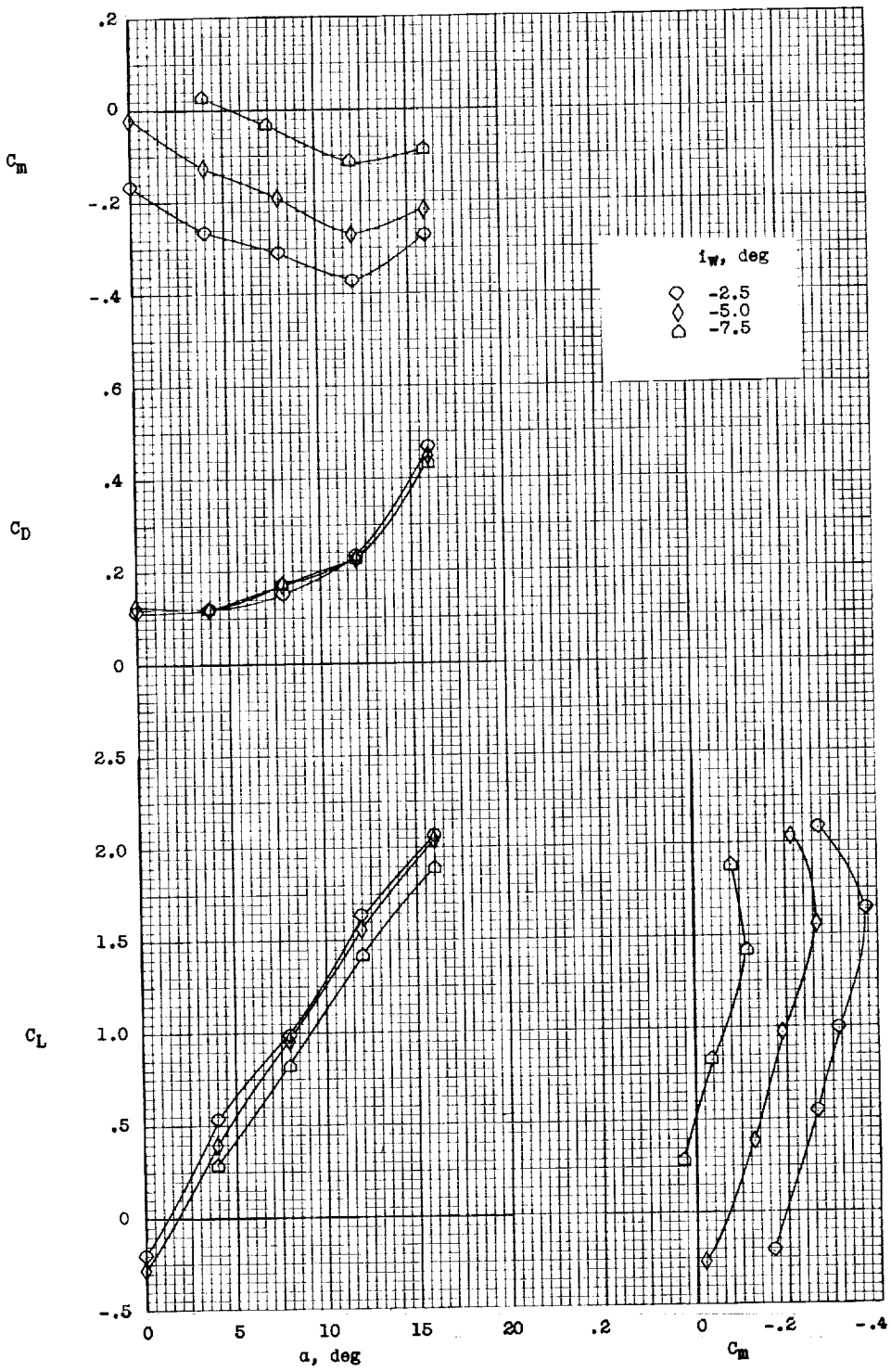

Figure 28.- Longitudinal stability and trim characteristics of OB-HI configuration. $i_{d,F} = -5^o$; $q = 5.0$; gaps sealed; ducts clean.

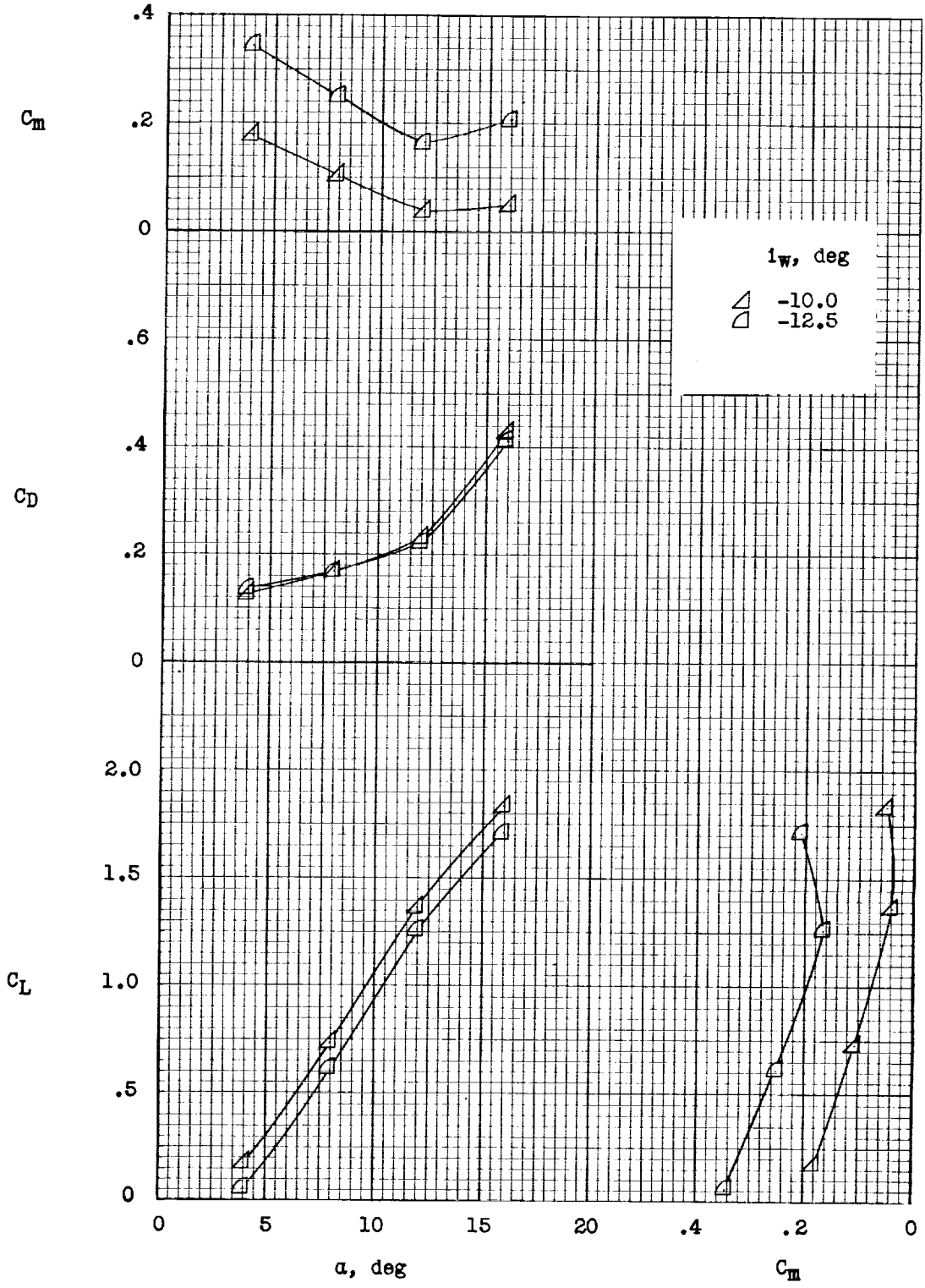

Figure 28.- Concluded.

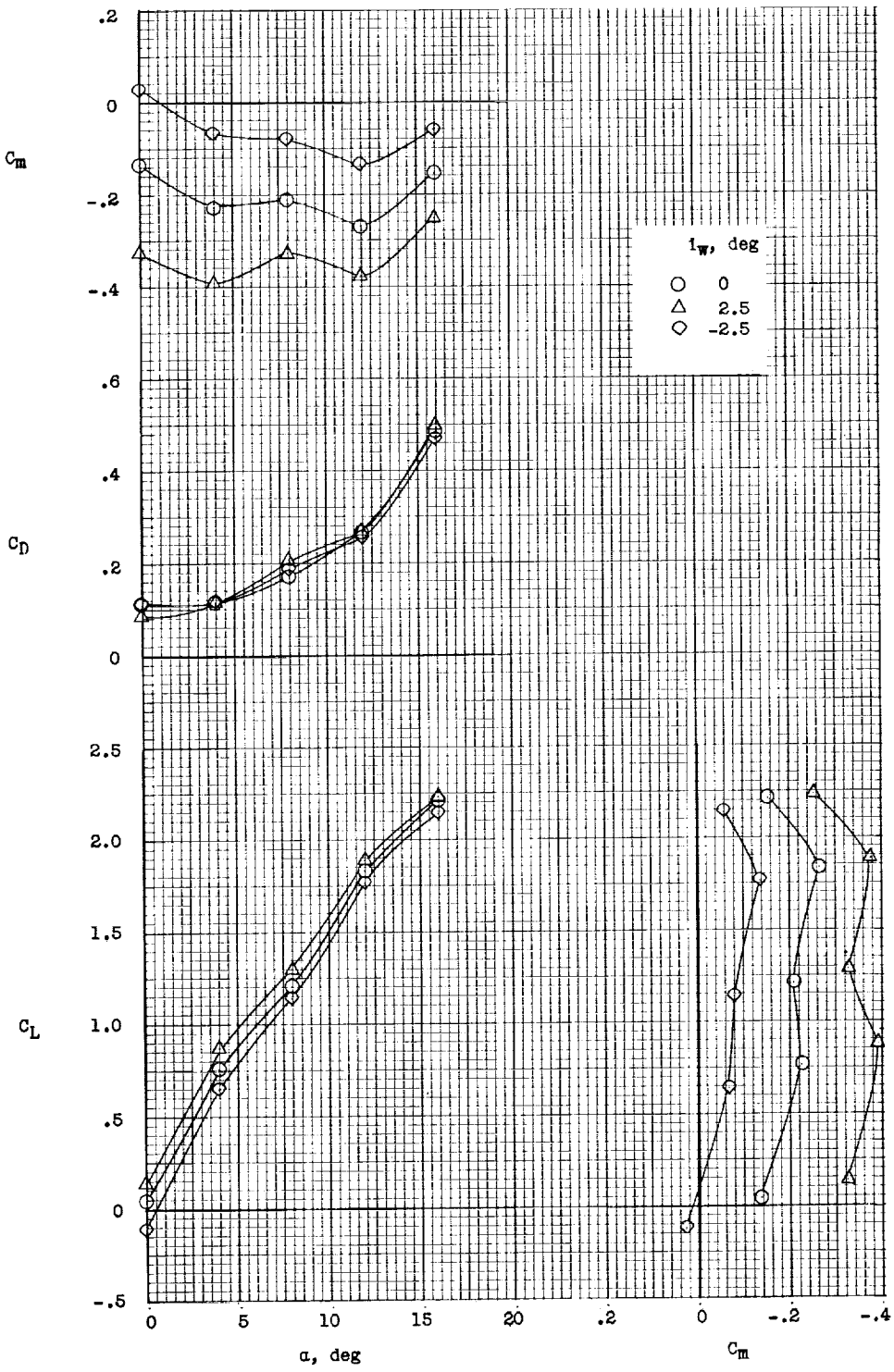

Figure 29.- Longitudinal stability and trim characteristics of OB-LO configuration. $i_{d,F} = 0°$; $q = 5.0$; gaps sealed; ducts clean.

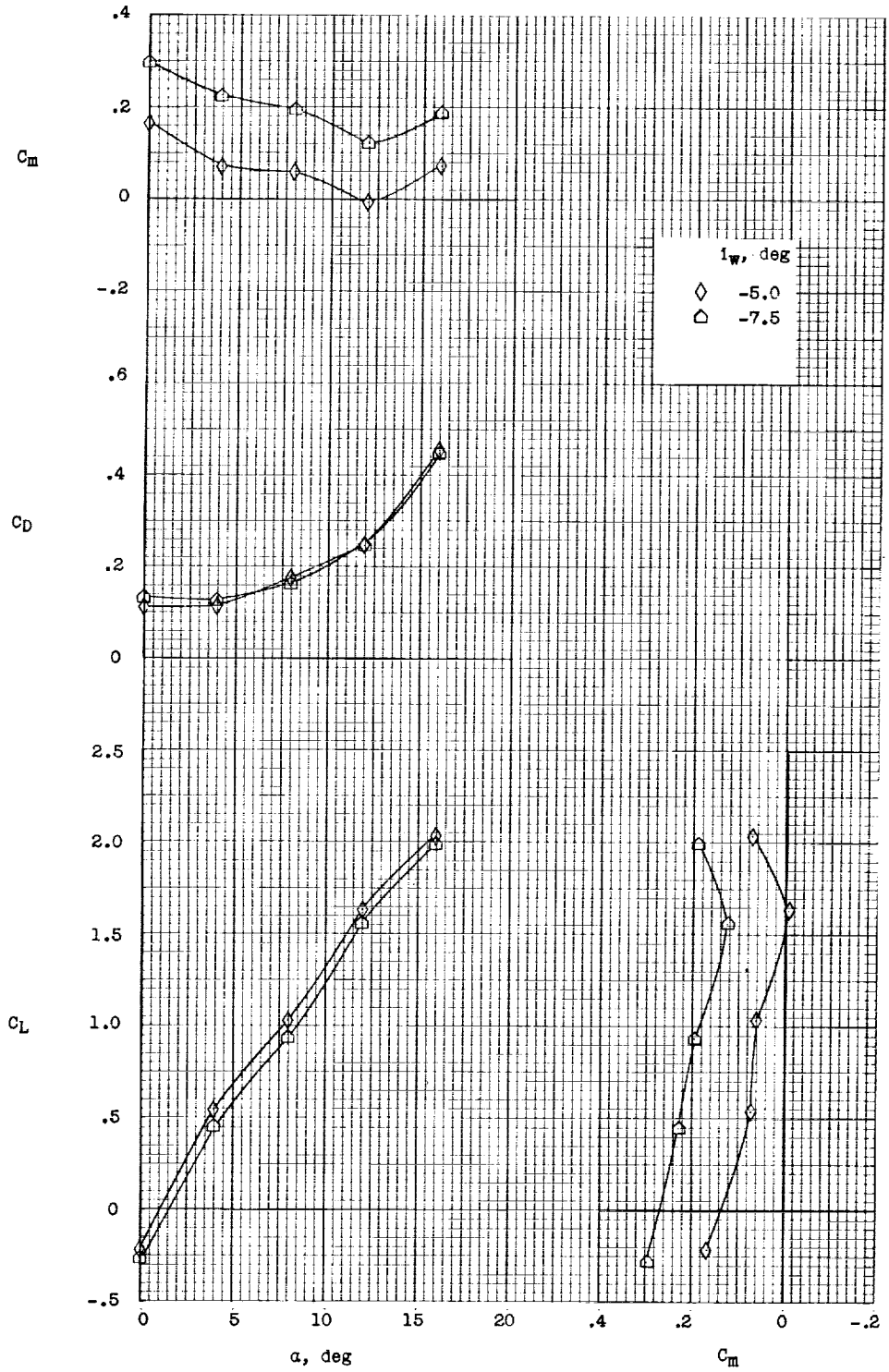

Figure 29.- Concluded.

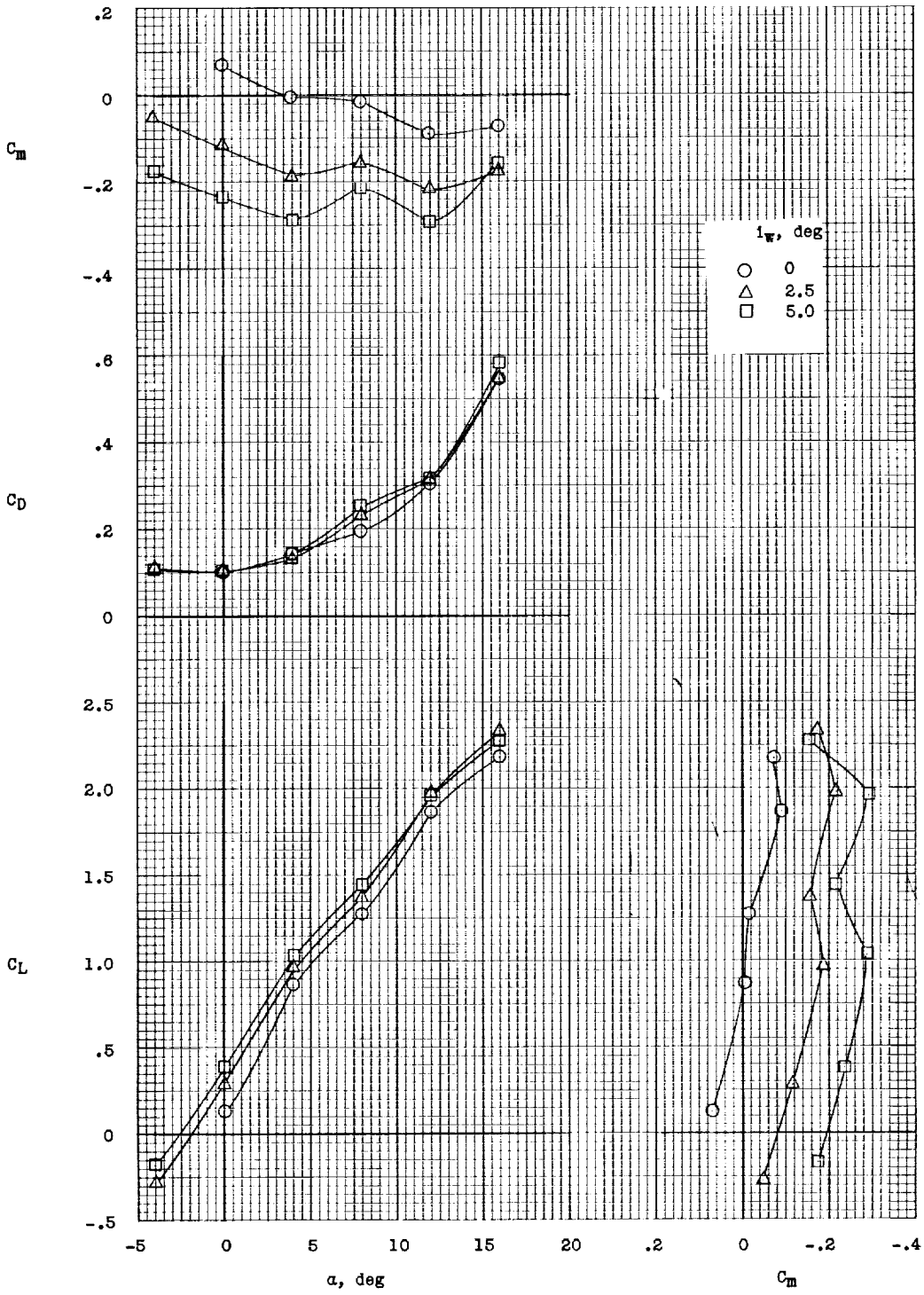

Figure 30.- Longitudinal stability and trim characteristics of OB-LO configuration. $i_{d,F} = 2.5^o$; q = 5.0; gaps sealed; ducts clean.

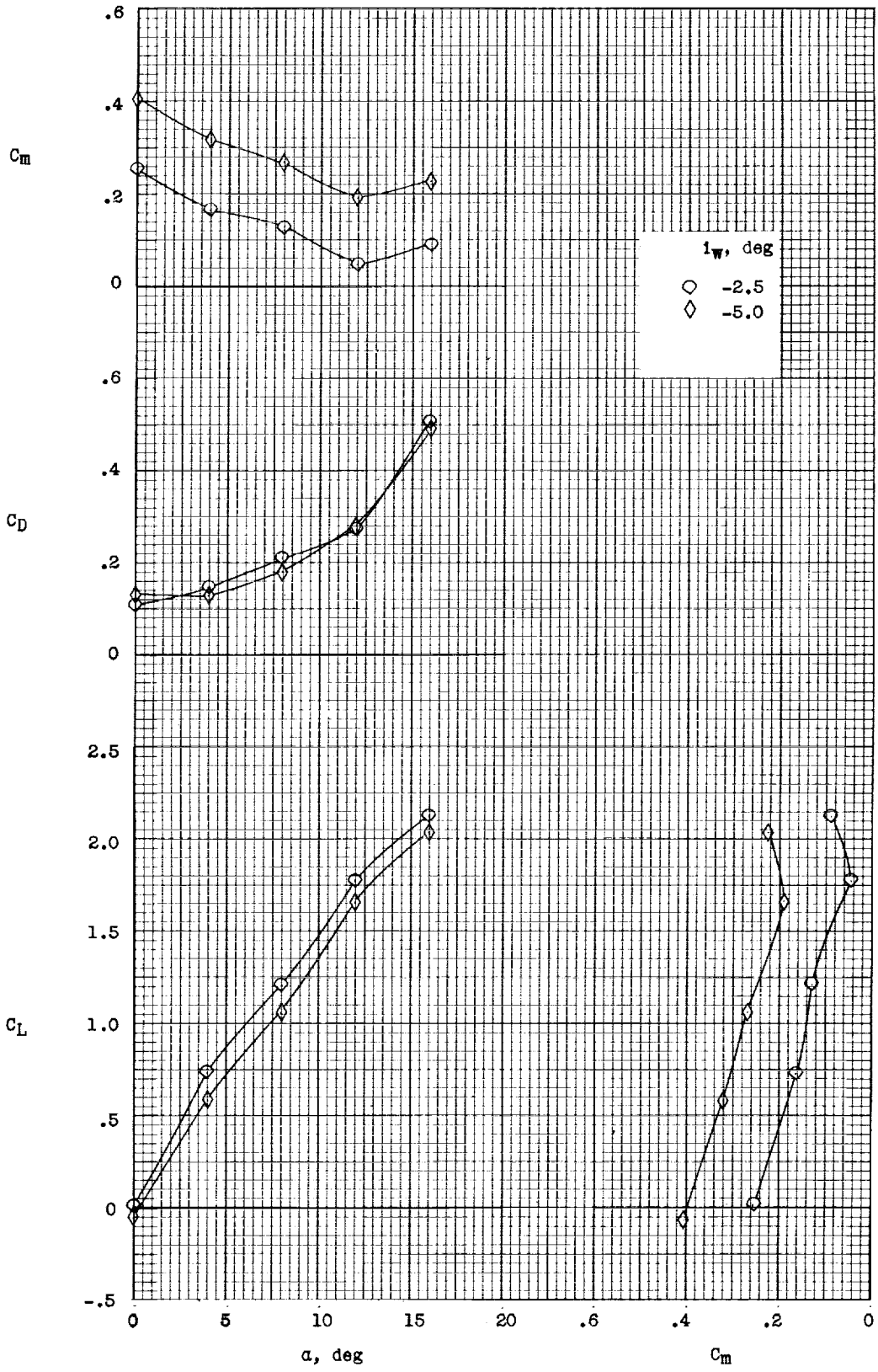

Figure 30.- Concluded.

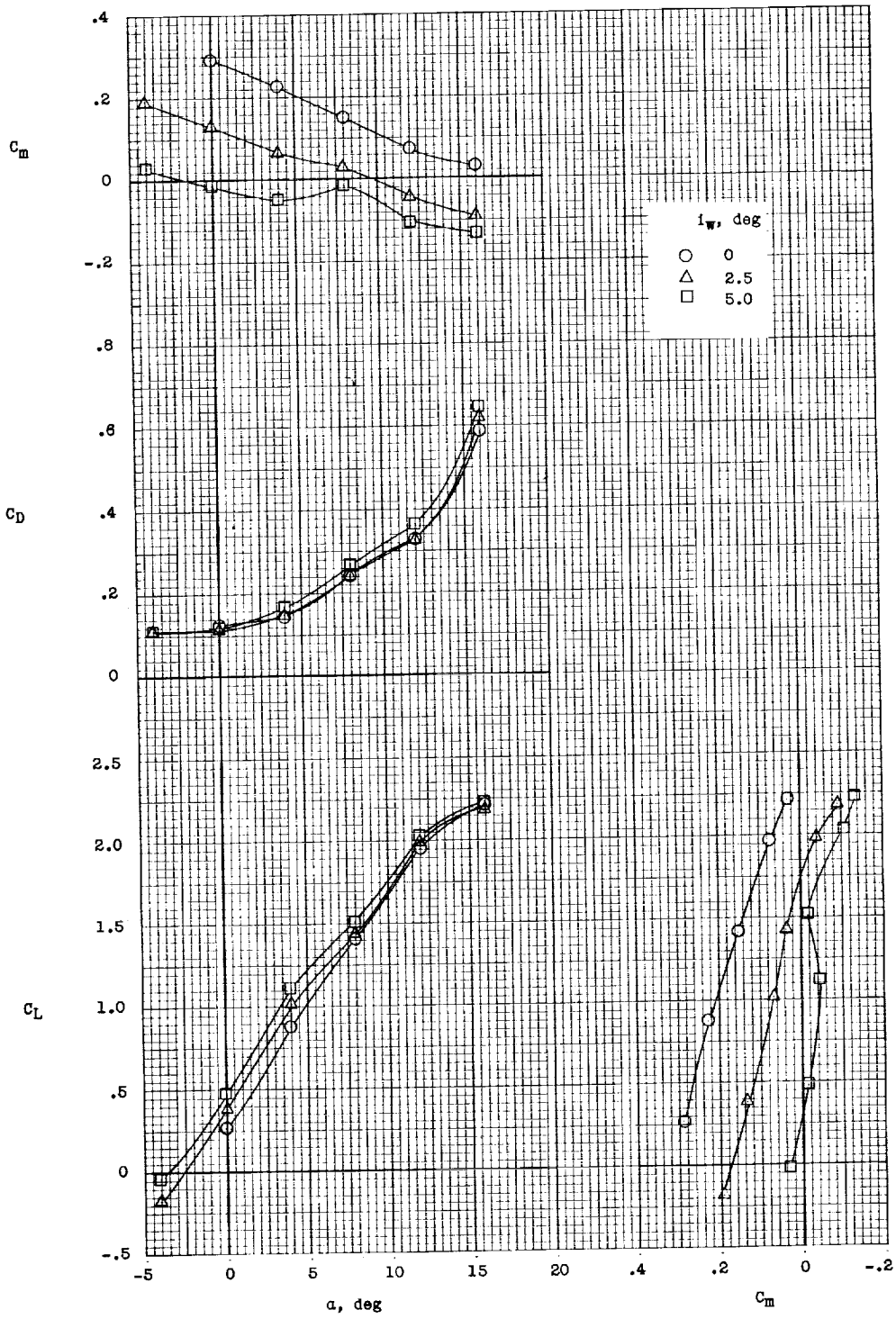

Figure 31.- Longitudinal stability and trim characteristics of OB-LO configuration. $i_{d,F} = 5^o$; $q = 5.0$; gaps sealed; ducts clean.

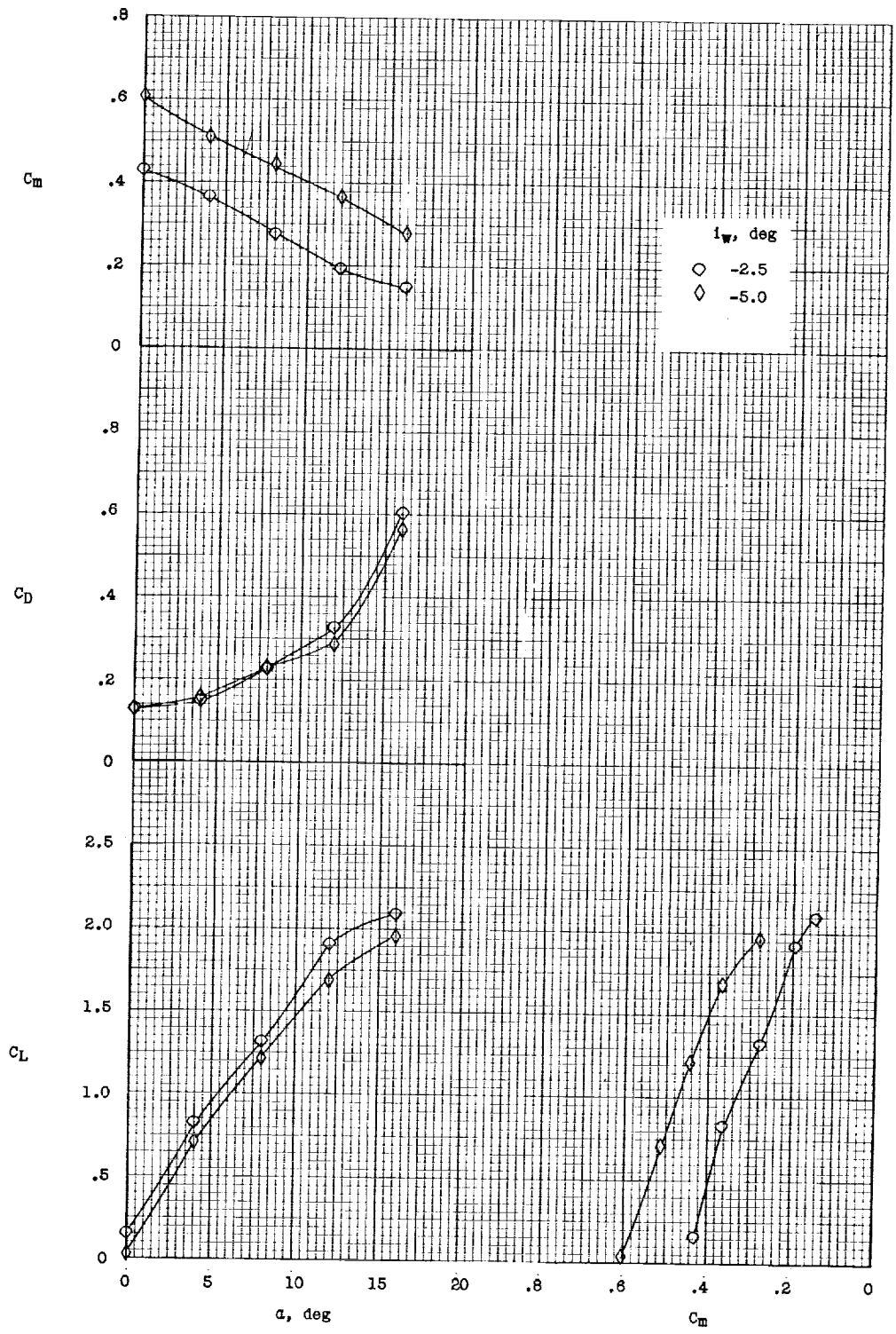

Figure 31.- Concluded.

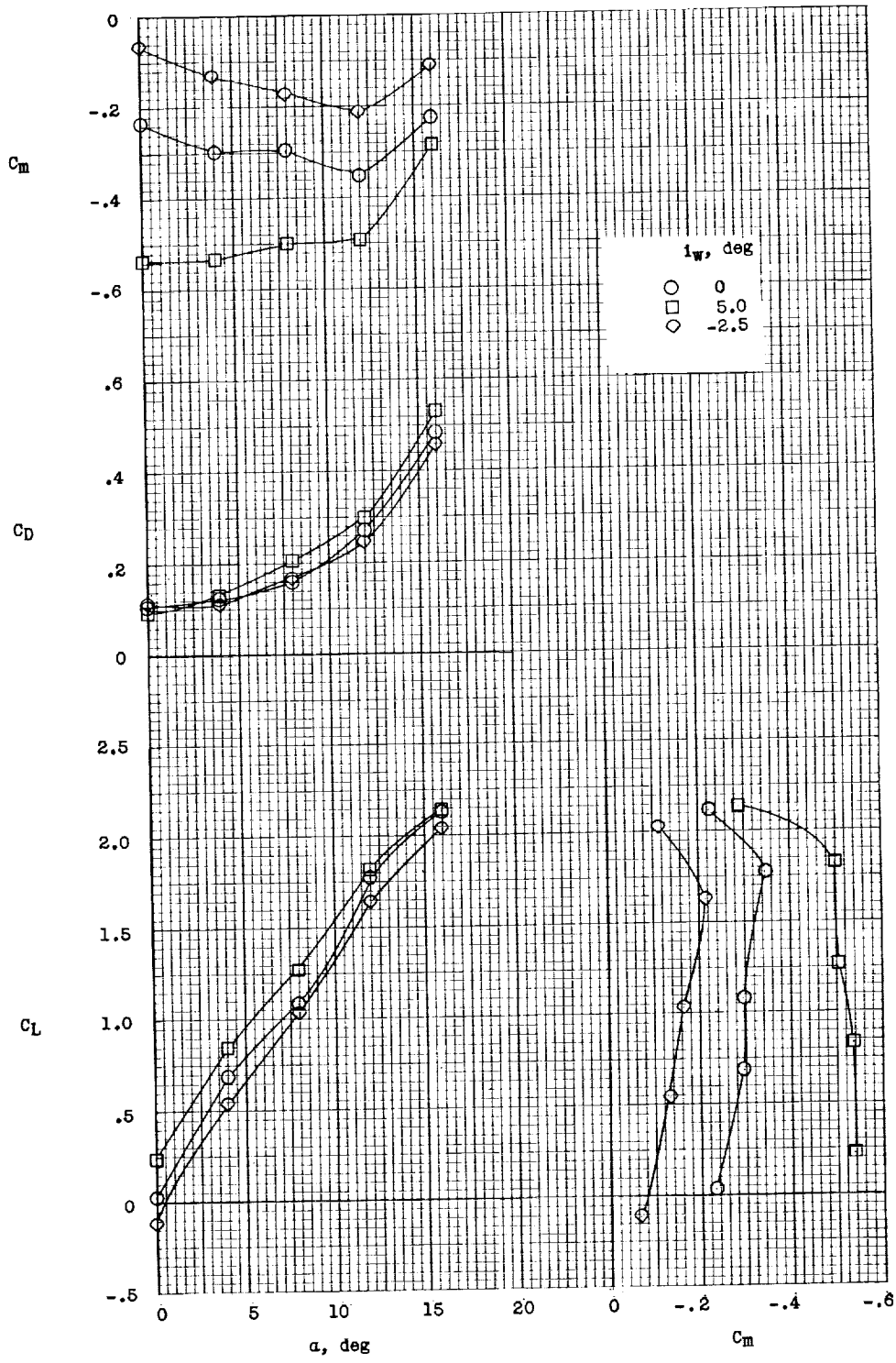

Figure 32.- Longitudinal stability and trim characteristics of OB-LO configuration. $i_{d,F} = -2.5°$; $q = 5.0$; gaps sealed; ducts clean.

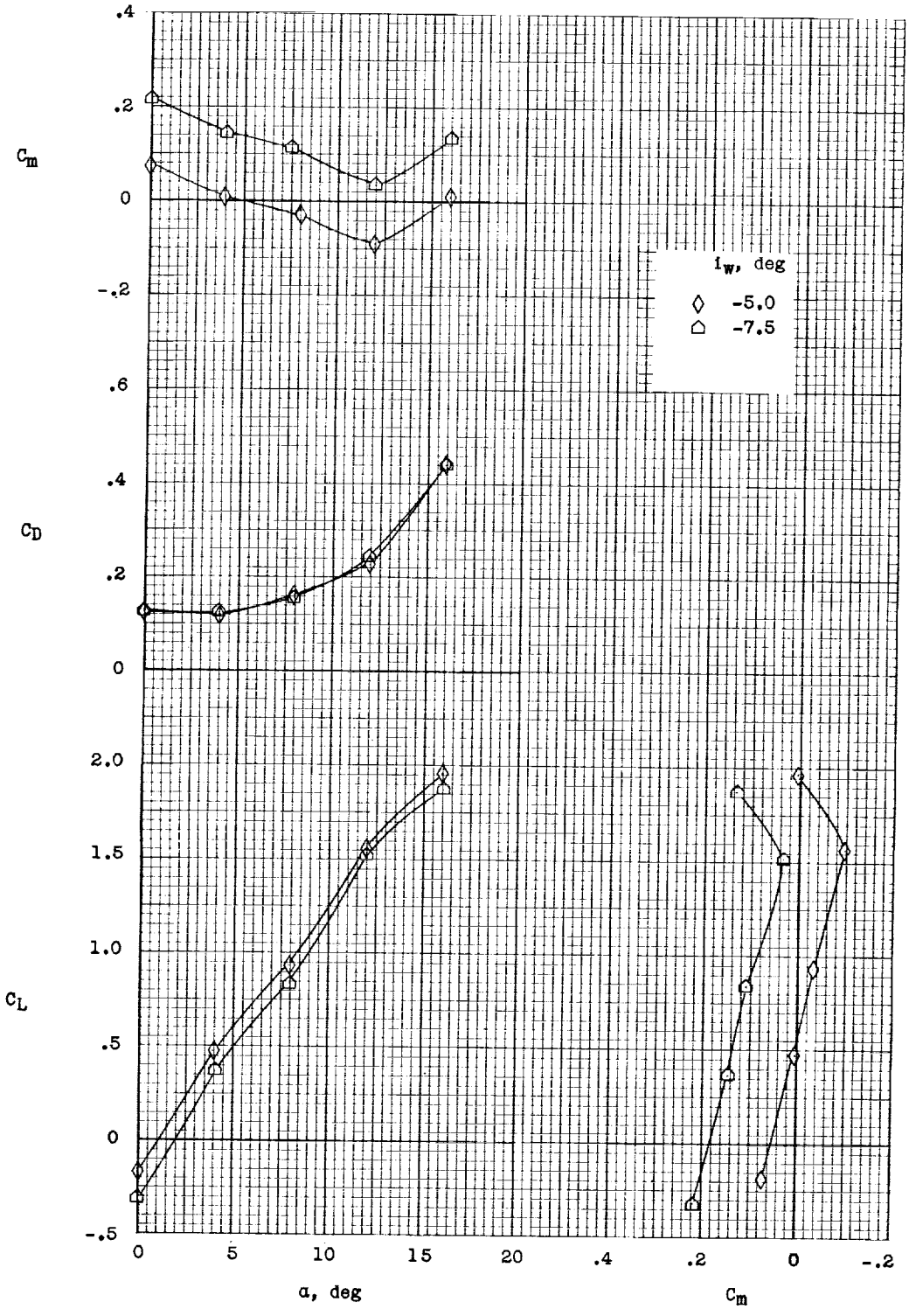

Figure 32.- Concluded.

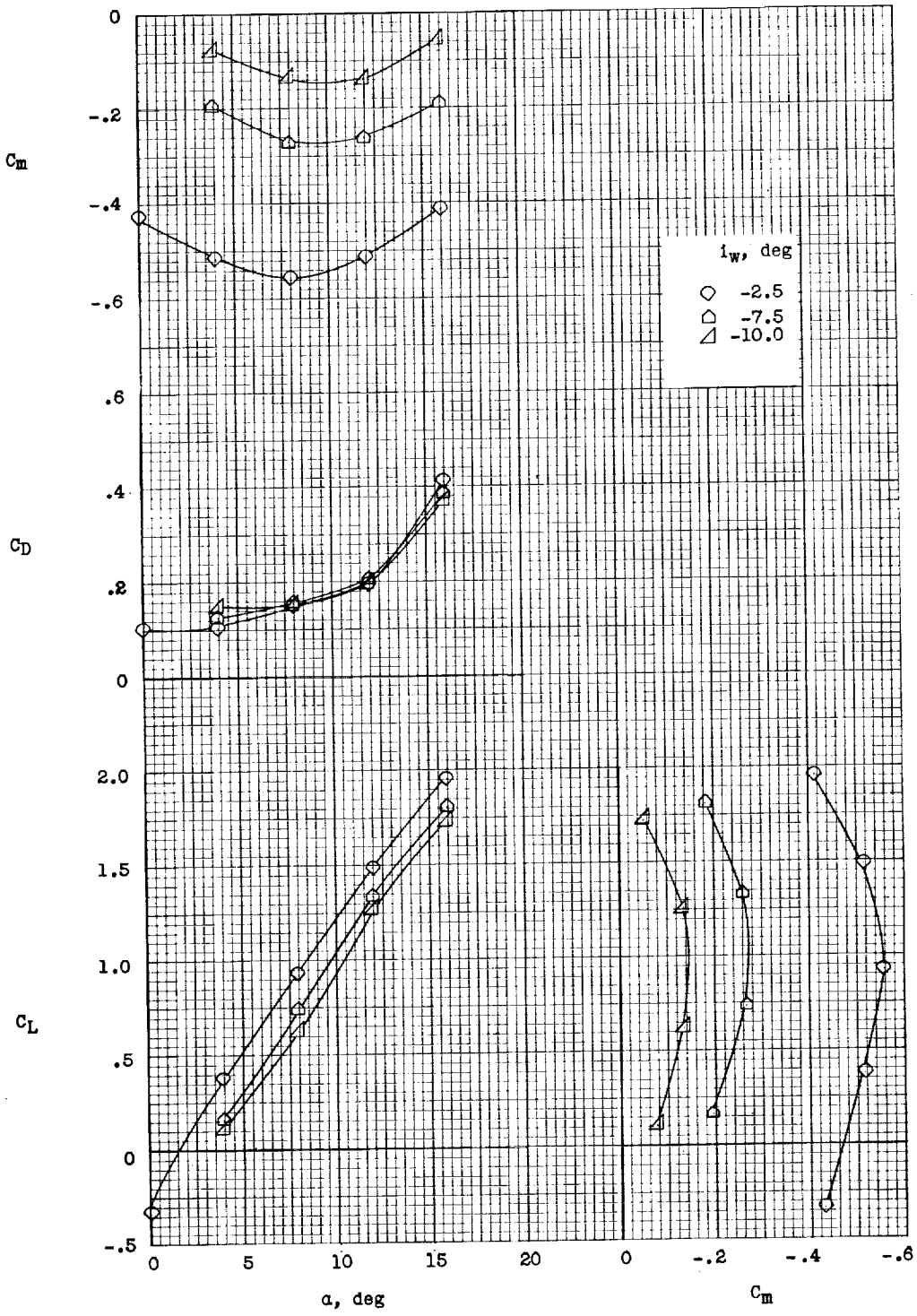

Figure 33.- Longitudinal stability and trim characteristics of OB-LO configuration. $i_{d,F} = -5^{\circ}$; $q = 5.0$; gaps sealed; ducts clean.

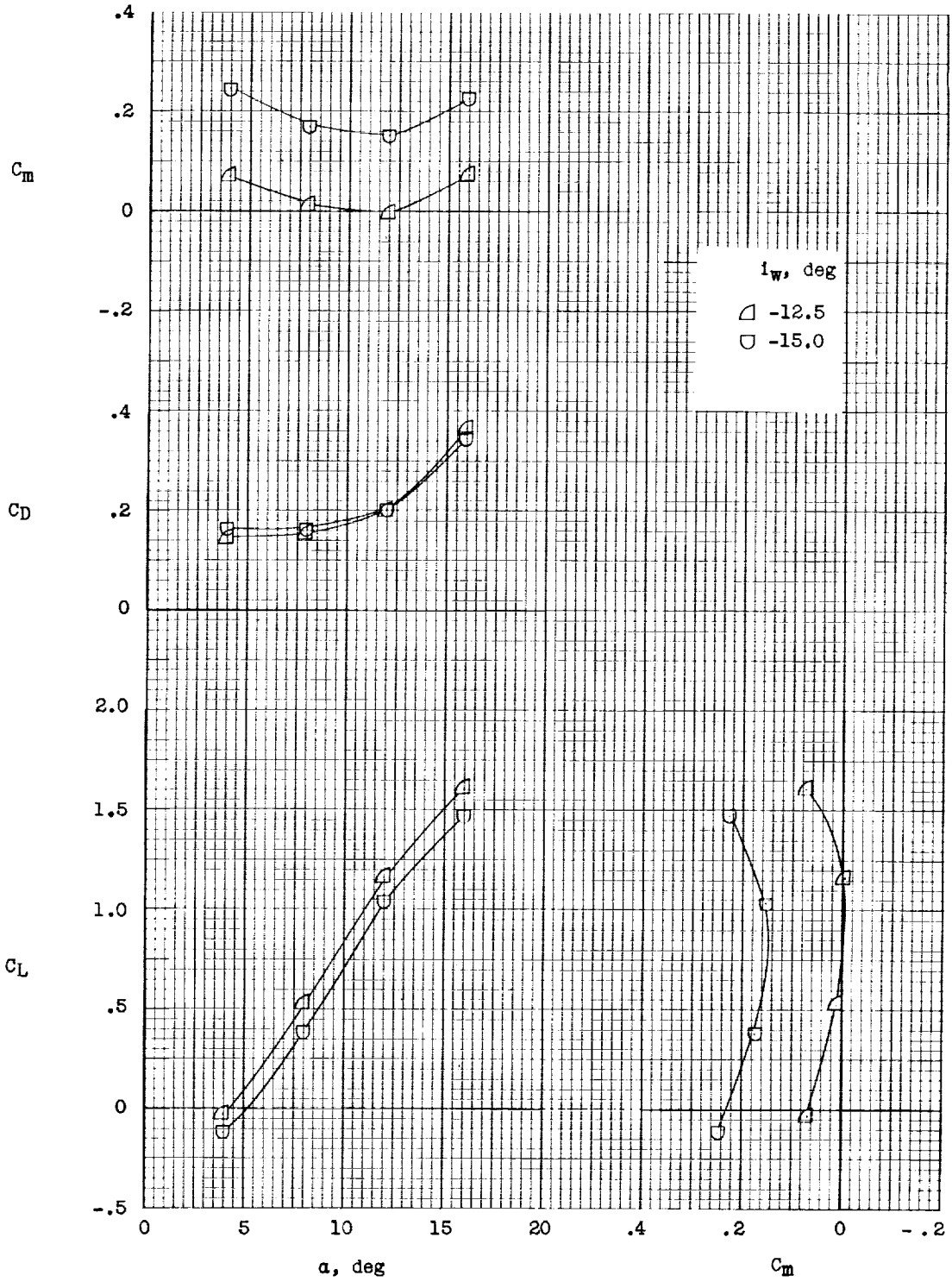

Figure 33.- Concluded.

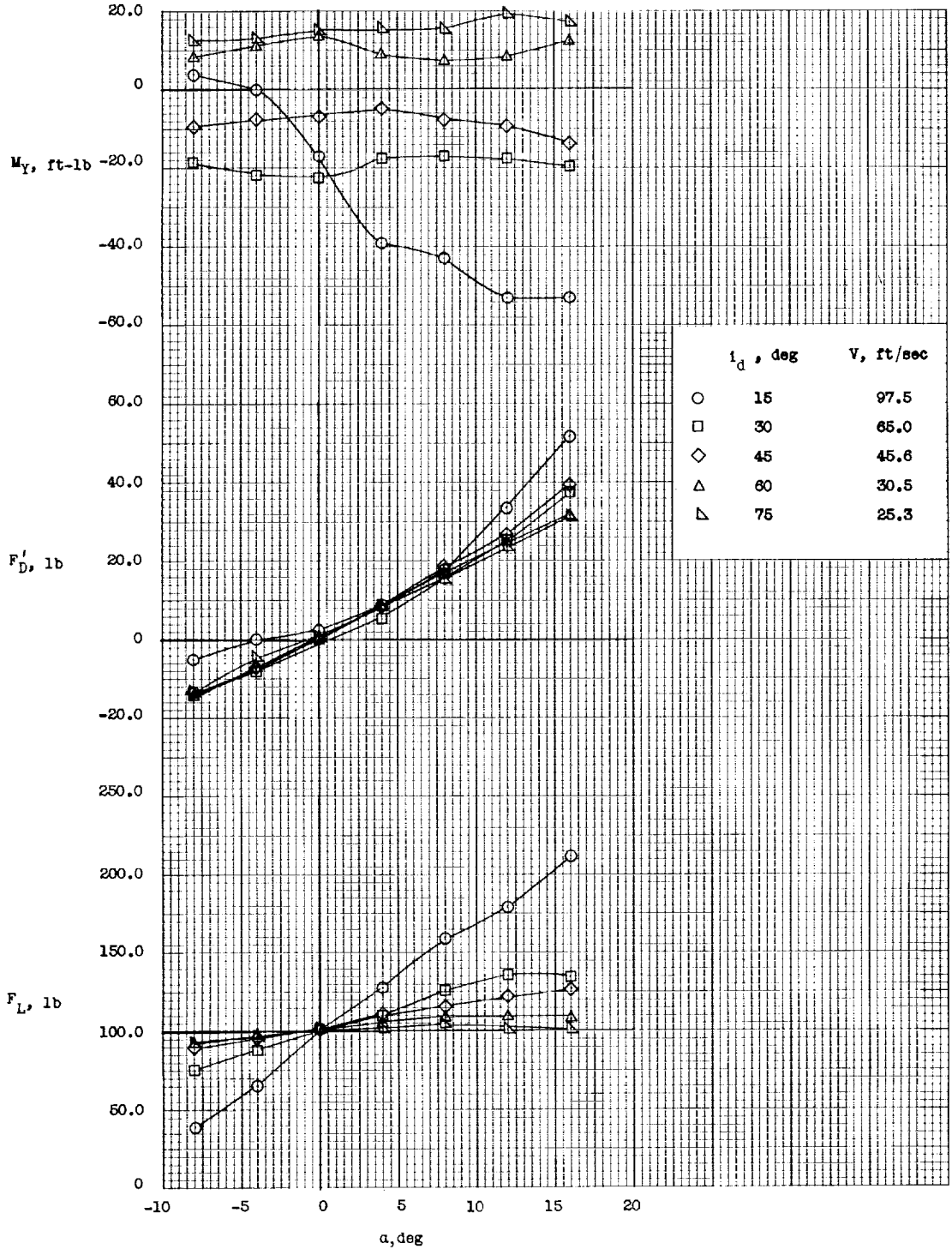

Figure 34.- Longitudinal stability and trim characteristics of IB-LO configuration during transition. $i_w = i_d - 15^\circ$; gaps unsealed.

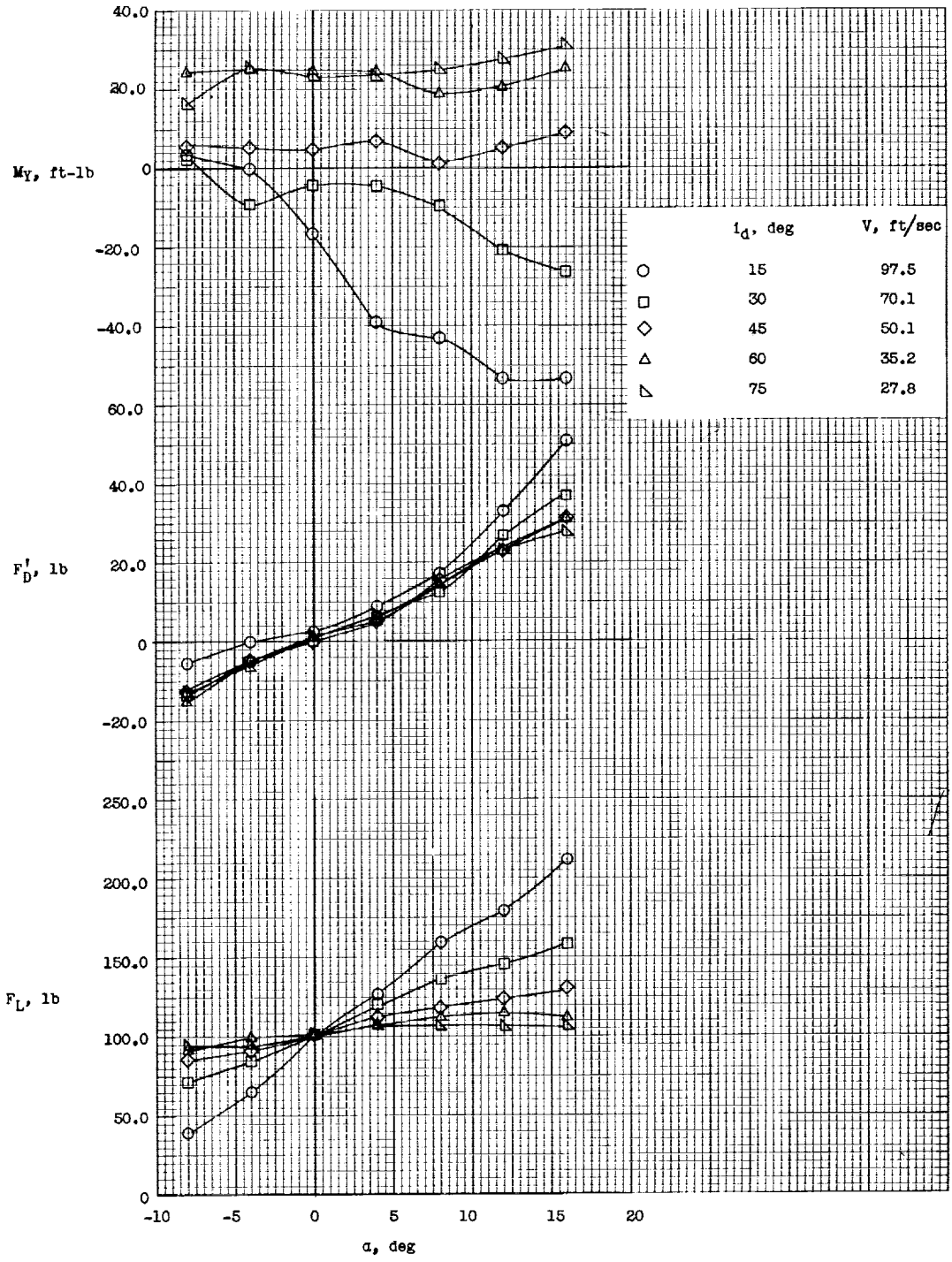

(a) Zero forward acceleration.

Figure 35.- Longitudinal stability and trim characteristics of IB-LO configuration during transition. $i_w = 0^o$; gaps unsealed.

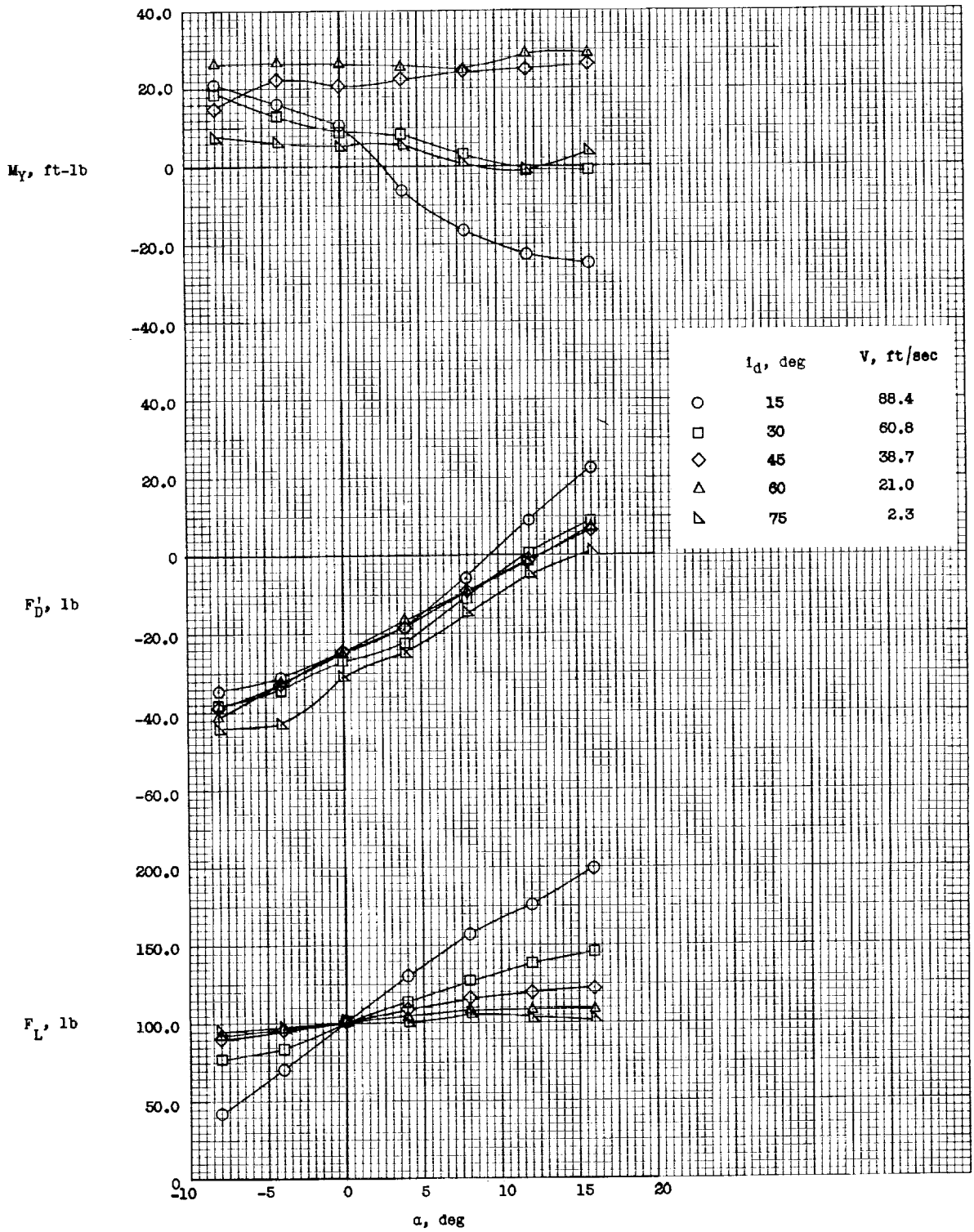

(b) 0.25g acceleration.

Figure 35.- Continued.

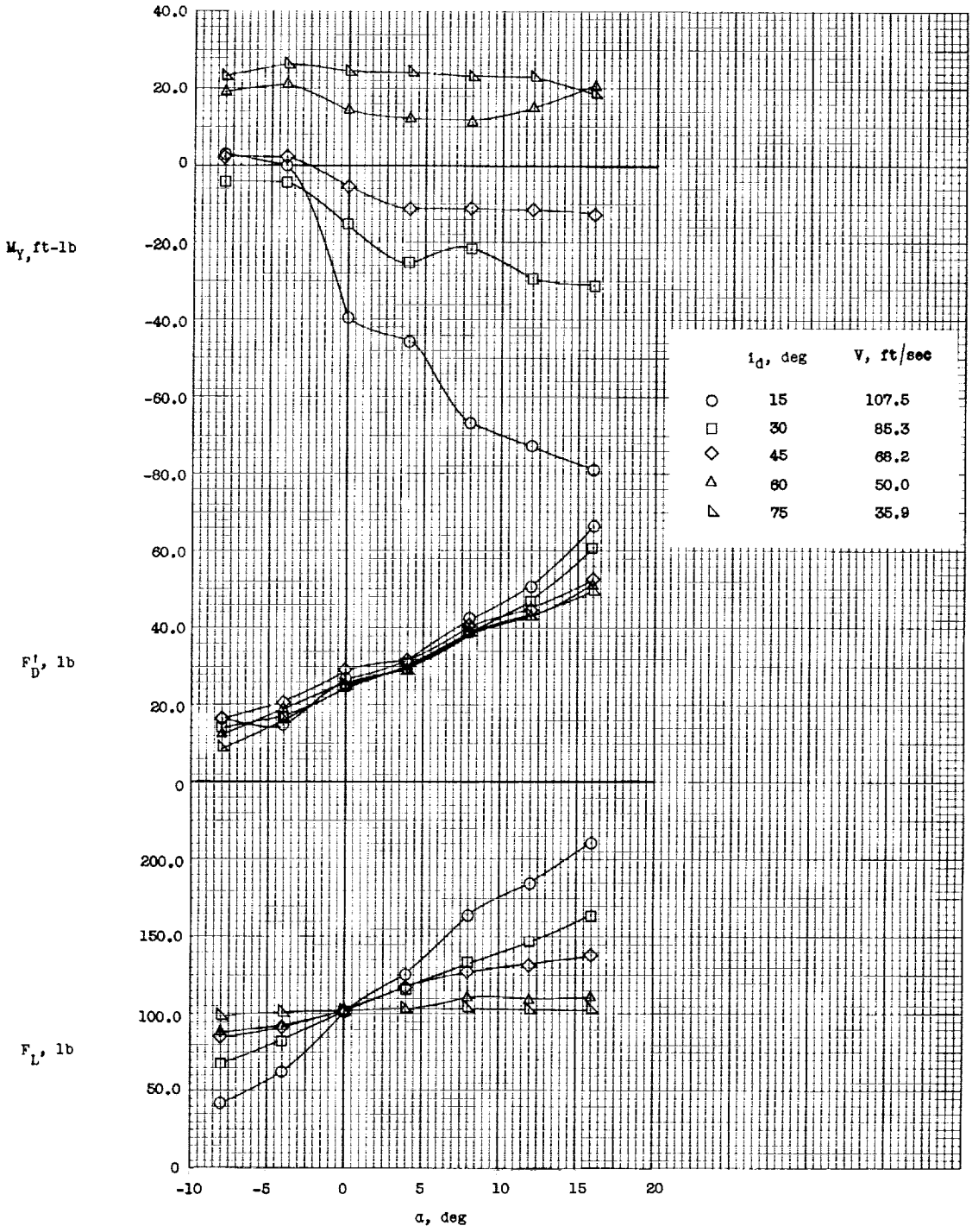

(c) 0.25g deceleration.

Figure 35.- Concluded.

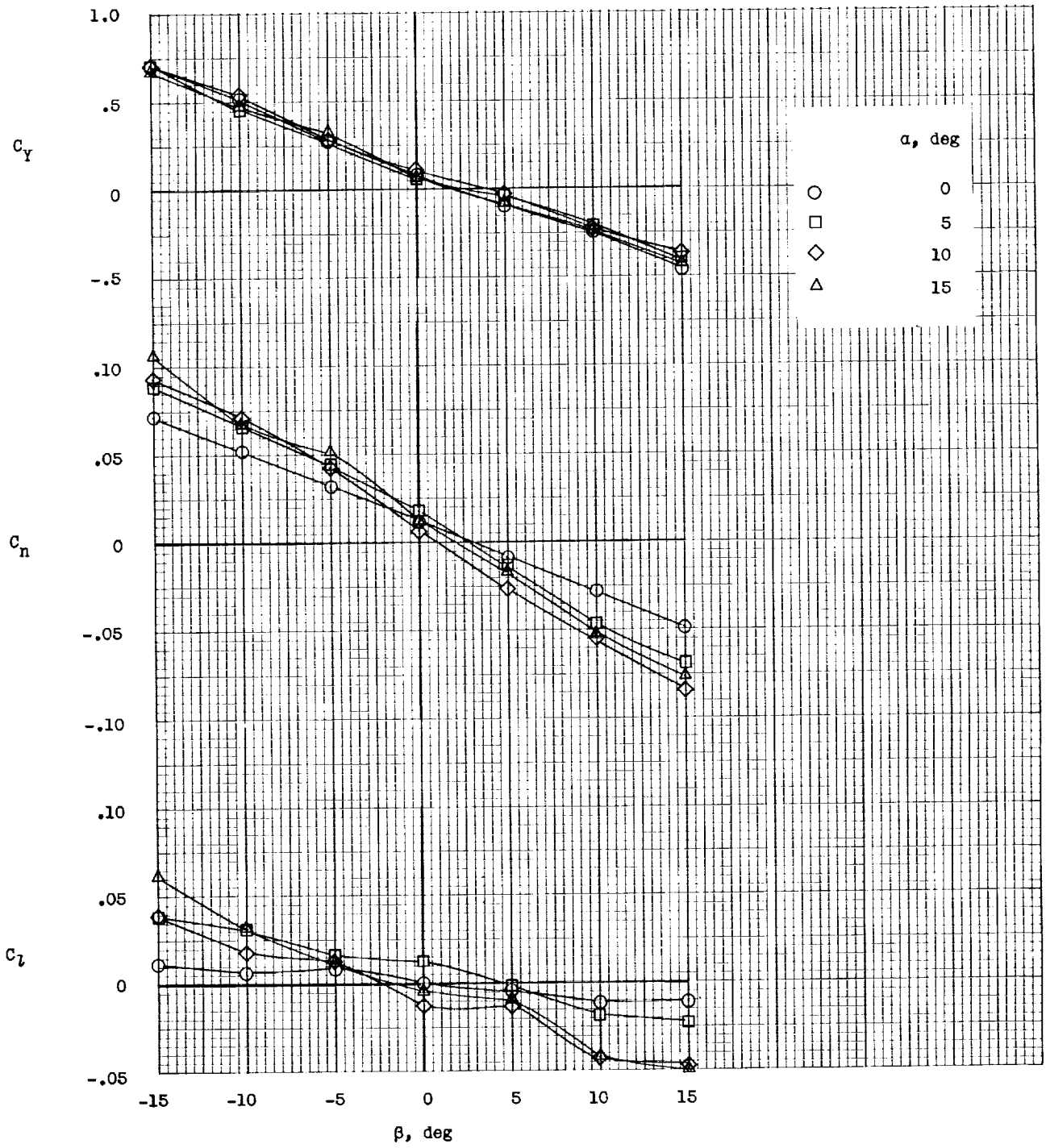

(a) Tail off.

Figure 36.- Lateral stability characteristics of IB-LO configuration in cruise flight with various tail arrangements. $i_d = 0^o$; q = 1.72; gaps unsealed.

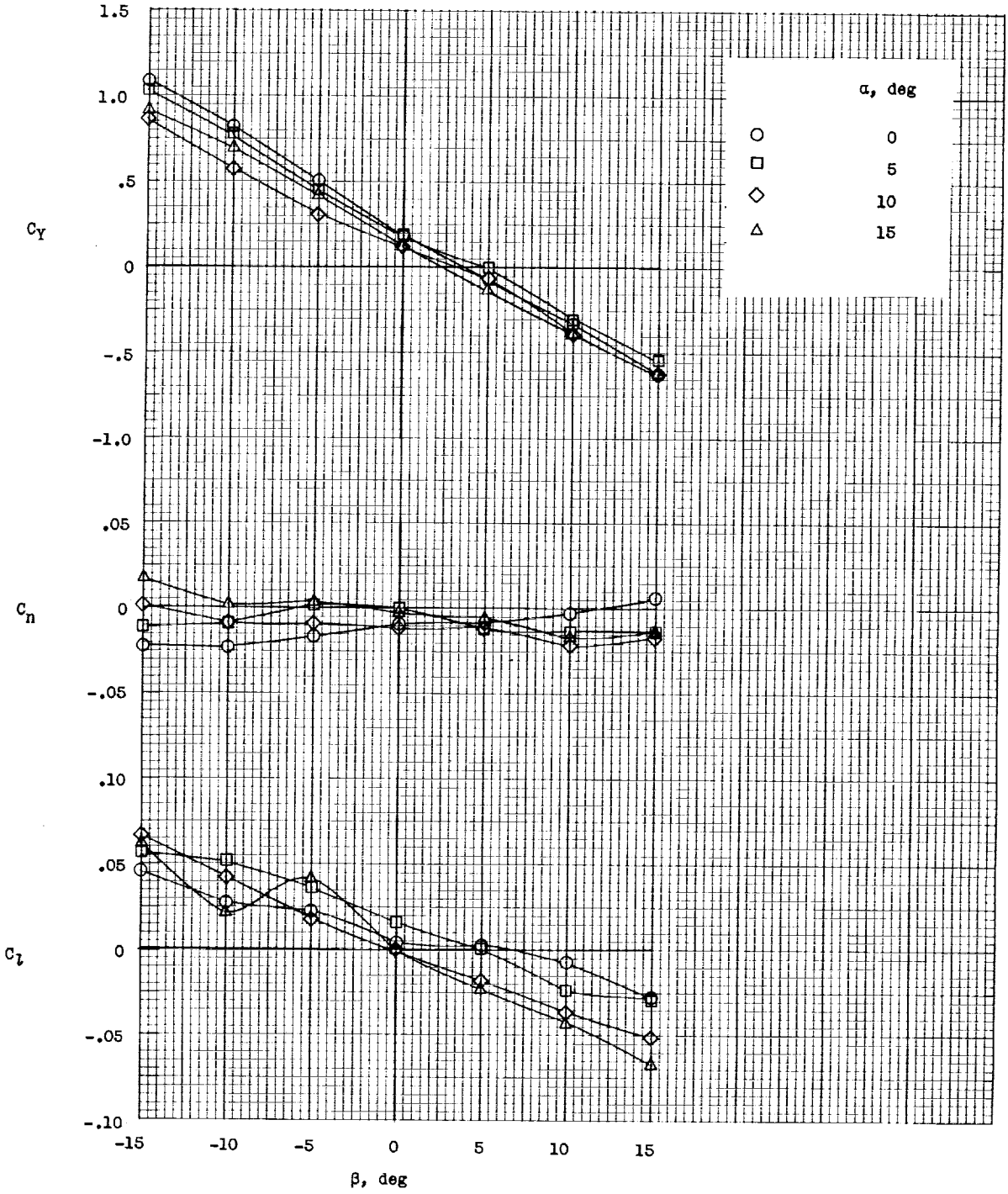

(b) Center tail.

Figure 36.- Continued.

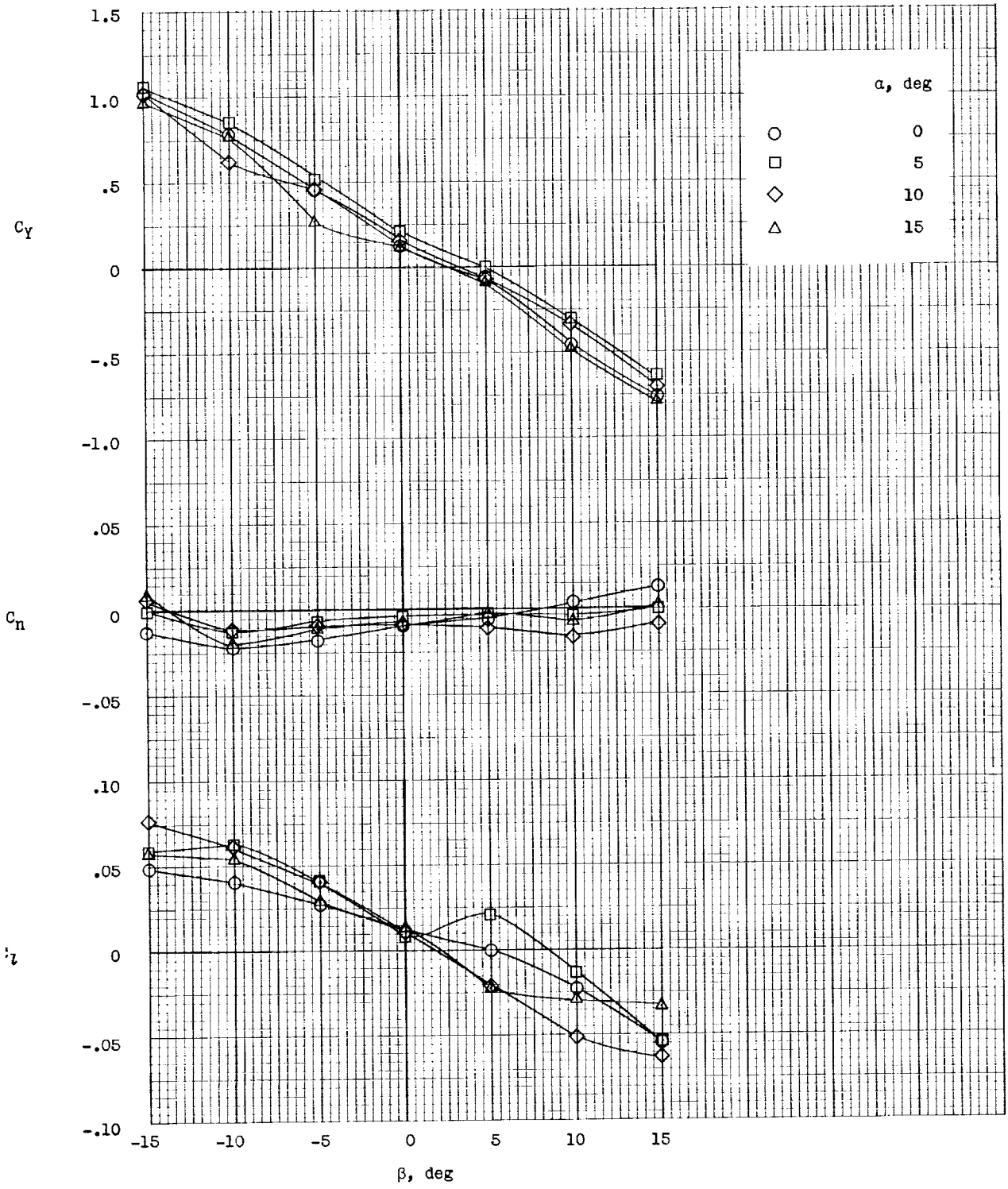

(c) Twin tails.

Figure 36.- Concluded.

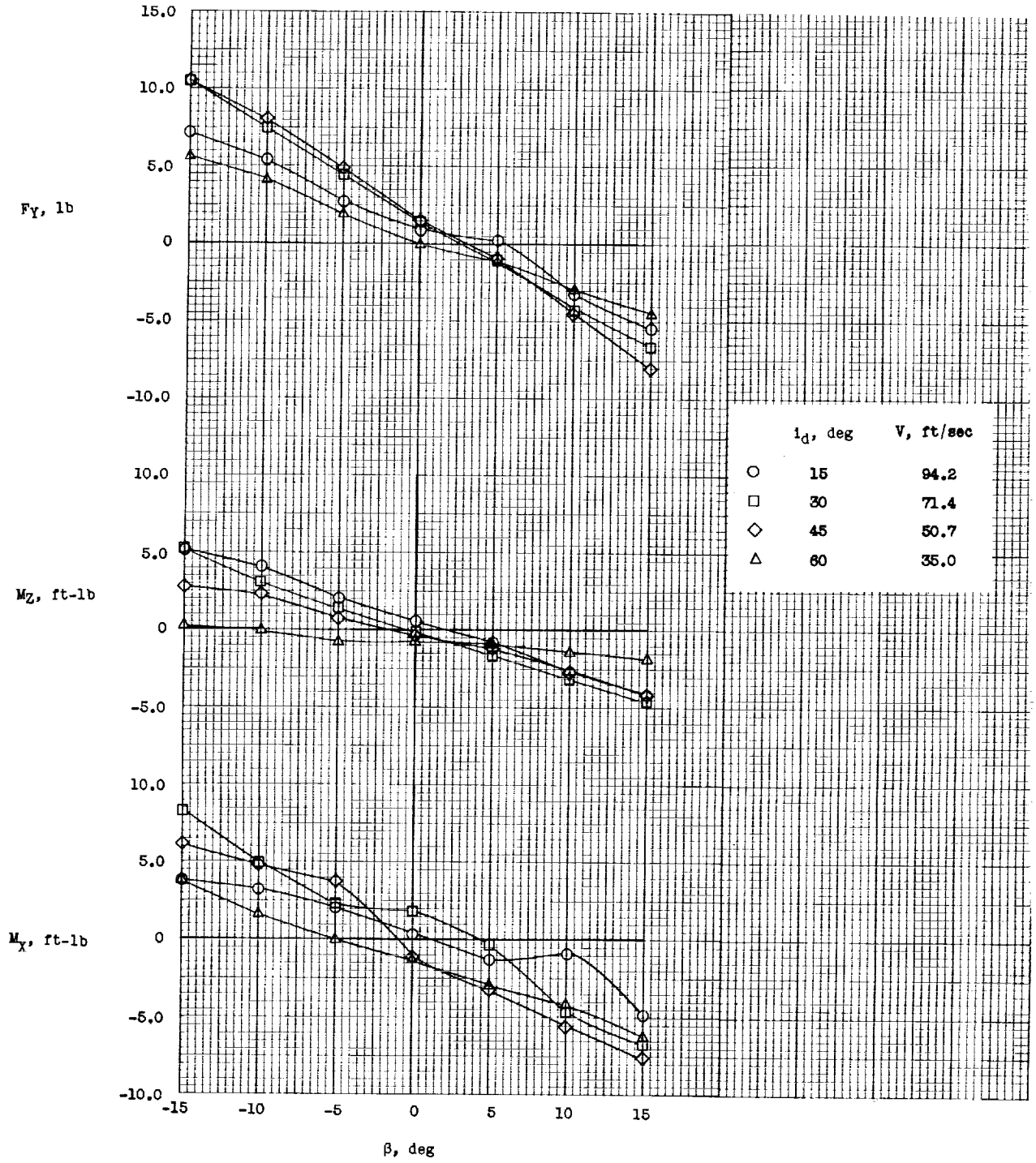

(a) Tail off.

Figure 37.- Lateral stability characteristics of IB-LO configuration during transition flight with two vertical-tail arrangements. Zero acceleration; gaps unsealed.

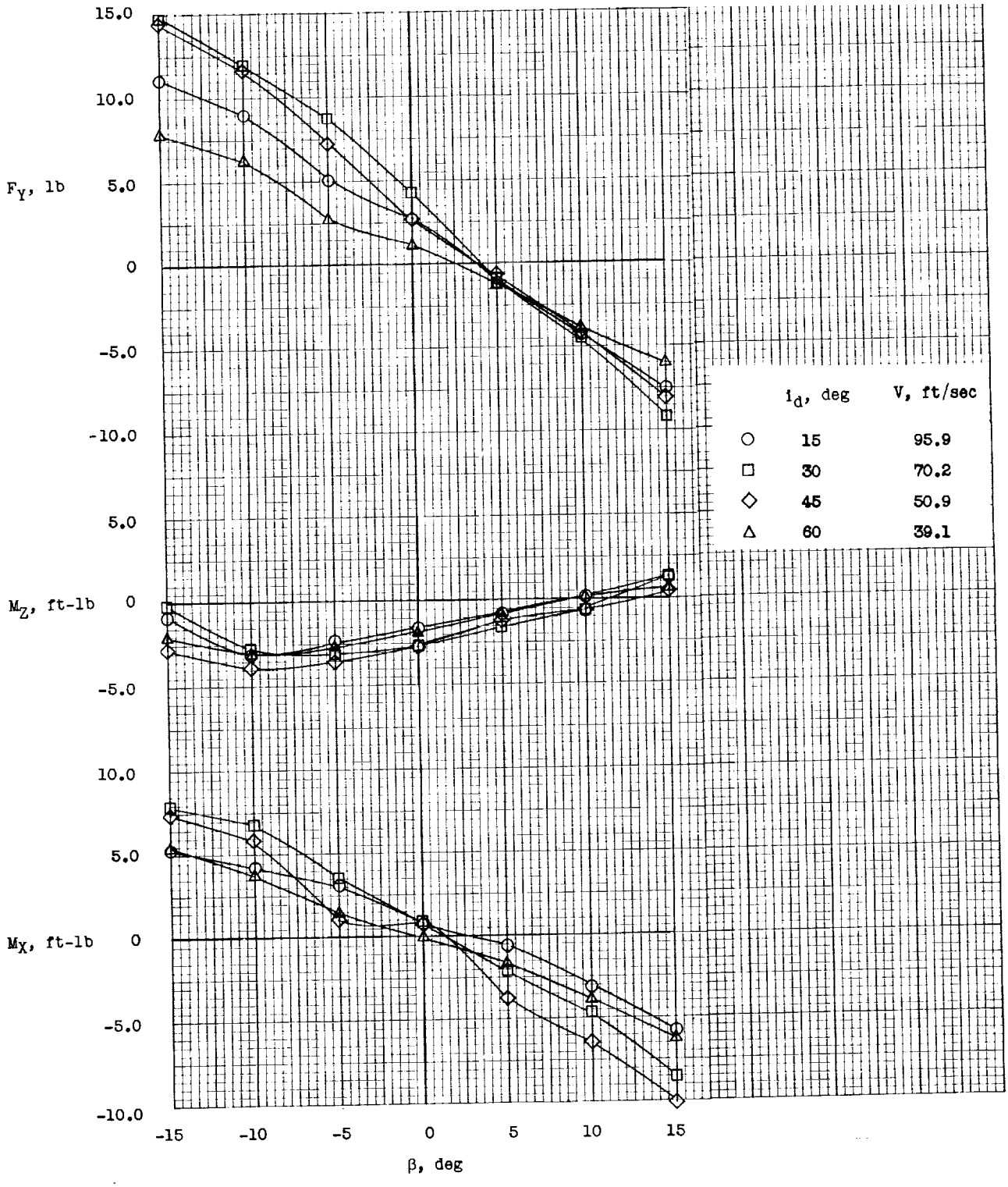

(b) Center tail.

Figure 37.- Concluded.

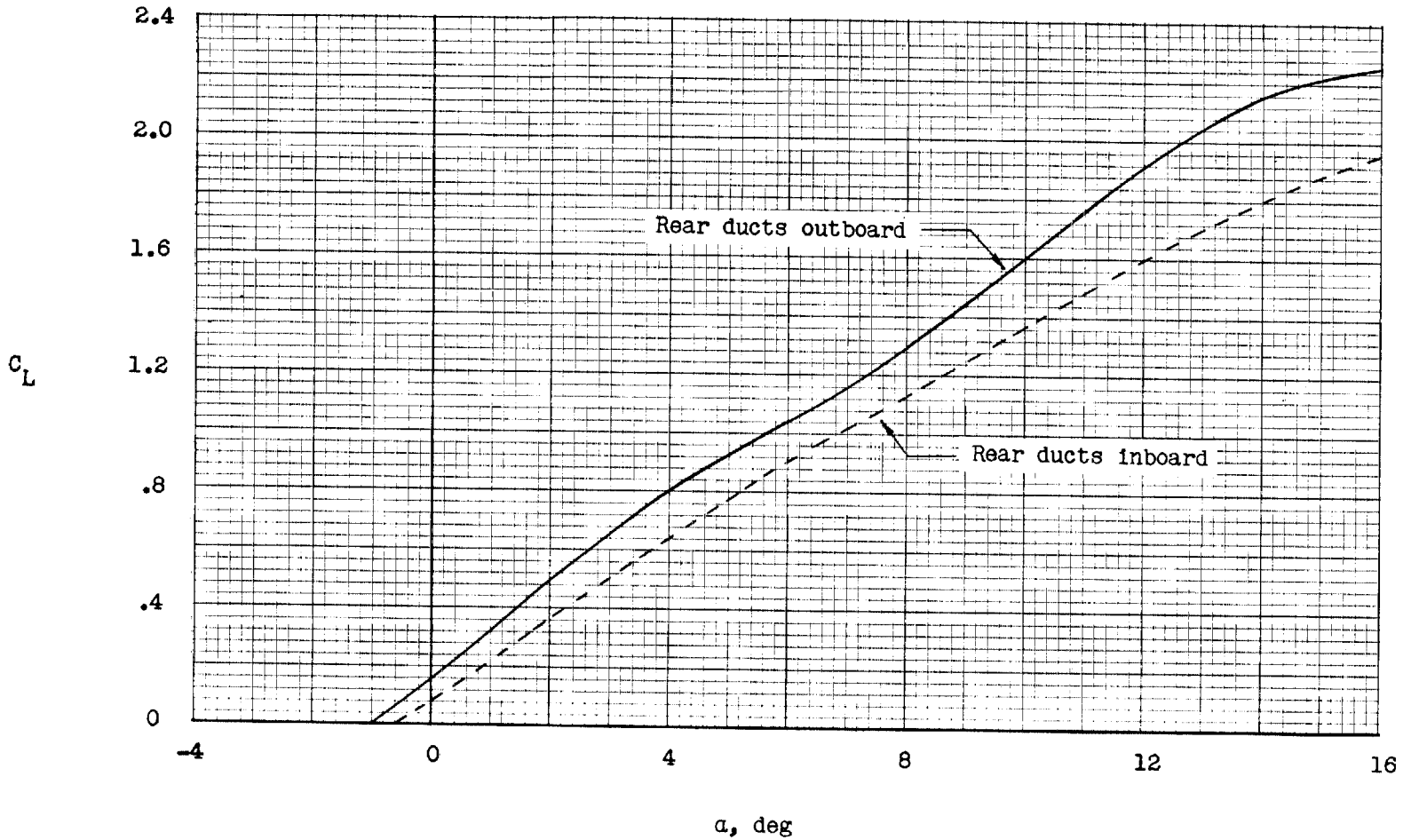

Figure 38.- Lift characteristics in cruise. $C_m = 0$. (Data from figs. 14 to 33.)

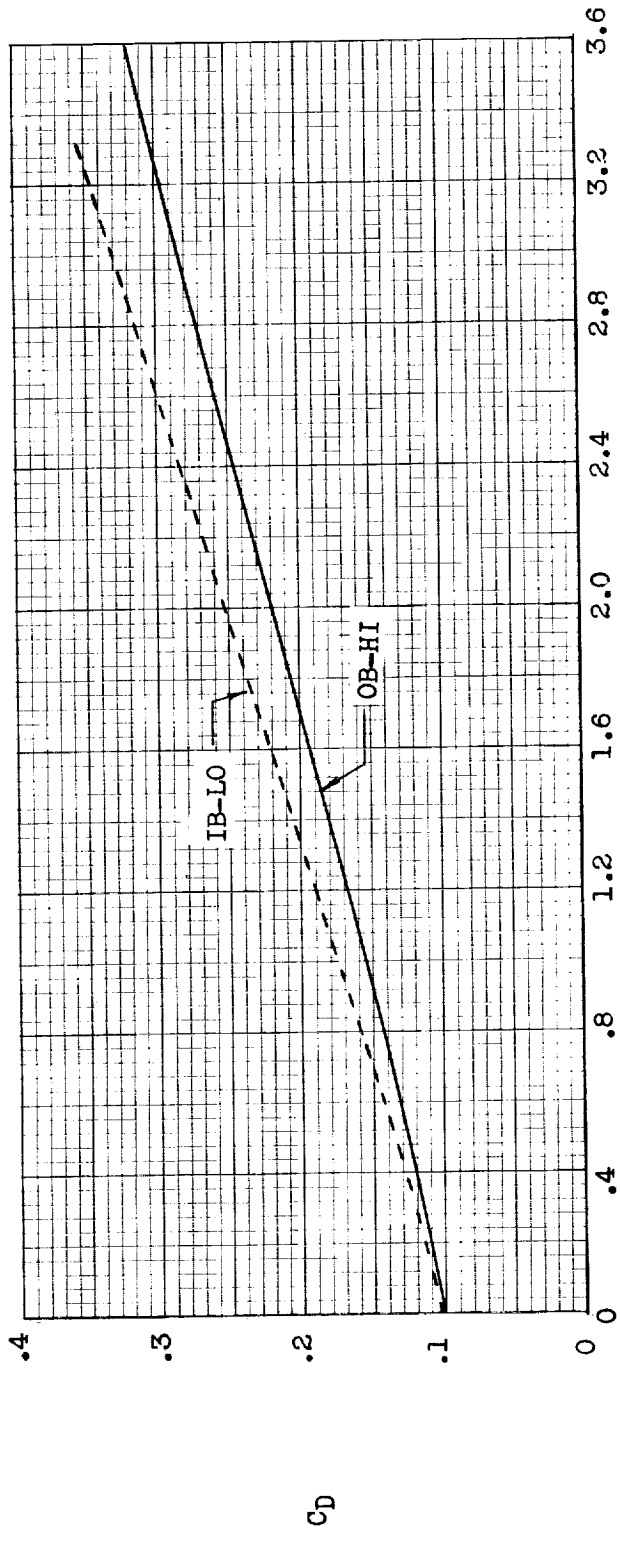

Figure 39.- Drag characteristics in cruise. $C_m = 0$. (Data from figs. 14 to 33.)

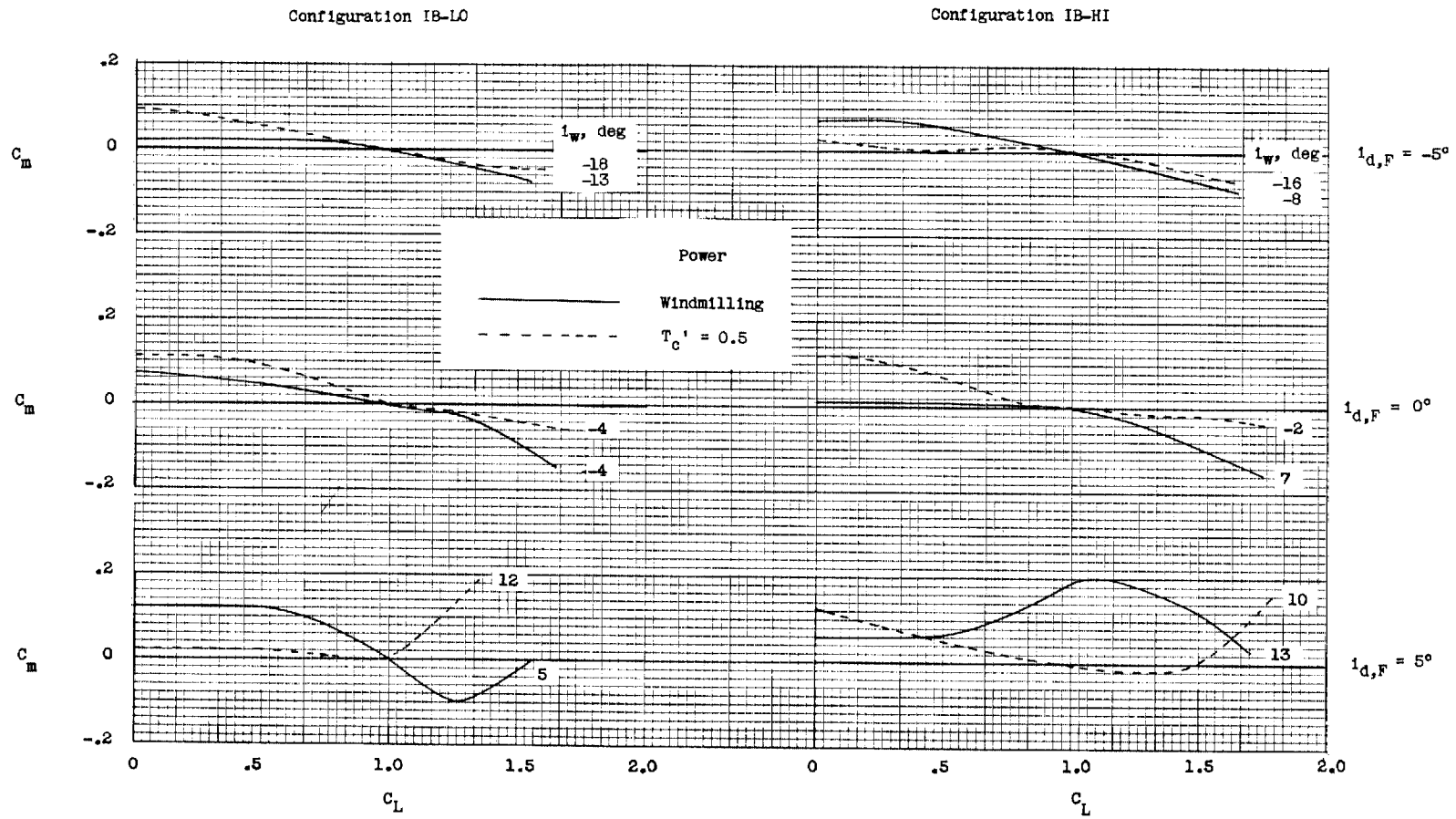

(a) Rear ducts inboard.

Figure 40.- Longitudinal stability in cruise. $C_m = 0$ at $C_L = 1.0$. (Data from figs. 2 to 13.)

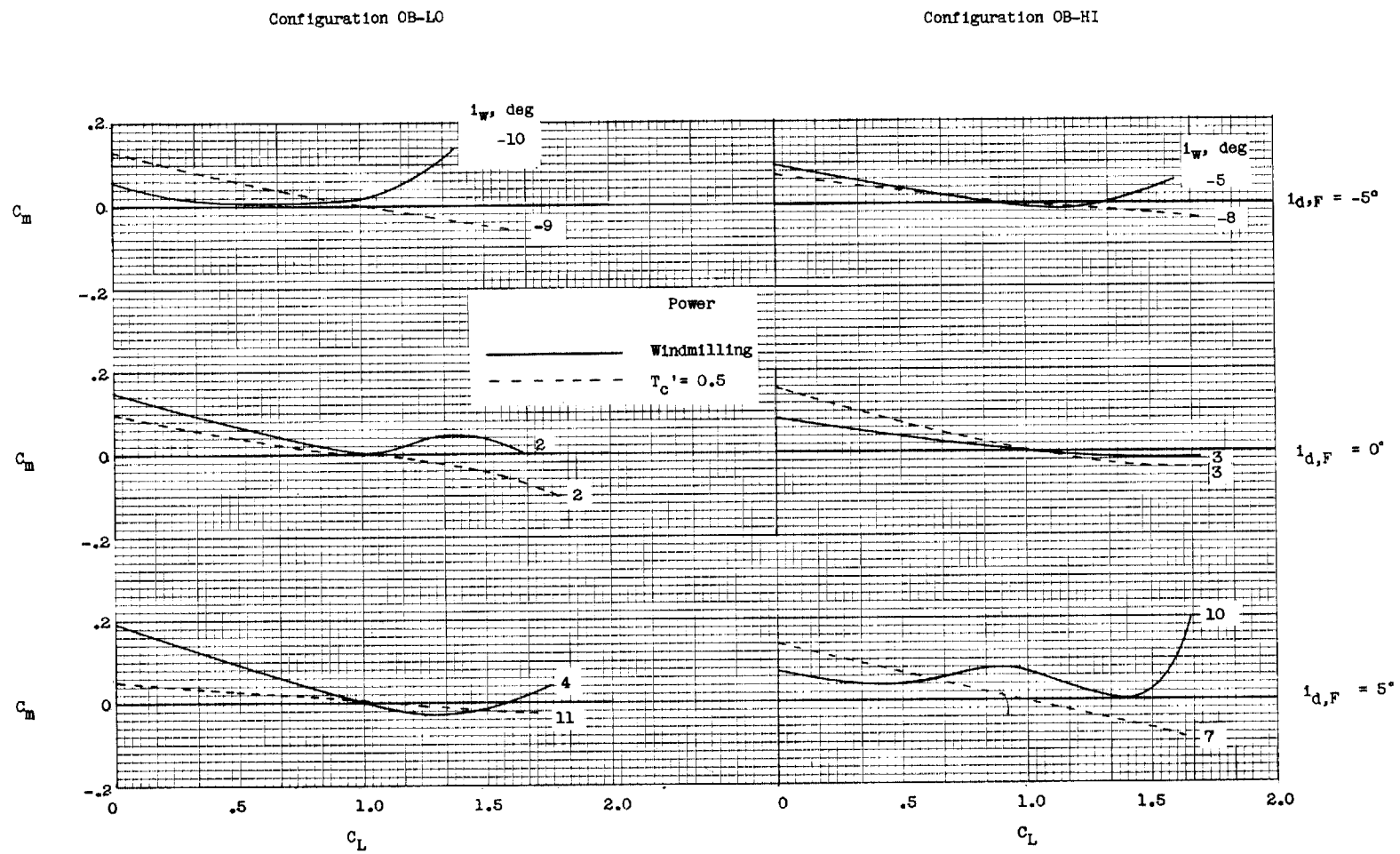

(b) Rear ducts outboard.

Figure 40.- Concluded.

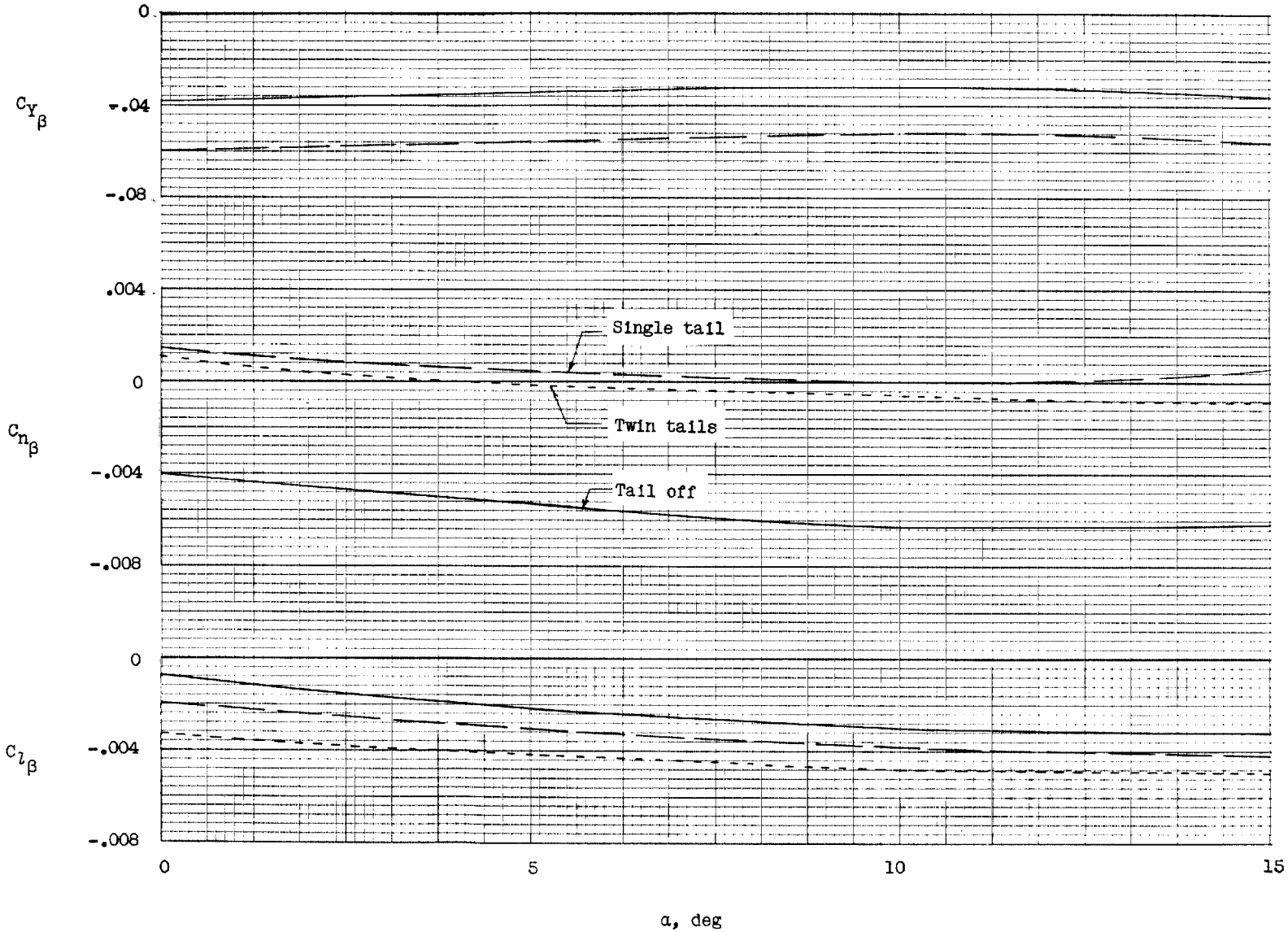

Figure 41.- Lateral stability in cruise for IB-LO configuration. $C_D = 0$. (Data from fig. 36.)

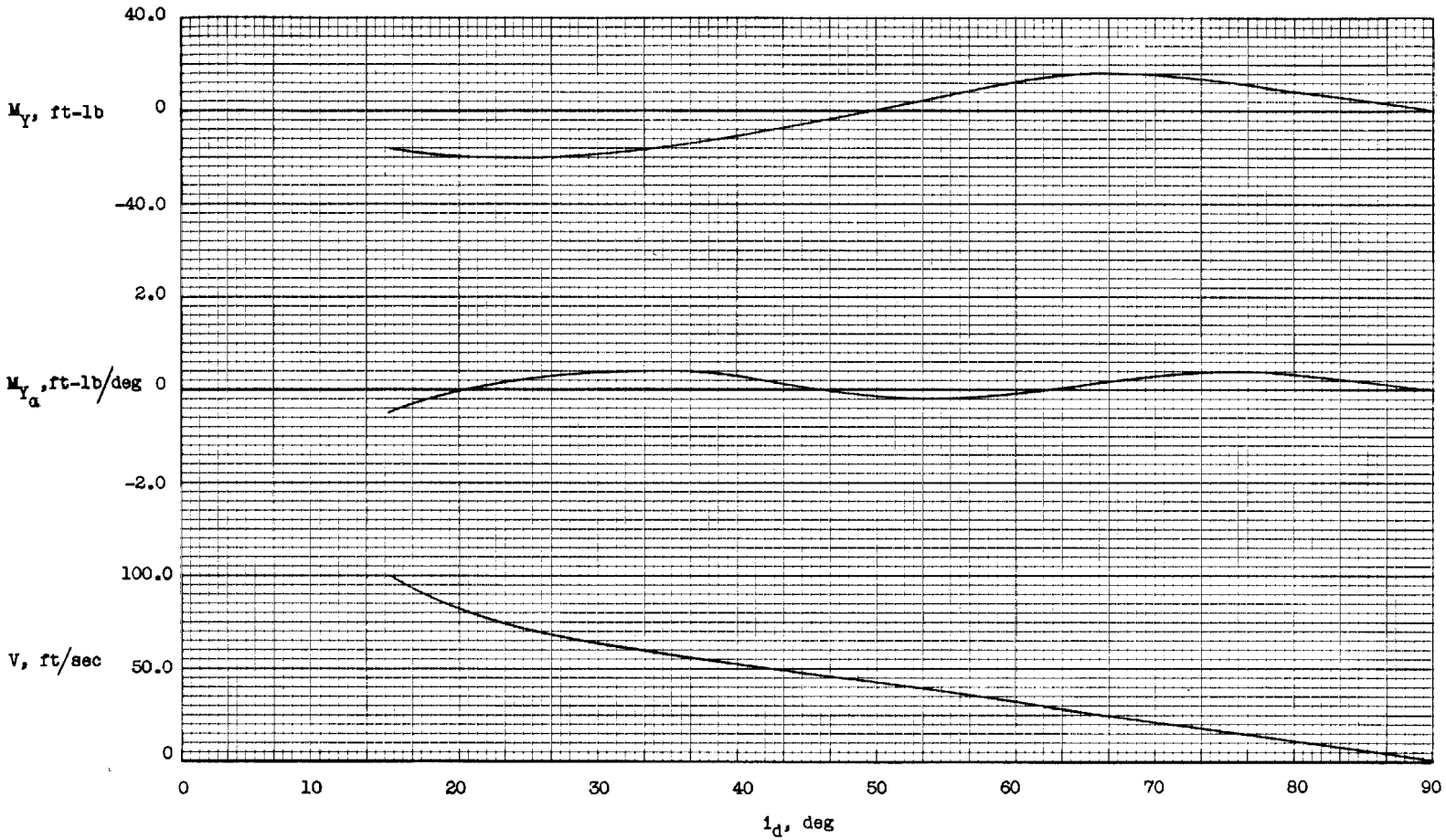

Figure 42.- Longitudinal stability and trim in transition for IB-LO configuration at $\alpha = 0^\circ$ and $C_D = 0$. (Data from fig. 34.)

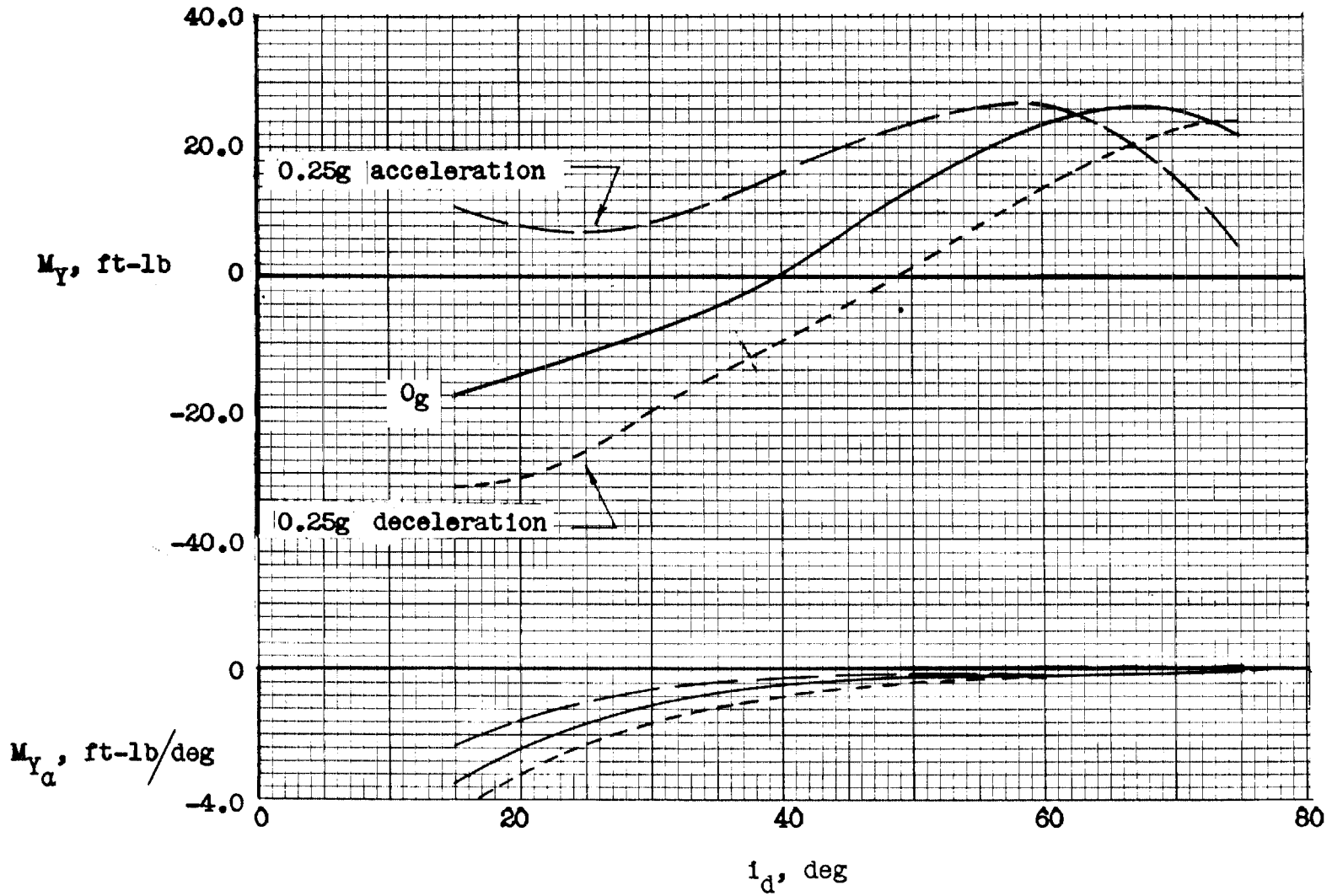

Figure 43.- Effect of longitudinal acceleration on IB-LO configuration. (Data from fig. 35.)

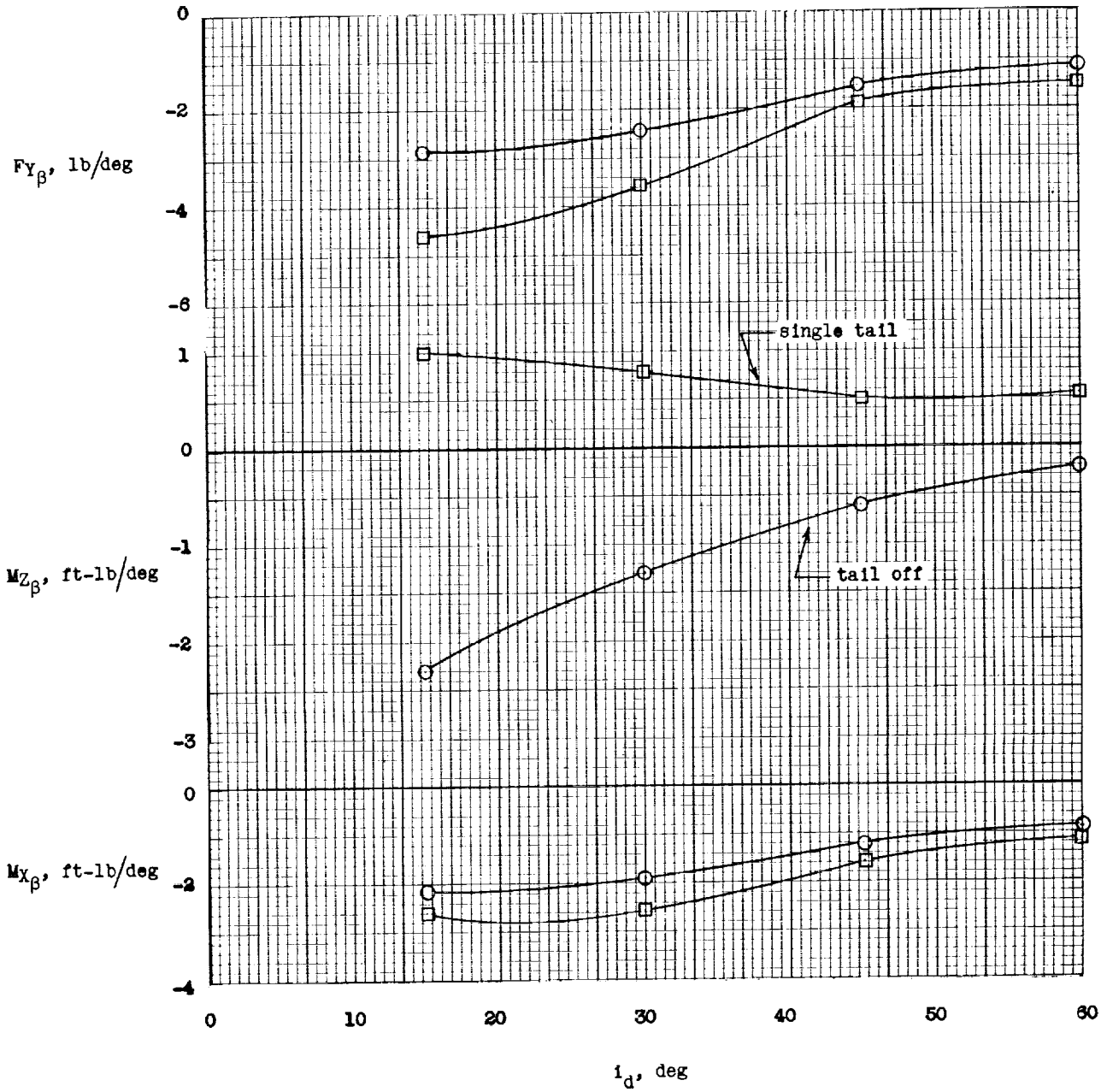

Figure 44.- Lateral stability in transition for IB-LO configuration. (Data from fig. 37.)